Design Considerations and Implementation of an Electromechanical Battery System

David Johnson Pr. Eng.

B.Sc.(Mechanical)1987, M.Sc. (Electrical) 2001

Thesis Presented for the Degree of

DOCTOR OF PHILOSOPHY

in the Department of Electrical Engineering

UNIVERSITY OF CAPE TOWN

August 2007

djohnson

Design Considerations and Implementation of an Electromechanical Battery System

Abstract:

This thesis covers the design and implementation of a low cost electromechanical battery using an outside rotor permanent magnet Halbach array with hybrid magnetic bearings and heat pipe cooling. The theoretical calculations include finite element analysis. A dipole Halbach array produces a uniform flux distribution inside the cylindrical stator, where straight windings on an iron-less stator are placed near the inner boundary.

Special emphasis is placed on implementing the Halbach array, using even and odd numbers of magnet segments. The aim was to establish a generic formula for the orientation of magnets in dipole- and multi pole arrays, using standard rectangular or square shape magnets.

The position of the windings inside this field does not affect the efficiency of the machine, as the flux distribution is homogeneous in the entire airspace. When the motor is operated continuously, these variations become insignificant.

The motor is suspended on a hybrid magnetic bearing without active control. Two radial repelling magnetic bearings are used in combination with an axial journal bearing, like a spinning top with the precession limited by radial magnetic bearings. The theoretical values were found to be consistent to those measured on a working model.

A high speed, ultimate energy density shape composite flywheel, which incorporates the electric machine and hybrid magnetic bearing was chosen. It is to be operated in a vacuum or partial vacuum, where the machine / bearing system approaches efficiencies in the upper 90s. One model, using an approximated Halbach array motor model showed an electrical to mechanical efficiency of

97%, disregarding mechanical losses. The ultimate shape model was designed to run at speeds up to 90000 rpm with a capacity of 300W-h.

The practical difficulties experienced with prototyping the laboratory model are discussed, manufacturing, as well as assembly difficulties operating problems with the flywheel are noted and solutions proposed.

International papers published were in "High-speed, low-cost flywheels for energy storage in sustainable power systems with distributed generation" IEEE PES (2001), [1] "High speed PM motor with hybrid magnetic bearing for kinetic energy storage" IEEE IAS (2001) [2].

Acknowledgements

I would like to acknowledge the following persons for their contributions to this project:

To my supervisor, Dr Pragasen Pillay, for his guidance

To the lab supervisor, Chris Wozniak, for his assistance and advice with equipment

To my wife, for her support.

To my son, for quality time lost with his father.

Table of Contents

Illustration Index

Index of Tables

List of symbols

a_{11} = fibre orientation factor to respect the reference system 123.

a_{22} = fibre orientation factor to respect the reference system 123.

c_e = Specific heat enclosure.

c_f = Specific heat flywheel debris.

d = diameter, fibre diameter. [m]

e, $e(k,w)$ = normalized specific kinetic energy.

k = normalized speed.

m_f = mass of flywheel debris. [kg]

m_e = enclosure mass. [kg]

n = Speed. [RPM]

g = gravitational constant of 9.81. [m/s^2]

i = current. [A]

l_c = critical length.

r = radius. [m]

r_1 = inner radius. [m]

r_2=outer radius. [m]

t = time. [s]

t_d = time to decelerate. [s]

y = thickness of section. [m]

A = Area. [m^2]

A_s = characteristic area for shear. [m^2]

B = Magnetic Flux, resultant flux density. [T]

B_O = Bond number.

B_r = remanence of the rare earth magnet. [T]

C_D = Coefficient of pressure.

C_f = Skin friction coefficient.

D = Diameter of cylinder. [m]

E = Induced machine electromotive force [V], Voltage [V], Young's modulus[GPa], Specific energy. [J/kg]

E_D = Specific energy of disk. [J/kg]

$E_{(all)}$ = Young's modulus. [GPa]

E_{11}, E_{22} = Modulus of elasticity with respect to the reference system 123. [GPa]

F = Force. [N]

F_n = normal force. [N]

F_c = correcting force. [N]

F_0 = Force per unit length at circumference of the disk. [N/m]

G = Shear Modulus. [GPa]

F_D = Drag Coefficient.

F_P = Pressure drag.

F_f = Skin friction drag.

I = Winding Current {A], Mass Moment of Inertia.

K = machine constant.

K_U = Kutateladze number.

L = length of conductor. [m]

M = number of Magnet segments.

N = Number of poles, Number of turns, rotational speed. [RPM]

P_N = Frictional power loss. [W]

Q = Heat transfer rate. [W]

R = Resistance[Ohm], radius. [m]

ΣR = Sum of thermal resistances.

R_{as} = Thermal resistance of Condensing Acetone to Stainless steel.

R_{cr} = Thermal resistance of Copper to resin.

R_e = Reynolds Number.

R_{ga} = Thermal resistance of Composite to boiling Acetone.

R_{rg} = Thermal resistance of Resin to Glass fibre/epoxy composite.

R_{sa} = Thermal resistance of Stainless steel to air.

$S_R(R)$ = Radial stress at radius R [MPa]

$S_T(R)$ = tangential stress at radius R. [MPa]

S_{MAX} = Tensile strength. [MPa]

T = Torque, Frictional torque. [Nm]

T_c = Sink side temperature. [degrees C, K]

T_d = decelerating torque. [Nm]

T_h = hot end temperature. [degrees C, K]

V = the surface speed, Velocity of fluid over a body [m/s]

V_D = tip velocity of the ring or disk [m/s]

V_f = Volume fraction of fibres [$0 \leq V_f \leq 1$].

V_i = Induced Voltage [V]

V_l = Volume liquid [m^3]

V_c = Volume column [m^3]

$V_{L\text{-}L}$ = RMS Line to Line Voltage [V]

V_{PH} = RMS Phase voltage [V]

W = Kinetic energy in Joules

$W_{(R)}$ = function defining the disk thickness at radius R [m]

X = circumference of the Flywheel [m], distance from edge [m]

Z = plane of rotation

$2R_0$ = disk diameter [m]

α = angle of rotation from the normal (Figure 2.2)

δ = angle from the start angle [rad, degrees]

δ L off the centre, the point of contact will be at

δ L + δ l from the centre and normal to the arc R:

η = Machine efficiency

μ = Coefficient of friction, dynamic viscosity [N.s/m^2]

ν = Poisson's ratio

ω = angular velocity [s^{-1}]

ϕ = rotation angle [rad, degrees]

ρ = density [kg/m^3]

ρ_l = density, liquid [kg/m^3]

ρ_v = density, vapour [kg/m^3]

σ = Surface tension, [N/m]

σ_c = Ultimate tensile stress [MPa]

σ_f = tensile stress of fibres [MPa]

σ_m = tensile stress of matrix [Mpa]

σ_U = Ultimate axial stress [Mpa]

τm = Shear Stress on matrix

θ = displacement angle [rad]

ψ = Fill charge ratio [%]

ΔQ = Change in thermal energy in flywheel debris and enclosure

$\Delta\sigma_r$ = Change in radial stress

$\Delta\sigma_t$ = Change in hoop stress

Δy = Change to thickness of adjacent section

ϑ = angle to rotate the magnetization direction

Φ = Flux density

Γ = Material density [kg/m3]

Table of Acronyms

AC . . . . . Altenating current

ADC . . . . . Analog to Digital Converter

BIT . . . . . Binary Digit

CAD . . . . . Computer Aided Design

COTS . . . . . Commercial off-the-shelf

C-C . . . . . Carbon-Carbon

DC . . . . . Direct current

DC-DC . . . . . Direct Current to Direct current

DC-AC . . . . . Direct Current to Alternating Current

FET . . . . . Field Effect Transistor

IC . . . . . Integrated Circuit

IGBT . . . . . Insulated Gate Bipolar Transistor

IO . . . . . Input/Output

IR . . . . . Infra Red

LED . . . . . Light Emmiting Diode

LSB . . . . . Least Significant Bits

MMF . . . . . Magneto Motive Force

MOSFET . . . . . Metal Oxide Field Effect Transistor

PM . . . . . Permanent Magnet

RMS . . . . . Root Mean Square

RPM . . . . . Revolutions per Minute

1 Introduction

1.1 General

The electricity requirements in developing countries are unlike those in the developed world, and special consideration in terms of availability, location, source, storage and cost are needed. This study focuses on the application of kinetic storage, especially tailored for "island" type applications, for example a small town which is not connected to an electric grid and depends on renewable energy sources.

The availability of high strength fibre composites, low cost rare earth magnets, micro-electronics, modern design tools and computational abilities make it possible to produce Finala durable, non-polluting, non-toxic and cost effective kinetic battery. Kinetic batteries have an exceptionally good turnaround efficiency and are especially well suited for deep and frequent discharges, without the destructive effects suffered by chemical batteries. This makes them particularly attractive to be used with renewable energy sources that are intermittent in nature, where high and deep battery cycling is anticipated. The initial higher cost of kinetic energy storage can be offset by their improved efficiencies and longer life expectancy.

The problems posed by chemical batteries commonly used in rural electrification include their poor efficiencies, comparatively short life, environmental and toxicity factors. Consequently, this requires special handling, maintenance, storage and disposal procedures as well as frequent replacements. In a developing country, cost alone will cause consumers to push the limits in terms of size and usable life. Inadequate maintenance and the expense of proper disposal results in batteries being dumped inappropriately.

Poor battery efficiencies necessitates the use of larger, and thus more expensive solar panel arrays

than would be necessary if used with more efficient storage methods. The main constituents of lead acid batteries, lead and sulfuric acid, are both highly toxic and considered environmentally unsafe, yet it is widely used in rural Africa. These batteries are especially sensitive to high and deep discharges, often shortening and sometimes terminating, their ability to function.

Kinetic batteries come at a much higher initial capital layout, but outperform lead acid batteries in efficiency, reliability, life expectancy, suitability for frequent and deep discharging as well as being chemically inert. This thesis describes an investigation of optimally designing such a flywheel with locally available materials and manufacturing capabilities to suit a rural African application.

The use of these higher cost, sophisticated, yet durable devices are to be weighed against the high cost of solar power, inefficiencies of chemical storage, their comparatively short useful service life and their negative environmental impact. The medium to high volume manufacturing costs has to be tailored to what is feasible as well as what is available in rural Africa.

At the time of this writing, multi-rim filament wound and metal-filament wound designs are being used in all commercial composite flywheel designs. In this design an ultimate shape, one-piece, short fibre, composite flywheel is proposed. It is simple to manufacture and yields a flywheel almost double the specific energy of current commercial ones. This reduces the flywheel material cost by almost half.

The service life of kinetic batteries are expected to be in the order of fifteen years, after which the power electronics may need replacement. Using composite materials brings the overall weight and cost down and have fatigue endurances up to 100 – 200 thousand stress cycles according to S. Salekeen and D.L. Jones

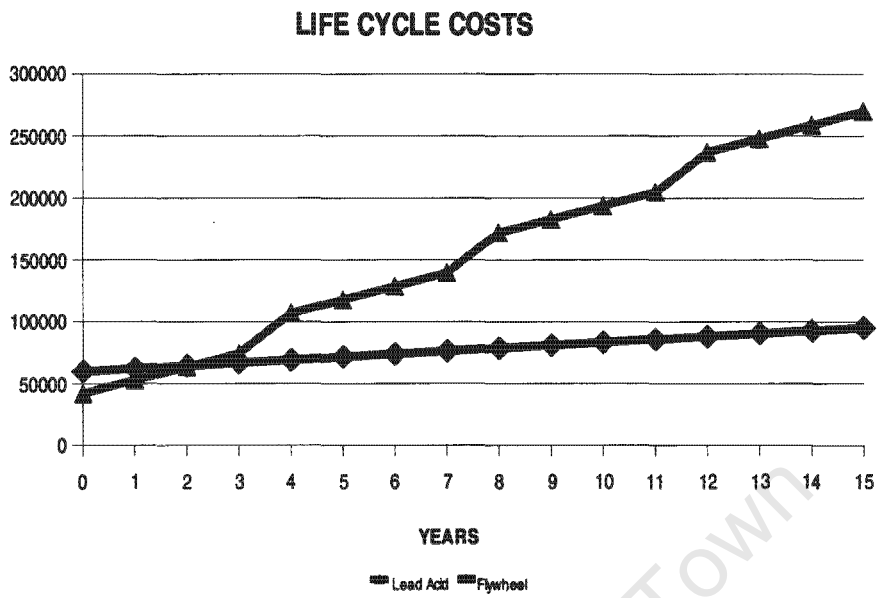

FIGURE 1.1: PENTADYNE LIFE CYCLE COSTS COMPARISON BETWEEN LEAD ACID AND FLYWHEEL BATTERIES

Shown in Figure 1.1 is a graph from Pentadyne showing how the cost of 189kW flywheel storage compares to that of a similar sized lead-acid battery bank.

1.2 Literature Survey

S.A. Michela,R. Kieselbacha, H.J. Martens did not find a fatigue strength per se, but a general trend in fatigue strength reduction exists above 5 x 10^6 cycles in carbon composites with tests to 10^9 cycles. Similar fatigue limit value results were obtained by S.M. Arnolda, A.F. Saleeb, N.R. Al-Zoubi

Using a vacuum or a low pressure helium atmosphere, for the high rotational speeds of composite flywheels, imposes a further challenge to remove the heat generated in the armature windings of the permanent magnet machine. The electrical resistive generated heat cannot be conducted out due to the heat insulating nature of the non magnetic armature. The resulting heat and radiation will heat

up the permanent magnets beyond their operational temperatures.

The use of a heat pipe is proposed to overcome this constraint, which at the time of this writing has not yet been implemented in kinetic energy storage.
The flywheel is to be suspended on a hybrid passive magnetic bearing system, based on the work of J.D. Stienmeyer, S.C. Thielman and B.C. Fabien which has a service life determined only by the wear characteristics of the synthetic gemstones used in the contact type axial bearing.

In case of material fracture, composite materials absorb almost all the energy in the fracture process, resulting in hot cotton wool and dust like debris. This property makes composite flywheels inherently safe, but a thorough numerical analysis of composite fracture behavior is required to confirm the theoretical model of composite fracture mechanics.

An overall efficiency of approximately 90 percent is estimated. This is still considerably higher than the 70 percent or less of lead acid batteries. The estimated efficiency is based on lower quality vacuum and converters, in order to stay within what is possible in rural applications, which results in higher losses.

1.3 Contributions

This thesis covers a manufacturable permanent flywheel system. a Halbach array permanent magnet machine is integrated into a flywheel, optimised for maximally utilising composite materials. This in effect minimizes the manufacturing cost and weight of the flywheel. The Halbach array has been extended to use, commercially off the shelf, odd numbers of magnets as well as multi-pole arrays, using fractional numbers of magnets per pole. Both radial and axial machine applications are evaluated.

The system combines the use of heat pipe technology for cooling across the low pressure barrier, required by the high surface speeds of flywheels. A DC-DC converter is an essential part of the design, to compensate for the low inductance of the stator. The brush-less DC motor drive implementation is directly usable for such applications.

This work presents and applies a large number of alternative technologies into a working flywheel system and is a valuable contribution for both theoretical reference and industry applications.

1.4 Objectives

The objectives of this thesis are:

- To examine current flywheel manufacturing techniques and methods to assess the applicability of these technologies to developing countries.
- To investigate and propose a new way to design and manufacture composite flywheels inexpensively.
- To evaluate and introduce a generalized methodology to design dipole and multi pole outside rotor Halbach arrays from standard shape magnets.
- To identify the requirements and problems with the introduction of heat pipe technology in the cooling of the machine windings inside a vacuum or partial vacuum.
- To design and build a low cost system in order to demonstrate the feasibility of such a flywheel for rural African applications.

2 Chapter 2 - Magnetic Design

2.1 Introduction

The use of Halbach arrays in high efficiency machine applications was introduced by the Lawrence-Livermore Corporation, using a dipole form of the original Halbach array. The dipole is extremely well suited for flywheel applications, as it has a uniform flux distribution inside the rotor.

The author has deviated from the circular segment approach as part of a development of a low cost unit and replaced the segments with, "off the shelf", rectangular magnets and expanded on the four magnet model used by B.P. Hills, K.M. Wright and D.G. Gillies.

The empirical formulas for the magnet orientation in the dipole and multi pole arrays are the result of original work performed by the author, using the finite element method and comparing it with real models. As shown in the simulation results below, it can be seen that the resulting flux lines are still of very high quality and consistent with the work of K. Halbach

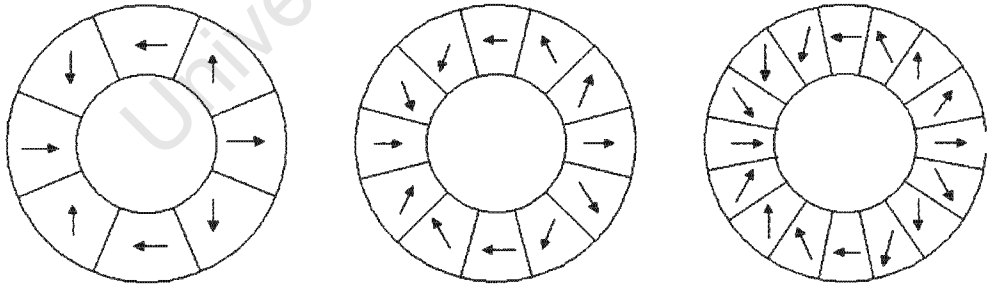

FIGURE 2.1: MAGNETIZATION ORIENTATIONS FOR AN 8, 12 AND 16 SEGMENT HALBACH DIPOLE

In order to use "off the shelf" magnets, one may be constrained by the fact that, in practice, even numbers of magnets are used in Halbach arrays, including the four magnet model of B.P. Hills, K.M. Wright and D.G. Gillies and structures shown by J.M.D. Coey. In situations when odd

numbers of magnets can be used, it would greatly improve the flexibility of the array design, thereby obtaining the maximum possible magnet density, and the maximum possible flux for any size desired, using standard shape magnets.

It was determined that in deviating from the circular segment approach, as part of a development of a low cost unit, the segments can be replaced with, commercial off the shelf (COFS), rectangular magnets. The B.P. Hills, K.M. Wright and D.G. Gillies four magnet model was expanded upon where it was determined that even and odd numbers of segments are not just usable, but yields Hallbach dipoles with parallel flux lines similar to the segmented approach.

The empirical formulas for the magnet orientation in the dipole and multi pole arrays are the result of original work performed by the author, using the finite element method and comparing it with real models. As shown in this chapter, it can be seen that the resulting flux lines are still highly parallel and consistent with the work of K. Halbach.

The equations to describe the machine is derived from first principles. These are used to design the desired machine and some practical examples are given.

2.2 Halbach Array Design

The objectives are:

- To prove that it is possible to deviate from the traditional, even numbered, segmented approach, using "off the shelf" magnets to create a high quality Halbach array, maximizing the magnet density for the given design and therefore the field strength for a given size
- To verify that the quality of the flux densities are consistent with theory.

2.3 The Segmented Halbach Array

K. Halbach describes the flux density inside a circular dipole array with equation 2.1:

$$B = B_r \ln\left(\frac{r_2}{r_1}\right)\frac{\sin\left(\frac{2\pi}{M}\right)}{\frac{2\pi}{M}} \qquad (2.1)$$

,where:

B = resultant flux density

B_r = remanence of the rare earth magnet

r_1 = inner radius

r_2=outer radius

M = number of segments used.

It is possible to design and implement Halbach arrays, with uniform flux distributions, by using standard shape magnets instead of the segmented approach. This work is an expansion of the work of Dr. Halbach with the rotation angle of the magnets given by 2.2:

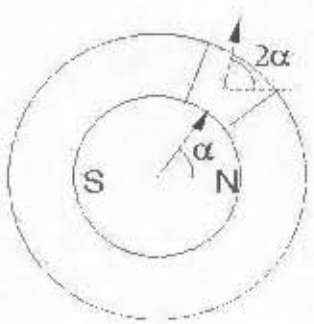

FIGURE 2.2: ROTATION ANGLE OF MAGNETS

$$\phi = 2\alpha \qquad (2.2)$$

where,

ϕ = rotation angle of the magnetization direction and

α = angle of rotation from the starting position, measured radially outwards from the centre (Figure 2.2)

Applying this rule to varying numbers of segments the results, shown in Figure 2.3, were obtained by means of finite element analysis. The results in 5 degree increments are shown in Appendix I.

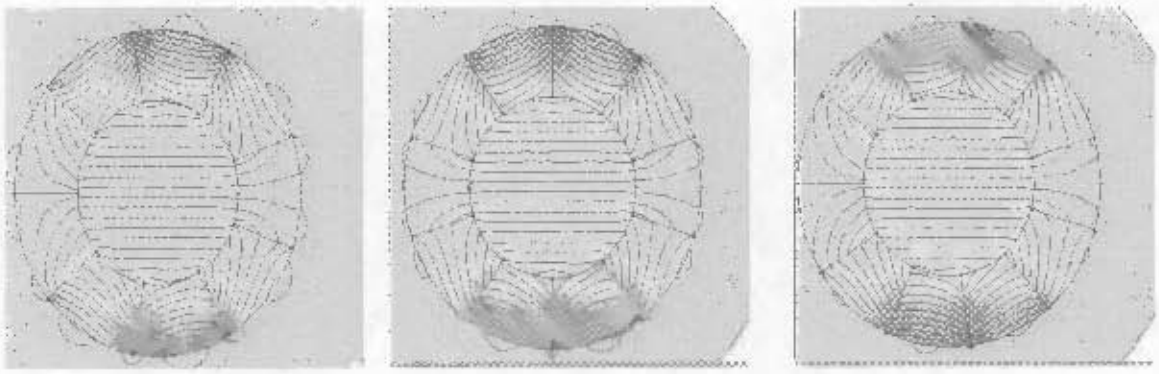

FIGURE 2.3: FEA RESULTS FOR HALBACH DIPOLES WITH 9, 10 AND 11-SEGMENTS

Equation 2.2 can be used to predict the angles of different numbers of segments for the Halbach dipole. Illustrated in Figure 2.3 are examples of the finite element results, which was done for M = 3- up to 13 segments. It is observable that a negating effect exists for M = 5 and higher, on the outside the arrays. Furthermore, as M increases, the flux lines become more parallel.

FIGURE 2.4: FEA RESULTS OF 12 SEGMENT HALBACH ARRAYS WITH 10, 20 AND 30 DEGREE OFFSETS

When the segment magnetization is offset by an angle, the resulting flux is still of the same quality. Shown in Figure 2.4 are the results of a 12-segment Halbach array, with angles offset from the starting position. The starting angle was rotated in increments of 5 degrees and the results noted. At an angle of 90 degrees, the resulting problem is the same as the original, turned through 90 degrees, due to symmetry.

Adding a rotation angle, at the starting position, to equation 2.2 gives the more generalized form:

$$\phi = -2(\alpha + \delta) \qquad (2.3)$$

where:

δ = angle at the starting position

ϕ = rotation angle of the magnetization direction and

α = angle of rotation from the starting position (refer to Figure 2.2)

While this effect is of little practical value for direct implementation, it does show that for magnets, coming from the same magnetizing oven and thus similar deviation from the normal, the effect on the final Halbach array only results in a slight shift in the direction of the flux lines.

2.4 Halbach dipole using rectangular magnets

With the use of rectangular magnets, the effect of different numbers of "segments" were studied using the finite element method. The resulting fluxes were found to be of similar quality to that of circular segments, but slightly reduced. This is due to the reduced amount of magnetic material when using rectangular magnets instead of circular segments.

The magnetic remanence in equation 2.1 has to be replaced by the effective remanence, which is proportional to the ratio of the rectangular area to the area of the segment that the rectangular magnet replaces.

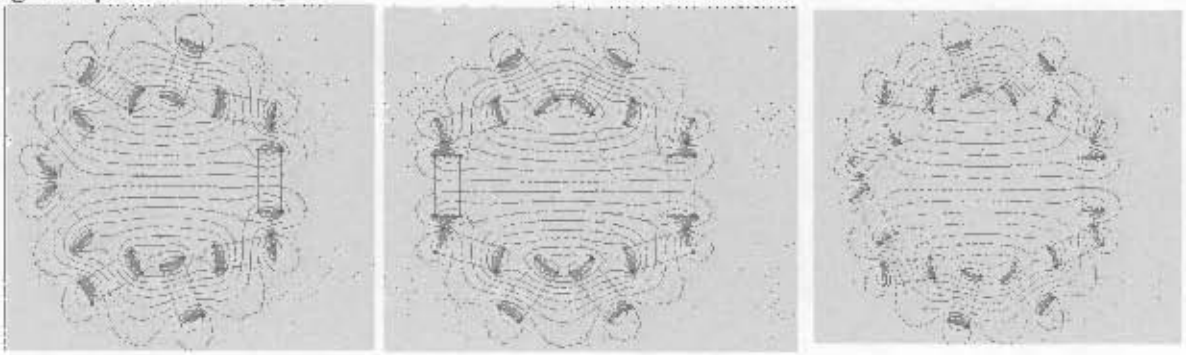

FIGURE 2.5: FEA RESULTS OF HALBACH ARRAYS WITH 9, 10 AND 11 RECTANGULAR MAGNETS

Shown in Figure 2.5 are examples of finite element results of 3- to 11-segment Halbach dipoles using rectangular magnets. c. Evaluating the results it is clear that the rectangular segmented approach still gives reasonable results, in accordance with the modification to the theory of K. Halbach.

Furthermore, using odd numbers of magnets has little effect on the uniformity of the field inside the array, except that for higher M, the lines are closer to parallel. A nine segment array, for example, produces flux lines that better approximates truly parallel lines than an eight magnet array, a ten magnet array approximates truly parallel lines better than a nine magnet array etc. The magnets can also be stacked to increase the ratio of magnetic to non-magnetic material in an array. One such arrangement was used for the prototype, shown in Figure 2.6.

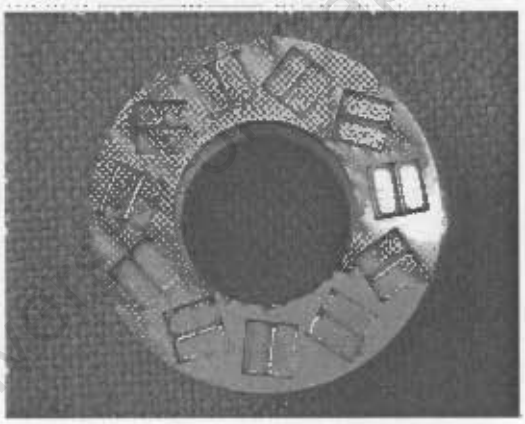

FIGURE 2.6: HALBACH ARRAY 0.4T DIPOLE PROTOTYPE 11 SEGMENTS, 22 RECTANGULAR MAGNETS

From these results it is concluded that odd numbers of rectangular magnets will result in adequate quality magnetic fields for use in high efficiency machines. The Finite element results are shown in Appendix I.

2.5 Multi pole arrays

K. Halbach also described the method involving multi pole arrays. This was investigated using the

finite element method to determine whether the use of odd numbers of discrete magnets will still prove true for the theory. The analysis was taken one step further and fractional numbers of magnets per pole pair, i.e. fewer magnet- than pole pairs, were attempted. This in itself is, of course, not possible for a dipole due to the geometrical limitation. In order to determine the magnetization angles, an empirical formula was derived.

For the dipole, the magnetization angle was taken through one full rotation from one pole to the next. The logical sequence for a multi pole array would be to have the poles pointing radially from and to the centre in alternating fashion.

360 degrees rotation for 2 poles, i.e. 2 times the angle off the starting position,

270 degrees rotation for 4 poles, i.e. 3 times the angle off the starting position,

240 degrees rotation for 6 poles, i.e. 4 times the angle off the starting position,

225 degrees rotation for 8 poles, i.e. 5 times the angle off the starting position,

216 degrees rotation for 10 poles, i.e. 6 times the angle off the starting position and so forth.

Therefore the angle of rotation of the magnetization direction is:

$$\vartheta = \frac{180 + \frac{360}{N}}{\frac{360}{N}}\ degrees = \frac{\pi + \frac{2\pi}{N}}{\frac{2\pi}{N}}\ radians \qquad (2.4)$$

N = Number of poles.

ϑ = angle to rotate the magnetization direction

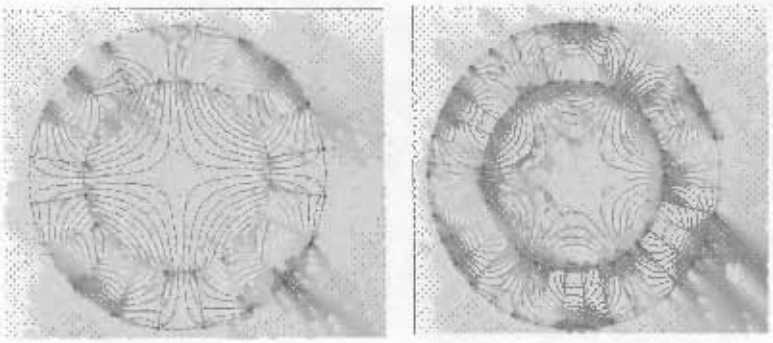

FIGURE 2.7: FEA RESULTS OF A 20-SEGMENT QUADRUPOLE AND A 36-SEGMENT, 6-POLE HALBACH ARRAY

This sequence was simulated on multi pole arrays and the results are shown in Figure 2.7 and Figure 2.8.

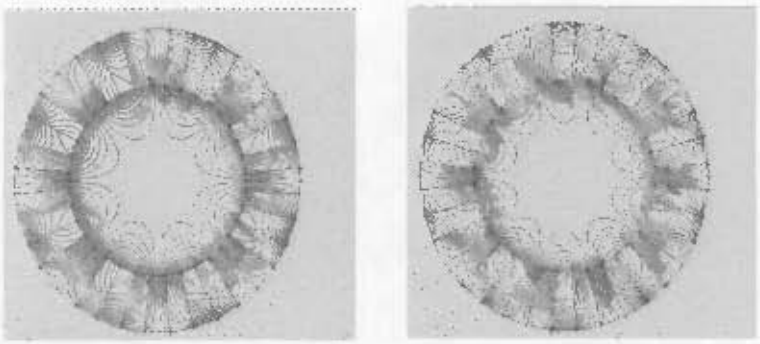

FIGURE 2.8: FEA RESULTS OF A 36-SEGMENT 8-POLE AND A 36-SEGMENT 10-POLE HALBACH ARRAY

Note how the central area inside the array is practically free of magnetic flux lines and increases in diameter with increased number of poles for the same physical geometry. This attribute can be put to use where the mechanical properties and thermal properties of metallic materials are required. The finite element models and results are shown in Appendix I.

2.6 Stacked Dipole Prototype Design

Several prototypes were constructed to verify the dipole theoretical calculations and finite element analysis.

By doubling up standard rectangular magnets, a higher magnet solidity, ie the magnetic- v.s structral material ratio, is acquired. This resulted in a higher effective magnetic flux inside the Halbach array.

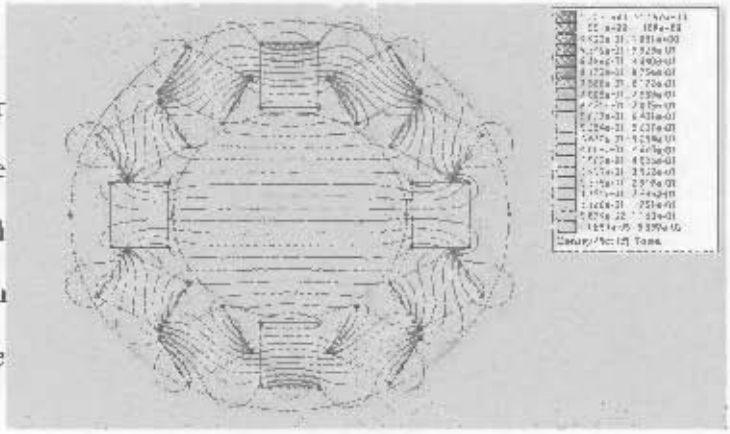

FIGURE 2.9: FEA RESULT OF A STACKED 12 SEGMENT HALBACH DIPOLE

The configuration chosen to fit the specific design is shown in Figure 2.9.

Equation 2.2 was used to calculate the orientations of the magnets for the dipoles, shown in Figure 2.10, and was laser cut from non-magnetic, grade 316, Stainless steel.

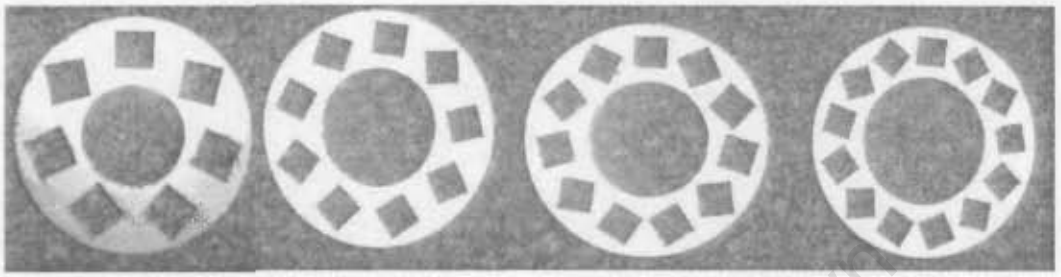

FIGURE 2.10: 7, 9, 11 AND 13 SEGMENT HALBACH DIPOLE PROFILES

The resulting field strengths were calculated by means of a spreadsheet. A finite element analysis of the Halbach arrays was done and Gauss meter used to measure the resulting flux in the Halbach constructed dipoles. As seen in the comparative table 2.1 below, the theoretical, finite element result and actual measured values were found to be consistent. The picture in shows a actual Gauss test being performed.

r_i	r_o	M	B_g	B
30	50	8	0.94	0.4334
25	56	7	1.05	0.7383
34	65.5	9	1.08	0.6535

TABLE 2.1 : CALCULATED STRENGTHS FOR 7, 9, 11 AND 13 MAGNET DIPOLES

The results of all the FEA studies done are listed in Appendix I.

2.7 Halbach machine Design

The objective is to determine the equations for the brushless Halbach machine from first principles and rewritten in terms of a DC machine equation. The machine can be single or poly phase, determined by physical and economical constraints.

Consider a set of three phase coils consisting of copper windings wound onto a non-magnetic, non conductive, core. With the permanent magnetic field rotating, large eddy currents will be generated in any magnetic and conductive circuits in the vicinity of the field.

Having a conductor in a uniform flux, the air gap between the coils and the rotor inside the perimeter is of no significance for this machine's efficiency. The torque generated is directly proportional to the ampere turns and radius from the rotational centre in a Halbach array and the fundamental relationships, for a single conductor, are given by:

$$F = B \cdot l \cdot i \qquad (2.5)$$

$$T = B \cdot l \cdot i \cdot r \qquad (2.6)$$

and:

$$P = T \cdot \omega \qquad (2.7)$$

, where:

F = Force [Newton]

B = Magnetic Flux [Tesla]

L = length of conductor [meters]

i = current [Amperes]

r = radius [meters]

T = Torque [Newton meters]

ω = angular velocity [radians per second]

To accurately estimate the magnetic forces in a machine, the torque and power should be integrated along the circumferential direction of the conductors in the air gap. For simplicity, the conductors are considered as a single wire.

Consider the drawing in Figure 2.12. The field windings are shown as 5 wires. In the actual machine these pairs represents several windings. Say a current is running in one phase only. This will cause a force on the winding and the magnetic field, which are equal and opposite.

In this machine the windings are kept stationary and the Halbach array is free to rotate. Assuming a rotational centre coincides with the geometric centre, the forces, described by equation 2.5, acts between the magnetic field and the windings. This translates into a net torque, as described by equation 2.6.

The voltage of this machine is purely a function of wire resistance and the machine induced electromotive force (emf). In order to control the device will require:

- Controlling the current to and from the machine
- Limiting the maximum voltage

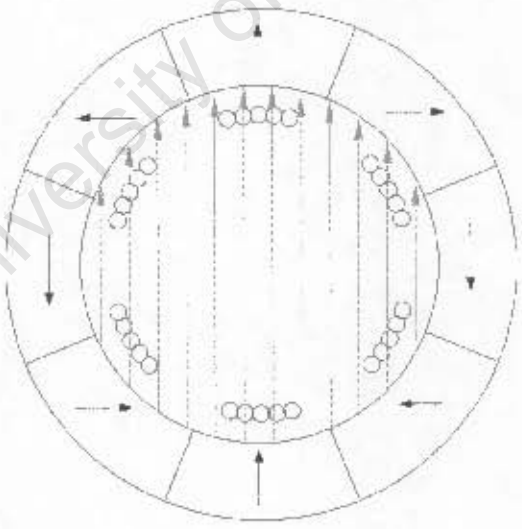

FIGURE 2.12: HALBACH ARRAY MACHINE MODEL

A constant current, which can be controlled to a required value, can be used to accelerate the

machine, given that the induced torque is larger than the frictional forces. The machine is a true two pole permanent magnet, 3-phase AC synchronous machine. Looking from the DC side of the converter, the machine plus the converter can be described in terms of DC machine equations, hence the term brush less DC machine.

By switching the current in a controlled manner results in a square wave current output on the 3-phase side. With the rotor being a fixed magnetic field and the windings on a non-magnetic core, the voltage equation for a DC machine, on the DC side of the converter, applies i.e.:

$$E = K\Phi\omega + I \cdot R \qquad (2.8)$$

, where

E = Induced machine EMF (electromotive force)

Φ = Flux density, fixed for a permanent Halbach array

ω = angular velocity in radians per second

I = Winding Current

R = Resistance measured over the switches and the windings.

K = machine constant.

The induced voltage can be estimated by the the induction law (A.E. Fitzgerald, D.E. Higginbotham and A. Grabel):

$$V_i = N\frac{d\Phi}{dt} \qquad (2.9)$$

,where

V_i = Induced Voltage

N = Number of turns

$\frac{d\Phi}{dt}$ = Rate of change of magnetic flux

For a conductor loop the induced voltage becomes:

$$V_i = \omega\Phi_{max}\sin(\omega t) \qquad (2.10)$$

djohnson

,where

ω = angular velocity in radians per second

Φ_{max} = Magnetic flux given by the relationship

$$\Phi_{max} = BA \qquad (2.11)$$

, where:

B = calculated Flux density of the Halbach array equation 2.1, and adjusted according to the magnetic area reduction described in section 2.4

A = Area enclosed within a conductor loop

For this machine running at 90000 rpm with a flux density of 0.4 Tesla and a mean area of 0.025 X 0.020m per winding, the induced Voltage in equation 2.10 reduces to: $V_i = 2.43N\sin(\omega t)$ per winding, with N = number of windings. The RMS, the Root Mean Square or DC equivalent, value for a sinusoidal wave shape has a value of $\frac{2.43}{\sqrt{2}} = 1.72$ volts per phase per winding at maximum speed.

The fundamental equations for three phases are:

$$V_{L-L} = V_{ph} \qquad (2.12)$$

, for a delta or:

$$V_{L-L} = \sqrt{3} \cdot V_{ph} \qquad (2.13)$$ for a star, or Y connected machine, where:

V_{L-L} = RMS Line to Line Voltage

V_{ph} = RMS Phase voltage

Different configurations of windings was tested. Their respective estimated maximum values is shown in Table 2.2. This dictates the ratings for the choice of switching device, as semiconductor devices are generally more sensitive to over voltages and currents than a typical brushed DC

djohnson

machine.

Windings	$V_{L\text{-}L}$ *(Delta Connected)*	$V_{L\text{-}L}$ *(Star Connected)*
14	24 V	41.6 V
20	34.3 V	59.4 V
25	42.9 V	74.3 V

TABLE 2.2: MAXIMUM CALCULATED VOLTAGES FOR DIFFERENT STATOR WINDINGS

Substituting for $K\phi$ in equation 2.8 we get :

$$E = \frac{K\Phi}{900}\omega + I \cdot R \qquad (2.14)$$

where:

E =Maximum rated voltage for the machine

R = Combined resistance of the switches (MOSFET, IGBT etc.) and the windings.

2.8 Hybrid Magnetic Bearings

R. Moser, J. Sandtner & H. Bleurer describes Earnshaw's 1942 discovery that passive magnetic bearings cannot reach a stable equilibrium on their own, also known as Earnshaw's theorem. Furthermore they describe the principle of diamagnetic levitation for flywheels, which could not be made to work in their present configuration.

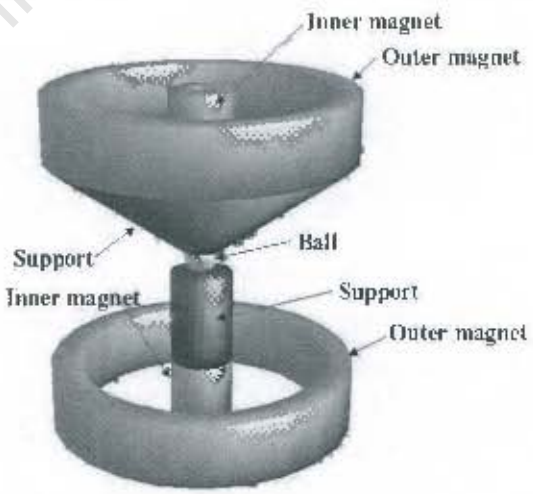

FIGURE 2.12: HYBRID MAGNETIC BEARING CONSTRUCTION

J.D. Stienmeyer, S.C. Thielman and B.C. Fabien describes an inherently stable hybrid type bearing. Shown in Figure 2.12, the bearing consists of an axial journal ball bearing, combined with two radial, repelling type passive magnetic bearings.

The radial bearings can consist of two axially magnetized rings or a ring and a disk as the forces and stiffness are independent of the direction of magnetization (J.P. Yonnet), i.e. radial or axial magnetization. The former is simpler to manufacture and commercially available.

J.D. Stienmeyer, S.C. Thielman and B.C. Fabien calculated the journal bearing losses to be small enough to allow for run down times of over 200 days. O. Bouty had shown a method for quantifying the magnetic bearings losses analytically. This is necessary to determined the heating effect on the magnets in a low pressure environment.

2.1 Hybrid Magnetic Bearing Stability

The stability of the J.D. Stienmeyer, S.C. Thielman and B.C. Fabien model is based on the stability of a spinning top and limiting the precession (wobble) by using two pairs of radial magnetic bearings. Jr-Yi Shen and Brian C. Fabien describe the active control of this system, which is required for dynamic applications and machines types where the air gap is critical.

In this prototype, the application is stationary and the outside rotor Halbach array machine is insensitive to fluctuations in the air gap as the magnetic field is uniform in the entire airspace, as described by K. Halbach.

2.9 Radial Magnetic Bearing Stiffness

The stiffness of the radial magnetic bearing can be analytically calculated as per J.D. Stienmeyer,

S.C. Thielman and B.C. Fabien, assuming perfect magnets.

The stiffness for this magnetic bearing was determined by the size of commercially available magnets that are best suited for the geometry of the flywheel. The theoretical stiffness was determined by finite element analysis and physically measured on a prototype bearing model shown in Figure 2.13.

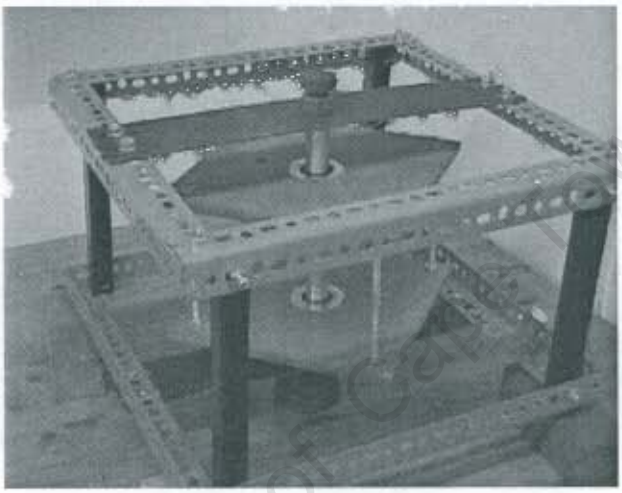

FIGURE 2.13: HYBRID MAGNETIC BEARING MODEL

The bearing stiffness was measured on the free end, i.e. the end without the journal bearing. The bearing experimental results are listed in table 2.3

Inner diam. *[mm]*	*Outer diam.* *[mm]*	*Disk diam.* *[mm]*	*Height* *[mm]*	*Stiffness [N/m]*
30	60	22	10	3000

TABLE 2.3: EXPERIMENTAL RADIAL MAGNETIC BEARING STIFFNESS

In comparison, J.D. Stienmeyer, S.C. Thielman and B.C. Fabien achieved a radial stiffness of 600 N/m and 8760N/m.

2.10 Radial Magnetic Bearing Losses

The radial magnetic bearings consists of two axially magnetized rings or a ring and a disk as shown in Figure 2.14.

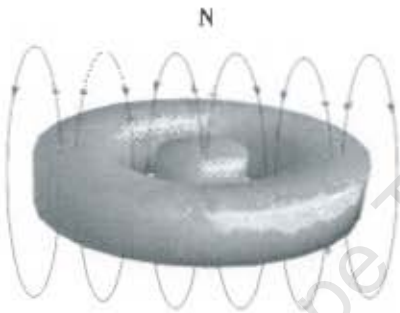

FIGURE 2.14 : AXIALLY MAGNETIZED RADIAL MAGNETIC BEARING

Shown in the Figure 2.15 and Figure 2.16 are the simulated results of O. Bouty of magnetic bearing losses.

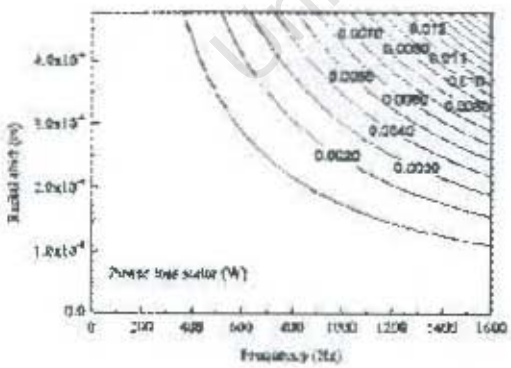

FIGURE 2.15: MAGNETIC BEARING STATOR LOSS

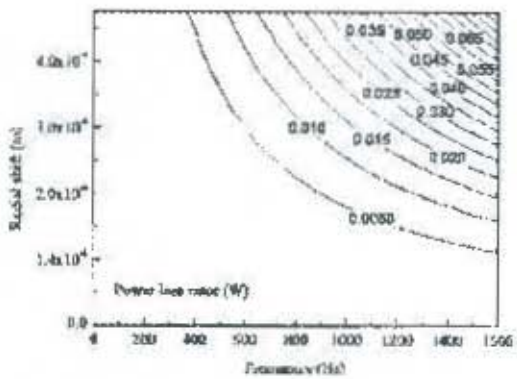

FIGURE 2.16: MAGNETIC BEARING ROTOR LOSS

From these simulation results, a machine running at 1600 Hz or 96 000 rpm, has a resulting rotor loss of 1mW and a stator loss of 5 mW at a displacement of 0.1 mm.These losses have to be added to the total bearing loss. The 5 mW stator loss has to be added to the heat that needs to be removed by the heat pipe.

The heat from the rotor loss is generated in the magnet and conducts into the flywheel structure. In a near perfect vacuum, this heat is cumulative, as an insignificant amount is radiated to the containment. This heat cannot be removed from the rotating part in a perfect vacuum and therefore a low pressure inert containment is preferable, which adds to the total frictional loss.

2.11 Axial Journal Bearing

The J.D. Stienmeyer, S.C. Thielman and B.C. Fabien hybrid magnetic bearing contains an axial thrust bearing, consisting of a ball resting on a flat platform, with the frictional loss of given by the relationship:

$$T = 0.9\pi r^2 F \cdot \mu \qquad (2.15)$$

, where:

T = Frictional torque

r = radius of ball rest

μ = Coefficient of friction between the two surfaces

For a flywheel exerting 20 N, the frictional losses will be as follows [Table 2.4]

Ball material	*Platform material*	*Coefficient of Friction*	*Torque [Nm]*	*Power loss @ 90 000 rpm [mW]*
Ruby / sapphire	Sapphire	0.1	5.089e-05	480
Hard Steel	Hard Steel			

Ball material	*Platform material*	*Coefficient of Friction*	*Torque [Nm]*	*Power loss @ 90 000 rpm [mW]*
		0.42	2.14e-04	2014
Cast iron	Cast Iron	0.15	7.634e-05	719
Teflon	Steel	0.04	2.036e-05	192

TABLE 2.4: FRICTION VALUES FOR BEARING MATERIALS

The prototype axial journal bearing is shown in Figure 2.17 with a ball dimension of 6mm running on a Polytetrafluorethylene (Teflon™)coated steel platform.

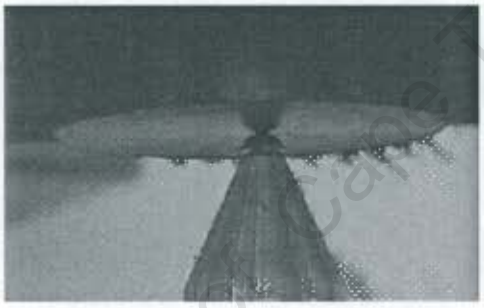

FIGURE 2.17: AXIAL JOURNAL BEARING MODEL

2.12 Conclusion

It was proved through the use of the finite element method that it is possible to create high quality Halbach arrays from off the shelf standard magnets.

It was shown that the start angle in the array does not influence the quality of the resulting magnetic fluxes.

The theorem was extended to that of multi pole arrays and it was shown that using fractional numbers per pole still yields a valid Halbach array.

The relationship between the magnet and their respective orientation angles has been established for both dipole and multi pole arrays and extended to an offset start angle.

The theory was verified by finite element analysis and actual prototypes and proved to be consistent with the theoretical and finite element analysis.

The theoretical principles of machine design was derived for designing a Halbach machine and verified with a prototype.

It was shown that cooling will be required for the machine generator as well as the flywheel itself, as there are heat sources to both.

3 Chapter 3 - Heat pipe cooling design

3.1 Introduction

When permanent magnet machines are operated in a vacuum / low pressure environment, the heat generated by losses accumulates inside the machine. An insignificant amount of heat escapes through conduction in the wire, some through convection if an atmosphere is present, and the rest radiates into the nearest object, in this design the Halbach array. It was found that, after several hours of operation, the NeFeB magnets heats up enough to move into the reversible demagnetization regime. Despite the resistive losses in the machine being small, in time the windings eventually overheat, which in turn results in insulation breakdown.

The resistive losses in an Halbach array machine is small and lack magnetization losses, since there are no magnetic materials in the stator The heat generated can easily be conducted to the environment, although most materials that conduct heat well, also conducts electric current and will result in additional eddy current losses from the rotating magnetic field from the Halbach array. One such material is diamond, with the restriction of availability, cost and difficulty to machine. Mica is another candidate, but too brittle for most structural applications.

Heat pipes on the other hand lend themselves well to cooling the machine in this environment, subject to conditions dealt with in the objectives. These are automatic devices that move heat by means of a phase change from a hot to a cold end. Generally, heat pipes include a wick to pump the condensed fluid back to the hot end by capillary action.

In a thermosyphon, a special case of heat pipe, the condensate moves back to the hot end by means of gravity. These are operated in both vertical and inclined configurations.

3.2 Objectives

The objective of this chapter is:

- to establish the principles required for heat pipe / thermosyphon design for vacuum / low pressure operated electric machinery and
- to develop, build and test a prototype for testing in a kinetic storage device.

A constraint from a magnetic point of view requires the heat pipe not to be magnetic or electrically conductive, otherwise it will act as an eddy current brake to the rotating, with the rotating permanent magnet rotor.

3.3 Heat pipe operation

The principle of operation is to remove the energy by phase change of a coolant. Various coolants have successfully been used for various temperature ranges and amongst others include ammonia, water, CFCs, alcohols, Acetone, Sodium and Mercury, depending on the operating temperatures and desired cooling requirements.

According to J.P Holman and L. L. Vasiliev, heat pipes in particular can move substantial amounts of heat through comparatively small surface areas and have very low thermal resistances, allowing for compact heat exchangers.

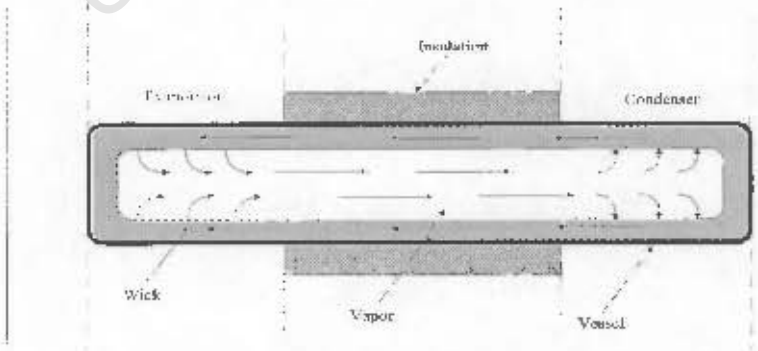

FIGURE 3.1 : HEAT PIPE OPERATION

djohnson

A heat pipe consists of a hollow vessel with the inner wall covered with a wick material. Shown in Figure 3.1 is a schematic of a heat pipe.

The working fluid inside the pipe evaporates on the evaporator side of the heat pipe and the gas travels to the cold end where it condenses to give off the latent heat. The condensed liquid is moved back to the hot end by capillary action of the wick. The capillary pump allows the device to work in any orientation.

Several different types of wick materials are used in heat pipes. Most recently added are the porous sintered metal wicks, commonly found in computer processor heat sinks. Z.J. Zuo, M.T. North and D.M. Ernst showed heat transfer rates for uniform wick structures and ethanol as work fluid of just over 5.6 W/cm^2 with uniform graded wicks and up to 7.9 W/cm^2 for graded wicks.

The heat transfers of several configurations are listed in table 3.1, and some typical operating characteristics in Table 1.

Temperature range [°C]	*Working Fluid*	*Vessel material*	*Axial Heat flux [W/cm^2]*	*Surface heat flux [W/cm^2]*
-200 to -80	Nitrogen	Stainless steel	67	1.01
-70 to +60	Ammonia	Nickel, Aluminium, Stainless Steel	295	2.95
-45 to +120	Methanol	Copper, Nickel, Stainless	450	75.5
5 to 230	Water	Copper, Nickel	670	146
190 to 550	Mercury	Stainless steel	25100	181
400 to 800	Potassium	Nickel, Stainless steel	5600	181
500 to 900	Sodium	Nickel, Stainless steel	9300	224

Temperature range [°C]	*Working Fluid*	*Vessel material*	*Axial Heat flux [W/cm²]*	*Surface heat flux [W/cm²]*
900 to 1500	Lithium	Niobium	2000	207
1500 to 2000	Silver	Tantalum	4100	413

TABLE 3.1 : OPERATING CHARACTERISTICS OF HEAT PIPES - J.P HOLMAN

T. Payakaruk, P. Terdtoon and S. Ritthidech describes heat pipe operation in a vertical or inclined position, without the need for a wick. The limitation is that the evaporator has to be in the lower part and the condenser at the top. Y.J. Park, H.K. Kang and C.J. Kimo refers to this configuration as a "thermal diode" that has a wide operating temperature range and are commonly referred to as thermosyphons.

In the thermosyphon, liquid boils at the hot end [Figure 3.2] and the evaporated gas travels from the surface of the boiling liquid along the centre of the pipe to the cold end. At the cold end, the working fluid condenses on the inner surface and the liquid is fed back to the boiler end by means of gravity.

The simplicity of thermosyphons greatly reduces manufacturing complexity and cost, as shown in Figure 3.2. as compared to heat pipes and orders smaller than conduction mode heat sinks [Table 1]. This attribute makes it the most attractive alternative for use to lower the cost.

Contrary to the simplicity of construction, the analytical and numerical analysis of the diffusion inside a thermosyphon is highly complex, as documented by A. Rodriguez-Bernal and E.S van Vleck. Fortunately, empirical models exist which simplifies the design of a practical thermosyphon greatly, which will be used for the low cost system described in this thesis.

djohnson

It was shown by A. Meyer & R.T. Dobson that an inclined thermosyphon is more efficient than a vertical one, an attribute that can be utilized to make the heat pipe more compact when required.

3.4 Heat transfer

According to A. Meyer & R.T. Dobson. the heat transfer relationships for a vertical thermosyphon are as follows. A drawing of the thermosyphon processes is shown in Figure 3.2.The maximum heat transfer is:

$$\dot{Q}_{max} = 1.6553 x 10^{6} Bo^{0.3156} Ku^{1.6048} \qquad (3.1)$$

where,

the Bond number is given by:

$$B_o = \frac{d}{\sqrt{\sigma / g \cdot (\rho_l - \rho_v)}} \qquad (3.2)$$

and the Kutateladze number by:

$$K_U = \frac{\dot{Q}}{[\rho_v h_{fg} \frac{\sigma g (\rho_l - \rho_v)}{\rho_v^2}]^{0.25}} \qquad (3.3)$$

where,

Q = Heat transfer rate [W]

d = diameter [m]

σ = Surface tension, [N/m]

g = gravitational constant of 9.81 [m/s2]

ρ_l = density, liquid [kg/m3]

ρ_v = density, vapour [kg/m3]

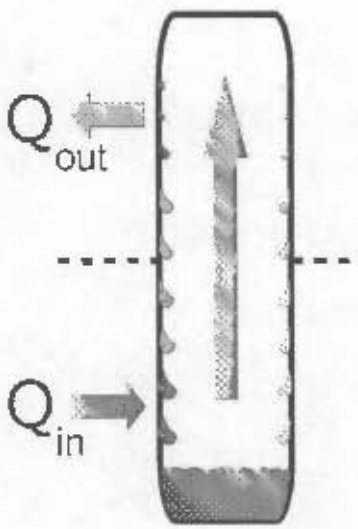

FIGURE 3.2: THERMOSYPHON OPERATION

The heat transfer is represented as a series of thermal resistances as shown in Figure 3.3.

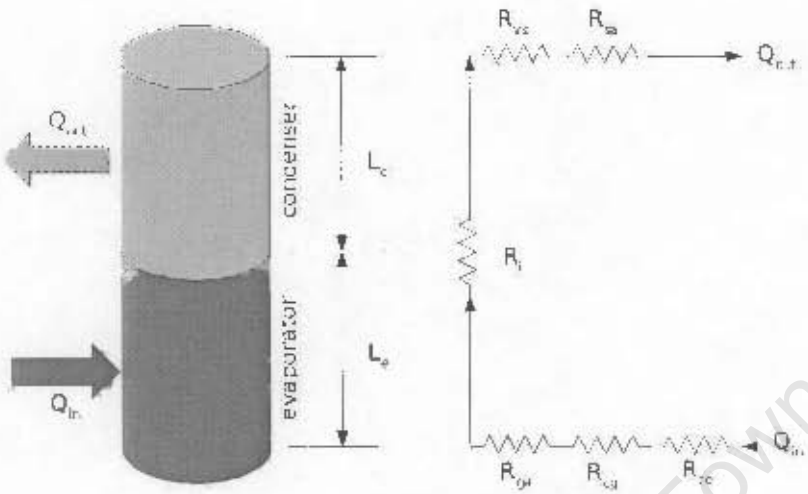

FIGURE 3.3: THERMAL RESISTANCE MODEL

$$\dot{Q} = \frac{\bar{T}_h - \bar{T}_c}{\sum R} \qquad (3.4)$$

where,

T_h = hot end temperature

T_c = Sink side temperature.

ΣR = Sum of thermal resistances

The resistances indicated on the thermal resistor network in Figure 3.3 are :

R_{cr} = Copper to resin

R_{rg} = Resin to Glass fibre/epoxy composite

R_{ga} = Composite to boiling Acetone

R_{as} = Condensing Acetone to Stainless steel

R_{sa} = Stainless steel to air

3.5 Fill charge ratio

The fill charge ratio is the ratio of liquid to the total volume of the thermosyphon or heat pipe. Y.J. Park, H.K. Kang and C.J. Kimo demonstrated the relationships between fill charge ratio (equation 3.5) and other performance parameters for two phase thermosyphons.

Most notably, that for low fill charge ratios (<20%) a dry out heat transfer limit exists where no liquid exists at the bottom of the thermosyphon and localized heating of the tube starts from the bottom upwards. In this mode of heat transfer, all the liquid boils away from the walls of the evaporator before any of it reaches the bottom of the tube. Also, for high fill ratio charges, the maximum heat transfer is limited by flooding. Lastly the change in transfer coefficient was negligible for all fill charge ratios.

$$\psi = \frac{V_l}{V_c} \qquad (3.5)$$

where,

ψ = Fill ratio [%]

V_l = Volume liquid

V_c = Volume column

Only fill charge ratios that will maximize the heat transfer will be considered, hence the following relationship noted by Y.J. Park, H.K. Kang and C.J. Kimo will apply, rather than equation 3.3 from A. Meyer & R.T. Dobson.

$$Q_{max} = \frac{\frac{\pi K_{ll} h_{lv}}{4} \cdot Bo_2 \cdot \sigma^{\frac{5}{4}}}{|g(\rho_l - \rho_v)|^{\frac{3}{4}}} \cdot \left[\rho_v^{\frac{-1}{4}} + \rho_l^{\frac{-1}{4}}\right]^{-2} \qquad (3.6)$$

where, the only new quantity, h_{lv} = latent heat of vaporization [J/kg], is introduced.

D.A. Reay states that fill ratios of 40% and higher are required to avoid problems with start up and the dry parts of the evaporator heats up much more than the immersed part, causing local overheating. Furthermore that an entrainment limit exists for high axial heat flows and the shear forces between the counter current liquid and vapour flows restricts the liquid to return to the evaporator side causing failure on the evaporator side. When this is encountered, a barrier is required between the returning liquid and the gases from the evaporator.

3.6 Prototype Design

The requirements for the thermosyphon is set by the prerequisite of non magnetic and non conductive materials in the proximity of the rotating magnetic field of the Halbach array machine. Furthermore, the machine design dictates the physical dimensions of the evaporator part of the thermosyphon.

It was decided to use non magnetic stainless steel as the magnetic bearing holder and condenser, offering the benefit of high resistivity against eddy currents generated by stray fluxes and good corrosion resistance. The latter presumes that it may be necessary to accommodate different types of work fluids in the testing phase. For the stator/boiler, Pyrex ™ glass was chosen for it's stiffness, fair thermal conductivity and non magnetic properties.

Acetone was chosen as the working fluid, having a boiling point of only 56.1 oC, K. Geick, J. Walters. L. L. Vasiliev describes a 16mm diameter, stainless steel heat pipe and acetone as working fluid, used to transfer 2kW of heat.

During the flywheel assembly, it was found that the glass was not tough enough to survive the assembly process, where two pairs of repelling magnetic bearings and a Halbach array had to be forced past each other and it was opted to use a fibre glass /epoxy tube. The latter has a much higher

thermal resistance, it's usability for this purpose had to be qualified by analytical calculation, shown below. A picture of the fibreglass thermosyphon is shown in Figure 3.4.

The expected maximum heat loss in the wire is calculated using the following parameters from K. Geick, J. Walters

	Wire Data	
Parameter	QTY	Unit
Cross section	1	mm^2
Length	0.9	m
Resistivity	0.0172	$\Omega.mm^2/m$
Resistance	0.0155	Ω
Density	8.9	kg/dm^3
Mass	0.0089	kg
Specific heat	394	J/kg.K

TABLE 3.2: WIRE DATA

FIGURE 3.4: STATOR / THERMOSYPHON

Resistive heat dissipation: $P = I^2 R = 20^2 . 0.0155 = 6.2W$

It is necessary to transfer all of the heat out through the thermosyphon,hence:

$\dot{Q} = P = 6.2W$

Assume a working pressure of 2 bar, i.e. the gaseous density of 277 kg/m^3 doubles and substituting in equations 3.2 though 3.4 and 3.6

Bond number: $B_o = \frac{d}{\sqrt{\sigma / g.(\rho_l - \rho_v)}} = \frac{0.016}{\sqrt{33.10^3.(8900 - 555)}} = 9.642e\text{-}07$

The Kutateladze number becomes:

$$K_U = \frac{\dot{Q}}{\left[\rho_v h_{fg} \frac{\sigma\, g(\rho_l - \rho_v)}{\rho_v^2}\right]^{0.25}} = \frac{34317.8}{555 \cdot 500.9 \frac{28.8 \cdot 9.81(8900-555)^{0.25}}{555^2}} = 14.0985$$

, which gives a maximum possible heat flow at a maximum fill charge ratios of:

$$Q_{max} = \frac{\frac{\pi K_U h_{lv}}{4} \cdot B_o^2 \cdot \sigma^{\frac{5}{4}}}{[g(\rho_l - \rho_v)]^{\frac{3}{4}}} \cdot [\rho_v^{\frac{-1}{4}} + \rho_l^{\frac{-1}{4}}]^{-2} = 7.958[W/m^2]$$

Using the A. Meyer & R.T. Dobson thermal resistance method for the thermosyphon, the thermal resistances are as follows:

Regime	λ^* *[W/m°C]*	t^+ *[mm]*	*R [°C/W]*
Copper to resin	379	3	2.6×10^{-7}
Resin to Glass fibre/epoxy composite	0.35	1	2.87×10^{-3}
Composite to boiling Acetone	0.04	3	7.5×10^{-2}
Condensing Acetone to Stainless steel	0.16	1	6.25×10^{-4}
Stainless steel to Air	250	3	4×10^{-7}
Total thermosyphon resistance			7.848×10^{-2}

** = Thermal resistivity, + = thickness*

TABLE 3.3: THERMOSYPHON THERMAL RESISTANCES

Substituting from Table 3.3, the heat transfer becomes:

$$\dot{Q} = \frac{T_h - T_c}{\sum R} = \frac{T_h - 25}{629.55} = 7.848 \cdot 10^{-2}[W/m^2]$$

Solving for Th results in a wire temperature Th = 78.16 oC

3.7 Conclusion

- Within confined spaces, the heat pipe can provide heat transfer rates to allow feasible machine designs operating in a vacuum or near vacuum. It will be especially suited for low cost electromechanical battery applications, where the armature windings may be operating in a partial vacuum environment.
- The heat pipe has no moving parts that can wear out.
- Materials for manufacture are inexpensive.
- Simple to construct.

4 Chapter 4 - Novel shape flywheel

4.1 Introduction

At the time of writing, filament wound designs were being used exclusively in composite flywheel designs. In this design an ultimate shape, one-piece, short fibre, composite flywheel is proposed, which is simple to manufacture. This will reduce material- and manufacturing costs significantly.

The service life of kinetic batteries are expected to be in the order of fifteen years, after which the power electronics may need replacement. Using composite materials brings the overall weight and cost down and have a typical endurance of 100 – 200 thousand stress cycles according to S. Salekeen and D.L. Jones. The flywheel is to be suspended on a hybrid passive magnetic bearing system, which has an indefinite service life.

The use of these high cost, sophisticated, yet durable devices are to be weighed against the high cost of solar power, inefficiencies of chemical storage and their comparatively short useful service life. The medium to high volume manufacturing costs has to be tailored to what is feasible as well as what is established and possible for the developing countries such as those in Africa.

4.2 Objectives

The objectives of this section are to:

- Maximize the energy density of the flywheel design to lower the material requirements.
- Evaluate the materials and processes required to make composite flywheels.
- Propose a method to manufacture complex shaped flywheels inexpensively.

4.3 Flywheel physics

The specific energy of a flywheel is the quantity that represents the amount of energy that is stored per unit mass of flywheel.

R.F. Post, S. F. Post defines specific energy as:

$$E = \frac{S_{MAX}}{2 \cdot \rho} \qquad (4.1)$$

, where:

E = Specific energy [J/kg]

S_{MAX} = Tensile strength [MPa]

ρ = density [kg/m3]

This equation shows that materials with high tensile strengths and low densities have higher specific densities. This implies the use of composite materials for flywheels rather than metals, they being less costly than traditional materials.

FIGURE 4.1: THIN CYLINDRICAL FLYWHEEL , MULTIPLE RIM FLYWHEEL AND ULTIMATE SHAPE FLYWHEEL.

M. Berger and I. Porat showed, that by using a combination of piece-wise optimal shapes, the ultimate shape reduces to a combination of maximum strength and minimum thickness sections only. This result yields a energy density of 1.9 times that of a thin walled cylinder.

Furthermore that a uniform thickness solid disk has an energy density of 1.52 times-, and a uniform strength disk 1.65 times that of a thin cylinder. Shown in Figure 4.1 are models of a thin cylindrical-, multiple rim and ultimate shape flywheels. P.P. Benham & F.V. Warnock defines the total kinetic energy stored in a rotating body as:

$$W = \frac{1}{2} I \omega^2 \qquad (4.2)$$

,where:

W = Kinetic energy in Joules

I = moment of inertia of the body

ω = Angular velocity in radians / sec

Furthermore, for a cylinder the mass moment of inertia is defined as:

$$I=\frac{1}{2}\cdot m\cdot\left(r_o^2+r_i^2\right) \qquad (4.3)$$

,where : m = mass

r_o and r_i = outer and inner diameters, for a uniform strength disk.

Using these relationships, Table 4.1 shows the theoretical energy densities for combinations of different materials and shapes for a thin walled cylinder, a uniform strength and ultimate shapes.

For the uniform strength and ultimate energy shapes, the strength values of short fibre composites were used. It is assumed unnecessarily complicated and costly to attempt to manufacture complex shapes with continuous fibres and keep the fibre orientations in the plane required.

Material	$U_{Cylindrical}$	$U_{Uniform\ Strength}$	$U_{Ultimate\ Shape}$
Mild Steel	4.2	5.9	8.1
Aluminium	4.5	6.3	8.6
High Tensile Steel	47	66	89
E-glass/ Epoxy	73	102	139
Graphite/ Epoxy	327	458	621
E-glass fibre	190	N/A	N/A
Graphite fibre	545	N/A	N/A

TABLE 4.1 SPECIFIC ENERGIES FOR SELECTED MATERIALS AND SHAPES

4.4 Ultimate Shape Flywheel with Central Hole

The M. Berger and I. Porat model does not provide for a central hole, which is required to embed

the bearings and a PM (Permanent Magnet) machine The impact of a central hole on the specific energy was investigated algebraically. The central hole is required to fit shafts, machines and bearings etc. to the flywheel. Adding the central hole to the M. Berger and I. Porat model redefines the generalized flywheel shape as shown in Figure 4.2.

This model is analysed by a differentiable configuration of piecewise defined disk profiles. The profile in Figure 4.2 is made up from 5 basic shapes and are, from left to right, defined by the boundaries from points P_1 to P_6: Central hole (P_1 - P_2), Exponential- (P_2 - P_3), Minimum Thickness- (P_3 - P_4), Maximum slope- (P_4 - P_5) and maximum thickness profiles (P_5 - P_6).

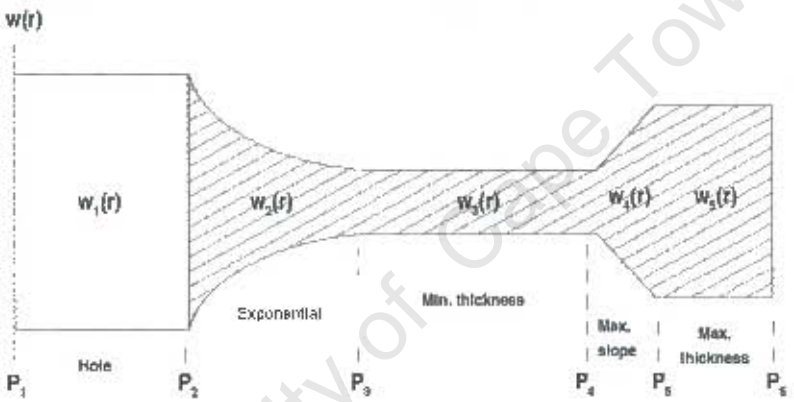

FIGURE 4.2: PIECEWISE DEFINED DISK PROFILE WITH CENTRAL HOLE

In this study an analytical derivation is demonstrated, of shape formulas, using a mathematical approach. The objective was finding the constant continuous functions for which the SKE is maximal. The ultimate shape, with the central hole, derived was consistent with that of the original from M. Berger and I. Porat.

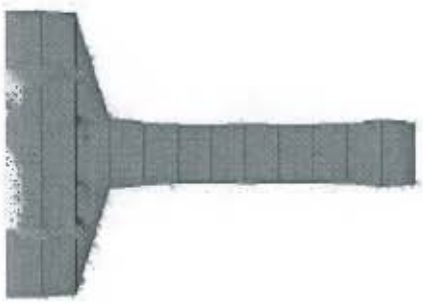

FIGURE 4.3: GA ISOTROPIC MATERIAL FLYWHEEL SHAPE

The resulting analytical shape is similar to those derived using genetic algorithms such as the work of D. Eby, R.C. Averill, E. Goodman, and W. Punch, shown in Figure 4.3.

Applying the conventions used by M. Berger and I. Porat, and expanding the model to include the central hole, the flywheel shapes are redefined as follows.

$2R_0$ = disk diameter [m]

R = radius from the centre [m]

Γ = Material density [kg/m3]

$W_{(R)}$ = function defining the disk thickness at radius R [m]

Z = plane of rotation

These quantities are rewritten in dimensionless form:

$$r = \frac{R}{R_0} \qquad (4.4)$$

, where:

R = radius

$$w(r) = \frac{W(R)}{R_0} \qquad (4.5)$$

$$s_R(r) = \frac{S_R(R)}{S_{MAX}} \qquad (4.6)$$

, where:

$S_R(R)$ = Radial stress at radius R

S_{MAX} = ultimate tensile stress

$$s_T(R) = \frac{S_T(R)}{S_{MAX}} \qquad (4.7)$$

djohnson

, where:

$S_T(R)$ = tangential stress at radius R

$$f_0 = \frac{F_0}{(S_{MAX} R_0)} \geq 0 \qquad (4.8)$$

, where:

F_0 = positive load per unit length at circumference of the disk

For a thin ring of the same diameter and material maximal tangential velocity is:

$$V_R^2 = \frac{S_{MAX}}{\Gamma} \qquad (4.9)$$

The specific kinetic energy is:

$$E_R = \frac{V_R^2}{2} \qquad (4.10)$$

Normalizing these quantities and using the thin ring as reference, the speed and specific kinetic energy or SKE are expressed as:

$$k = \frac{V_D}{V_0} \qquad (4.11)$$

and

$$e = \frac{E_D}{E_0} \qquad (4.12)$$

, where:

V_D = tip velocity of the ring or disk

E_D = Specific energy of disk

The differentiable configuration of the piecewise disk profile is a hole when the specific kinetic energy SKE that provides the shape is Zero. According to the fundamental theorem of Calculus the paths at the boundaries are equal.

This implies that the first shape $w_1(r)$ is equal to zero and the SKE is defined by:

$$e(k,w)=k^2\frac{\int_0^1 r^3 w_1(r)\,dr}{\int_0^1 r\,w_1(r)\,dr} \qquad (4.13)$$

$$e(k,w)=0 \Rightarrow w_1(r)=0 \qquad (4.14)$$

,where:

$e(k,w)$ = normalized specific kinetic energy

For the exponential shape, at the location P_2 to P_3, the SKE results in a two axis-symmetrical problem: The logarithmic curve on top and the exponential curve below the r-axis.

The problem is to find the exponential function which becomes a logarithmic curve for a rotating disk. This is proved by equations 4.15 to 4.30:

$$e(k,w)=k^2\frac{\int_r^{q_3} r^3 w_2(r)\,dr}{\int_r^{q_3} r w_2(r)\,dr} \qquad (4.15)$$

$$e(k,w)=\frac{1}{2}(q_3^2+r^2) \qquad (4.16)$$

Equation 4.16 is obtained after solving equation 4.15. The SKE $e(k,w)$ at r, q_3 is an exponential shape, which gives:

$$w_2(r)=e^{\frac{1}{2}(q_3^2+r^2\{k^2} \qquad (4.17)$$

$$-q^2=p_3^2 \; with \; q_3^2=-2\frac{\ln(\delta)}{k^2} \qquad (4.18)$$

q_3 is pushed to the left and reaches P_3, hence:

djohnson

$$w_2(r)=w_3(r)e^{\frac{1}{2}(p_3^2-r'^2)k^2} \qquad (4.19)$$

In geometric language, for the minimum thickness, P_3, P_4 is an ordinary point and the tangent at this point is a straight line i.e. a constant.

$$w_2(r)=w_3(r) \qquad (4.20)$$

Solving e(k,w) provides the following result after it's calculations in the interval:

$$4(p_3,r)\,with\,r\to p_4 \qquad (4.21)$$

The result is :

$$w_3(r)=\frac{1}{2}(p_3^2+r^2)k^2 \qquad (4.22)$$

, which, at the smallest value of k, gives the constant value, δ_L. , hence:

$$w_3(r)=\delta_L \qquad (4.23)$$

which approximates:

$$\delta_L=0.0 \qquad (4.24)$$

The maximum slope from the piecewise differentiable thickness to the interval $(r,p_5)\,where\,r\to p_4$ from the outer section. From the geometrical restriction the following applies:

$$\left|\frac{\partial w(r)}{\partial r}\right|\le 2\sigma \;with\; \sigma>0 \qquad (4.25)$$

By the theory of non-linear differentials as described by E. Goursat , $\frac{\partial w(r)}{\partial r}$ approaches 2, when r tend to P_4. This results in the following equation:

$$\frac{\partial w(r)}{\partial r}=2\sigma\,(r-p_4) \qquad (4.26)$$

djohnson

knowing that:

$$p_4 = p_3 + d, \qquad (4.27)$$

After analysis the Slope at the point P_4 becomes:

$$w_4(r) = \delta_L + 2\sigma(r - p_4) \qquad (4.28)$$

The analysis of this profile is similar to the minimum thickness for the interval [P_5, P_6] and the minimum provided by the set of the smallest k, r in this closed interval is bigger than the one provided at the minimum shape, hence:

$$w_5(r) = \delta_U, \text{ approximating } \delta_U = 0.01 \qquad (4.29)$$

Following the M. Berger and I. Porat methodology, similar optimum designs for three different speed ranges were found, namely:

- Low-speed range: $k_1 = 0$ to 1.131,
- Medium-speed range: $k_2 = 1.132$ to 5.132
- High-speed range: $k_3 = 5.132$ to 6.720

Each of the ranges has been studied, by means of the mathematical package Maple 5, and it's optimal profile found.

The aim was to find the shape for which the SKE is maximized in order to minimize the material requirement of the flywheel. This point is reached at the ultimate speed when k^2=6.720.

The low-, medium and high-speed range profiles are shown in Figure 4.4,Figure 4.5 and Figure 4.6 respectively.

FIGURE 4.4: OPTIMAL FLYWHEEL PROFILE FOR LOW-SPEED

FIGURE 4.5: OPTIMAL FLYWHEEL PROFILE FOR MEDIUM-SPEED

FIGURE 4.6 : OPTIMAL FLYWHEEL PROFILE FOR HIGH-SPEED, K2 = 6.720

For the high-speed range, starting from 5.132 to 6.720, the centre thickness must be limited from violating both the stress and the maximum thickness constraints. The optimal shape of this rotating free-disk in the high-speed range is terminated at the maximum slope thickness. The SKE converges to the upper bound below the possible limit value of 2.

djohnson

While the disk is rotating, it creates strength constraints, namely tangential S_T and radial stress S_R. thus produces the following results after solving the two boundary problem Equations for the system of two differential equations by a shooting method as suggested by M. Berger and I. Porat:

$$\begin{cases} \dfrac{ds_R}{dr} = \dfrac{s_R - s_T}{r} - \left[\dfrac{w'(r)}{w(r)} s_R + k^2 r\right] \\ \dfrac{ds_R}{ds} = \dfrac{s_R - s_T}{r} - \mu\left[\left[\dfrac{s\,w'(r)}{w(r)} s_R + k^2 r\right]\right] \end{cases} \tag{4.30}$$

, with:

$$0 \le r \le 1 \text{ and }, Bound_{conds}: s_R(0) = s_T; \quad s_R(1) = f_0 \Big/ w(1) \tag{4.31}$$

The Maple solution of equation 4.30, at the speed of 6.720, is shown in table 4.2.

k^2=6.720		
r interval	s[R]	s[t]
0.000000	1	1
0.356283	1	1
0.366284	1	1
0.711929	1	1
0.721929	0.649766	0.89493
1.000038	0.327935	0.798381
1.0000038	0.328	0.7984

TABLE 4.2: SOLUTION FOR K^2 IN EQUATION 4.30

The stress differential equations at the centre are singular. This singularity is removed by solving the following system of equations for the shape $w(r)$ at the centre i.e. radius $r = 0$.

djohnson

$$\begin{cases} \dfrac{ds_R}{dr} = -\dfrac{2+\mu}{3}\dfrac{w'(0)}{w(0)}s_R(0) \\ \dfrac{ds_R}{dr} = -\dfrac{1+2\mu}{3}\dfrac{w'(0)}{w(0)}s_R(0) \end{cases} \qquad (4.32)$$

Each configuration obtained has its own graph of stresses from Low to High speed. For the High-speed range, point q_3 (Figure 4.2), the evolved exponential shape starts to retreat towards the centre of the disk and meet with point P_3 at the critical point. This affects the stresses, which are dropped to their permitted level in the exponential section.

The behaviour of the stresses from the centre to the outer section of the free-disk at the high speed are shown graphically in Figure 4.7. Note that, as this optimization was derived in normalized form, the quantities shown in the graphs are dimensionless.

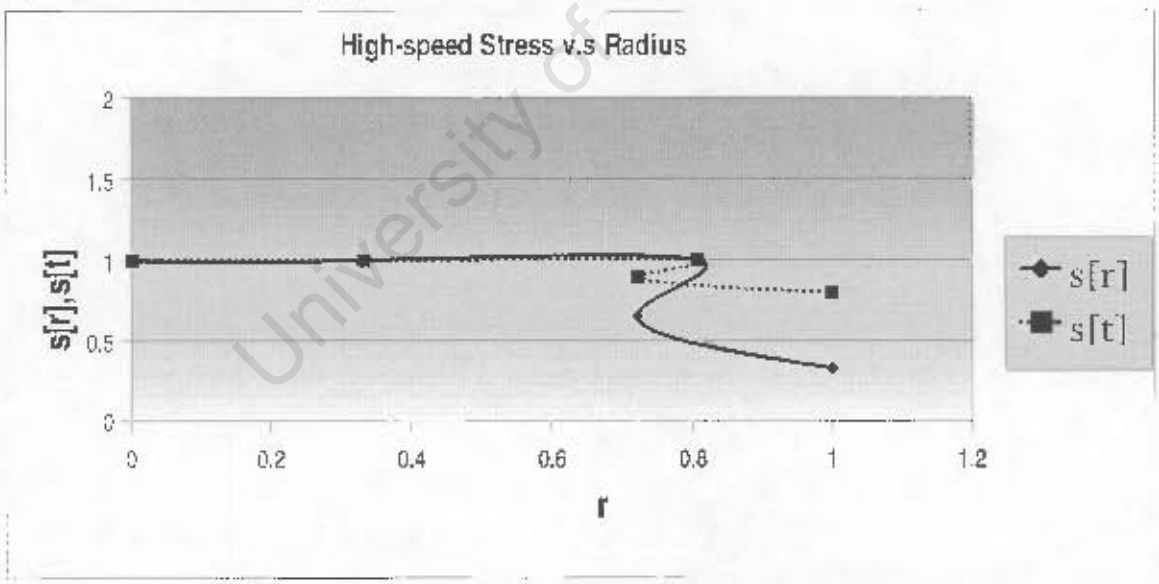

FIGURE 4.7: STRESS DISTRIBUTION OVER FLYWHEEL AT HIGH-SPEED $\bar{\kappa}^2$=6.720

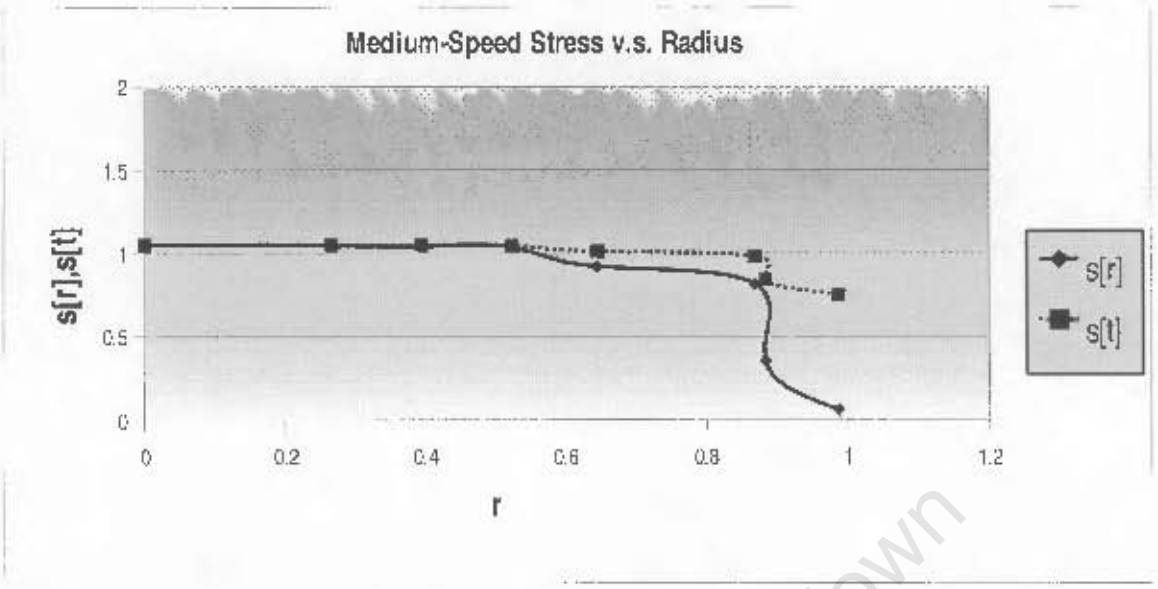

FIGURE 4.8: STRESS DISTRIBUTION OVER FLYWHEEL AT MEDIUM SPEEDS

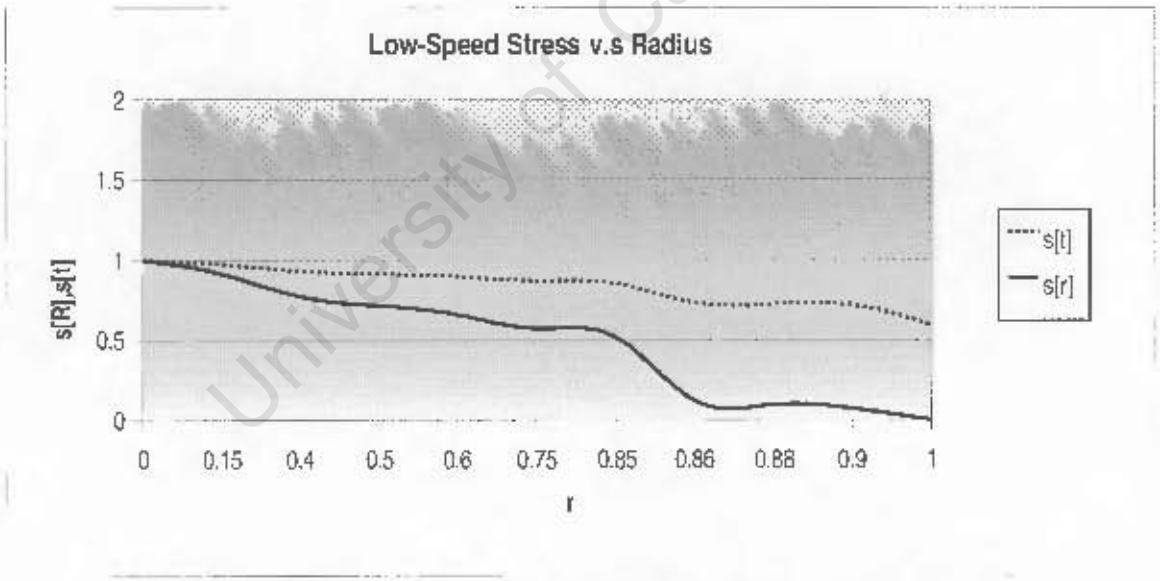

Figure 4.9: Stress distribution over flywheel at Low speeds

By comparison to the stress-graph at the medium speed, the stress-graph proposed by M. Berger and I. Porat is similar with this Medium speed, where the stresses have violated the constraint limit value.

The finite smooth curves is a path created by the radius r with parameter interval $[P_1,P_6]$. This interval was subdivided into five parts or shapes and each interval varied and provides a path which is a continuous function at the subinterval. Every single location in the subdivision of a radius for a free-disk creates its own path, see fig. 4.9

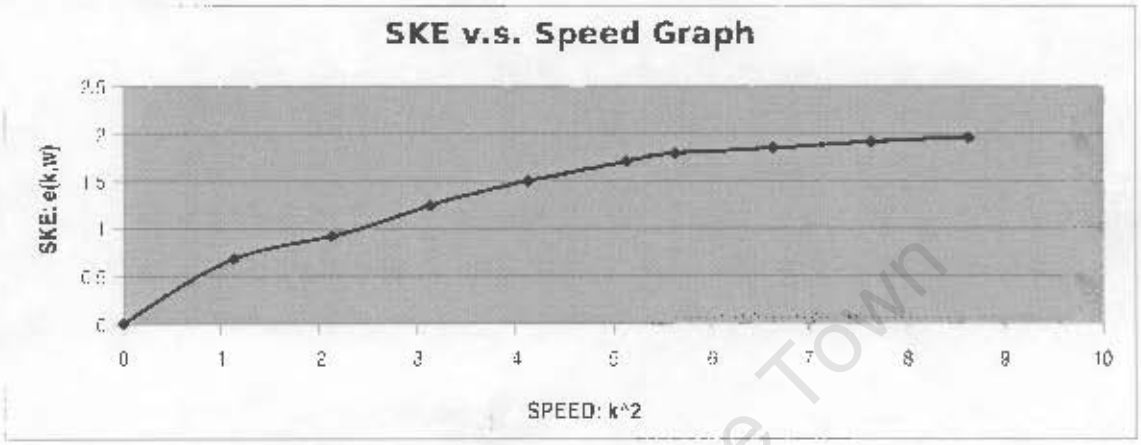

FIGURE 4.10: SKE V.S. SPEED

From Figure 4.9, it can be observed that the optimal profile is a continuous mathematical function for which the SKE converges to the upper bound limit value of 2, i.e.:

$$e(k,w) \rightarrow upper\ bound, 2 \qquad (4.33)$$

The SKE, from low speed to high speed converges to the higher value, called the upper bound, but remains strictly less than two. The graph in figure 4.9 shows the specific energy of the three speed intervals as a function of speed.

The algorithm for obtaining the optimal shape in the High-speed requires setting the simulation variables and then find the final shape w(r) composed of a constant stress profile and the minimum thickness. The SKE e(k) is calculated with a given final shape. Finally the SKE e(k) is plotted for $k^2 = 0 \ldots 6.720, 6.760, 7.720$ and shown in figure 4.10. This proves that the ultimate speed is 6.720 and cannot be exceeded.

Shown in fig.4.11, the dotted line depicts the maximum possible SKE limit. The graph shows an improvement beyond the possible maximum SKE of two. It is physically impossible, however, because the flywheel material would have exceeded it's maximum tensile strength and fractured.

This may be achieved in an application where a compressive force is applied at the edge of the disk, e.g. by shrink fitting a rim, which will raise the maximum possible SKE above two.

This possibility, however, is considered too complicated for a low cost design and was not pursued further at this point of the design.

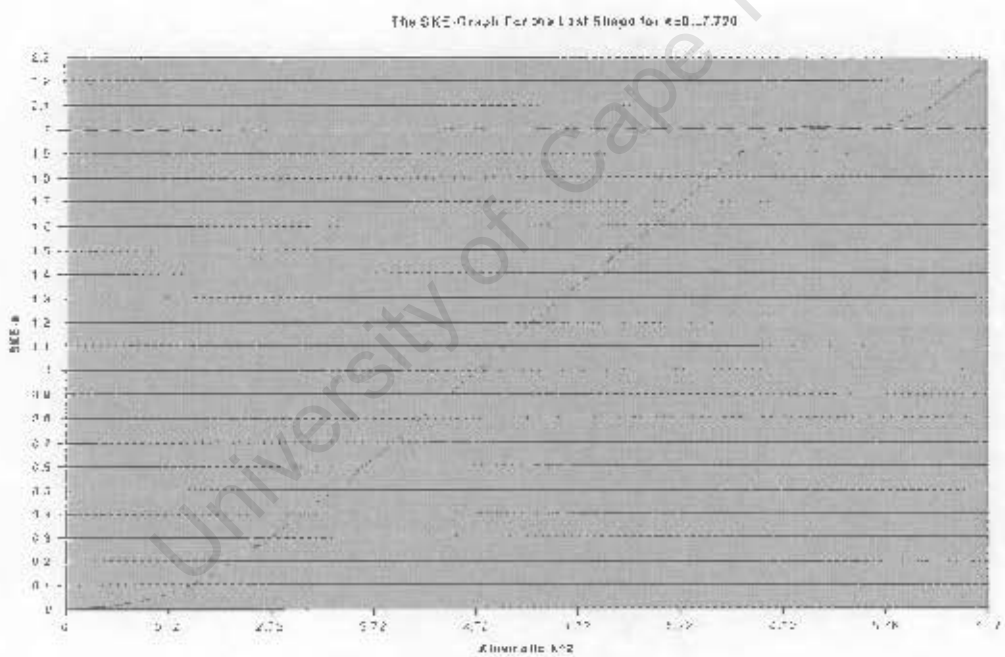

FIGURE 4.10: SKE OF THE OPTIMAL SHAPE FOR THE SPEED RANGE FROM 0 TO 7.720

The Maple 5 worksheets used to determine the flywheel parameters are in Appendix II. A safety factor of 2 was used in the iterative process to determine the place where $P_4 \approx P_5 \approx P_6$, coinciding with the high speed profile of $k_2 \approx 5.2$ The following results were obtained:

djohnson

$k = 2.280350850$

$p_1 = 0$

$p_2 = 0.00491352$

$p_3 = 0.9410683564$

$p_4 = 1.006068064$

$p_5 = 1.056068064$

$p_6 = 1$

For a 300W-h flywheel, these values translates to the following dimensions:

$P_2 = 0.03$ m

$P_3 = 0.0884$ m

$P_4 = P_5 = P_6 = 0.112$ m

The volume and mass of a flywheel of these dimensions is calculated using a Maple 5 spreadsheet.

The volume of the exponential profile is given by:

$$V_e = 2\delta\pi \frac{\left[-1 + e^{\left[\frac{1}{2}k^{(p_4 - p_3)}\right]}\right]}{k^2} \qquad (4.34)$$

, where:

δ = thickness of the minimum thickness profile, and the volume of the minimum thickness profile is given by:

$$V_d = \pi\delta(p_4^2 - p_3^2) \qquad (4.35)$$

The values of the parameters used in equations 4.34 and 4.35 are as follows:

$p_2 = 0.03$ m

$p_3 = 0.0884$ m

$p_4 = 0.112$ m

djohnson

$\delta = 0.02$ m

$\rho = 1960$ kg/m^3

k = 2.429

The calculated volumes and mass of the profiles comes to:

$V_e = 0.00043869642$ m^3

$V_d = 0.000297008832$ m^3

$V_{total} = 0.001174395672$ m^3

mass = 2.3018 kg

The energy density of this flywheel is therefore E = 300 / 2.3 = 130 W-h/kg. The energy densities obtained for flywheels of various flywheel storage projects are listed in table 4.3.

Material	*Type*	*E [W-h/kg]*	*Source*
Carbon fibre	-	80	G. Ries and H.W. Neumueller
Carbon T1000	Multi rim	350	B. Bolund, H. Bernhoff and, M. Leijon
Carbon	Multi rim	168	R.F. Post, S. F. Post

TABLE 4.3 : SPECIFIC ENERGY DENSITIES ACHIEVED IN VARIOUS PROJECTS

J.H. Faupel and F.E. Fisher describes a discrete analytical method for flywheel calculations and was used to verify the strength of the determined flywheel profile. The method, shown in Figure 4.11 was implemented, using a spreadsheet, where the flywheel strength is evaluated using interconnected uniform thickness concentric rings, with free boundaries defined at the central hole and at the rim.

The method can be viewed as a crude approximation of the principles used in finite element

analysis, where the segments chosen are much smaller.

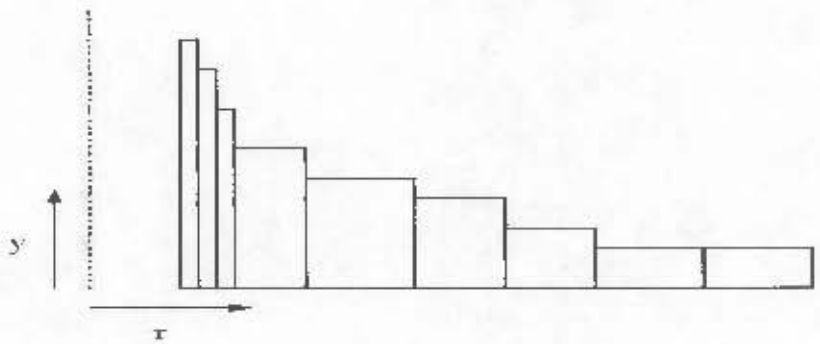

FIGURE 4.11 : APPROXIMATING FLYWHEEL SHAPE WITH DISCRETE RINGS

J.H. Faupel and F.E. Fisher describes the methodology of stress change from one section to the next as:

$$\Delta\sigma_r = -\Delta y \frac{\sigma_r}{(y+\Delta y)} \qquad (4.36)$$

,where:

$\Delta\sigma_r$ = Change in radial stress

Δy = Change to thickness of adjacent section

y = thickness of section, and:

$$\Delta\sigma_t = \nu\Delta\sigma_r \qquad (4.37)$$

, where:

$\Delta\sigma_t$ = Change in hoop stress

ν = poisons ratio for the material

Applying these principles to the result for the prototype obtained with the analytical method, the stresses are calculated with an OpenOffice spreadsheet and are shown in Table 4.4. The maximum stress occurs in the hoop direction, on the outer boundary of the flywheel, at just over 90Mpa, well

within a factor of safety of 2 for the fibre glass - epoxy composite.

σ_{rd}	0 Psi
ω	90000 Rpm
ν	0.3
ρ	0,07
$\beta_1\omega^2$	7362.54
$\beta\omega^2$	4233.28

Section	r	r²	ωx10³	$\beta_1\omega^2\rho^2$	$\beta\omega^2\rho^2$	Y	$-\Delta Y/(y+\Delta Y)$	σ_{rj}	$\Delta\varepsilon$	Δt	σ_{tj}
1	3.94	15.52	1932.54	114137.83	65715.72			0			48422.11
2	3.48	12.11	2477.21	89042.15	51266.7	0.787	-2.53E-003	25095.68	-63.61	-19.08	62871.14
3	3.32	11.02	2721.73	81042.6	46660.69	0.789	-1.27E-003	33031.62	-41.81	-12.54	67476.94
4	3.16	9.99	3004.33	73419.48	42271.83	0.790	-2.53E-003	40612.92	-102.56	-30.77	71802.39
5	3	9	3333.33	66172.83	38099.51	0.792	-2.52E-003	47757.02	-120.29	-36.09	75932.9
6	2.84	8.07	3719.5	59302.82	34143.93	0.794	-1.26E-003	54506.94	-68.56	-20.57	79785.92
7	2.68	7.18	4176.88	52808.86	30405.1	0.795	-1.26E-003	60932.13	-76.55	-22.96	83404.45
8	2.52	6.35	4724.11	46691.55	26883.01	0.796	-1.25E-003	66972.9	-84.06	-25.21	86857.98
9	2.36	5.57	5386.38	40950.89	23577.67	0.797		72628.73			90086.77

TABLE 4.4 : STRESS CALCULATION USING DISCRETE ANALYTICAL METHOD

These results were used to construct the following flywheel shape by means of a CAD package. The shape and the main dimensions shown in Figure 4.12.

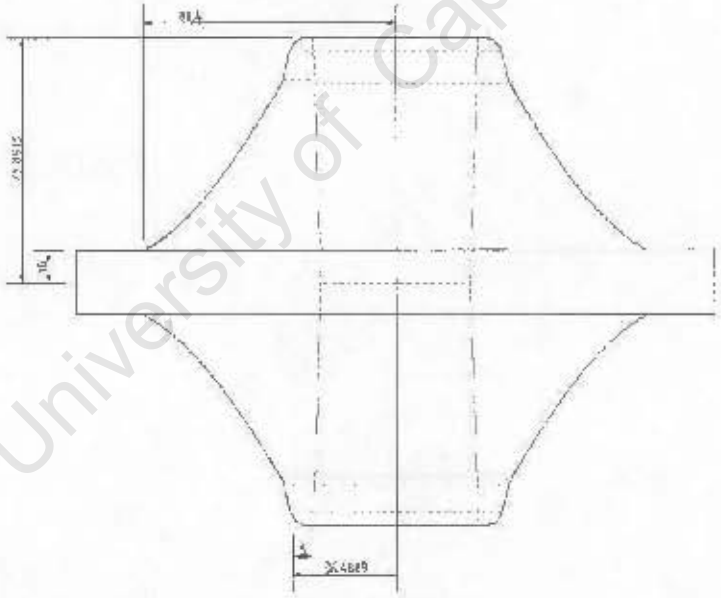

FIGURE 4.12: CAD DRAWING OF ULTIMATE SHAPE 300 WH FIBRE GLASS COMPOSITE FLYWHEEL

4.5 Material Strength

The materials under consideration for flywheel manufacture are either in the metal or fibre composite category.

Metals are easy to use for mass production, their physical properties well documented and they are, except for some special cases, homogeneous. These benefits are, however, quickly offset by the required size and mass thereof, because of their low specific energies, safety issues and cost of containment.

Metal flywheels are contained in massive metal or reinforced concrete/metal housings. Metal flywheel systems are bulky and difficult to handle and are usually fixed installations. The mode of metal failure is elastic, which stores large amounts of elastic energy into the fragments before severing off the structure. Metals are known to suffer from fatigue when loaded repetitively.

Composite flywheels, on the other hand, are much smaller and lightweight because of their high specific kinetic energy. Their physical properties are not homogeneous, like metals, and has to be taken into consideration. Composites fail differently, commonly de-bonding, fibre pull-out and de-lamination. De-lamination is prevented in current filament wound designs by using a multi-rim approach, which is a function of wall thickness. The process of filament winding and separating the rims with an elastomer and balancing the resulting structure is cumbersome and reflected in the price of commercial flywheels.

P.J.E. Forsyth and L. Holloway gives the strength of continuous fibre reinforced materials, with all the fibres aligned in the direction of the applied force as:

$$\sigma_c = \sigma_f \cdot V_f + \sigma_m \cdot (1 - V_f) \qquad (4.38)$$

,where:

σ_c = Ultimate tensile stress [MPa]

σ_f = tensile stress of fibres [MPa]

σ_m = tensile stress of matrix [MPa]

V_f = Volume fraction of fibres [$0 \leq V_f \leq 1$]

Short fibre composites for fibres longer than the minimum critical length are only marginally weaker than a continuous fibre composite. Fibres shorter than this critical length will not be considered for this design. The advantages of short fibre composites are that they can be easily formed into complex shapes, by casting, injection, layering and spraying.

Having the strength requirement (M. Berger and I. Porat,) only in the plane of rotation, requires to have have the fibres oriented in that plane.

The critical length of a fibre is determined by evaluating the process of load transfer. The load to the fibre is transferred through the shear strength between the fibre and the matrix interface. The resulting tensile stress is not the same along the length of the fibre. Shown in Figure 4.14, the stress along the fibre starts from zero, increases to a maximum, then reduces back to zero at the other end of the fibre.

From the force balance on a short fibre, shown in Figure 4.13, the force acting normal to the element δF is equal to the shear force acting on the edge of the element. The force on the edge is the product of the shear stress, τ_m, and the area it acts upon therefore :

$$\delta F = \pi d \tau_m \cdot \delta x \qquad (4.39)$$

, where:

d = diameter of fibre.

τ_m = Shear Stress on matrix

P.P. Benham & F.V. Warnock defines that, for the Tresca criterion, the shear stress is half the difference between the two principal stresses. The only stress, σ m, is applied parallel to the fibres and none perpendicular thereto. Principal stresses act at right angles to each other and are expressed

djohnson

as :

$$\tau_m = \frac{\sigma}{2} \qquad (4.40)$$

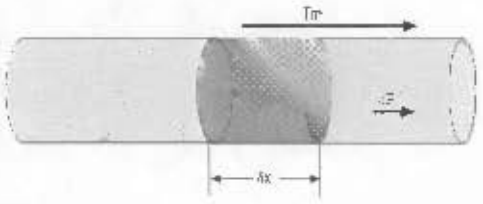

FIGURE 4.13: SHEAR STRESS ELEMENT

From Equations 4.39 and 4.40 the total force acting upon a fibre is given by:

$$F = \int_0^x \frac{\pi d \sigma_m}{2} dx \qquad (4.41)$$

The equation for the stress at any point along the fibre, measured from either of the free ends, by dividing the force by the cross-sectional area of the fibre becomes:

$$\sigma(x) = \frac{\int_0^x \frac{\pi d \sigma_m}{2} dx}{\frac{\pi \cdot d^2}{4}} = 2\sigma_m \frac{x}{d} \qquad (4.42)$$

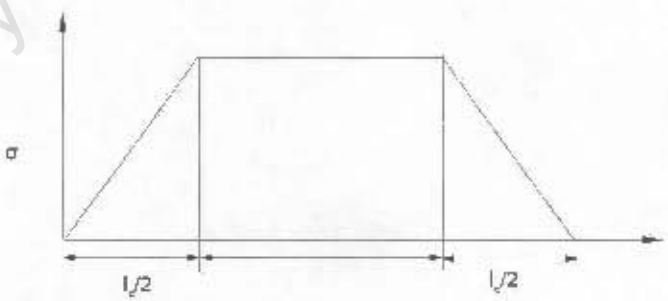

FIGURE 4.14: STRESS DISTRIBUTION OVER A SHORT FIBRE

This relationship is illustrated in Figure 4.14. The stress rises linearly from zero at the end to a constant maximum at the centre of the fibre and drops back to zero at the other end.

P.J.E. Forsyth and L. Holloway defines the critical length l_c as:

djohnson

$$l_c \geq \frac{\sigma_f d}{2 \cdot \tau} \qquad (4.43)$$

Substituting 4.40 in 4.42 yields the critical length to be:

$$l_c = \frac{\sigma_f d}{\sigma_m} \qquad (4.44)$$

P.J.E. Forsyth gives the average stress on a fibre as:

$$\overline{\sigma} = \sigma_f (1 - \frac{l_c}{2} l) \qquad (4.45)$$

Substitute the average fibre stress of equation 4.45 for the fibre stress in equation 4.38 giving the strength of the short fibre composite i.e.:

$$\sigma = V_f \sigma_f (l - \frac{l_c}{2l}) + (1 - V_f) \sigma_m \quad (4.46)$$

From equation 4.46 it is clear that, for fibres much longer than the critical length of equation 4.44, the strength approaches that of continuous fibre composites, where the term: $(l - \frac{l_c}{2l})$ tends toward unity in equation 4.46, which tends to equation 4.38, i.e. the strength equation for long fibre composites.

The principle stresses in the ultimate shape flywheel has been determined to be in the plane of rotation, i.e. in the radial and hoop directions. In the manufacturing of the flywheel, the fibres can be layered, sprayed or injected to orientate randomly in this plane. Consequently, all the fibres will not be aligned in the principle directions, but random with respect to them.

The fibres angled to those of principle directions will share the load between the two, in proportion

to it's angle. It will therefore be reasonable to assume that, as a mean average, half of the fibres will carry the load in the radial direction and the half in the hoop direction.

The resulting strength of the composite can therefore be assumed to be half that of a unidirectional laminate and adding an adequate factor of safety will result in a structurally sound design.

4.6 Flywheel Safety

For a complex shape flywheel, a short fibre composite is more suitable for low cost manufacturing. Assuming a uniform distribution and fibre orientation, the dominant mode of failure will be fibre pull-out. defines the pull-out work of a single fibre as:

$$W_{fp} = \left(\frac{l_c}{l}\right) \cdot \frac{\pi d \tau l_c^2}{24} \qquad (4.47)$$

,where:

W_{fp} = fibre pull-out work

l_c = critical fibre length

l = fibre length

d = fibre diameter

τ = maximum interface shear stress

The number of fibres per volume fraction can be written as.

$$N = \frac{V_f}{\pi \cdot d^2} \qquad (4.48)$$

, where:

N = number of fibres

V_f = volume fraction

d = fibre diameter

Multiplying equation 4.47 with 4.48 gives the total amount of work as:

$$W_{fp} = \frac{\tau V_f l_c^3}{24 l d} \qquad (4.49)$$

During flywheel failure, the energy that can be dissipated by this mechanism becomes:

$$W_{fp} = \frac{\tau V_f l_c^3}{24 l d} = \frac{40\text{x}10^6 \cdot 0.6 \cdot 0.05^3}{4 \cdot 0.02 \cdot 0{,}05} = 2250\text{MJ} = 135\text{kWh}$$

This value is an order of four hundred and fifty times higher than that of stored energy in the flywheel and the bulk of the structure's energy can be converted to heat and fine fibrous particles.

The effect on the ultimate tensile strength of the composite material, due to fibre orientation, can be calculated from the results of S. Fara and A. Pavan. They showed that a critical fibre orientation factor exist, Figure 4.15, at which the component will show shortcomings in preventing crack propagation though the structure.

This effect will cause large, energetic fragments to be severed off the flywheel structure during failure, similar to that of elastic material failure. To prevent such failures, the fibre orientation has to be kept within safe limits in order to reduce the need for expensive containment.

It is shown that even for fibre orientations as low as 0.3, the strength is higher than 200MPa. These values are for short fibres in Polyarylamide and the actual values do not directly apply to glass fibre-epoxy in this design. It is of importance, however, showing that the strength contribution of random orientated fibres in the plane is better than half that of 90% aligned fibres.

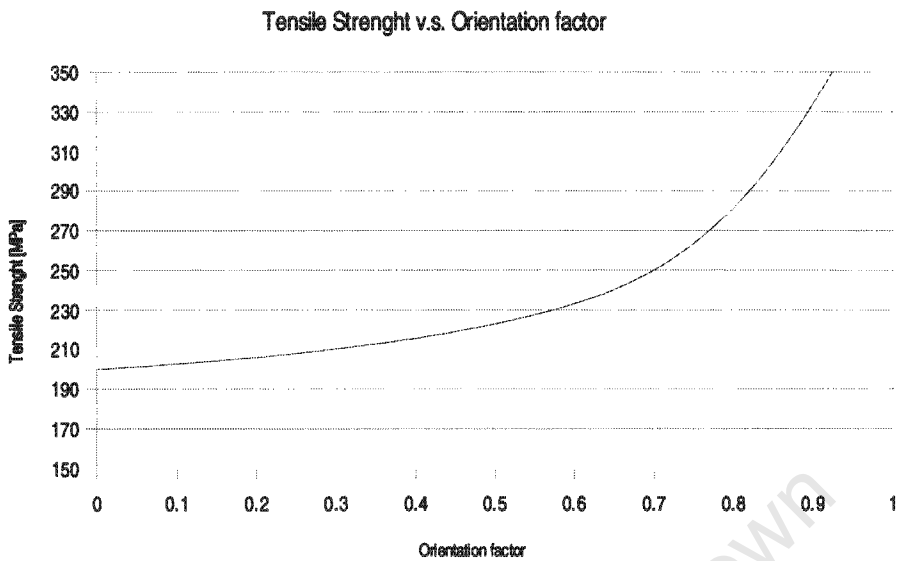

FIGURE 4.15: YIELD STRENGTH VERSUS. FIBRE ORIENTATION. [S. FARA AND A. PAVAN]

S. Fara and A. Pavan [34] cites an empirical best curve fit for the ultimate axial stress:

$$\sigma^u = \left[\frac{(a_{11})^2}{(\sigma_{11}^u)} - \frac{(a_{11})^2 \cdot [1-(a_{11})^2]^2}{(\sigma_{11}^u)} + \frac{[1-(a_{11})^2]^2}{(\sigma_{22}^u)}\right]^{-\frac{1}{2}} \qquad (4.50)$$

, where:

σ_U = Ultimate axial stress [MPa]

a_{11} = fibre orientation factor to respect the reference system 123

a_{22} = fibre orientation factor to respect the reference system 123

In a similar manner, the composite elasticity is affected, shown in Figure 4.16 and equation 4.51.

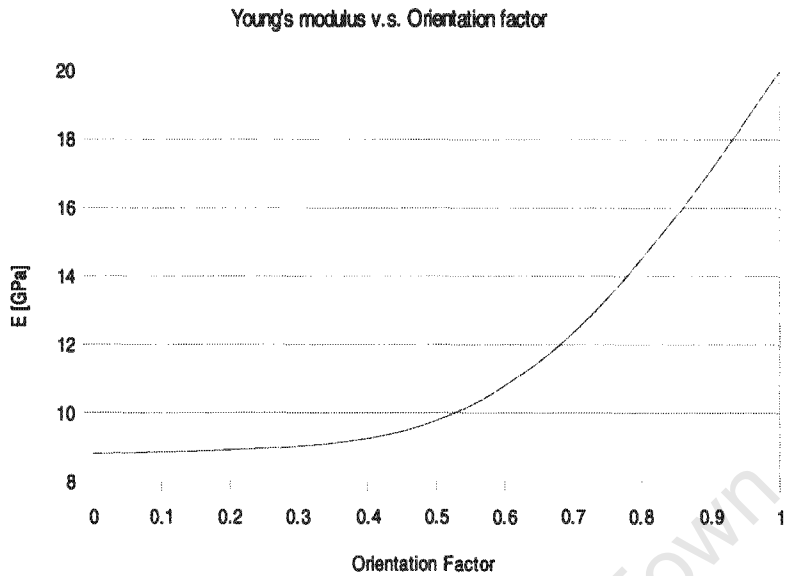

FIGURE 4.16: YOUNG'S MODULUS VERSUS ORIENTATION FACTOR. [S. FARA AND A. PAVAN]

$$E(a_{11})=[\frac{(a_{11})^2}{E_{11}}-\frac{(1-a_{11})^2}{E_{22}}+(\frac{1}{G_{12}}-\frac{2\cdot\nu}{E_{11}})]^{-1} \qquad (4.51)$$

,where:

$E_{(a11)}$ = Young's modulus [Gpa]

E_{11}, E_{22} = Modulus of elasticity with respect to the reference system 123

a_{11}= fibre orientation factor with respect to the reference system 123

ν = Poisson's ratio

G = Shear Modulus [GPa]

Note that for fibre orientation factors below 0.4, the ultimate tensile strength changes little and given an adequate factor of safety, the effect on the composite strength will go unnoticed. It is however important for safety during failure, where the energy contained in the individual fragments breaking free from the rotating mass does matter. This effect is of high importance in low cost applications, such as this one.

J.A. Epaarachi, P.D. Clausen determined empirical fatigue strength data for glass fibre-epoxy, shown in Figure 4.16. According to the graph in Figure 4.17, the measured fatigue strength of the glass fibre-epoxy composite is approximately 200MPa at 100 000 cycles, well over twice the maximum calculated stress in this prototype flywheel.

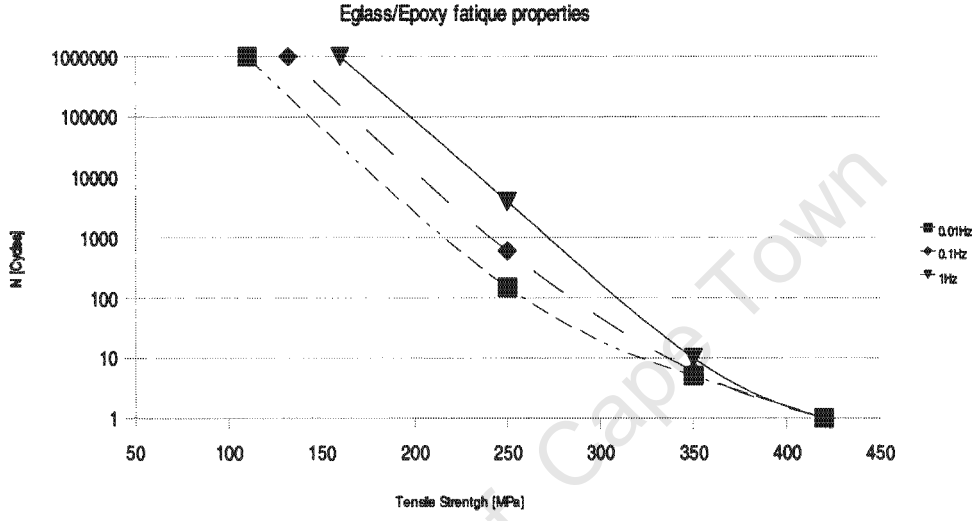

FIGURE 4.17: GLASS-EPOXY FATIGUE [J.A. EPAARACHCHI AND P.D. CLAUSEN]

4.7 Composite Material Properties

The properties of polyester and epoxy thermosetting matrix materials are given in tables 4.5, as cited by E.A. Avallone and T. Baumeister III

Material	*E* [GPa]	*Tensile Strength* [MPa]	*K* [$MNm^{-3/2}$]	T_{glass}, [°C]	T_{melt}, [°C]	T_{max}, [°C]
Polyester	1 to 4	30 to 70	0.5	-	-	-
Epoxy	2 to 5	40 to 80	1	-	-	-

TABLE 4.5: PROPERTIES OF COMMON MATRIX MATERIALS

The difference between Thermosetting and Thermoplastic materials is that the latter can be re-melted and moulded, while the first cannot. The more common thermosetting matrices used in composites are Polyester and Epoxy. Abbreviations of common matrix materials are listed in Table 4.6.

Fibre	E [GPa]	Strength [MPa]	ν	Density[kg/m^3]	T_m or T_g (°C)
E-Glass	72	1700 - 2100	0.2	2500	1500
AR Glass	70	1500 - 1900	-	-	-
S Glass	80	2000 - 2500	0.22	2540	1400

TABLE 4.6: PROPERTIES OF GLASS FIBRES [R F POST, S. F. POST, E.A. AVALLONE AND T. BAUMEISTER III]

The different types of glass is used for the following applications:

- E Glass - All purpose fibre; resistant to leaching in water.
- S Glass - Highest strength and stiffness
- AR glass- Alkali resistant; used for strengthening cements.

Carbon-Polymer composites are made of carbon fibres, either unidirectional, woven, knitted or 3-dimensionally embedded in a polymer matrix. The polymer matrix can be either thermosetting or thermoplastic. The majority of carbon fibre is pre-coated or pre-impregnated with the polymer.

Carbon-Carbon (C-C) composites consisting of highly-ordered graphite fibres embedded in a carbon matrix. C-C composites are manufactured by gradually building up a carbon matrix on a fibre form through a series of impregnation and chemical vapour deposition. C-C composites are stiffer, stronger and lighter than steel or other metals. Manufacturing of C-C composites, however, are prohibitively expensive and the facilities to manufacture these are not generally available in the

djohnson

developing countries.

Trade Name	Grade	Density [kg/m^{-3}]	Stiffness [GPa]	Strength [MPa]	% Strain at Failure
Celion	G30	1780	234	3790	1.62
	G40	1770	300	4970	1.66
	G50	1780	358	2480	0.7
Magnamite	AS4	1800	235	3800	1.53
	IM6	1730	276	4380	1.50
	HMU	1840	380	2760	0.7
Thornel	T-650/35	1770	241	4550	1.75
	T-650/42	1780	290	5030	1.70
	T-50	1810	390	2420	0.7

TABLE 4.7: PROPERTIES OF CARBON FIBRES [E.A. AVALLONE AND T. BAUMEISTER III[36]

It possible to determine the properties of composites by choosing different material combinations and calculating the resulting properties thereof substituting the manufacturer's data into equation4.38 and 4.46 gives rise to Table 4.8.

Matrix	Fibre	f	E [GPa]	E [GPa]	σ [MPa]	σ [MPa]
Polyester	Continuous E-Glass	0.4	29.2	3.3	800	< 30
Polyester	Chopped E-Glass	0.4	28	2	300	< 30
Polyester	Continuous E-Glass	0.5	36	3.9	720	< 30
Polyester	Chopped E-Glass	0.5	42	2	380	< 30
Polyester	Continuous E-Glass	0.6	42.8	4.8	856	< 30
Polyester	Chopped E-Glass	0.6	35	2	450	< 30
Epoxy	Continuous E-	0.4	31	8	800	< 50

Matrix	**Fibre**	**f**	**E** [GPa]	**E** [GPa]	σ [MPa]	σ [MPa]
	Glass					
Epoxy	Chopped E-Glass	0.4	30.5	5	600	< 50
Epoxy	Continuous E-Glass	0.5	37.5	9.3	1000	< 50
Epoxy	Chopped E-Glass	0.5	37	5	800	< 50
Epoxy	Continuous E-Glass	0.6	44	11.3	1200	< 50
Epoxy	Chopped E-Glass	0.6	43	5	1000	< 50

TABLE 4.8: CALCULATED PROPERTIES OF E-GLASS FIBRE AND THERMOSETTING PLASTIC COMPOSITES

The trend is that the better materials are more costly. Graphite fibre is about twice the price of glass fibre, though it is four times stronger, resulting in a lower cost per W-h stored.

A composite mixture was manufactured from Pyrograf™ micro fibre and epoxy. Test specimens were molded, vacuum bagged and tested for tensile strength. These vapor grown fibres has projected cost of $2 per kg and was designed to be used as an additive to improve the thermal conductivity of thermoplastics. The objective of this design was to use a low cost, high strength material, which could be cast into moulds for low cost production of flywheels.

The results were disappointing and the test results are listed in Table 4.9. The resulting ultimate tensile strength measured was only a fraction of that of the epoxy itself at 85MPa.

Material mixture by volume	***Breaking force [N]***	***Tensile strengh[MPa]***
3 parts VGCF, 4 parts Epoxy	1512.4	15.124

3 parts VGCF, 4 parts Epoxy	1401.2	14.012
4 parts VGCF, 3 parts Epoxy	1379.0	13.79
4 parts VGCF, 3 parts Epoxy	934.1	9.34
1 parts VGCF, 1 parts Epoxy	2135.2	21.35
1 parts VGCF, 1 parts Epoxy	Clamping broke sample	~

TABLE 4.9: EXPERIMENTAL VGCF/EPOXY TENSILE STRENGTH VALUES

Closer inspection, see Figure 4.18, reveales that the cured specimens were very porous as gas bubbles were trapped inside the cured composite mixture. This was despite vacuum bagging the curing specimens, a process which is generally used in industry to remove air inclusions from curing composite materials.

A means of eliminating the bubbles from the VGCF composite material has to be developed to be usable as a structural material. Such a material will be promising in terms of strength and cost, as the graphitized form of VGCF has a claimed tensile strength of 9GPa and the projected mass produced price is in the order of R12 / kg.

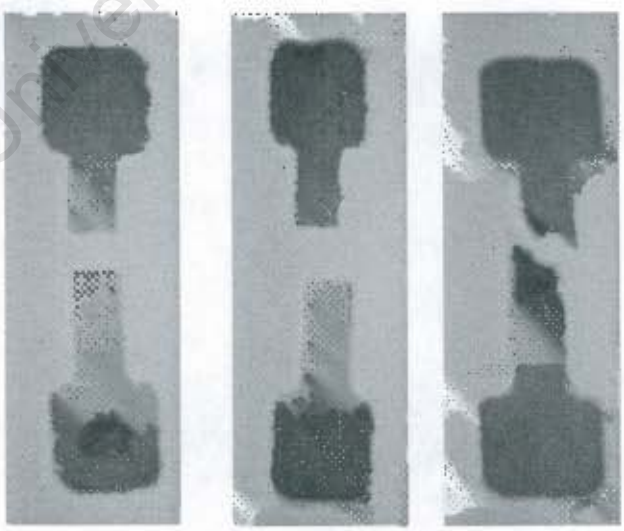

FIGURE 4.18 : VGCF-EPOXY TEST SAMPLES

4.8 Flywheel Manufacture

The manufacture of the flywheel in one piece was cumbersome, especially with the heat generated during curing of the thick centre section. The problem was solved partially by splitting the flywheel in two halves. The cracking reduced significantly, but use of aluminium moulds or adding aluminium powder to the resin to remove the heat, will be essential for production. The addition of aluminium powder to the resin will affect the material properties, which should be taken into consideration in the design.

Once the epoxy has cured, the two halves are surfaced and glued together with a milled fibre-epoxy composite. This does not affect the strength of the structure, because all the stresses are limited to the plane of rotation i.e. perpendicular to the axis of rotation. Using this method, flywheels can be manufactured inexpensively, given the basic tools and skills.

For a mass produced flywheel of ultimate shape, the moulds can be relatively inexpensively manufactured with aluminium. The mould surface has to be coated with a release agent, typically wax. To create the central hole and reduce the curing mass and material wastage, a core of either wood or a reusable aluminium one, is waxed and inserted into the mould. The epoxy and short fibres are now measured, mixed and poured into the moulds.

M.D. Afendi, W.M. Banks, D. Kirkwood showed that adding a bubble nucleation agent such as Scotch–Brite and vacuum bagging reduces bubbles in the infusion process. Vacuum bagging consists of a simple pump and a plastic bag to draw a slight vacuum on the work piece. Once the work piece is sufficiently cured, it is forced out of the mould with pressurised air and the next cast can be made. It is possible to make about two casts per mould per day.

Shown in Figure 4.19 are two disposable moulds made from thermoplastic, which caused thermal cracking in the work piece. The two halves have to be surfaced and bonded, using a mixture of milled fibre and resin, of the same material as the flywheel.

The benefits of this method of manufacturing the flywheel are that the special shape yields a higher SKE, reduced material cost and lower overall cost of production.

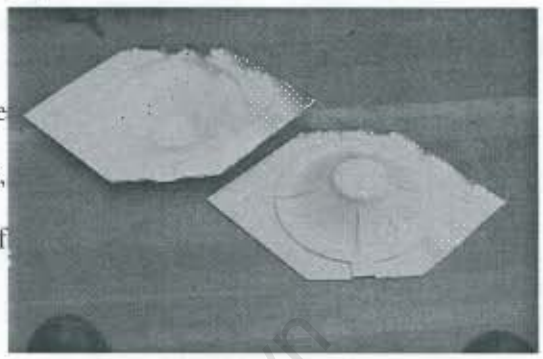

FIGURE 4.19 : DISPOSABLE PLASTIC MOULDS

4.9 Air Frictional Losses

The air friction losses becomes significant at higher speeds, than that of the preliminary tests. True analytical solutions do not exist for compressible fluids. Conventional engineering practice is to assume either i) adiabatic or ii) isothermal flow.[16, 36]. To simplify the problem, consider a rotating cylinder as an infinite flat plate and the fluid as incompressible for an approximation of the magnitudes.

The drag force arises from two sources. The pressure drag F_p and skin friction drag F_f arise due to a shear stress τ_0. According to R. L. Daugterty, J. B. Franzini, the drag coefficient over an infinite flat plate, as depicted in Figure 4.20, is made up of two parts namely:

$$F_D = F_P + F_f = \frac{C_D \cdot \rho \cdot A_x \cdot V^2}{2} + \frac{C_f \cdot \rho \cdot A_y \cdot V^2}{2} \qquad (4.52)$$

, where:

djohnson

F_D = Drag Coefficient

F_P = Pressure drag

F_f = Skin friction drag

C_D = Coefficient of pressure

C_f = Skin friction coefficient

ρ = density

V = Velocity of fluid over body and

A_s = characteristic area for shear

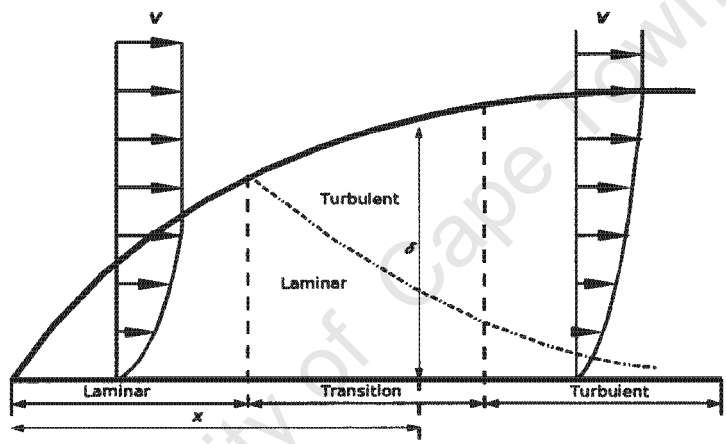

FIGURE 4.20: BOUNDARY LAYER ALONG A SMOOTH FLAT PLATE[R. L. DAUGTERTY, J. B. FRANZINI]

The boundary-layer thickness and skin friction drag may be calculated with the following equation [R. L. Daugterty, J. B. Franzini]:

$$R_e = \frac{\rho \cdot V \cdot X}{\mu} \qquad (4.53)$$

, where

R_e = Reynolds Number

X = distance from edge (in the case of a rotating cylinder this approximates infinity)

μ = dynamic viscosity = $2.025X10^5$ N.s/m2 for air at 20 °C

djohnson

R. L. Daugterty, J. B. Franzini describes Laminar Flow:

$$\frac{\delta}{X}=5.2\cdot\sqrt{R_e} \quad \text{for } 0 < R_X < \ 5X10^5 \qquad (4.54)$$

$$C_f=1.382\sqrt{R_e} \quad \text{for } 0 < R_X < \ 5X10^5 \qquad (4.55)$$

From equation 4.52, an infinite plate, in this case a rotating cylinder:

$$\lim_{X\to\infty}\frac{\delta}{X}\to 0 \qquad (4.56)$$

, because the surface of a cylinder does not have a starting edge.

It is concluded that it is safe to assume that the Reynolds number will be smaller than $5x10^5$ for all subsonic speeds and the flow will be laminar for the pressure drag component.

It is known that the fluid adjacent to the boundary of the plate is stationary irrespective of the surface roughness. For laminar flow CD is given in table 4.9.

Re	*10*	*10^2*	*10^3*	*10^4*	*10^5*	*10^6*
C_D	0.838	0.265	0.0838	0.0265	0.0084	0.00265

TABLE 4.9: SKIN DRAG COEFFICIENTS FOR A FLAT PLATE [R L DAUGTERTY]

For the skin friction drag X = circumference of the Flywheel and V = the surface speed, given by:

$$X=\pi D \quad (4.57)$$

, and

$$V=\pi\cdot D\cdot\omega \qquad (4.58)$$

, where:

D = Diameter of cylinder

ω = angular velocity

Substituting in equation 4.55 and assuming turbulent flow will commence for $R_e = 5x10^5$,

$$C_f = \frac{1.296 \cdot \pi \cdot D^2 \omega}{2.025 x 10^5} \qquad (4.59)$$

assuming a density of 1.296 kg/m^3 at 1 bar and 20 °C. The power loss component of the surface drag is given by :

$$P_D = T\omega = \frac{F_D D \omega}{2} \qquad (4.60)$$

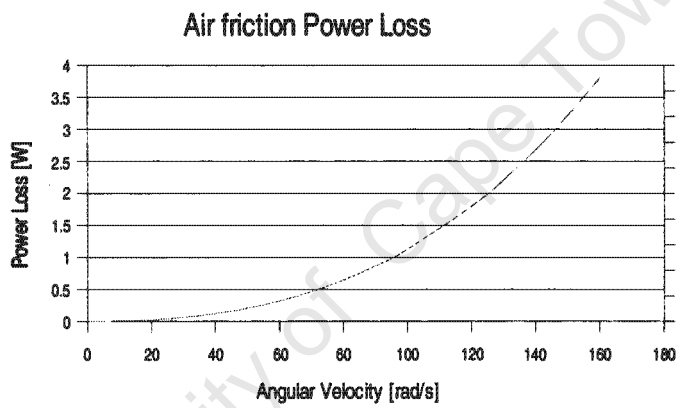

FIGURE 4.21: AIR FRICTION LOSS FOR FLYWHEEL AT LOW SPEEDS

Substituting equations 4.52 to 4.59 into 4.60 gives:

$$P_D = \frac{[C_D + C_F] \cdot \rho A_s \cdot \pi^2 \cdot D^3 \cdot \omega^2}{4} \qquad (4.61)$$

For the speeds at which the cylindrical model has been tested i.e. < 1500 rpm (or 157 rad/s) the calculated air friction losses are shown in Figure 4.21.

It is therefore essential that the air frictional drag is minimized if the energy in a flywheel system is going to be stored for any length of time, with a small sized machines, and high efficiencies.

The frictional component from air friction can be eliminated by evacuating the flywheel housing, but it is difficult and expensive to sustain indefinitely, due to the dissolved gasses in the metals, the porosity thereof and leaking though the seals. One possibility is to reduce the pressure and using a near ideal gas e.g. Helium.

Substituting the air with helium at 0.5 bar reduces this frictional component from 3.75W to 0.28W @ 1500 rpm, a reduction of 92.5%, shown in Figure 4.22.

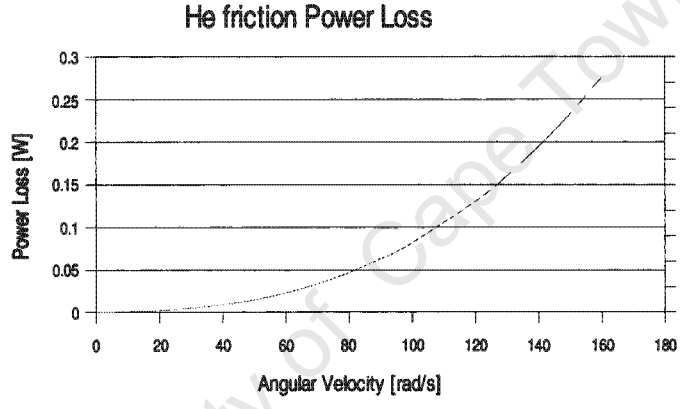

FIGURE 4.22 : HE FRICTION LOSS FOR FLYWHEEL AT LOW SPEEDS

The air frictional losses described by Y. Suzuki, A. Koyanagi, M. Kobayashi, R. Shimada was in the order of 10W @ 4000 rpm with He at 1 bar for a flywheel of 378mm diameter, which correlates well with this theoretical estimate of equation 4.61 for 0.5 bar Helium.

The losses for the ultimate shape flywheel will be less than these calculated, because of the conical-like shape and the average radius is less than that of a cylinder. The calculation is complicated by the cross flow over the length of the flywheel by centrifugal action on the gaseous fluid from the inner to the outer radius over the profile. It does however give an indication of the expected theoretical frictional loss due to friction with the surrounding atmosphere and the improvement of

using a low pressure Helium atmosphere.

4.10 Conclusion

- The material requirements have been optimised for a practical flywheel requiring a central hole.
- The safety considerations of flywheel storage has been addressed by using less material more effectively, combined with the inert nature of composites, the energy absorbing nature of the fracture process, the fibre orientation factor on composite strength and the fatigue effects of cyclic loading has been taken into account.
- An inexpensive manufacturing method was proposed to implement the M. Berger and I. Porat- ultimate shape flywheel, within the manufacturing capabilities in the developing world.
- The friction reduction benefit of using a low pressure inert gas atmosphere has been addressed.

5 Chapter 5 – Drives and converters

5.1 Introduction

The electric machine used has specific drive requirements to operate properly. Two topologies are investigated namely three- and single phase brushless operation.

The permanent magnet synchronous machine requires that the drive has to keep the MMF frequency in synchronism with the position of the rotor's magnetic field. The magnitude of the back emf generated by the machine is speed dependent and the consumer side voltage has to be matched with that of the machine. Furthermore, the low inductance of the iron less stator requires a very fast current response in order to protect the semiconductors and motor windings.

Commercial drives available at the time of writing have an under voltage cut out, too high to be able to drive and start up the machine without causing serious over currents. Commercial drives are often prohibitively expensive for this application in developing countries. A custom drive and control system is proposed with simplicity, cost, ruggedness and availability as the main criteria.

DC-to-DC converters are discussed in order to show some topologies of converting between the variable voltage level of the motor/generator side and the demand/supply side of the the consumer.

5.2 Objectives

The objectives are:

- To investigate commercial drive topologies applicable to kinetic energy storage.
- To propose custom control schemes to control the machine.
- To build and test controllers on the machine.

5.3 Control Topologies

5.3.1 Introduction

The control topologies investigated are the following:

- Micro processor based controllers
- Hall effect integrated bipolar controllers
- Discrete logic control
- Current control
- Analog control

5.3.2 Microprocessor based control

A microprocessor controlled H-bridge drive was designed to drive the machine.

The advantages offered by this configuration are:

- Simple and inexpensive
- Software configurable
- Programmable protection

An ATMEL AVRMega128 microprocessor was used on a backplane PCB, interfacing to the peripherals by means of riser boards. This configuration is convenient for development, as it can be used for many applications by changing the interfacing boards. The backplane schematic and pc board layout are shown in Appendix III.

The backplane bus, consisting of three 32-pin connectors, has a ground, supply voltage to the board, processor voltage and selected IO pins connected in parallel. Two edge connectors were added to

access the remainder of the IO pins to the processor.

The riser boards supplies the interfacing peripherals, required to drive any possible application. For driving the brush less machine, two analog-to-digital pins were needed for the hall probe and temperature feedback. Furthermore, four output pins to drive the upper and lower transistors of the H-bride. The MOSFET gate supply was supplied from two 220V-to-2x12V PCB mount transformers.

The gate drive riser board was built on protoboard and consisted of an opto-isolator, transistor smoothing capacitor, diode, zener diode and a few resistors. Shown in Figure 5.1, the drive signals are applied to the photo diode side of the opto isolator, which in turn, pulls down a pull-up resistor, which keeps the transistors T1 and T2 on, to the reference level i.e. the mid point and ground respectively.

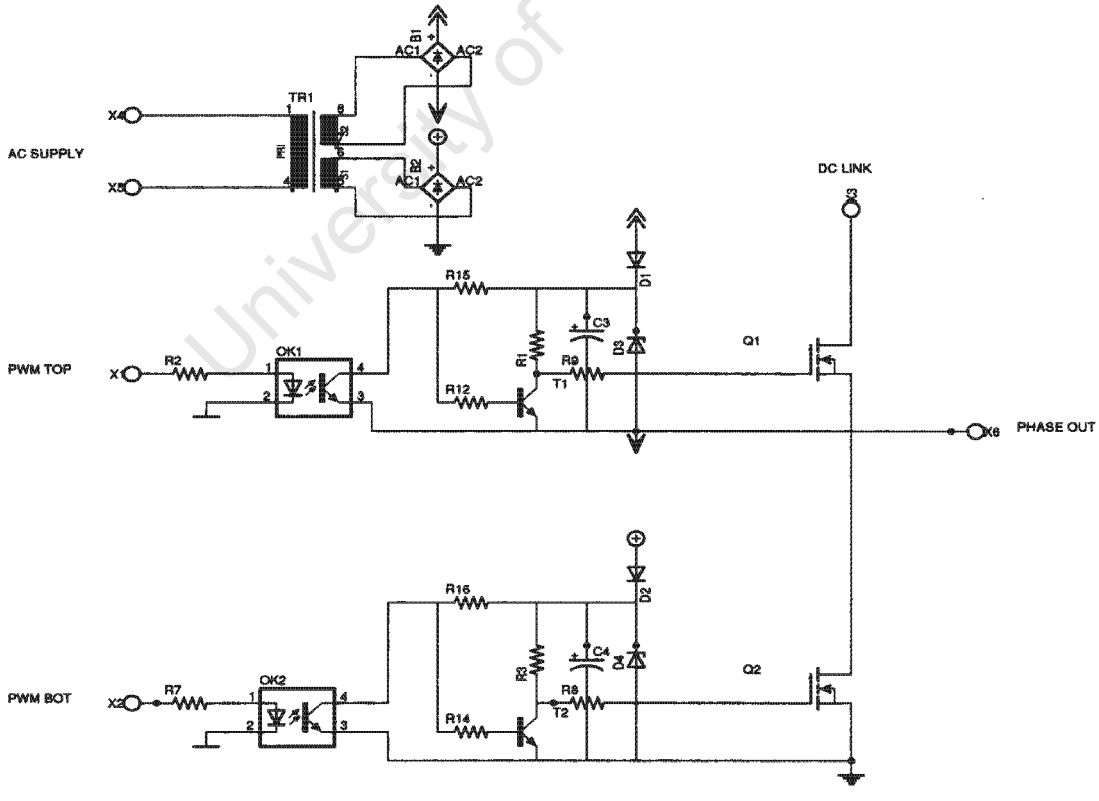

FIGURE 5.1: TWO PHASE DRIVE SCHEMATIC DIAGRAM

This in turn enables the pull-up resistors, R1 and R3 to output a gate drive voltage to the Mosfet though a 10 Ohm resistor. The supply voltage to the gates are supplied from an external transformer, as the DC-link voltage can be below the minimum drive voltage for the Mosfets. The ground of the upper Mosfet is referenced to the mid point of the inverter leg, in order to always have the gate supply 12 Volts above the Mosfet source.

FIGURE 5.2: TWO PHASE INVERTER DRIVE PROTOTYPE

The hall probe and temperature sensors were both supplied from the same 5V as the microprocessor, so their outputs were fed directly to the microprocessor via one of the riser connectors.

5.3.2.1 brush less machine operation

Three phase topologies

Several commercial controllers exist to control three phase brush less machines. The following were considered and evaluated.

- MSK4470/1
- SA828

djohnson

- MC3Phac

5.3.2.1.1 MSK4470/1

The MSK447x series controllers are full featured single or three phase controllers. It features an impressive performance with low inductance machines, but not sufficient for this application without the addition of a small inductance. The integrated circuit contains the control, drive and switches internally and requires minimal external components.

These controllers were developed recently and were intended for military use, reasons quoted for the high cost thereof. Depicted in Figure 5.3 is the schematic of the MSK4470. showing the sophistication of the drive.

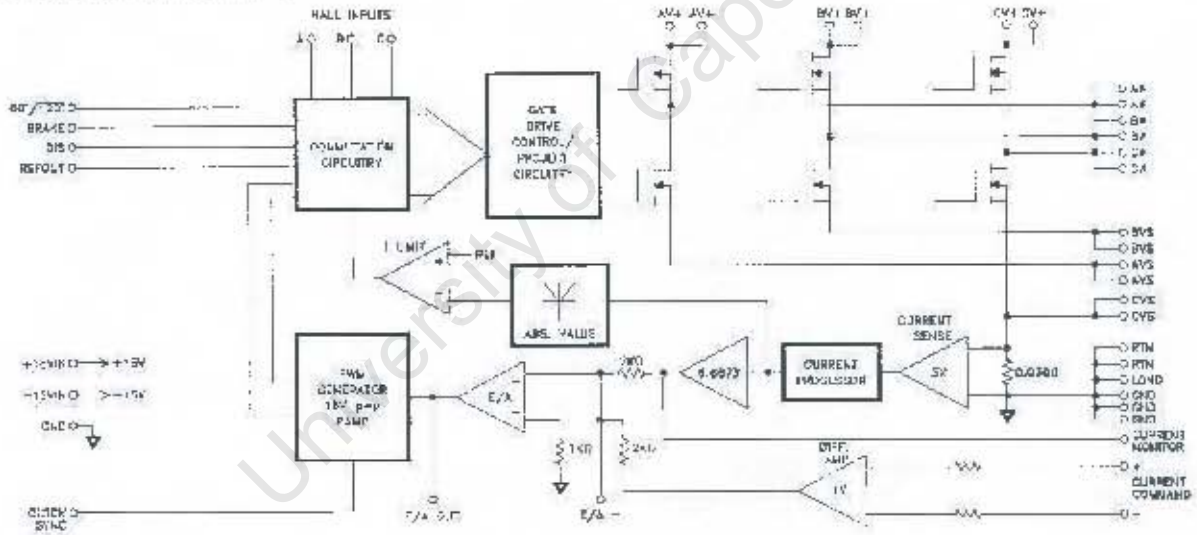

FIGURE 5.3: MSK4470 SCHEMATIC

These drives will be a good turnkey solution for this flywheel application, however the high cost thereof disqualifies it for low cost applications such as this one.

5.3.2.1.2 SA828

The SA828 is the replacement integrated circuit for the obsolete MA828 controller. It is a sophisticated single or three phase PWM drive which is controlled from any microprocessor or discrete logic input. An existing 8051 based board was used to control the MA828, however, the drive current had to be controlled externally to prevent over currents in the machine. The block diagram for the SA828 it shown in Figure 5.4.

An available laboratory implementation of the MA828 and a KIB54 printed circuit boards are shown in Figure 5.4 .

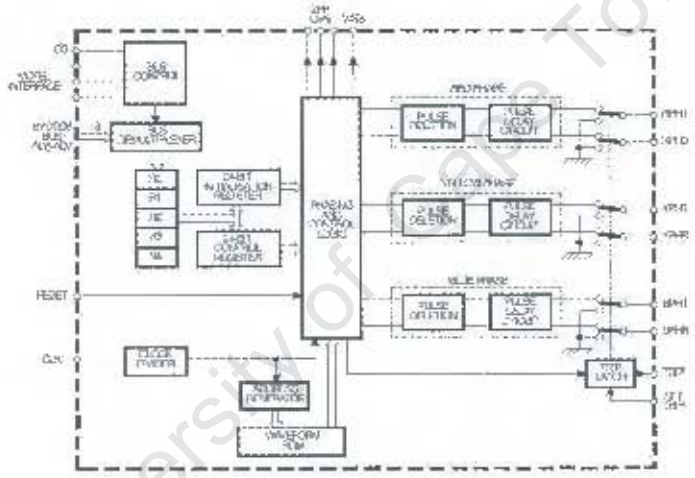

FIGURE 5.4 : BLOCK DIAGRAM OF THE SA828

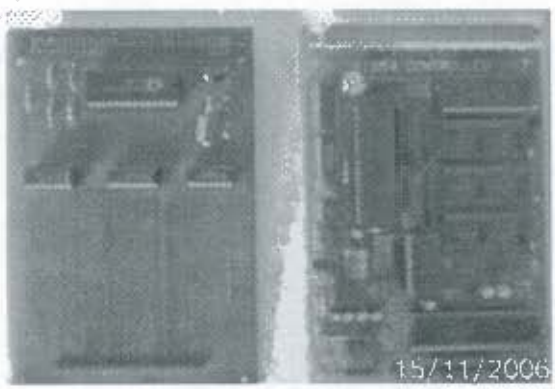

FIGURE 5.5 : MA828 AND 8051-BASED KIB054 CONTROLLER BOARDS

The drawback of this device is that it is at the end of it's manufacturing life and more recent integrated circuits will be better suited for new designs.

5.3.2.1.3 MC3PHAC

The MC3PHAC is a DSP based single or three phase PWM controller that can be operated in either stand alone or PC control mode.

As a single phase machine, the stator windings only consists of two coils instead of three, which are alternately switched in synchronism with the position of the rotor field. Shown in Figure 5.6 is a MC3PHAC board, designed to fit the AVRMega128 backplane board.

FIGURE 5.6: MC3PHAC DRIVE

The advantage of this configuration is that it is simpler to control and easier to manufacture around the confined space around the heat pipe in this application. Fewer switching devices are required to drive the windings i.e. either two or four, depending on the configuration chosen by the designer.

Some disadvantages are that the rectified DC side has a much higher ripple when generating, which in turn requires larger filters and produces higher torque pulsations. The latter will contribute to higher vibration of the radial magnetic bearings.

5.3.3 Hall-effect sensors bipolar integrated circuits

The UGN3235 Hall effect sensor lends itself favourably for simplicity, ease of use and low cost. The hall probe is mounted inside the magnetic field of the Halbach array and connected to external power transistors to drive the brush less motor. They are often found as direct drive devices in small brush less dc fans. The manufacturer's suggested circuit is shown in Figure 5.7.

Shortcomings of the manufacturer's suggested circuit is that it is unidirectional and the high on state losses associated with the Bipolar Junction Transistor. Also, the hall device is limited to operation between 4 and 24 volts. These limitations can be overcome by replacing the BJT's with Mosfets and adding a separate supply to the Hall switch.

A more practical drive circuit is shown in Figure 5.8, with the Mosfet protection components not shown. The hall device requires a separate supply, higher than the gating voltage of the Mosfet used. Two totem pole gate drives are used to switch the FETs, freewheeling diodes, zener clamps and snubber circuitry is required to protect the FET's from spikes generated by the stray inductance on switch off.

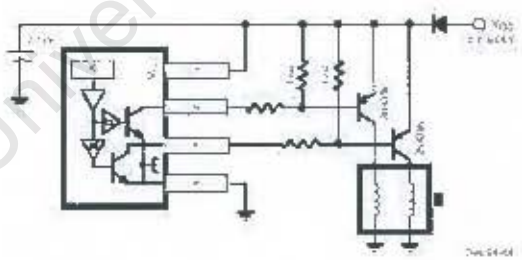

FIGURE 5.7: UGN3235 BRUSH LESS DRIVE

Power Mosfet's generally have built in body diodes, which will allow for this circuit to work in bidirectional mode, i.e. an uncontrolled rectifier in generation mode.

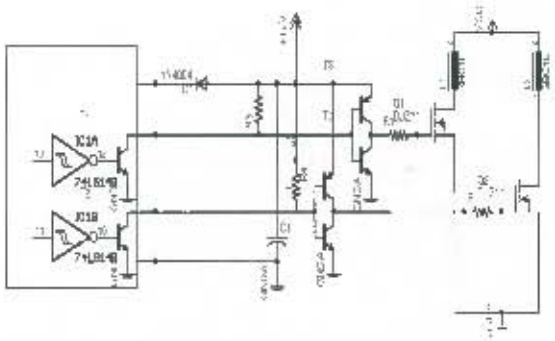

FIGURE 5.8: IMPROVED UGN3235 BRUSH LESS MOSFET DRIVE

5.3.4 Discrete Logic Control

The discrete logic controller is based on the use of elementary logic devices to synchronise the switching devices to that of the orientation of the magnetic field in the machine.

The discrete logic control switches the DC current between the motor phases in the sequence shown in Figure 6.3 and Table 6.1. The voltage wave shape is stipulated by the motor back emf, which is approximately sinusoidal for the approximated- and exact for a pure Halbach array.

The discrete logic control system consists of the following sub components:

- Optical Encoder
- Control logic
- Transistor drivers

Due to the movement of the magnetic bearing,` a non-contact reflective type optical switch sensor was used. A reflective encoder layer is bonded or painted onto the flywheel and the sensors mounted in close proximity.

For a given direction, the firing sequence remains unchanged [Fig 5.3 Table 5.1]. To determine the

logic circuitry for the encoder, Table 6.1 has to be translated into the truth table shown in Table 6.2.

Angle	T_{A+}	T_{A-}	T_{B+}	T_{B-}	T_{C+}	T_{C-}
0	1	0	0	1	0	0
60	1	0	0	0	0	1
120	0	0	1	0	0	1
180	0	1	1	0	0	0
240	0	1	0	0	1	0
300	0	0	0	1	1	0

TABLE 5.1: TRUTH TABLE FOR A-B-C PHASE SEQUENCE

This sequence is generated by connecting six optical switches directly to the Semikron MOSFET driver inputs through an inverting Schmitt-trigger, using two tracks with a 120 degree on and 240 degree off sequence as shown in Figure 5.9.

The optical sensors are placed 60 degrees apart, alternating between the inner and outer track. A Schmitt-trigger is used to sharpen the pulse to the clock the AND gates.

FIGURE 5.9: TWO TRACK ENCODER

From inspection of Table 5.1 it becomes apparent that there is a 120 degree repetitive sequence. This allows the circuit to be reduced into a single track, 3 sensor configuration, alternating between the positive and negative legs of a bridge rectifier.

FIGURE 5.10: SINGLE TRACK ENCODER

Detecting the direction of rotation is done by comparing the status of the other two inverter legs . This can be achieved by combining J-K Flip-flops, (Table 5.2) AND gates (Table 5.3) and NOT into a logic circuit that conforms to this requirement and uses a single track encoder, shown in

Figure 5.10, and three optical sensors.

Clock	*J*	*K*	*Set*	*Clear*	*Q*	*Q*	*Q*
↑	1	X	0	0	0	1	0
↑	X	0	0	0	1	1	0
↑	0	X	0	0	0	0	1
↑	X	1	0	0	1	0	1
↑	X	X	0	0	X	No change	
X	X	X	1	0	X	1	0
X	X	X	0	1	X	0	1
X	X	X	1	1	X	1	1

TABLE 5.2: J-K FLIP FLOP TRUTH TABLE

At any one time only two input signals can be low. The circuit uses 15V logic devices, conforming to the 15V requirement of the Semikron drivers used, as well as giving the system higher noise immunity. For the flywheel to start up successfully, the state of the different flip-flops have to be relayed to each other.

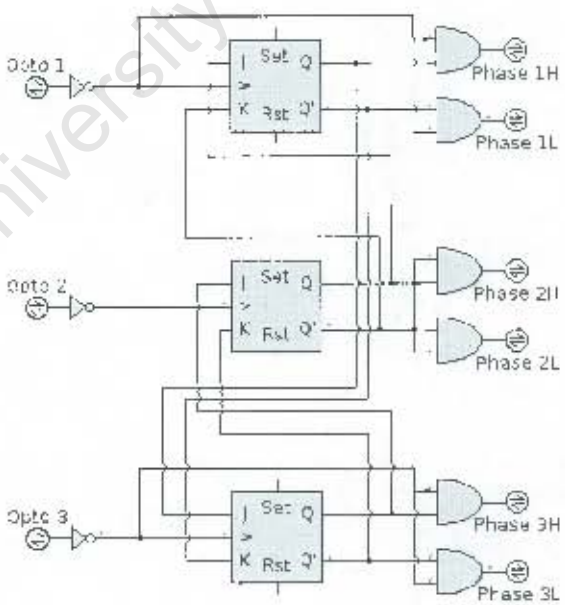

FIGURE 5.11: DISCRETE LOGIC CIRCUIT FOR BRUSH LESS DC OPERATION

Furthermore there is no indication of the orientation of the magnetic field. Firing the gates in an assumed direction of rotation will cause the motor to start rotating in the reverse direction when the magnetic field be 180 degrees out of phase to the assumed position

To ensure successful start up, the firing sequence has to be auto-correcting. Figure 5.11 shows the logical circuit and links between Q to K and Q' to J of the flip-flop prior to it in the sequence.

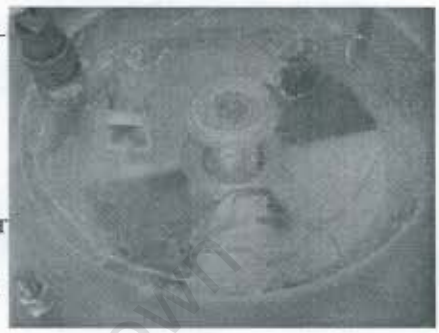

Shown in Figure 5.12 is the top view of the optical encoder assembly, mounted on a transparent Acrylic (Perspex) cover.

FIGURE 5.12: REFLECTIVE ENCODER

Shown in Figure 5.13 is a protoboard prototype that was built and tested on the motor. The light emitting diodes (LED's), on the lower right, were added for debugging and setup purposes.

This circuit started the flywheel up reliably on a single reset.

The availability and low cost of 8-bit micro controllers makes them very attractive for this application. Micro controllers require position feedback from the motor. Some alternatives are zero crossing, optical switches or hall effect sensors.

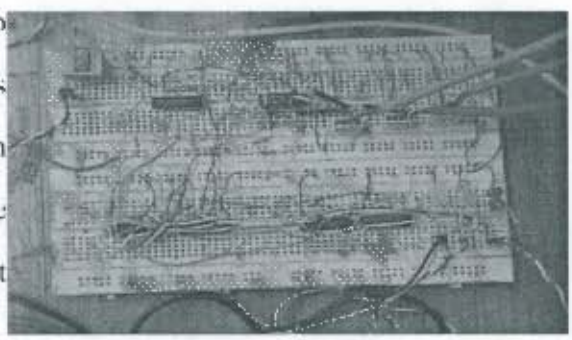

FIGURE 5.13: DISCRETE LOGIC CONTROLLER BREADBOARD

The device has to be started up from zero volt back emf, zero crossing detection will not give any

feedback at this point. It will also vary over a wide range of operating conditions, which can be catered for in the design. Start up trials showed that the inertia of the flywheel is too high to start up successfully by giving it a low frequency MMF.

Optical feedback is possible, but the less expensive slotted types are difficult, if not impossible to use. This is due to the movement of the rotor at low speeds on the magnetic bearing, caused by mechanical and torque imbalances.

The hall sensor feedback was implemented for this application. It provides real time analog feedback of the orientation of the field and with a little control logic, can be limited to one device to get accurate position feedback.

5.3.5 Current control

Due to the low inductance of the motor windings, a way of limiting the current in and out of the machine is needed. In order to maximize efficiency and lower cost, resistive and inductive components should be avoided or limited as far as possible.

The dc-dc converter has the following requirements:

- Current limiting
- High efficiency
- Low cost
- High speed response
- Maintainable in the developing world

Types of control were investigated:

djohnson

- Digital
- Analog

5.3.5.1 Digital current control

Digital processing for control of DC-DC and DC-AC converters can be achieved by various digital processors.

The main concern in this application is the speed limitation of the Analog to Digital (ADC) converter incorporated in microprocessors. Regardless of how powerful the processor is, the minimum response time is determined by the speed at which the feedback data can be converted. Over and above this time, a finite time will be required to process the data and adjust the output to the controlled device.

It is possible to add inductance a circuit, which is likely to be required in any case for a DC-DC converter. The question remains whether it is possible to avoid adding unnecessarily additional parasitic components, to patch the problems imposed by the low inductance of the high efficiency machine.

The issue at hand is whether it is worth the expense to add a more costly processor into the circuit, which has the additional limitation of the ADC conversion time, while proven, simpler and more cost effective analog means exist that does not suffer from these limitations.

5.3.5.2 Analog current control

Analog control by means of basic electronics has proven itself over many years. A simple op amp

based controller can be built inexpensively and outperform digital based controllers.

While lacking the adaptability of digitally controlled circuits, which can be programmed to suit the application, many off-the-shelf controller IC's are available for most power converter applications and are hot configurable by adding control potentiometers to the circuits.

5.3.6 5.Analog Control Techniques

5.3.6.1 Introduction

Analog control has an excellent track record for all kinds of applications.

Analog controllers generally come at a lower premium, are highly configurable, simple, readily available and serviceable in the developing world. As mentioned above, the response of analog control outperforms any digital controller due to the instantaneous nature of the feedback, without the time lag introduced due to the analog to digital conversion and processing.

5.3.6.2 LM1578 series controllers

The LM1578A is a switching regulator which can be set up for DC-to-DC voltage conversion circuits. It uses an internal comparator, the output can switch up to 750 mA and has output pins for both the collector and emitter. It features an external current limit terminal which can be referenced to the ground or input voltage terminal. It has an on board oscillator, which is adjustable from 1Hz to 100 kHz. Feedback for current limiting can be added.

This controller is inexpensive and requires little external components to function. Shown in Figure 5.14, is a suggested circuit from the manufacturers for a buck-boost configuration and an external BJT power transistor. To lower the on state losses, the circuit has to be adjusted to utilize a MOSFET.

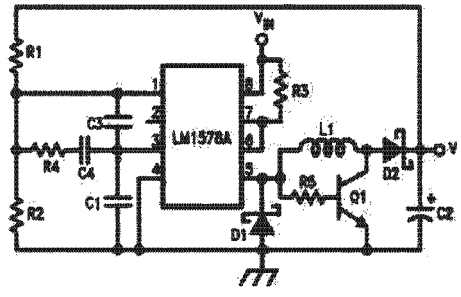

FIGURE 5.14: NATIONAL LM1578 BUCK-BOOST DC-DC CONVERTER.

For use to as a bidirectional converter, modifications are required.

5.3.6.3 555-Timer Based Controller

Configured correctly, the 555 timer can be used as an analog DC-to-DC converter controller. Using the built in analog comparator, the output duty ratio can be modified through a voltage divider connected to the output of the converter.

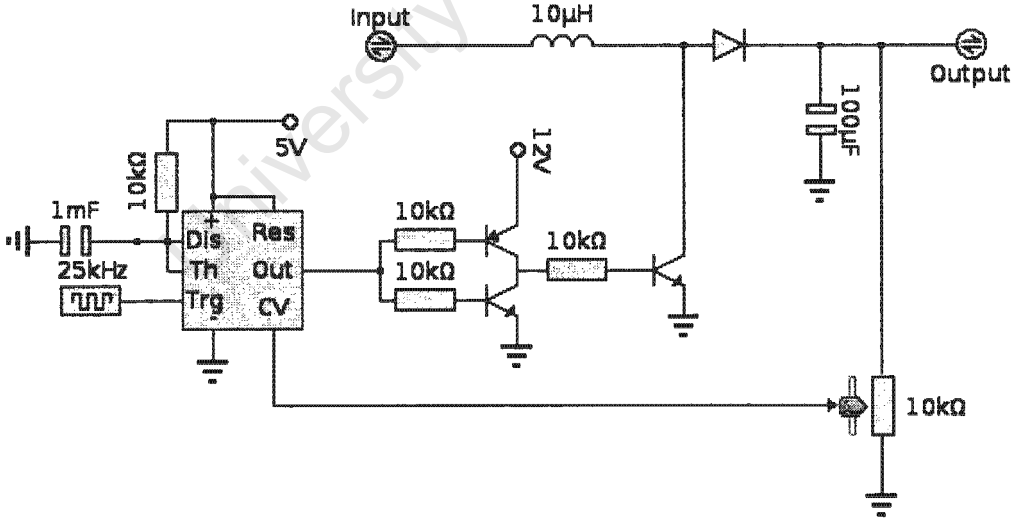

FIGURE 5.15: SIMPLE 555-BASED BOOST CONVERTER.

Shown in Figure 5.15 is an basic circuit for driving a boost converter using a 555 timer. The output

drives a Mosfet with a totem-pole arrangement and the switching frequency is determined by the clock supplied to pin 2. Note that it requires an external clock to operate which can be either another 555-timer or other means of clock generation.

5.3.6.4 LTC3780

Linear Technology advertises the LTC3780 controller for exactly this purpose . The design notes claim efficiencies higher than that of a SEPIC converter approaching percentages in the upper nineties over the operating range at low loads. The manufacturer's schematic diagram is shown inFigure 5.16

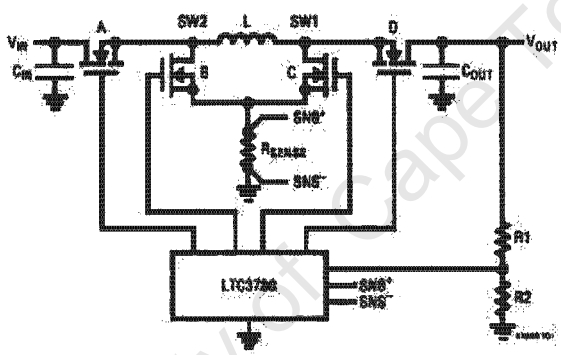

FIGURE 5.16: LTC3780 BIDIRECTIONAL SYNCHRONOUS CONVERTER

This layout is essentially two back to back series connected buck-boost converters. The advantage of this topology is that it is bi-directional, which is required for this application.

5.4 Converter Topologies

5.4.1 Introduction

Due to the variable speed nature of the flywheel, due to variations in stored energy, the voltage levels of the utility will have to be balanced with that of the machine.

While it is possible to apply kinetic storage as a AC uninterruptable power supply (UPS), it is

assumed that the battery will be servicing a DC utility e.g. a solar installation or DC wind turbine. In the case of a UPS the inverter drive usually has a DC-bus before the inverter.

It is therefor important to look at DC-DC converters in general as well as finding the most appropriate converter topology for this application.

5.4.2 Buck converter

N. Mohan, T.M. Undeland and W.P. Robbins gives a good description of the Buck converter. Buck converters are used to lower DC voltages with high efficiencies and are easy to control. Being a unidirectional device, buck converters are not suited for this application, however, it may be used in cases where the motor and generator are separate machines and serves as a foundation for what is to follow.

The principle of operation is to lower the voltage by chopping the input voltage. The output current it filtered with an inductor and the voltage by a capacitor, shown in Figure 5.17.

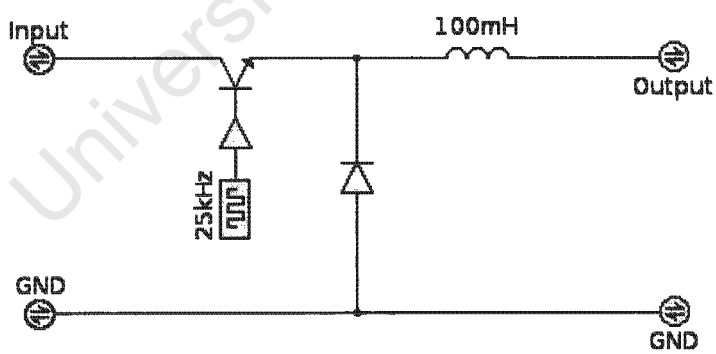

FIGURE 5.17: BUCK CONVERTER

5.4.3 Boost converter

The boost converter, as described by N. Mohan, T.M. Undeland and W.P. Robbins ,works on the

principle of shorting the output current to ground and allowing the current to boost the output voltage using the energy stored in the inductor. The inductor serves as a current filter and capacitors on the output are added to filter the voltage. As in the case with the buck converter, the boost converter (Figure 5.18) is unidirectional and not suitable for use on it's own. In order to achieve bidirectional conversion, a buck- and boost stage can be used in tandem, sharing a common inductor.

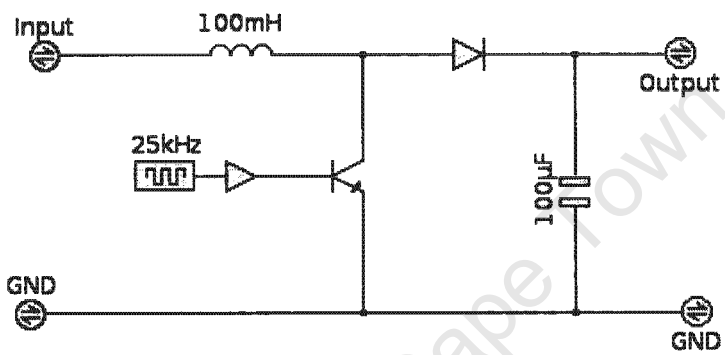

FIGURE 5.18: BOOST CONVERTER

5.4.4 Synchronous buck boost converter

Using the two synchronous buck converters in tandem, sharing a single inductor, a 4-switch converter can be constructed allowing bi-directional power flow and voltage conversion to suit the requirements for both sides.

The generalised form of the converter is shown in Figure 5.19.

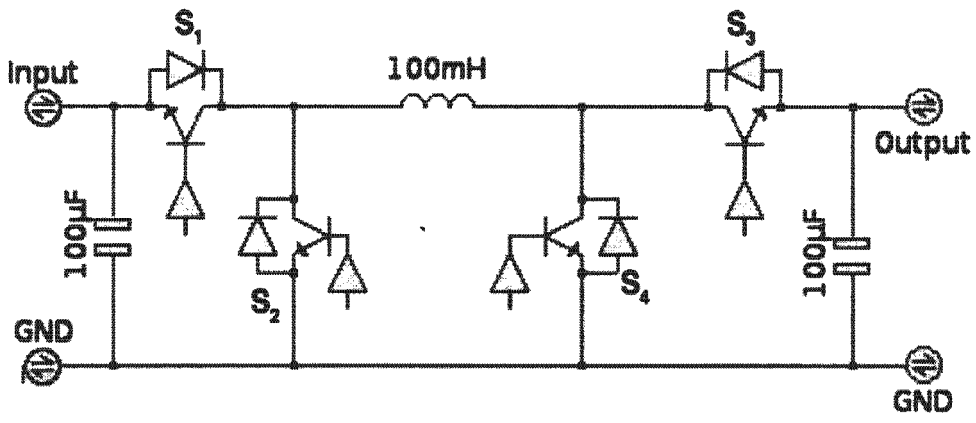

FIGURE 5.19: BIDIRECTIONAL SYNCHRONOUS CONVERTER.

The voltage conditions will dictate in which modes the DC-DC converter will operate.

5.4.5 Tapped inductor converter

F.A. Himmelstoss & P.A. Wurm propose bi-directional converters using tapped inductors for achieving high input to output voltage ratios.

In Figure 5.20 consider V_1 as the motor/generator side and V_2 the consumer side. In an application where the consumer side voltage is always higher than the motor/generator side, Q_1 can be omitted, as no boosting in the direction of the motor/generator will be needed. If the consumer voltage is on the lower side, however, it is likely that the boost switch, Q_1, will be needed if deep discharging is required, otherwise it can be omitted and the bottom useful limit will be equal to the consumer side voltage.

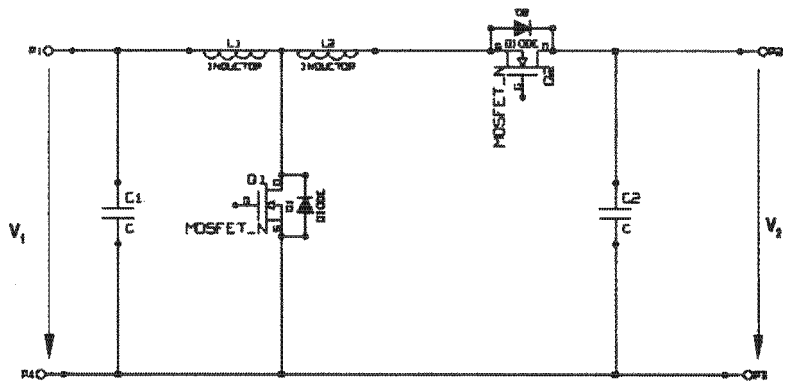

FIGURE 5.20 : F.A. HIMMELSTOSS & P.A. WURM BOOST CONVERTER

5.4.6 Non inverting Buck-Boost converter

By using a buck and boost converter in series, a non-inverting buck boost converter can be created, sharing a single inductor. It is essentially the same as the bidirectional synchronous converter in Figure 5.19, with switches S_2 and S_3 omitted.

Shown in Figure 5.20 is an actual converter of this type. It was done as part of a commercial prototype design for a local company. The specifications are shown in Table 5.3:

Rated Power	100kVA
Input voltage	160 to 1600 Volt
Load	2 variable speed inverter drives
Efficiency	>90%

TABLE 5.3: DC – DC CONVERTER SPECIFICATIONS

FIGURE 5.21: A) BUCK BOOST CONVERTER B) CONVERTER CONNECTED TO 100KW RESISTIVE LOAD

Shown in Figure 5.21a is the actual converter, not showing the inductor. Figure 5.21b shows the converter connected to a 100 kW resistive load.

5.5 Feedback

5.5.1 Signal Conditioning

Feedback signals are mostly quite different to that which is required to drive the power side of the drive. Often the signals contain noise, are distorted, has the wrong voltage levels and lack the power capability to drive the power side and combinations of these.

As an example, reflective type optical sensor used in an infra red light emitting diode, (LED) which switches the photo-transistor on when a reflective object is brought into close proximity.

Shown in Figure 5.22 is the circuit representation of an optical switch. The photo transistor is triggered by the reflection of the infra-red LED.

This circuit on it's own was unreliable as the photo-transistors would not always switch between 15 and 0 Volts, but the high and low states was as low as 13- and 9 Volts respectively.

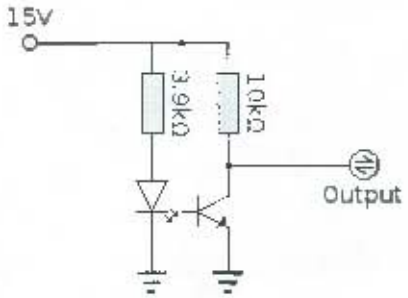

FIGURE 5.22: OPTICAL SENSOR CONFIGURATION

Conditioning of the signal is required for the signal to switch the Schmitt-trigger.

The requirements for the circuit are:

- Widen the output voltage
- Convert the output voltage to the logic devices' range

This can be achieved by using a simple inverting operational amplifier, as described by P. Horowitz and W. Hill, giving it a sufficiently large gain and driving it into saturation. (It resembles a Schmitt-trigger, except that it is tunable). The configuration in Figure 5.23 will switch between an output voltage of 2 and 13 volts for any input signal switching between an upper limit of 11 to 15 Volts and a lower limit of Zero to 8 Volts.

The output of this conditioned signal is already inverted, thus it is passed through two inverting Schmitt-triggers instead of one. Stringing of the Schmitt-triggers in this way makes the rising edge of the pulse even sharper, a desirable attribute in digital logic circuits.

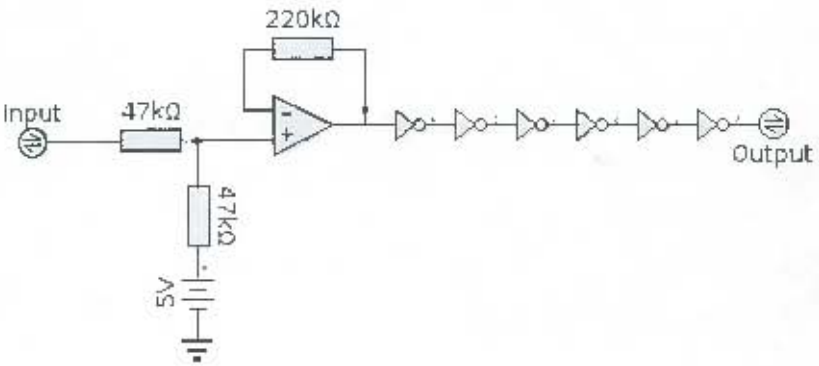

FIGURE 5.23: SIGNAL CONDITIONING CIRCUIT

FIGURE 5.24: HALL EFFECT SENSOR

Shown in Figure 5.24 is the heat pipe, with copper windings and the hall effect probe for magnetic field sensing.

5.6 Conclusion

- Drive topologies for driving single and three phase winding arrangements has been investigated and selected configurations were tested.
- The advantages of analog and digital current control was discussed
- The general methods for DC-DC conversion available has been investigated.
- The series connected buck-boost topology was built and tested.
- The converter chosen should be both bidirectional and current limiting, thus the commercial off the shelf LTC3780, shown in Figure 5.19, will be the most viable solution. The LTC3780, however, cannot operate right down to zero volts, thus a custom controlling circuit e.g. A micro controller , should be used instead.

6 Chapter 6 – Implementation and Experimental results

6.1 Introduction

A prototype flywheel was constructed along the principles outlined above. Several pitfalls were encountered and adjustments to the design were made in order to obtain a working prototype. The block diagram in Figure 6.1 outlines the workings of the electromechanical battery system.

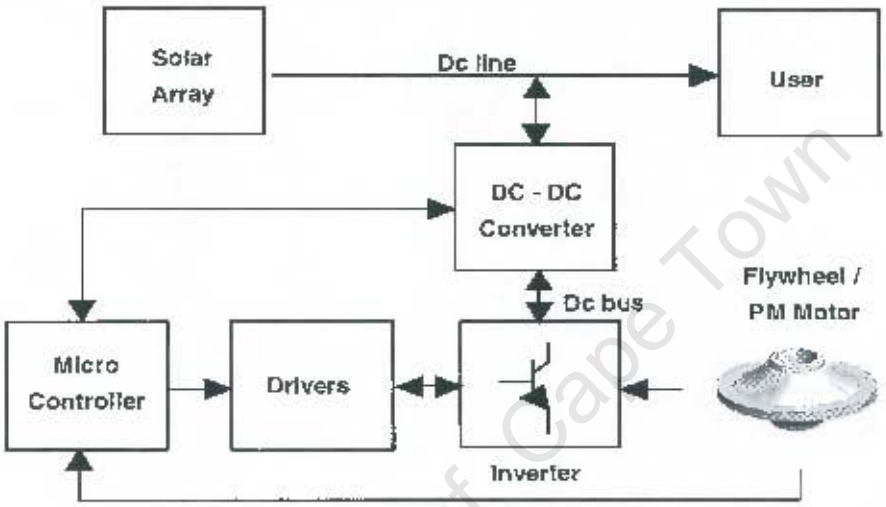

Figure 6.1: Block Diagram of the flywheel system

6.2 Objectives

The objectives of this section are:

- To address the issues, not yet covered, in designing a working system
- To physically verify the principles of the design variables outlined in the preceding chapters.
- Identify the shortcomings and pitfalls in the design
- Rectify the shortcomings and make recommendations for future work.
- Determine the machine characteristics

6.3 Housing

The housing, shown in Figure 6.2, was manufactured from a section solid steel pipe and the bottom permanently capped by an air tight weld.

The following criteria was used to determine the housing:

- The housing had to be strong enough to contain the moving parts in case of catastrophic failure
- The housing has to be massive enough to absorb all the heat generated in a fracture without weakening the structure.
- The structure should have enough abrasion resistance to withstand the abrasion of a fibre composite, whether fractured or not.
- 4.A standard pipe section will be used for the cylindrical part.

To calculate the expected maximum temperature of the housing and disintegrated flywheel the following assumptions are made, with the error on the safe side:

- The flywheel debris and the enclosure will assume the same final temperature.
- The heat transfer is adiabatic, i.e. no heat is given
- way to the environment.
- Both the flywheel and the enclosure are at ambient temperature before fracture.
- No additional energy enters the system once the flywheel fractures.

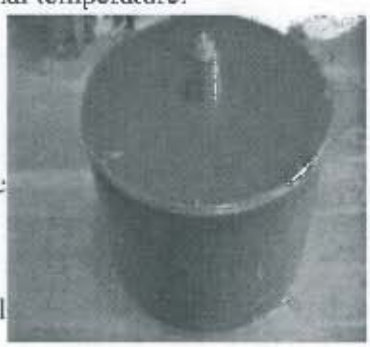

FIGURE 6.2 : PROTOTYPE HOUSING

The energy balance for the system before and after fracture is:

Total Energy before fracture = Total Energy after fracture

Because both the flywheel and enclosure are at the same temperature before fracture, the only heat transfer is the conversion of all the kinetic energy of the flywheel to heat and given in equation 6.1:

$$\Delta Q = (m_f \cdot c_f + m_e \cdot c_e) \cdot \Delta T \qquad 6.1$$

djohnson

, where:

ΔQ = Change in thermal energy in flywheel debris and enclosure

m_f = mass of flywheel debris

m_e = enclosure mass

c_f = Specific heat flywheel debris

c_e = Specific heat enclosure

The stored kinetic energy of flywheel before fracture can have a maximum of 300Wh = 1080kJ. All of this energy gets converted to heat when the system reaches equilibrium after fracture. Solve for ΔT in equation 6.1:

$$\Delta T = \frac{\Delta Q}{(m_f \cdot c_f + m_e \cdot c_e)} \qquad 6.2$$

The mass of the mild steel enclosure is:

$$m_e = \pi \cdot \frac{(D_o^2 - D_i^2)}{4} \cdot H \rho = \pi \frac{(.24^2 - .23^2)}{4} \cdot 0.23 \cdot 7800 = 6.62\text{kg} \qquad 6.3$$

The resulting rise in temperature of the enclosure then becomes:

$$\Delta T = \frac{1080}{(2.3 \cdot 0.8 + 6.62 \cdot 0.45)} = 225\,K \qquad 6.4$$

In other words, the rise in temperature for the fractured flywheel and enclosure will be 225 K above ambient, which is well within the working temperature of mild steel.

6.4 Flywheel

The prototype flywheel was manufactured from glass reinforced epoxy. The original intention was to have the flywheel manufactured in one piece, but several attempts by different local

manufacturers proved this to be very difficult to achieve. The main problem was thermal cracking due to the thickness of the work piece.

It was then opted to manufacture the flywheel in two halves and bonding them together with milled fibre-epoxy composite. This however still proved to be difficult, because of the size of the curing epoxy structure. The process being exothermic still resulted in cracking of the models. It was then hand layered, in stages, to minimise the heating problem. The layering and bonding are justifiable since the stresses are all perpendicular to the axis of rotation and in the plane of the glass layers, which is in line with the design parameters determined by M. Berger and I. Porat.

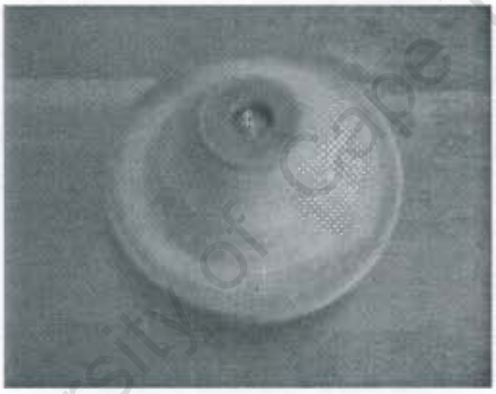

FIGURE 6.3: FLYWHEEL PROTOTYPE

For mass production, the moulds need to be made of aluminium for heat removal and a core used to preform the hole. The latter also serves to minimize the bulk at the centre of the flywheel, in order to minimize heat generation during curing as well as reducing the total material cost.

This photograph shows the prototype flywheel in Figure 6.3. It was manufactured from E-glass and Epoxy for a total capacity of 300Wh at 90 000rpm.

6.5 Hybrid magnetic bearings

Because of the layout, chosen according to the combined geometries of the motor generator, the

magnetic bearing and the thermosyphon, many problems were encountered.

- The stray magnetic flux from the Halbach array interacted with the lid, resulting in large eddy current losses
- The bottom magnetic bearing was located too close to the steel structure, resulting in poor operation
- The top magnetic bearing interacted with the magnetic field of the Halbach array, resulting in eccentricity of the top magnetic bearing and physical interference with the stator.
- Furthermore, with the bottom magnetic bearing in such close proximity to the bottom cover, being magnetic, aggravated the problem, as the magnetic bearings need reasonable good alignment to work properly.

As a first attempt, a means of providing alternative paths for the stray fields was implemented.

FIGURE 6.4: FINITE ELEMENT RESULTS FOR AIR AND STEEL MAGNETIC PATHS

The finite element results for this particular configuration showed that an increase in repelling force in the magnetic bearing was obtained with a little trial and error. The Finite element result in Figure 6.4 shows the decreasing flux in the magnetic plate below the bearing and the increase in flux in the air space between the inner and outer magnet. This improves the effect of the radial magnetic bearing.

With this principle applied, a smaller magnet for the radial magnetic bearing can be used, lowering the cost of production.

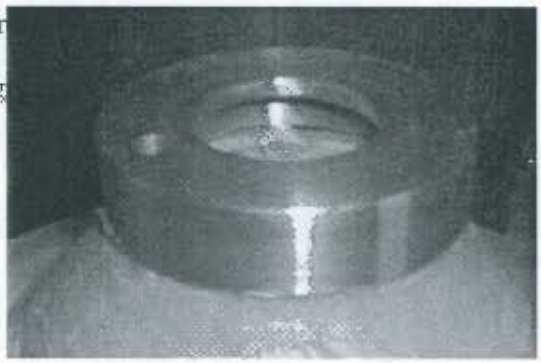

FIGURE 6.5 :MAGNETIC SHIELD FOR BOTTOM BEARING

The same Finite model was used for both cases and the properties of the cup was interchanged between air and soft steel. The shield is shown in Figure 6.5.

It was investigated whether the skewing effect would disappear at higher speeds. J.D. Stienmeyer, S.C. Thielman and B.C. Fabien showed that, at higher speeds, magnetic bearings automatically find an equilibrium between the magnetic centre, the geometric centre and the centre of mass. An 850W external drive was connected though the side of the flywheel housing, but all attempts were unsuccessful.

Roller bearings were introduced to enforce partial alignment of the upper bearing until satisfactory speeds could be reached. It was observed on the filament wound prototype, that the amplitude of flywheel vibration reduces as the speed increased past the second natural frequency. This point could not be reached on the new shape flywheel, due to excessive losses in the conventional bearings, as compared to that of the hybrid magnetic bearing and the power of the electric machine.

During the physical alignment the upper magnetic bearing, it was observed that the system was statically stable, while the bottom magnetic bearing was not in place. The possibility whether dynamic stability was possible, using the existing journal bearing in combination with the top radial magnetic bearing. The expected stability should be achieved by the gyroscopic effect of the rotating

flywheel on the journal bearing and the precession limited by the upper radial magnetic bearing.

During low speed operation the bottom bearing wandered, especially when the skewing of the upper bearing in this configuration was present. Consequently, it became apparent that a profile is needed on the journal bearing to guide the flywheel to the centre at low speeds. It should still be flat enough for minimising friction at higher speeds and be within the tolerance of the dynamically stable point of rotation.

The profile can be determined from elementary physics. Consider Figure 6.6 where it is given that a mass M with a curved surface of radius R is resting on a small sphere of radius r. Furthermore that the degrees of freedom [DOF] are only radial and axial, and kept in the rotational plane of the flywheel by it's gyroscopic effect and tilting sufficiently limited by the upper magnetic bearing. F is the vertical force exerted by the mass of the flywheel on the journal bearing.

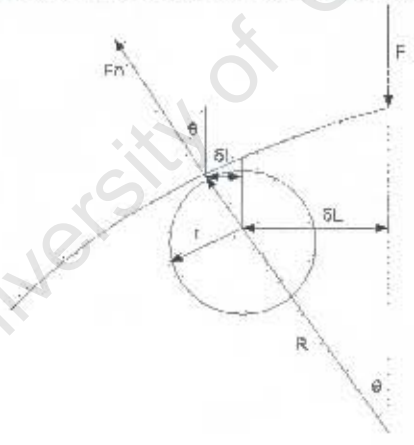

FIGURE 6.6: CORRECTING FORCES ON CURVED JOURNAL BEARING SURFACES

For a small movement from the centre, δ L, the resultant force normal onto the plane of contact is given by Fn at an angle of θ. θ is a function of R, r and δ L:

$$\theta = f(R, r, \delta L) \qquad 6.5$$

, and can be defined for any two curved surfaces in contact.

For a spherical curvature resting on a small sphere and a small movement δL off the centre, the point of contact will be at $\delta L + \delta l$ from the centre and normal to the arc R:

$$\delta L \div \delta l = (R+r)\cdot\theta \qquad 6.6$$

The normal force perpendicular to the surface becomes:

$$F_n = \frac{F}{\cos\theta} \qquad 6.7$$

The correcting force, F_c, acts towards the centre , i.e. the sine of F_r. Substitute in 6.6 to get:

$$F_c = F_n \cdot \sin\theta = \frac{F\cdot\sin\theta}{\cos\theta} \qquad 6.8$$

For small angles $\sin\theta \approx \theta$ and $\cos\theta \approx 1$, thus equation 6.8 becomes:

$$F_c = F_n \cdot \theta = F\cdot\theta \qquad 6.9$$

, where:

Fc = correcting force

F = Force exerted by flywheel

θ = displacement angle in radians

For the J.D. Stienmeyer, S.C. Thielman and B.C. Fabien hybrid magnetic bearing, the centre of rotation is an equilibrium between the geometric-, magnetic centres and the centre of mass. With the addition of a profiled journal bearing and omission of the lower radial magnetic bearing, the flywheel is free to spin like a top. The bottom profiled journal bearing centres around the profile centre, geometric and the centre of mass and the radial magnetic bearing limits the precession and act in the same way as the Stienmeyer model. Using equations 6.6 to 6.9 allows for the design of an arbitrarily stiff, self centring journal bearing.

The improvement was significant, though at the first order resonance, the added skewing, caused by

the interaction of the Halbach array and the upper magnetic bearing, resulted in permanent contact with the limiting mechanical bearings. Again, the self centring effect was not observed as adequate speeds could not be reached.

6.6 Thermosyphon

The thermosyphon was constructed of a combination of non magnetic stainless steel and pyrex glass tube. The glass was mechanically inadequate during assembly of the magnetic bearing. The Pyrex™ tube was replaced by a fibre glass-epoxy tube, shown in Figure 6.7, resulting in higher strength and toughness, however also much higher thermal resistance between the windings and the cooling medium inside the tube.

The thermosyphon was filled to about one third with Acetone, having a boiling point of 56.3 °C. The temperature on the windings was measured using a LM35Z probe. The controller monitored the winding temperature and a thermal cut-out temperature of 85 °C was selected.

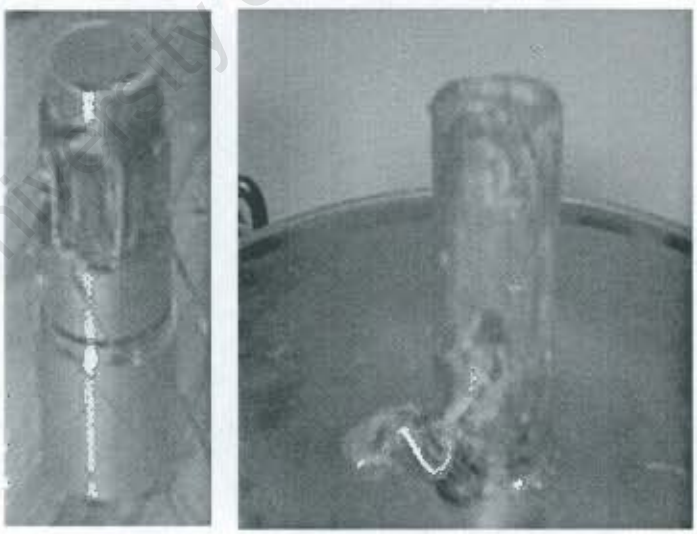

FIGURE 6.7: THERMOSYPHON WITH 3 AND SINGLE PHASE WINDING

While the LM35Z temperature probe is capable of handling temperatures of well over 100 °C, the

thermoplastic adhesives used to fix it to the stator started to become plastic at 85 ^{o}C, hence the limitation. Without the acetone in the thermosyphon, the temperature trip occurred within seconds after powering up, depending on the current though the windings varying from 1 to 20A. This time was increased to several minutes adding a acetone coolant to the thermosyphon at a current of 30 Amps. It was further improved when aluminium heat sinks were added to increase the heat transfer rate to air.

When the machine was operated at the rated current of 20A, the temperature stabilized between 70 and 80 degrees, as predicted by the thermal resistance model used to calculate the wire temperature in chapter 3.

In general, the thermosyphon performance depends on the combination of thermal resistances, the boiling point and heat capacity of the working fluid, the fill charge ratio and the efficiency of the heat sink. For energy storage it is not desirable to have forced convection as it imposes an additional power requirement on the energy supply, resulting in lower overall efficiencies. For high power applications, forced convection can be used reduce the size of the heat sink.

6.7 Electric Machine

6.1 Radial Flux Machine

The initial motor consisted of an outside rotor Halbach array and a stationary winding.

The Halbach array was constructed from laser cut, non-magnetic stainless steel laminates. The cost of low volume manufacturing of the magnet retainer by laser cutting is much lower than that of other methods.

The alternatives for manufacturing the magnet retainer are:

- Investment casting
- Spark erosion
- Punching
- Laser cutting

The manufacture of a mold for investment casting is prohibitively expensive, in the order of R200 000 - R300 000 rand. Investment casting will be a good choice for high volume manufacture. If low cost sand molds were used, machining is required afterwards, including spark erosion to clean up the surface of the square holes.

Spark erosion is time consuming and costly. This may be a good alternative, where cost is not an issue, for high budget, low volume prototyping.

Punching also requires expensive tools, in the order of several thousand rand per punch. Punches wear and have a limited life expectancy. Assembly of the laminates with the magnets can be problematic, especially when the punches are worn, bending occurs on the edges of the laminates and are no longer flat enough to be stacked.

Four laser cut disks were used, two on each end, as keepers for the array. Hand assembly was difficult because of the magnets' high affinity for each other. The halbach array, thermosyphon and flywheel is shown in Figure 6.8.

It proved to be difficult to fit three phase windings onto the thermosyphon, due to the thickening where the wires cross, thus a single phase winding was used.

The torque and performance was satisfactory as with a previous prototype, but problems with the alignment of the passive magnetic bearings was encountered. With the Halbach array in close proximity to the upper magnetic bearing, the nett effect was skewing of the bearing and the flywheel.

It proved to be difficult to fit three phase windings onto the thermosyphon, due to the thickening where the wires cross, thus a single phase winding was used.

FIGURE 6.8: RADIAL FLUX MACHINE PROTOTYPE

The torque and performance was satisfactory as with a previous prototype, but problems with the alignment of the passive magnetic bearings was encountered. With the Halbach array in close proximity to the upper magnetic bearing, the nett effect was skewing of the bearing and the flywheel. Furthermore, with the bottom magnetic bearing in such close proximity to the bottom cover, being magnetic, aggravated the problem, as the magnetic bearings need reasonable good alignment to work properly.

6.2 Axial Flux machine

The alternative was to design an axial flux machine, having the upper magnetic bearing in the same plane as the Halbach array, while still using commercial-off-the-shelf [COTS] rectangular magnets. It is desirable to maintain the high efficiencies of an Halbach array machine.

Starting from a linear array, where the magnets are rotated sequentially at 90 degrees, i.e. an array with an infinite radius, a sinusoidal distribution of flux is created above the array, similar to the

multi pole arrays presented in Chapter 2.

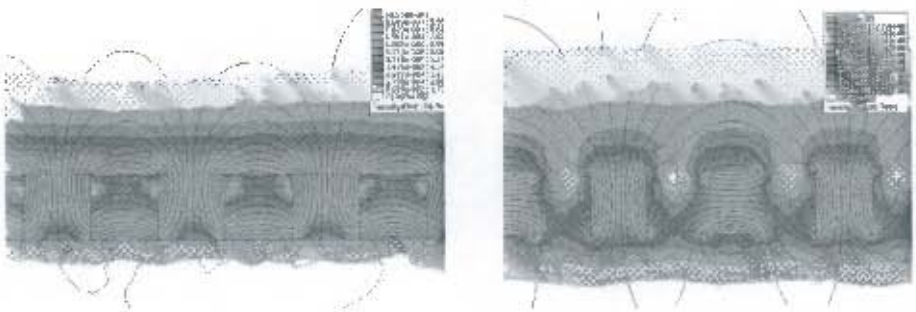

FIGURE 6.9: LINEAR HALBACH ARRAYS WITH DIFFERENT MAGNET SPACINGS

To form an axial flux machine, the segments are arranged in a concentric manner. The field strength can easily be determined by FEA. For the same diameter array, using the same size rectangular magnets, the field diminishes as the magnets separate further away from the centre. The two dimensional results for two sections through the array is shown in Figure 6.9.

The average, however, proved to be of similar magnitude at the same distance from the surface as compared to the radial Halbach array. The advantage of this configuration is that for the same current, the same force is applied at a much larger radius, equalling a much larger torque.

COTS rectangular magnets were used and was embedded into a non magnetic holder, with the magnets touching on the inner radius, parting as the radius increases. The net effect on the Halbach array by parting the magnets is clear in Figure 6.9.

This approach applies the Halbach array principles as an axial flux machine, with the benefits of high efficiency. Also, for the same flux density at the windings, the geometry requires fewer magnets than for the radial Halbach array. In essence, this is a superior configuration for this application, resulting in a less expensive PM part of the machine, which is easier to manufacture and simpler to assemble than the radial type.

Using a hall probe, the measured flux values at a varying distances of 3-, 6- and 9mm from the Halbach array surface, was consistent with that of the finite element analysis results shown in Figure 6.9, and are tabulated in Table 6.1. Figure 6.10 shows the the axial flux prototype.

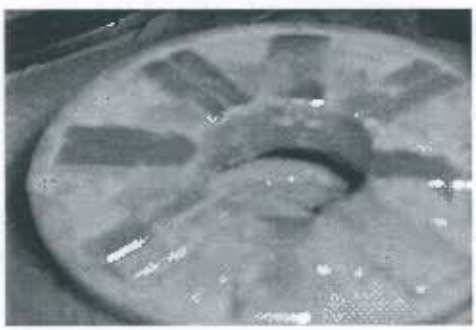

FIGURE 6.10: AXIAL FLUX HALBACH ARRAY

The lob sided effect of the magnetic bearing can be seen in the magnitudes of the measured fluxes.

	Inner			Midway			Outer		
Position \ Distance	3mm	6mm	9mm	3mm	6mm	9mm	3mm	6mm	9mm
N Pole face	110	52	17	177	99	56	116	52	20
In between	8.2	-7.2	-7.9	9.4	14.5	-1.2	22	-5.7	-5.4
S Pole face	-124	-82	-33	-214	-122	-60	-107	-70	-32
In between	-34	-22	-19	-57	-43	-13.2	-28	-27	-20.9

TABLE 6.1: MILLITESLA MEASURED OVER THE AXIAL FLUX HALBACH ARRANGEMENT

The windings are wound on a non magnetic, non conductive toroid and placed directly above the axial flux Halbach array. This can be either single phase, wound in alternating directions, or poly phase in order to create a rotating MMF. The returning wire on the other side of the toroid has an opposing effect on the array and the magnitude depending on the distance from the array. The effect can be minimized by thickening the toroid, as seen from Figure 6.9, the field lines quickly diminishes with distance from the array.

As expected, the magnetic bearing aligned properly with this configuration as there were no radial effect interfering with the radial magnetic bearing. The construction of a thermosyphon becomes simpler and can be kept to the upper side of the toroidal windings.

6.8 Machine drive

6.8.1 Introduction

The machine drive is the interface between the supply from the DC-bus to the machine. The in this permanent magnet machine, the windings experiences an AC waveform, thus the drive has to invert the DC to an appropriate AC waveform.

Furthermore, the machine is of the synchronous type and the converter has the added function of keeping synchronism with the position of the magnetic field.

6.8.2 Two phase drive

As a first attempt, a two phase arrangement was applied. The performance was not satisfactory, because of dead zones encountered. These dead zones were located where the the magnets of the rotor was halfway between the two phases, resulting in a too low torque to self-start. The pulsating torque from two phase operation also induced additional vibration, resulting in the mechanical parts of the machine touching and resulted in low speed operation only.

With the hall effect sensors, the relative movement between the magnets and the sensors often gave spurious triggers and the system was converted to an IR [infra red] optical arrangement to improve the triggering reliability, as shown inFigure 6.11 a) and b).

FIGURE 6.11: A) ENCODER TRACK AND B) OPTICAL SWITCHES, STATOR & MAGNETIC BEARING

6.8.3 Three phase drive

In order to drive the machine with three phase, a new drive was constructed as shown in Figure 6.12. Three IR2113 bridge driver was used to drive the MOSFET's from the original base board, taking a 12V supply from the base board for the drive side of the MOSFET bridge and responding to the 5V control signal from the micro processor.

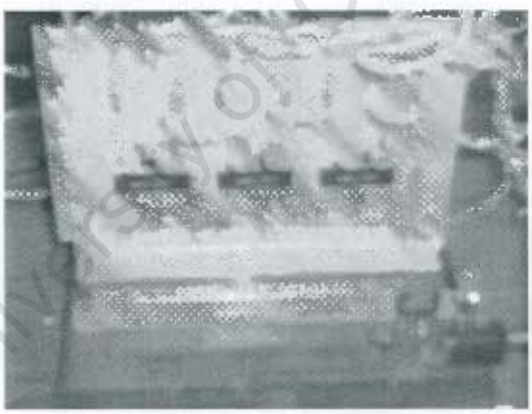

FIGURE 6.12: MOSFET DRIVE BOARD ON BASE BOARD

The optical position feedback was routed to the micro via a pull up resistor. Some level shifting was required to get all three signals on the same level. This was relayed directly into the microprocessor's ADC and was used to do the switching of the three phase bridge. Shown in Figure 6.13 is the microprocessor board with the driver board in the foreground and the level shift board in the background, providing adjustment for the signals from the optical sensors.

The firing sequence was determined by using an encoder track that has a 50% dark and 50% reflective surface. Household Aluminium foil was found to be adequate for the reflective surface. Shown in Figure 6.14 are typical signals recorded with a digital oscilloscope. The noisy shape on the lower part of the graph is the signal from the low quality reflective surface of the aluminium.

FIGURE 6.13: DRIVE AND LEVEL ADJUSTMENT BOARD

The sharp edge between the low and high states of the pull up resistor was adequate to achieve a good signal for switching the inverter and, once set up properly, no misfiring was recorded during experimentation. A typical trace of the microprocessor output for two phases is shown in Figure 6.15.

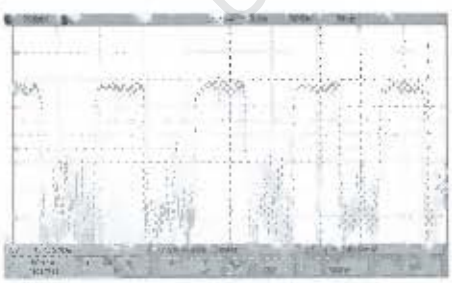

FIGURE 6.14: OPTICAL FEEDBACK SIGNAL

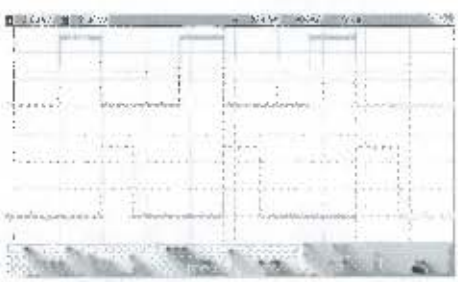

FIGURE 6.15: MICRO PROCESSOR BRIDGE OUTPUT

The drive program is listed in Appendix IV, showing the thresholds for the optical sensors and the

firing order of the bridge.

The firing sequence was calculated according to the following table:

Opto 1	Opto 2	Opto 3	Ph A_{HS}*	Ph A_{LS}+	Ph B_{HS}*	Ph B_{LS}+	Ph C_{HS}*	Ph C_{LS}+
H	L	H	L	L	H	H	L	L
H	L	L	L	H	L	L	H	L
H	H	L	L	L	L	H	H	L
L	H	L	H	L	L	H	L	L
L	H	H	H	L	L	L	L	H
L	L	H	L	L	H	L	L	H

TABLE 6.2: FIRING ORDER FOR OPTOCOUPLER STATES

* : HS = High side

+ : LS = Low Side

The machine performed as expected, however the close mechanical tolerances between the machine parts and the amplitude of the displacements experienced near the first resonant point did not allow the model to be operated at high speeds. Multiple attempts were made to pass the natural frequency, but this however was not attainable. In a final attempt to overcome this additional frictional loss near the natural frequency, a 600Watt external drive was applied, also proved unsuccessful

The resonant point is experienced where small imbalances in the rotating system nears the natural frequency of the spring-mass behaviour of the flywheel-magnetic bearing system. Except for small air- and axial journal bearing friction losses, the radial magnetic bearing acts like a perfect spring and the system becomes unstable abruptly when the natural frequency is approached.

The machine performs well at speeds below this frequency and enough data was recorded to analyse the machine and predict it's performance, shown in Appendix V.

The machine was analysed by first mechanically spinning up the system and letting it run down unassisted. The windage losses were determined by logging the speed and time on an Agilent DSO6012A mixed signal digital oscilloscope, as shown in figure 6.16.

6.9 Experimental setup

6.9.1 Introduction

The machine was analyzed by first mechanically spinning up the system and letting it run down unassisted. The windage losses were determined by logging the speed and time on an Agilent DSO6012A mixed signal digital oscilloscope, as shown in Figure 6.16.

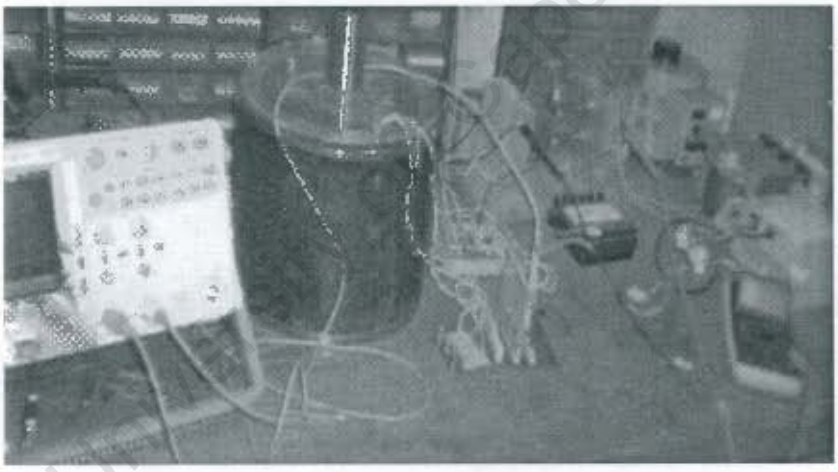

FIGURE 6.16: EXPERIMENTAL SETUP WITH OSCILLOSCOPE

The data was recorded with the digital scope and transferred to paper afterwards. This process was cumbersome, but the results reasonable.

In order to accelerate the data logging process, the calibrated 10 bit ADC of an Atmel AVRMega8 processor was used to log the data to a computer via the serial communications port of a STK500

development board. The experimental setup with the micro controller based data logging board is shown in Figure 6.17.

The ADC resolution was enhanced by oversampling 16 times, adding the 10-bit ADC results to a variable and then right-shifting the total by two bits in order to get a 12 bit result. The process of oversampling and decimation is described in great detail in the Atmel Application notes and is included in Appendix VI.

FIGURE 6.17: EXPERIMENTAL SETUP WITH ATMEGA8-BASED LOGGER

The following tests were performed:

- Rundown tests
- Motoring tests.

6.9.2 Rundown tests

The rundown test was performed by spinning the flywheel and then logging the speed v.s. time curve of the rundown.

This gives a good representation of the frictional losses of the flywheel system, which can later be subtracted from the motoring tests, in order to determine the machine performance characteristics.

Shown in Figure 6.18 is an example of a rundown curve obtained from the raw data of a rundown test. The curve was determined from capturing approximately 50000 data points. The deviating points on the graph was caused by a register overflow in the logging microprocessor and can be ignored, as the trend is clearly visible.

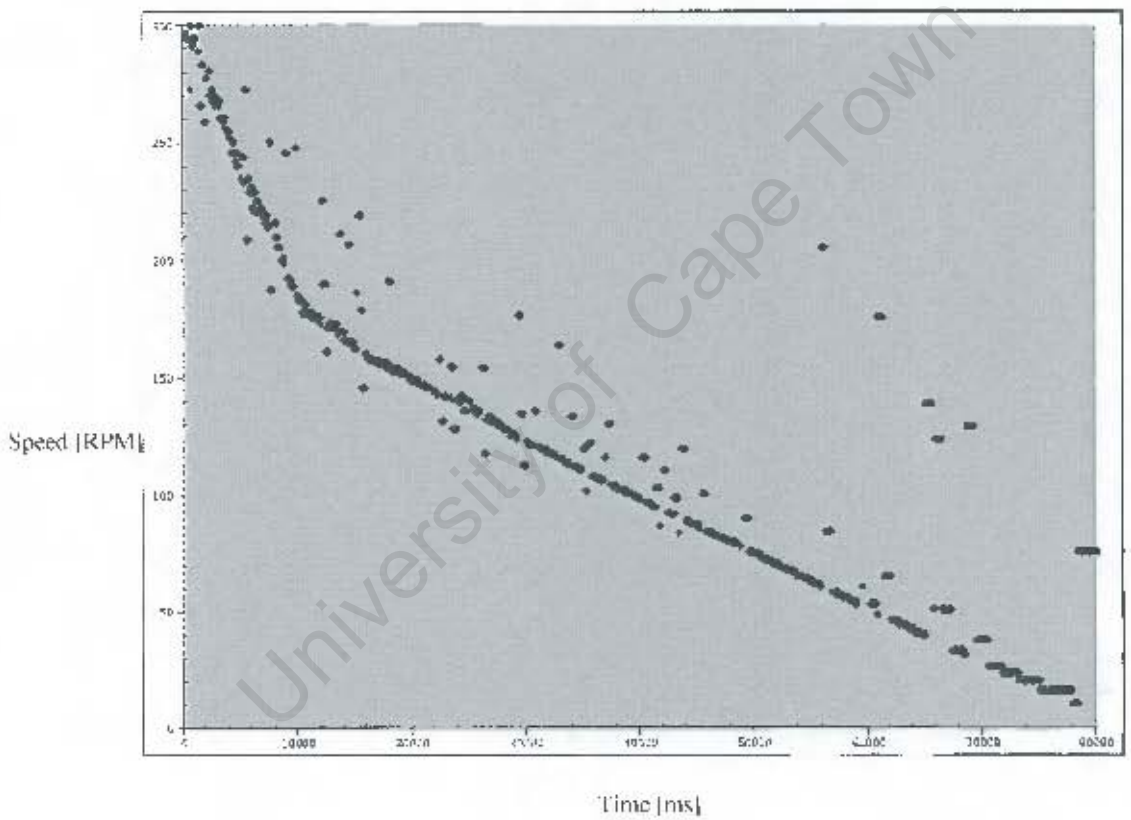

FIGURE 6.18: RUNDOWN CURVE FROM 12-BIT ENHANCED RAW DATA

On the graph, the first sharp drop in speed, corresponds with the natural frequency of the magnetic bearing. At this point, physical contact between the rotor and stator occurs, which results in audible sound and larger deceleration. This is also responsible for the maximum speed obtainable by means of motoring, as the machine was not powerful enough to ride through this point.

The there is also a small amount of air friction loss at this speed, which quickly disappears and the graph smoothen out to a linear deceleration. This is the loss associated with the axial journal bearing.

In order to make the readings more meaningful, the resolution was increased to 13 bits, by adding sixty four 10-bit samples, and right shifting the result by 3. The resulting data was much improved as can be seen in in Figure 6.19.

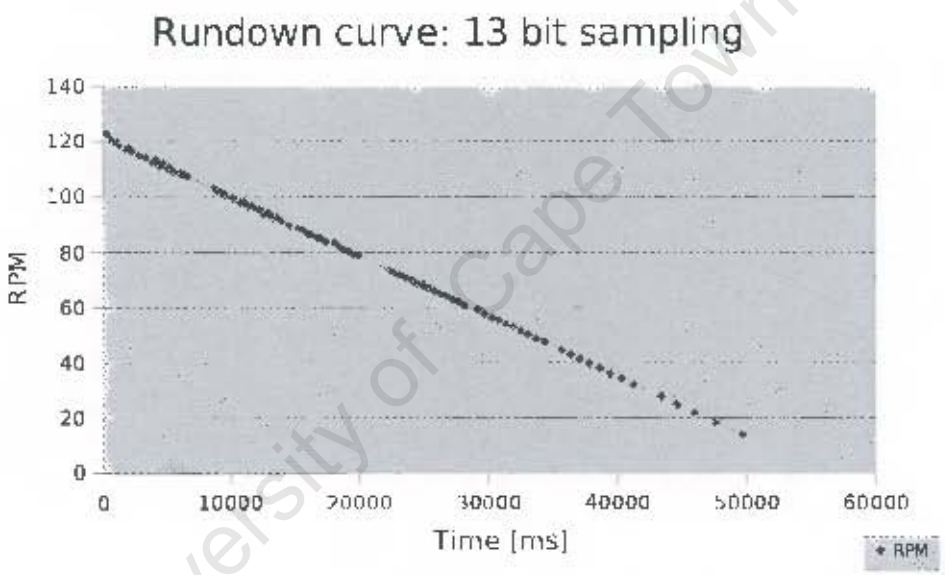

FIGURE 6.19: RUNDOWN CURVE FROM WITH 13-BIT RESOLUTION

The decelerating torque is given by:

$$T_d = \frac{I \cdot N}{9.55 \cdot t_d} \qquad 6.10$$

, where

T_d = decelerating torque

I = mass moment of inertia

N = average rotational speed in RPM

t_d = time to decelerate

It is known that at 90 000 rpm the flywheel possesses it's full charge of 300W-h. This energy is represented by the relationship, as given by P.P. Benham & F.V. Warnock:

$$W = \frac{1}{2} I \omega^2 \qquad 6.11$$

This gives us an Mass moment of inertia, as determined for the flywheel in chapter 4 :

$$I = \frac{2W}{\omega^2} = \frac{2 \cdot 300 \cdot 3600}{\left(\frac{90000 \cdot 2\pi}{60}\right)^2} = 2.432 \cdot 10^{-2} kg\,m^2 \qquad 6.12$$

Applying this to the data of Figure 6.19 yields the total Windage loss versus Speed relationship, for the flywheel system, and is listed in Table 6.3:

Time [ms]	RPM	Tw [Nm]	Power loss [W]
257	122.95		
502	121.46	1.27E+000	1.62E+001
746	119.52	1.26E+000	1.57E+001
1018	120	1.12E+000	1.41E+001
1262	118.58	1.24E+000	1.55E+001
2294	116.28	1.10E+000	1.33E+001
4384	111.11	1.05E+000	1.23E+001
4656	111.94	1.04E+000	1.22E+001
4927	110.29	1.04E+000	1.21E+001
5199	110.7	1.03E+000	1.20E+001
5470	109.09	1.03E+000	1.18E+001
6584	107.14	1.01E+000	1.13E+001
7154	105.63	4.75E-001	5.26E+000
7724	104.17	4.69E-001	5.11E+000
7995	104.53	9.81E-001	1.07E+001
8294	114.07	9.31E-001	1.11E+001
8593	103.09	9.25E-001	9.98E+000
8891	102.39	8.78E-001	9.41E+000
9190	101.69	8.69E-001	9.26E+000
9489	100.67	8.62E-001	9.09E+000
11308	96.46	7.61E-001	7.69E+000

TABLE 6.3: POWER LOSS V.S. SPEED TABLE

Plotting the data from Table 6.3 yields Figure 6.20.

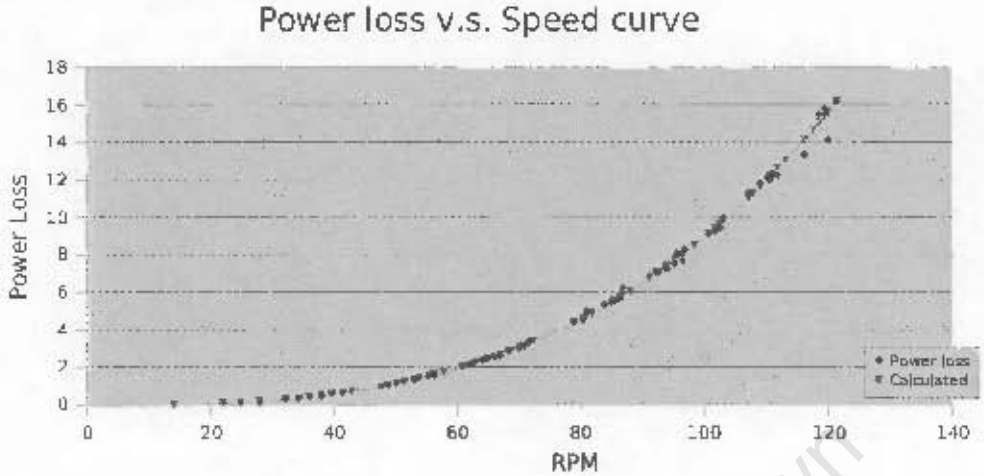

FIGURE 6.20: FRICTIONAL POWER LOSS V.S. SPEED CURVE

By means of the open source curve fitting program, Fityk version 0.7.6, the power loss at any given speed [RPM] is given by the polynomial curve 6.13 and has an accuracy of 99.9337%. The regression curve is shown superimposed in Figure 6.20.

$$P_N - 0.086465 - 0.0098312n + 0.00033362n^2 - 4.69796e\text{-}06n^3 - 1.806e\text{-}08n^4$$

6.13 , where:

P_N = Frictional power loss

n = Speed in RPM

This relationship can be used to calculate the frictional loss at any point and compared with the data obtained in the run tests, within the given range and the machine efficiency calculated in section 6.93. In order to process the recorded data, the ADC calibration values has to be determined.

The flywheel was locked in place and a voltage applied to the system. The current and voltage adc values were recorded, together with the corresponding RMS readings from standard laboratory meters. These results were taken over the entire range of the different tappings of the meters,

applicable to the values used to run the machine.

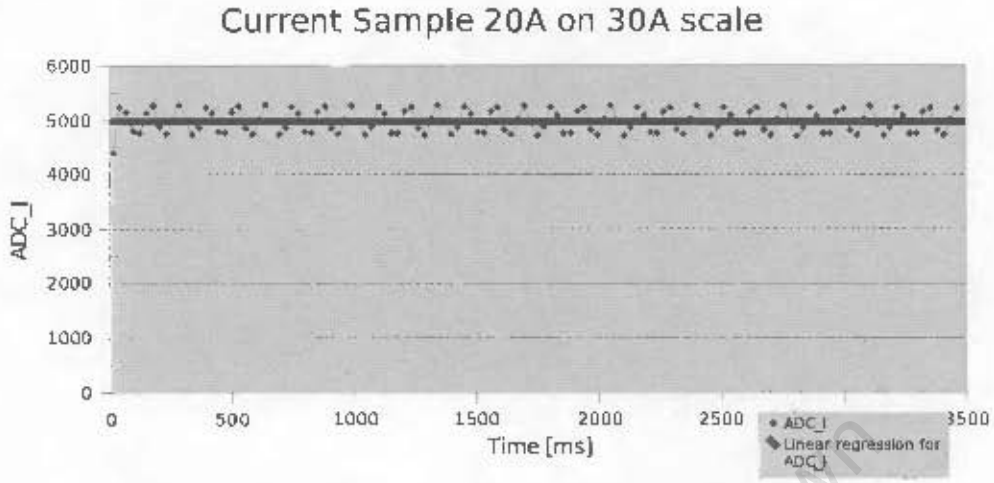

FIGURE 6.21: CURRENT SAMPLE AT 20A ON THE 30A AMMETER SCALE

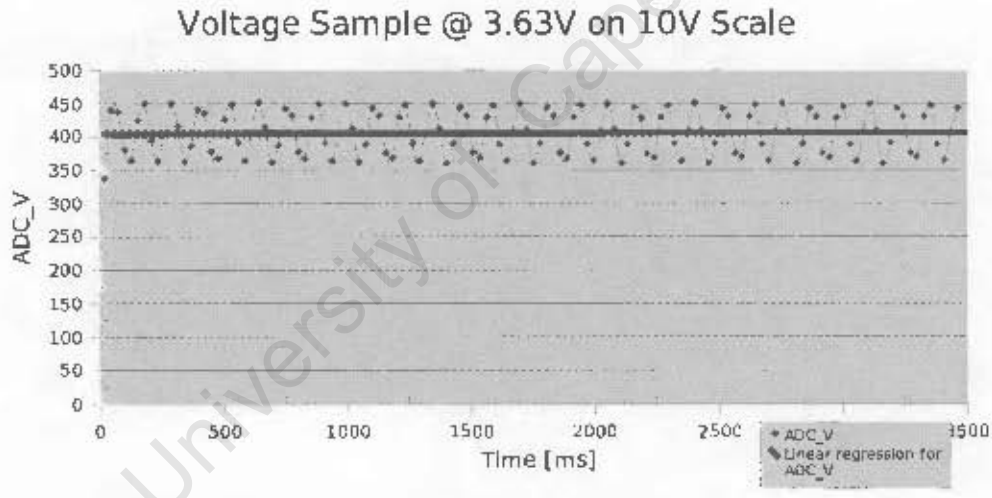

FIGURE 6.22: CORRESPONDING VOLTAGE SAMPLE AT 20A

The results of one such a test are shown for current is shown in figure 6.21 and the corresponding voltage figure 6.22. The thick line represents the RMS values on the individual graphs.

The amplitude fluctuations visible in the above graphs corresponds to the unregulated, full wave rectified, 50Hz supply used to drive the currents.

Table 6.3 shows the results and calculated scaling factors for the different ranges of currents and

voltages.

Ammeter Range	I	ADC value	Voltmeter range	V	ADC Value
1	0.2	46.1	2	0.0000	0.00
1	0.39	102.4	2	0.0750	1.00
1	0.61	179.5	2	0.1154	3.95
1	0.8	243	2	0.1394	6.50
1	1	301	2	0.1779	9.90
3	2	674	2	0.3780	32.00
3	2	674	2	0.3780	32.00
10	3	1155	2	0.6280	59.40
10	4	1491	2	0.7840	78.50
10	5	1835	2	0.9680	99.00
10	6	2105	2	1.0970	113.00
10	7	2447	2	1.2730	133.40
10	8	2780	2	1.4500	153.40
30	15	3625	2	1.9580	214.00
30	20	4970	10	3.6300	405.00

TABLE 6.4: ADC CALIBRATION VALUES

Plotting the ADC values against the Ammeter and Voltmeter readings reveals that the Analog ammeter calibration differs for the different ranges, as shown in figure 6.23.

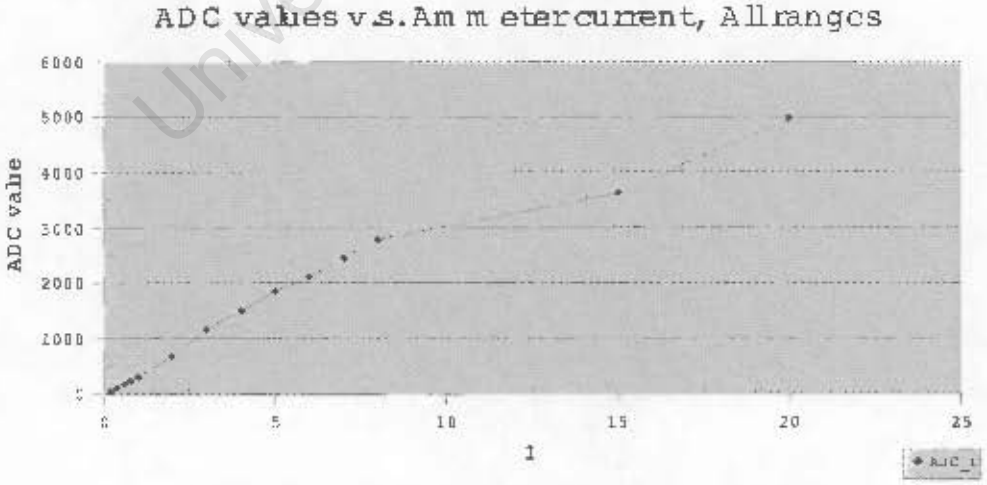

FIGURE 6.23: ADC VALUES V.S. AMMETER CURRENT, ALL RANGES

The graphs for the currents are linear for the individual Ammeter ranges and the 30A range is consistent to that of the 1 Ampere range, as shown in figure 6.24.

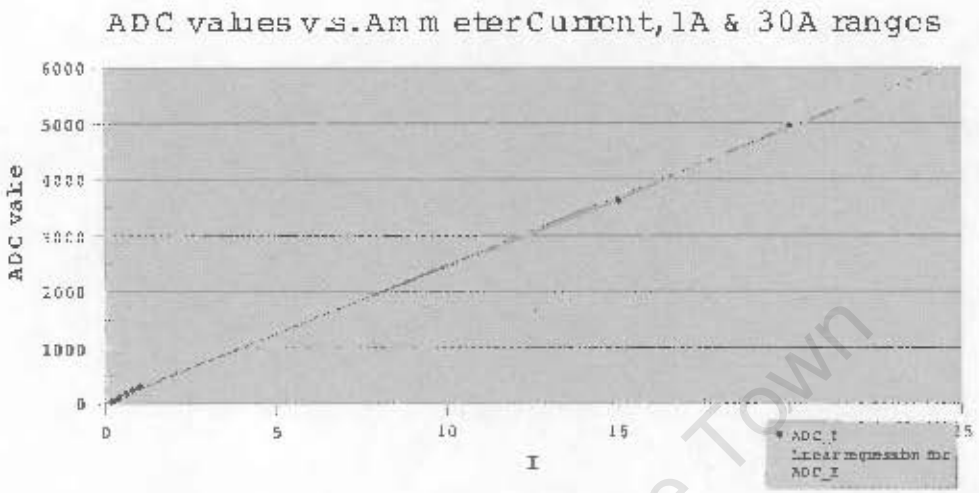

FIGURE 6.24: ADC VALUES V.S. AMMETER CURRENT, 1A AND 30A RANGES

The Digital Voltmeter used is linear for all practical purposes as shown in figure 6.25.

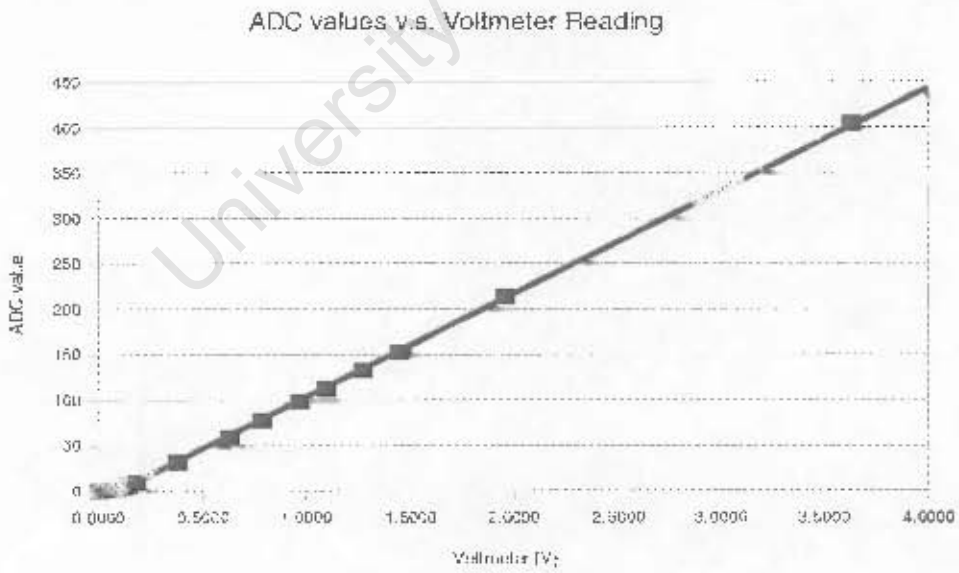

FIGURE 6.25: ADC VALUES V.S. VOLTMETER READING, ALL RANGES

Atmel's claims a linearity of the on-chip ADC to be 0.5 least significant bits (LSB) and the Absolute accuracy is 2 LSB over the 10-bit ADC range. By enhancing the ADC range to 13-bit, by means of oversampling, averaging and decimation, the accuracy of the measurement is improved and acts as a white noise filter. It is concluded that the accuracy of these readings are predominantly limited to that of the instruments it is calibrated against.

The calibration values shown in Figure 3.24 will be used for the calculations of the machine characteristics.

6.9.3 Run Tests and Processed results

The machine was run at different constant current inputs and the speed, Current and voltage ADC values logged against time. Shown in figure 6.25 is a typical result.

The power input measurement was taken on the DC supply to the Brushless DC drive and all efficiencies calculated reflects the overall efficiency of the system. Inefficiencies from the DC-DC converter are excluded for these tests and will generally vary with the drive used and the conditions under which it is operated.

The a minor resonant frequency was observed at around 70 RPM with an audible knocking sound. The effect thereof can be seen on figure 6.25, with a distinctive knee, as the rate of acceleration is reduced due to the addition frictional component. J.S. Lee,Y.H. Han, S. C.Han, S.K.Choi, S.J. Kim &T.H. Sung describes experiencing the same phenomena with their flywheel, and is typically expected with an undamped spring-mass system.

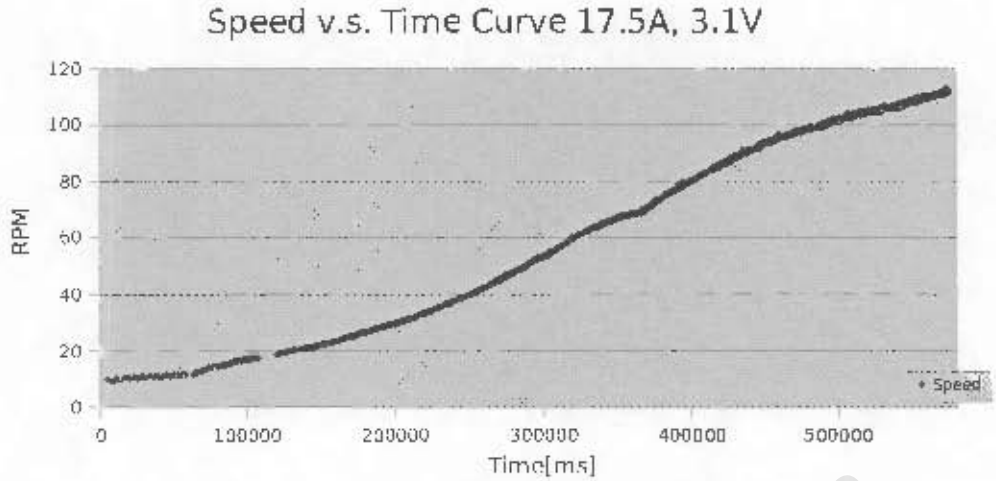

FIGURE 6.26: SPEED V.S TIME FOR CONSTANT CURRENT

The current and voltage recorded ADC values for the sample is averaged for the sample. This is converted to current and voltage, using the calibration values as determined in the previous section. The resulting average power supplied to the machine is calculated to be 53.98 W at an average DC supply current of 17.47A and 3.09 Volts.

The accelerating torque is calculated by using equation 6.10 and multiplied with the average speed over that sample to determine the power gain of the flywheel. The power loss at that speed is added to determine the total power output of the machine. This output is then divided by the average power input which indicates the power conversion efficiency of the machine at that speed, shown in figure 6.26.

From figure 6.26 it can be seen that the machine efficiency is still increasing at the upper end. The maximum efficiency is undetermined, because of the mechanical interference from the uncontrolled vibration of the magnetic bearing, and was not reached.

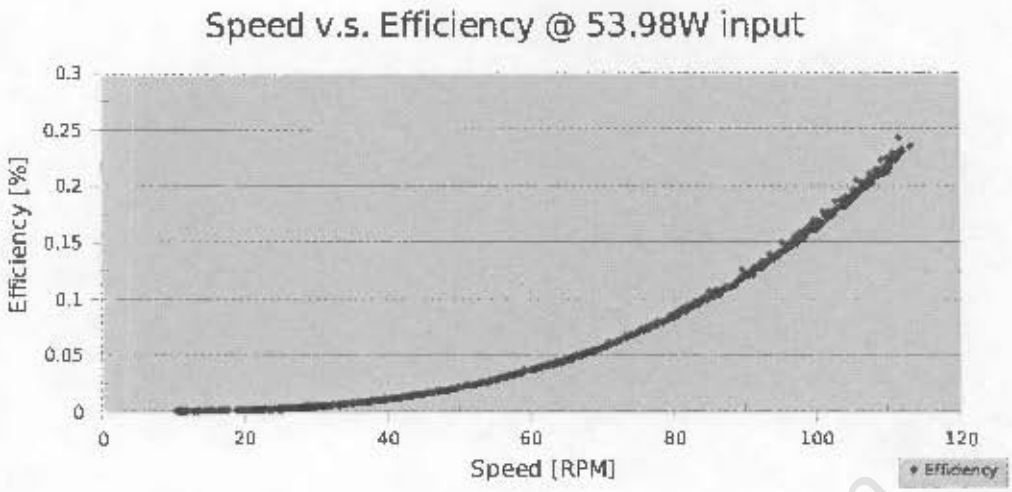

FIGURE 6.27: SPEED V.S. EFFICIENCIES GRAPH FOR CONSTANT POWER INPUT

B. Bolund, H. Bernhoff and, M. Leijon states that the highest efficiencies for flywheel applications are achieved with permanent magnet machines.

Fitting a curve to the data, with Fityk, results in equation 6.14 and follows the data with an accuracy of 99.9419%

$$\eta = 0.00119022 - 0.000139659n + 4.97281e\text{-}06n^2 + 1.03853e\text{-}07n^3 \quad 6.14$$, where:

η = Machine efficiency

n = Speed in RPM

The efficiency of this machine cannot be predicted from this equation, however, it serves as a course estimation that the machine will give start running with relatively good efficiencies at speeds of over 200 RPM.

The energy stored in the flywheel is calculated from equation 6.11 and is shown in Table 6.5:

Speed [RPM]	Stored Energy [J]
0	0
20	0.05
40	0.21
60	0.48
80	0.85
100	1.33
120	1.92

TABLE 6.5 : ENERGY VERSUS SPEED CALCULATION FOR THE FLYWHEEL

6.10 Assembly

Originally the design consisted of an upper and lower shell, shown in figure 6.8, but sealing considerations was a concern. A more practical solution was to have a permanently capped bottom shell with a close fitting lid. Not only is this simpler to manufacture, it also makes more sense in terms of sealing and assembly.

Shown in Figure 6.28 , is a photograph of the actual prototype. Visible are the bottom shell, the flywheel, the lid and the condenser side of the thermosyphon. Assembly was effortless, once the glass part of the thermosyphon was replaced by fibre composite.

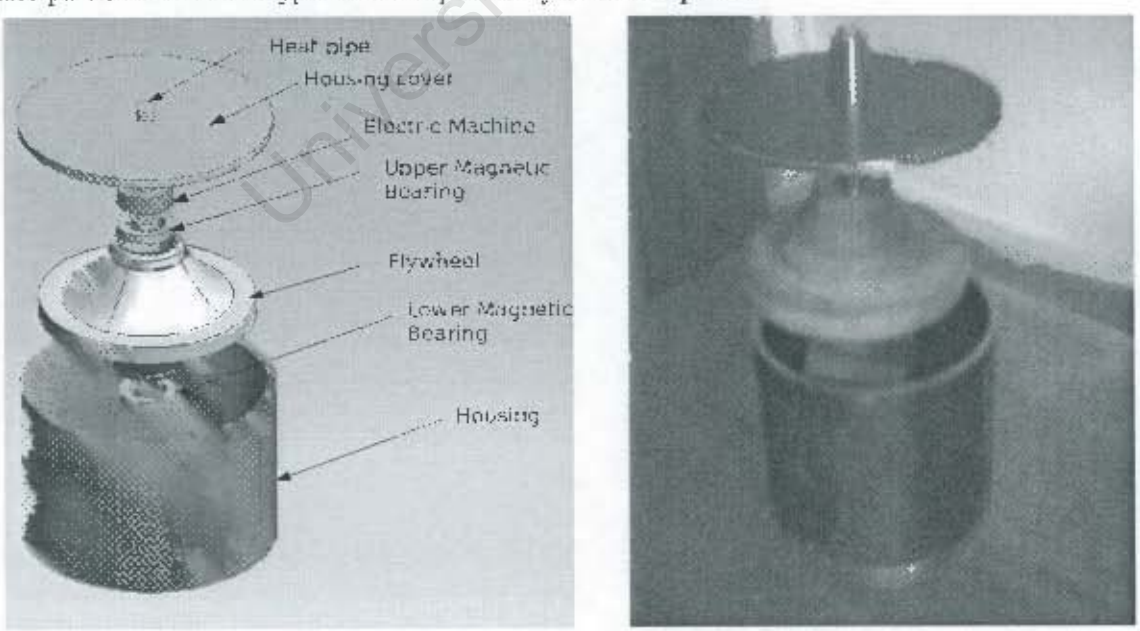

FIGURE 6.28 A):EXPLODED VIEW CAD DRAWING B):EXPLODED VIEW PROTOTYPE

The detail drawings are shown in Appendix VII.

6.11 Summary

This thesis demonstrates the technologies and processes involved in developing a working flywheel prototype. Some of the more common used technologies are presented, as well as new contributions in Halbach array construction, Permanent Magnet machine design, drive topologies, especially for low inductance machines, and heat pipe cooling over the low pressure barrier. Practical difficulties that were experienced are highlighted and practical solutions are presented and tested.

Conclusions:

- It was shown that the principles outlined in the theoretical sections of chapters 1 through 5 are sound an can be implemented in synergy to form a workable, compact and inexpensive EMB.
- Practical difficulties experienced with manufacture, assembly and operation of an EMB was highlighted and solutions determined, specifically:
  - Problems experienced with thermal cracking of the thick section of the flywheel was experienced and solutions proposed.
  - The influence of the magnetic field of a radial Hallbach array in close proximity of a radial magnetic bearing.
  - An axial flux, Halbach machine was designed and shown to not suffer from the skewing effects of the radial flux machine.
  - Difficulties with low speed resonance of the magnetic bearing was highlighted and proposals made of how to solve these.
  - Strength considerations of a heat pipe and the construction thereof to survive assembly in the presence of a magnetic bearing, within the required capacity, was demonstrated.
- An inexpensive casting technique was proposed to manufacture the flywheel was proposed.

- Inexpensive testing methodology was implemented by using low cost devices and equipment, commonly accessible to developing countries and low budget laboratories.
- Thermal requirements of an enclosure was determined and implemented in the design.
- It was shown that, using composite materials with bad thermal conductivities, the thermosyphon performed as calculated and kept the windings within the design temperature of 80 degrees Celsius.

Recommendations:

- Movement limiting of the radial bearing has to be imposed in order to achieve the speeds required to store substantial amounts of energy. This can be achieved by means of using active bearings, mechanical limiting, using a machine with enough power to ride through the resonant zones and by shaping the drive characteristics to the machine to compensate for vibration.
- Instead of the toroidal winding, which was used for simplicity of manufacture, a pancake winding should be used for an axial flux machine, in order to use the copper wire more effectively and reduce the copper losses.
- Destructive testing of the flywheel inside the actual housing should be performed to verify the assumption that the composite material absorbs enough energy to be safely contained in a simple metal enclosure.
- Proper aluminium molds should be used for manufacturing the flywheel and tests should be done to verify that adequate heat removal takes place in order to prevent thermal cracking of the moldings. This may be combined by inclusion of a heat carrier, e.g. pyrograph micro fibre or aluminium powder if required. Thermoset carbon molds may also be successfully used with the inclusion of a heat carrier.
- A simpler method of calculating the optimal flywheel dimensions for a given storage size will improve the design process for production purposes.

7 References

1. D. Johnson, P. Pillay, M.Malengret, "High speed PM motor with hybrid magnetic bearing for kinetic energy storage", IEEE, IAS, 2001
2. D. Johnson, P.Pillay, M. Malengret, "High-speed, low-cost flywheels for energy storage in sustainable power systems with distributed generation", IEEE, PES, 0-7803-7031-7/01 (C) 2001 IEEE
3. S. Salekeen and D.L. Jones, "Fatigue response of thick section fiberglass/epoxy,In Press, Corrected Proof, Available online 6 January 2006 composites"
4. S.A. Michela,R. Kieselbacha, H.J. Martens,"Fatigue strength of carbon fibre composites up to the gigacycle regime",International Journal of Fatigue 28 (2006) pp 261–270
5. S.M. Arnolda, A.F. Saleeb, N.R. Al-Zoubi,"Deformation and life analysis of composite flywheel disk systems",Composites: Part B 33 (2002) pp 433–459, Elsevier.
6. J.D. Stienmeyer, S.C. Thielman and B.C. Fabien,"Analysis and control of a flywheel storage system with a hybrid magnetic bearing",Transactions of the ASME, Vol. 119, December 1997.
7. B.P. Hills, K.M. Wright and D.G. Gillies , "A low-field, low-cost Halbach magnet array for open-access NMR",Journal of Magnetic Resonance, Volume 175, Issue 2, August 2005, pp 336-339
8. K. Halbach, "Design of permanent multi pole magnets with orientated rare earth cobalt material",Nuclear instruments and Methods, Vol. 169, 1980, North Holland Publishing Co.
9. J.M.D. Coey, "Permanent magnet applications", Journal of Magnetism and Magnetic Materials 248 (2002) pp 441–456.
10. A.E. Fitzgerald, D.E. Higginbotham and A. Grabel, "Basic Electrical Engineering", 5th Edition, Mc.Graw Hill, 1982.
11. N. Mohan, T.M. Undeland and W.P. Robbins, "Power Electronics, converters, applications and design", Second Ed., 1995.

12. R. Moser, J. Sandtner & H. Bleurer, "Diamagnetic suspension system for small rotors", Journal of Micromechatronics, Vol. 1, No. 2, pp. 131 – 137 (2001).
13. J.P. Yonnet, "Passive Magnetic Bearings with Permanent Magnets", IEEE Trans. on Magnetics. Vol Mag-14, No 5, September 1978.
14. O. Bouty, "Eddy current losses in passive magnetic bearings",Journal of Applied Physics, Vol 92, No. 11 1 Dec 2002, pp 68515-68565.
15. Jr-Yi Shen and Brian C. Fabien, "Optimal control of a flywheel energy storage system with a radial flux hybrid magnetic bearing", Elsevier, Journal of the Franklin Institute 339 (2002) pp 189–210.
16. J.P Holman, "Heat transfer", Mc Graw Hill, International student edition,1981.
17. L.L. Vasiliev, "Heat pipes in modern heat exchangers", Applied Thermal Engineering, Volume 25, Issue 1, January 2005, pp 1-19.
18. Z.J. Zuo, M.T. North and D.M. Ernst, "Improved Heat Pipe Performance Using Graded Wick Structures", International Mechanical Engineering Congress and Exposition, Anaheim, CA,November 1998.
19. T. Payakaruk, P. Terdtoon and S. Ritthidech, "Correlations to predict heat transfer characteristics of an inclined closed two-phase thermosyphon at normal operating conditions", Applied Thermal Engineering, Volume 20, Issue 9, June 2000, pp 781-790.
20. Y.J. Park, H.K. Kang and C.J. Kimo, "Heat transfer characteristics of a two-phase closed thermo-syphon to the fill charge ratio", International Journal of Heat and Mass Transfer 45 (2002) pp 4655–4661–4661.
21. A. Rodriguez-Bernal and E.S van Vleck, "Diffusion induced chaos in a closed loop thermosyphon", Society for industrial and Applied Mathematics, Vol 58, No. 4, August 1998, pp 1072 – 1093.
22. A. Meyer & R.T. Dobson, "Heat pipe heat recovery heat exchanger for a mini-drier" , Journal of Energy in Southern Africa, Vol 17, No 1, February 2006, pp 50-57.

23. D.A. Reay, "Heat Pipes", Phys. Technology.. Vol. 16. 1985 Printed in Northern Ireland.

24. K. Geick, J. Walters, "Technical formulae", Kurt Gieck, J. Walters, 6th English Edition, 1985 Heilbronn, N, West Germany.

25. L. L. Vasiliev, "State-of-the-art on heat pipe technology in the former Soviet Union", Applied Thermal Engineering, Volume 18, Issue 7, July 1998, pp 507-551.

26. R.F. Post, S. F. Post, "A high-efficiency electro-mechanical battery", Proceedings of the IEEE, Vol. 81, No 3, March 1993.

27. M. Berger and I. Porat, "Optimal Design Of Rotating Disk for Kinetic Energy Storage", ASME J. Appl. Mech., 1988, 55, pp. 164–170.

28. P.P. Benham & F.V. Warnock, "Mechanics Of Solid and Structures", London: Pitman, 1976 ,1981.

29. D. Eby, R.C. Averill, E. Goodman, and W. Punch, "Optimal Design of Flywheels Using an Injection Island Genetic Algorithm", Artificial Intelligence in Engineering , Design, Analysis and Manufacturing, 13, 1999, pp. 389-402.

30. E. Goursat, "Differential equations Part 2 of volume 2", Ginn & Company, 1917.

31. G. Ries and H.W. Neumueller, "Comparison of energy storage in Flywheels and SMES", Elsevier, Physica C 357±360 (2001) pp 1306–1310.

32. B. Bolund, H. Bernhoff and, M. Leijon, "Flywheel energy and power storage systems", Elsevier, Renewable and Sustainable Energy Review, Jan 2005.

33. J.H. Faupel and F.E. Fisher, "Engineering Design", Second Edition, New York, N.Y Wiley, 1964.

34. P.J.E. Forsyth, "Composite Materials", Institution of Metallurgists, British Crown Copyright, Illiffe Books LTD., London, 1966.

35. L. Holloway, "Design of composites", Design with advanced composite materials, sect 9,The Design Council, London, 1989.

36. S. Fara and A. Pavan, "Fibre orientation effects on the fracture of short fibre polymer

composites", Journal of materials science 39 (2004), pp 3619–3628.

37. J.A. Epaarachi, P.D. Clausen, "An empirical model for fatigue behavior pre-diction of glass fibre-reinforced plastic composites for various stress ratios and test frequencies", Elsevier, Composites: Part A 34 (2003) pp 313–326.
38. E.A. Avallone and T. Baumeister III, "Marks' Standard Handbook for Mechanical Engineers", Ninth Ed. McGraw Hill, 1987.
39. M.D. Afendi, W.M. Banks, D. Kirkwood, "Bubble free resin for infusion process", Elsevier, Composites: Part A 36 (2005) pp 739–746.
40. R. L. Daugterty, J. B. Franzini, "Fluid mechanics with engineering Application", 7th Edition,1977, McGraw Hill.
41. Y. Suzuki, A. Koyanagi, M. Kobayashi, R. Shimada, "Novel applications of the flywheel energy storage system", Elsevier, Energy 30 (2005) pp 2128–2143.
42. F.A. Himmelstoss & P.A. Wurm, "Simple bi-directional dc-to-dc converters with high input to output conversion ratio", EPSEC01_ bidi/fh/19.9.01//16.01.2002.
43. P. Horowitz and W. Hill, "The Art of Electronics", Cambridge Univ. Press, second edition, 1989.
44. J.S. Lee,Y.H. Han, S. C.Han, S.K.Choi, S.J. Kim &T.H. Sung, "300 W-h class superconductor flywheel energy storage system with a horizontal axle", Physica C 372–376 (2002) 1451–1456

Appendix I – FEA analysys models and results

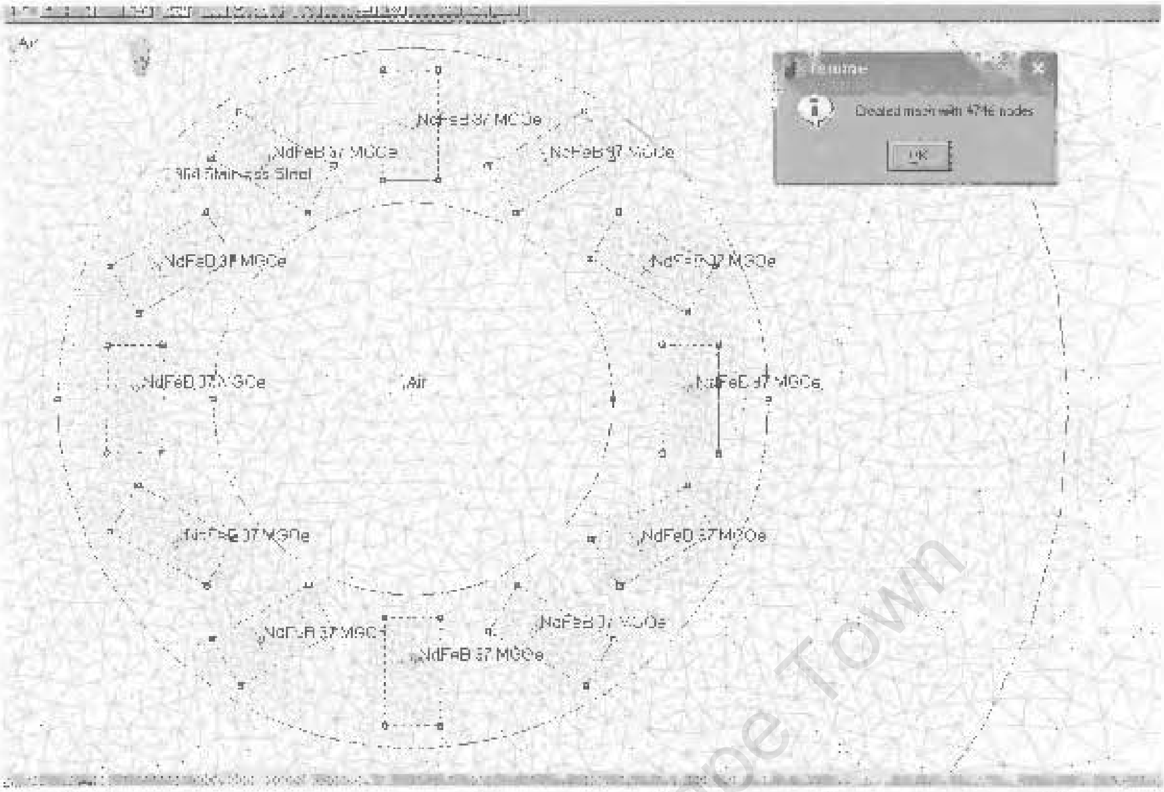

Created mesh with 4746 nodes

12 Segment rectangular magnet Halbach array Dipole model, Inner Diameter = 36mm

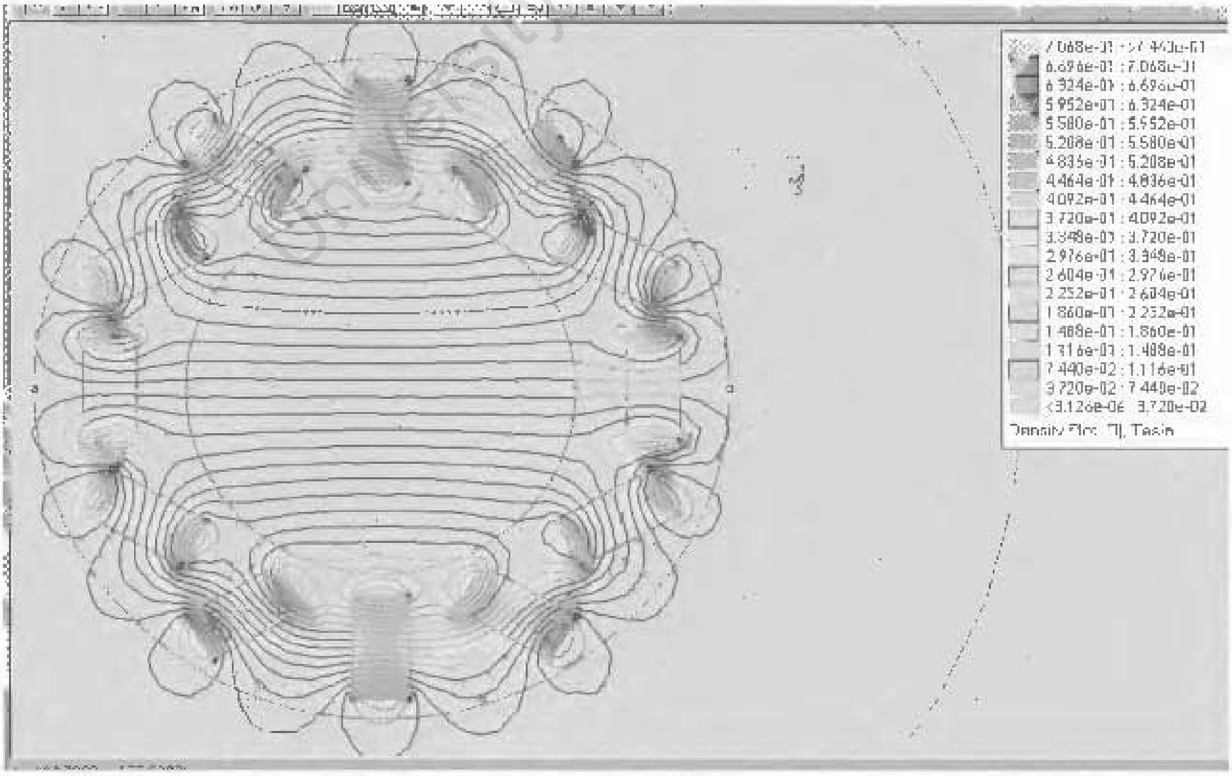

12 Segment, rectangular magnet Halbach array Dipole result, Inner Diameter = 36mm

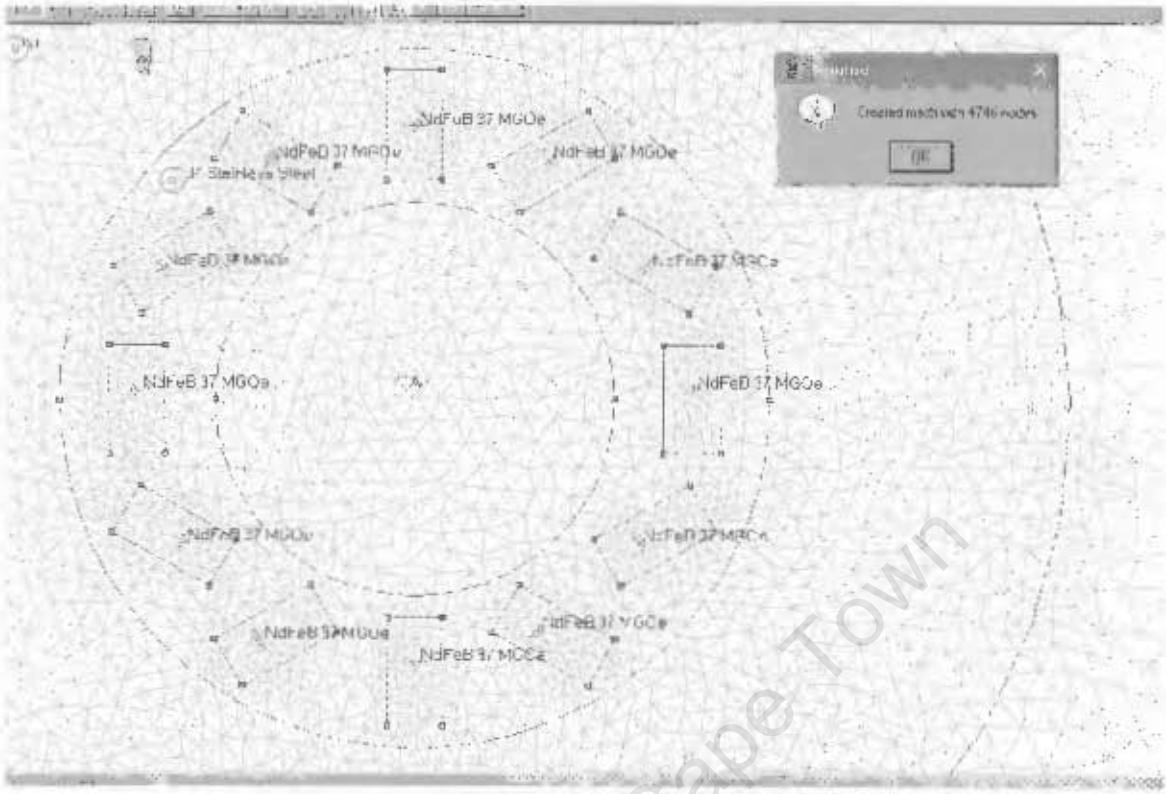

12 Segment, rectangular magnet Halbach array Dipole Model, ID = 40mm

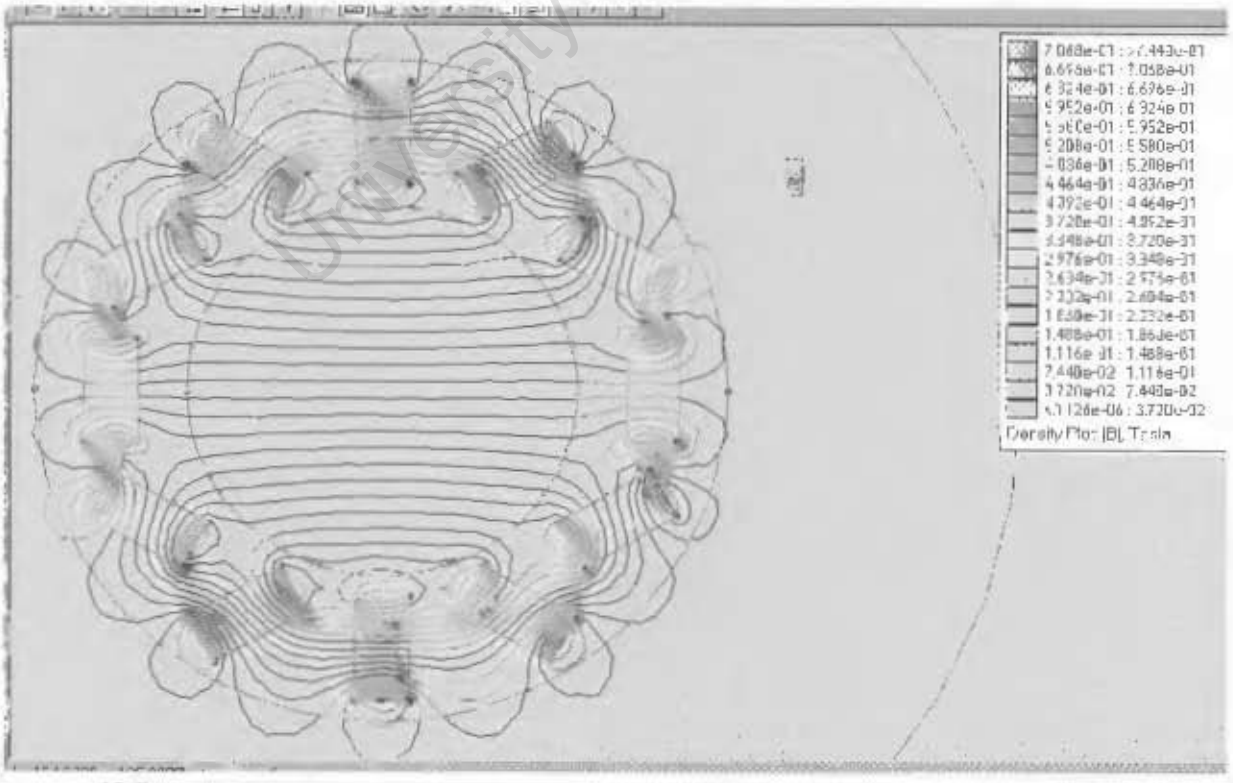

12 Sement, rectangular magnet Halbach array Dipole result, Inner Diameter = 40mm

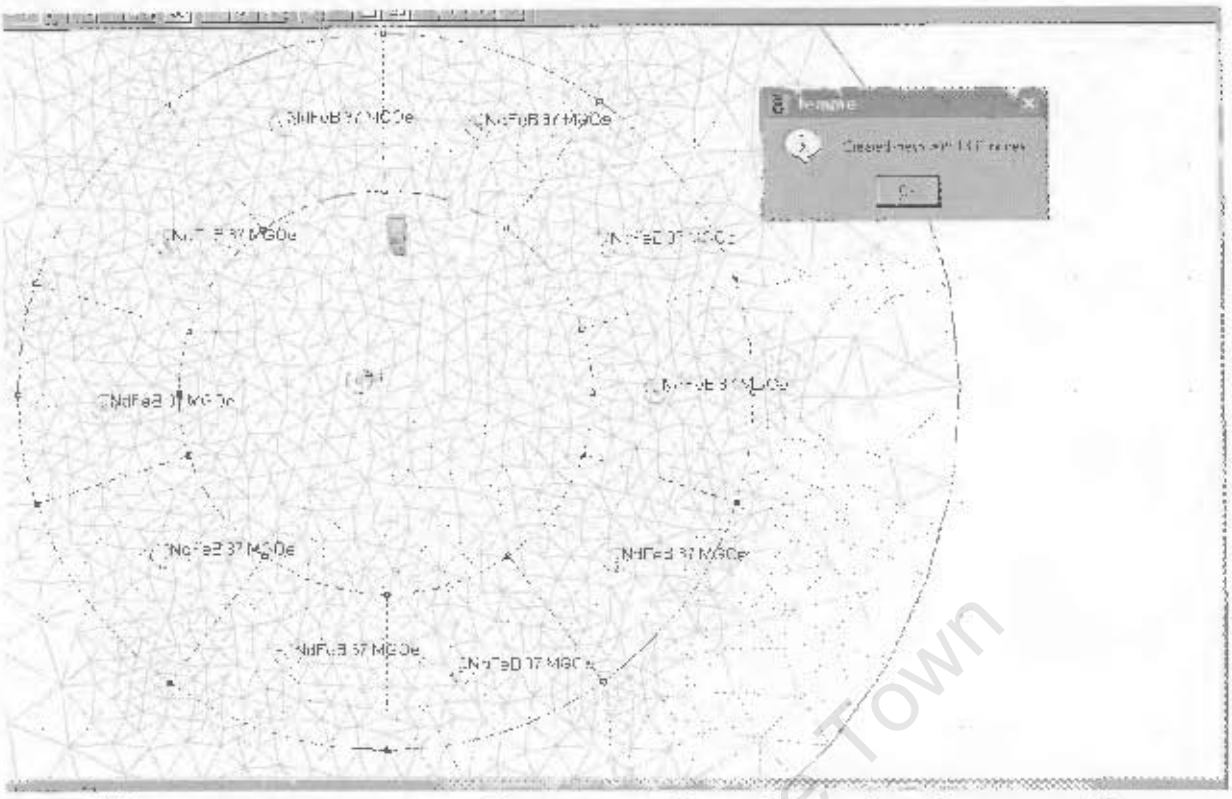

10 Segment, rectangular magnet Halbach array Dipole Model, Inner Diameter = 40mm

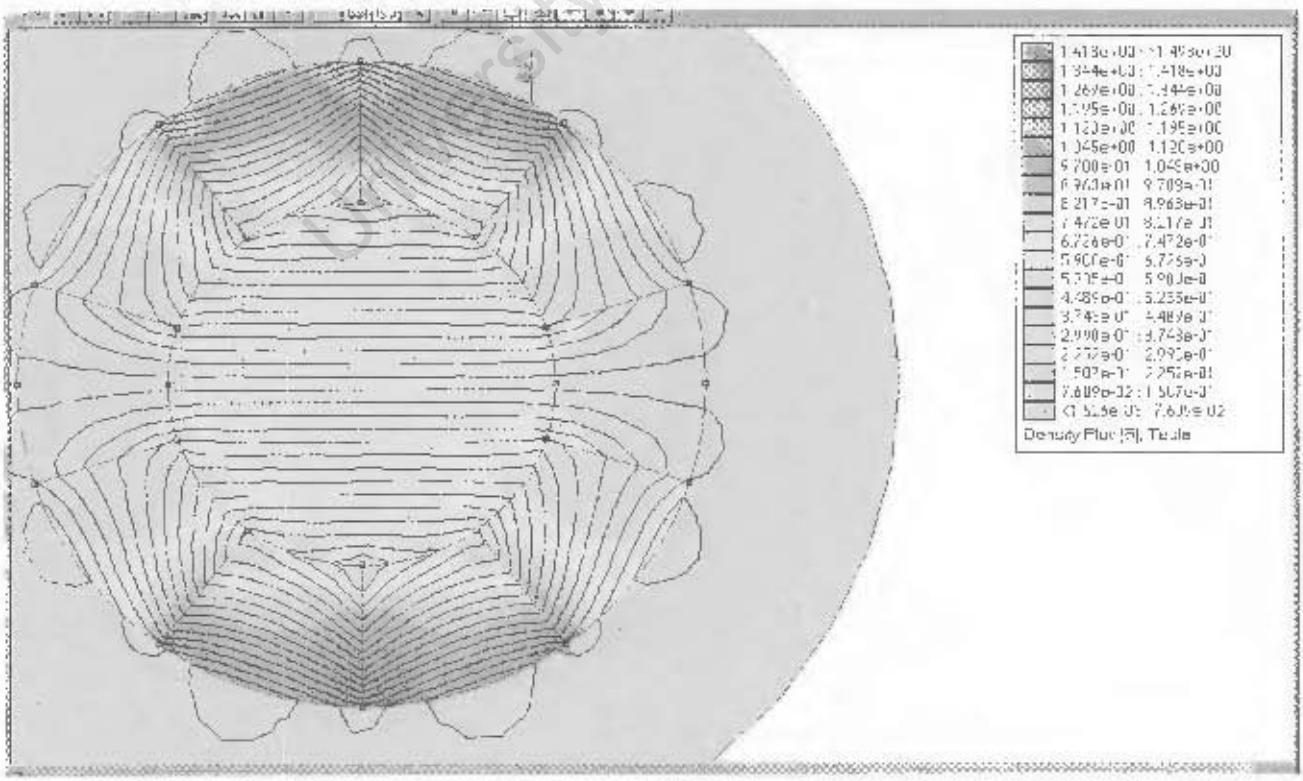

10 Segment, rectangular magnet Halbach array Dipole Result, Inner Diameter = 40mm

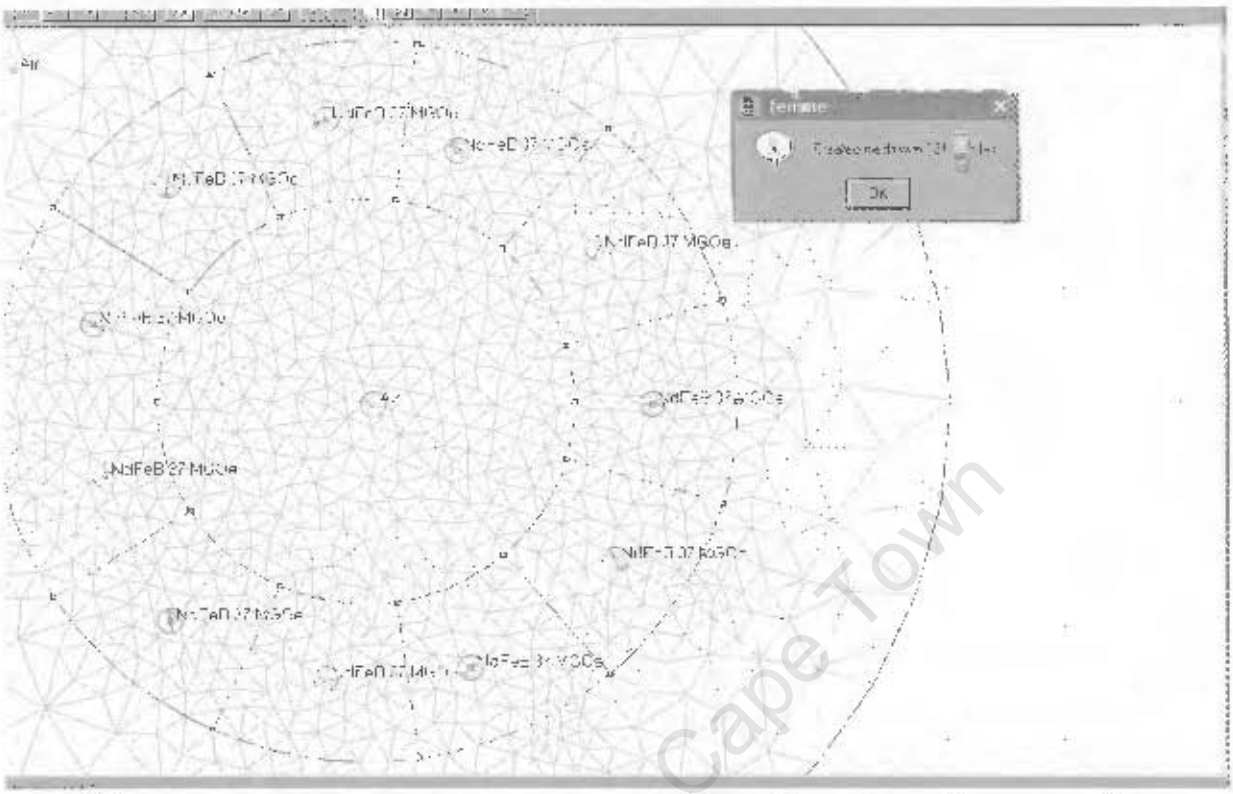

11 Segment, rectangular magnet Halbach array Dipole Model, Inner Diameter = 40mm

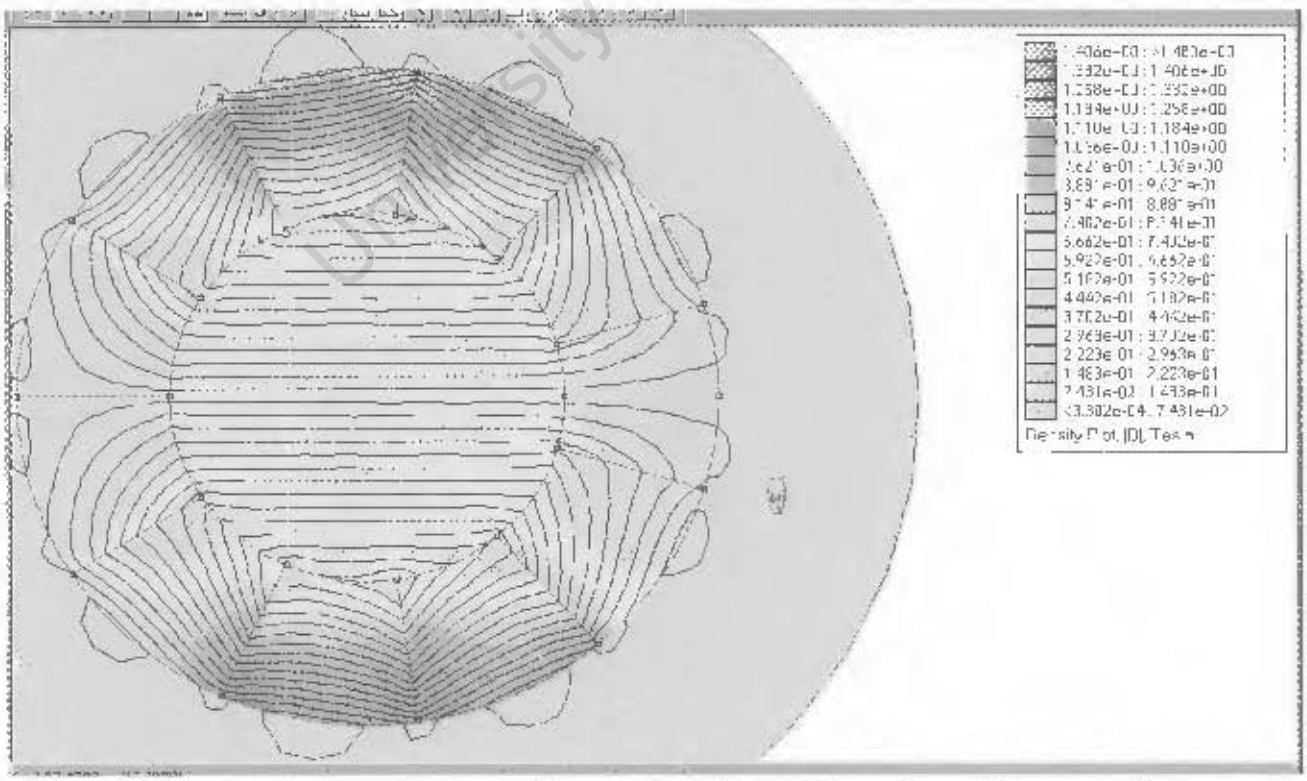

11 Segment, rectangular magnet Halbach array Dipole Result, Inner Diameter = 40mm

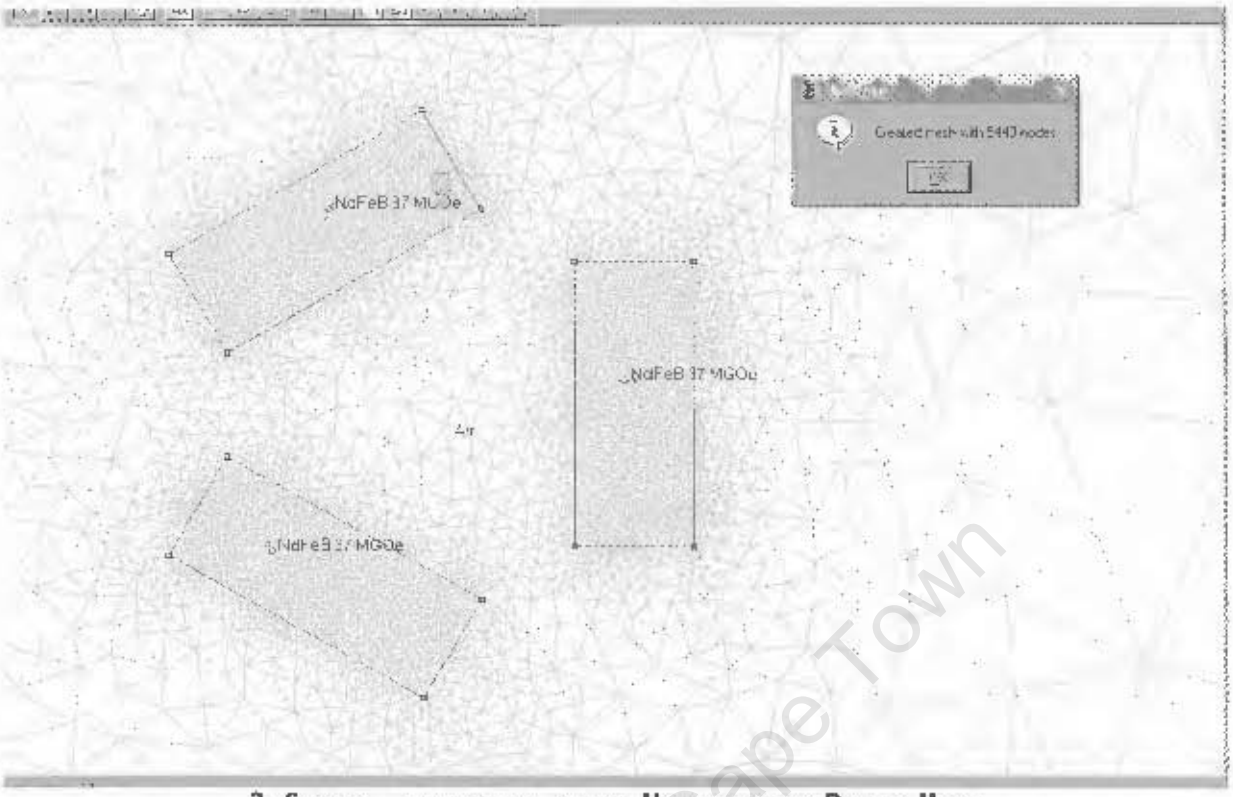

3 Segment, rectangular magnet Halbach array Dipole Model

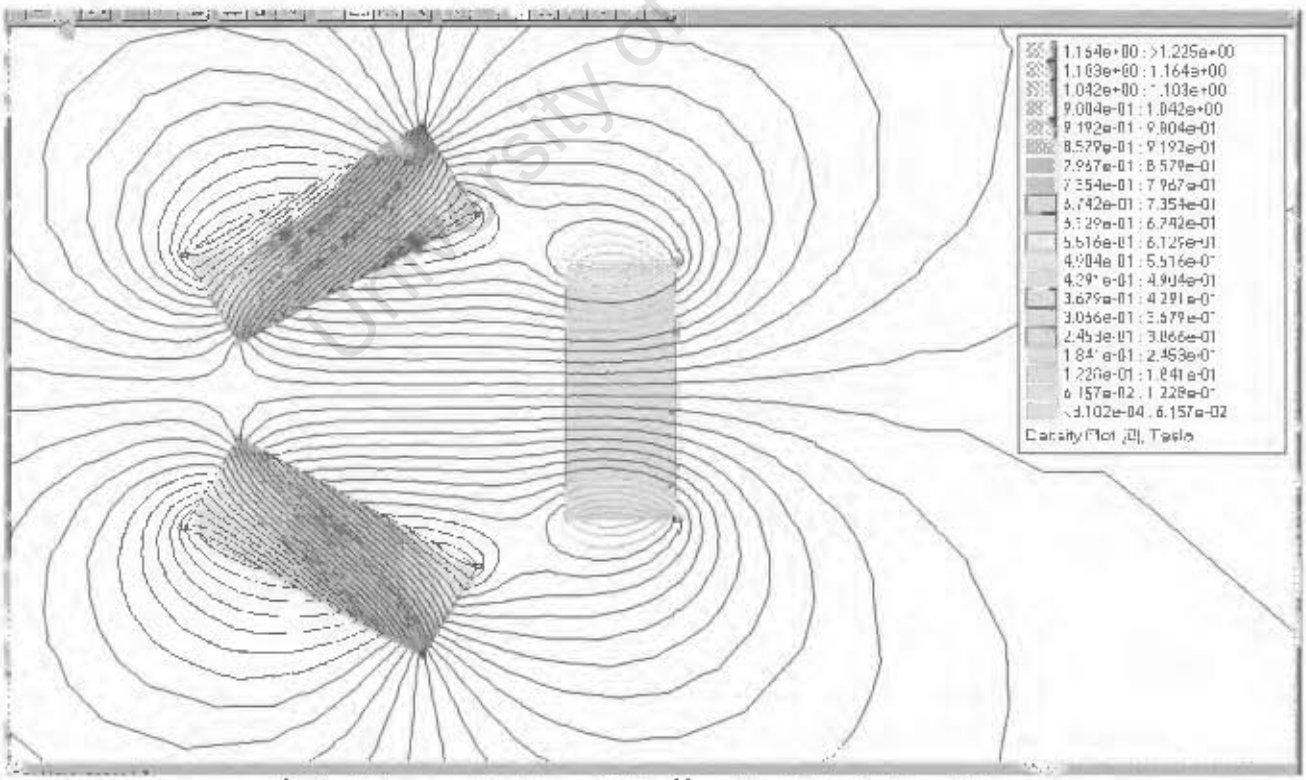

3 Segment, rectangular magnet Halbach array Dipole Result

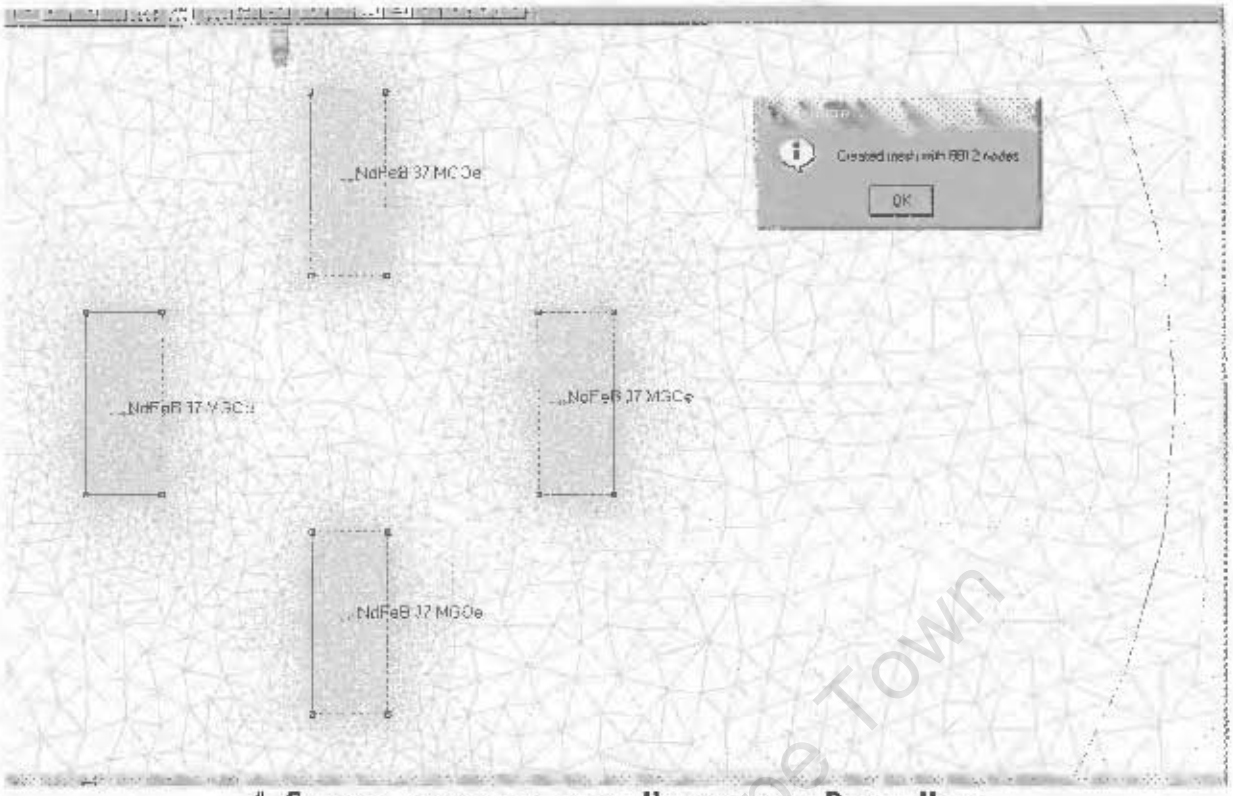

4 Segment, rectangular magnet Halbach array Dipole Model

rect - 04

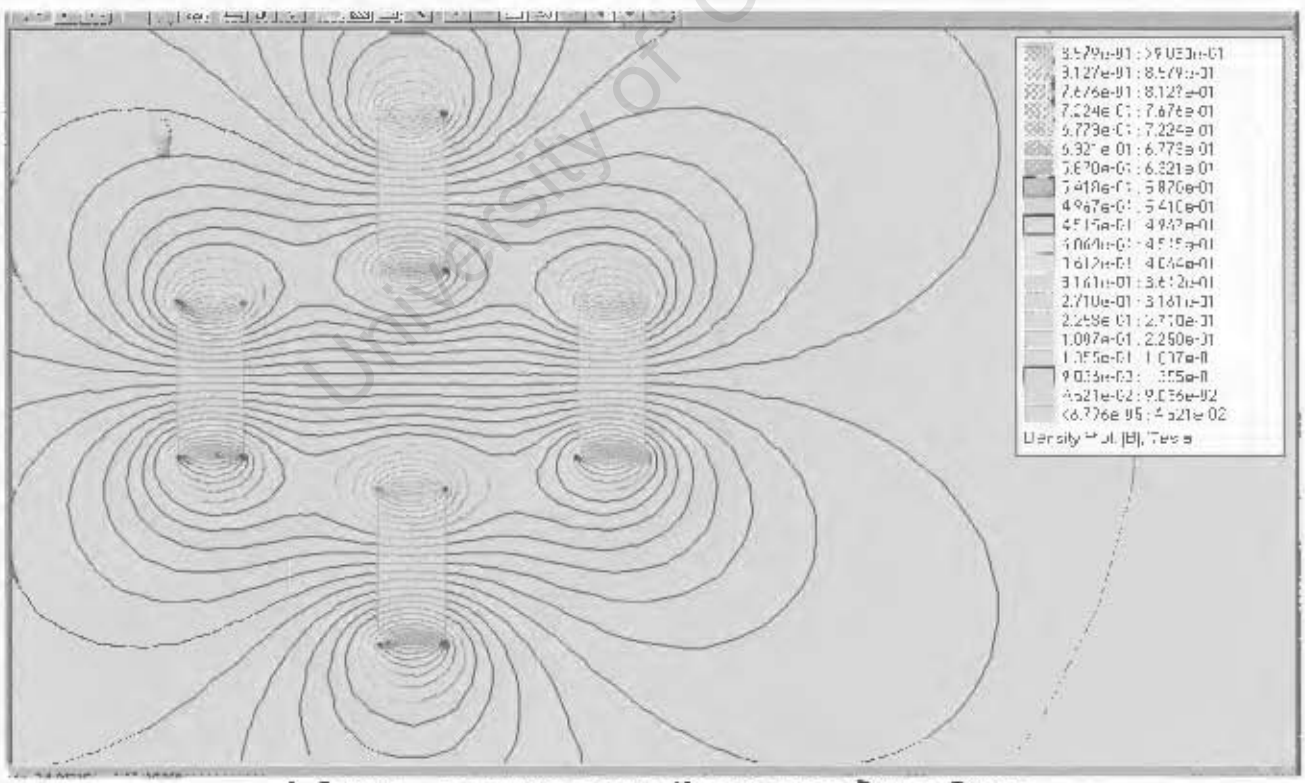

4 Segment, rectangular magnet Halbach array Dipole Result

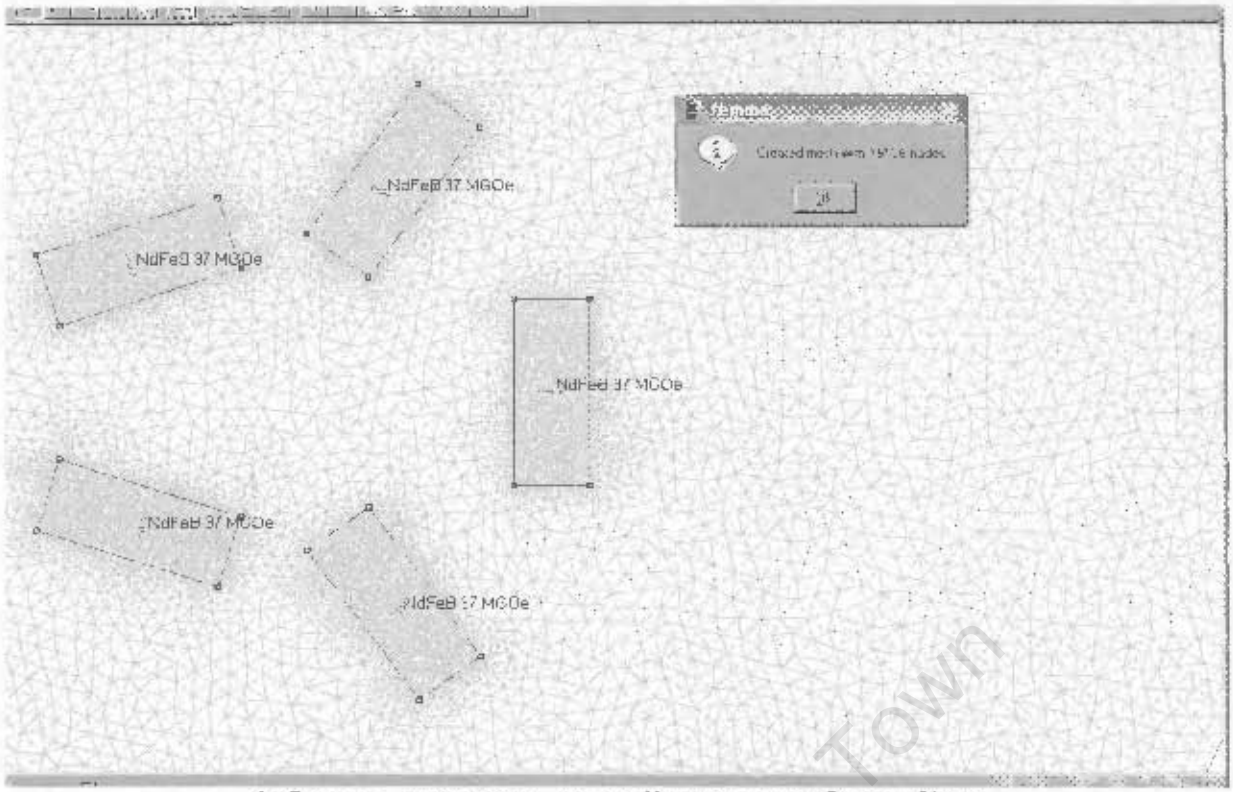

4 Segment, rectangular magnet Halbach array Dipole Model

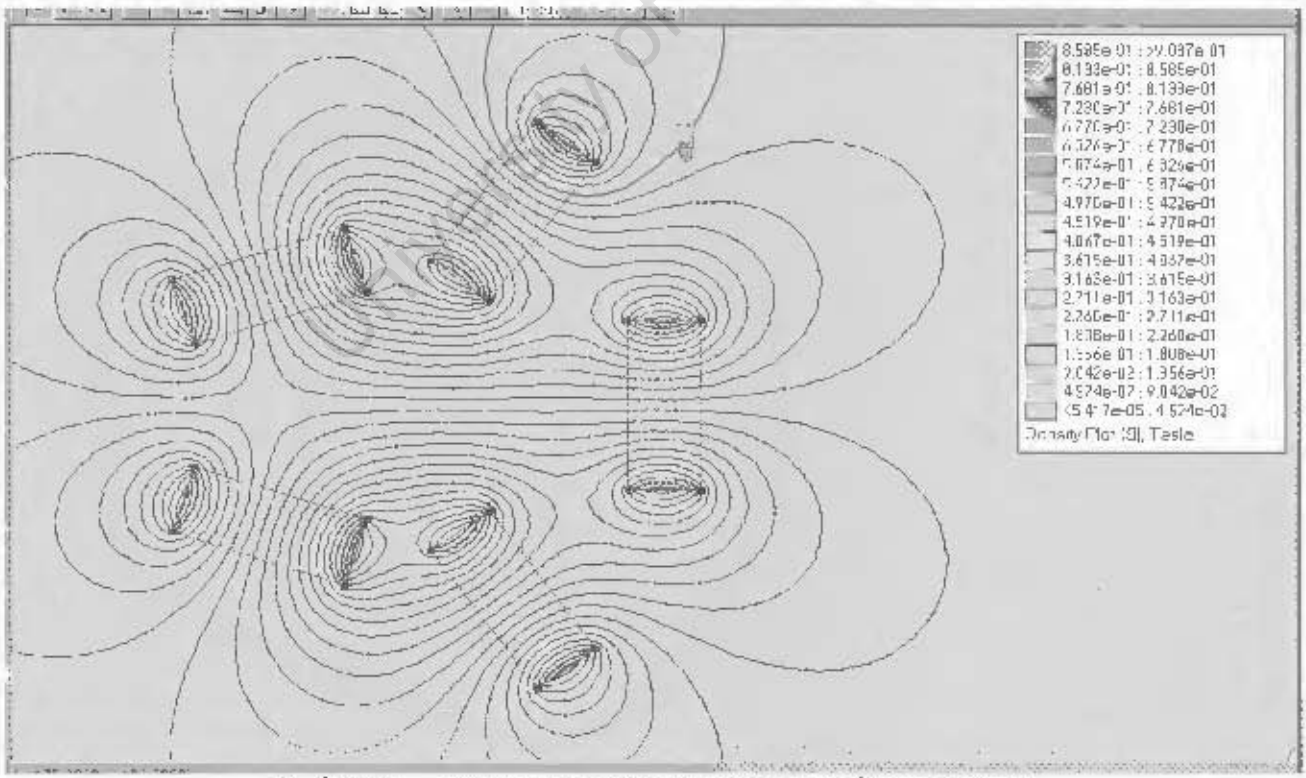

5 Segment, rectangular magnet Halbach array Dipole Result

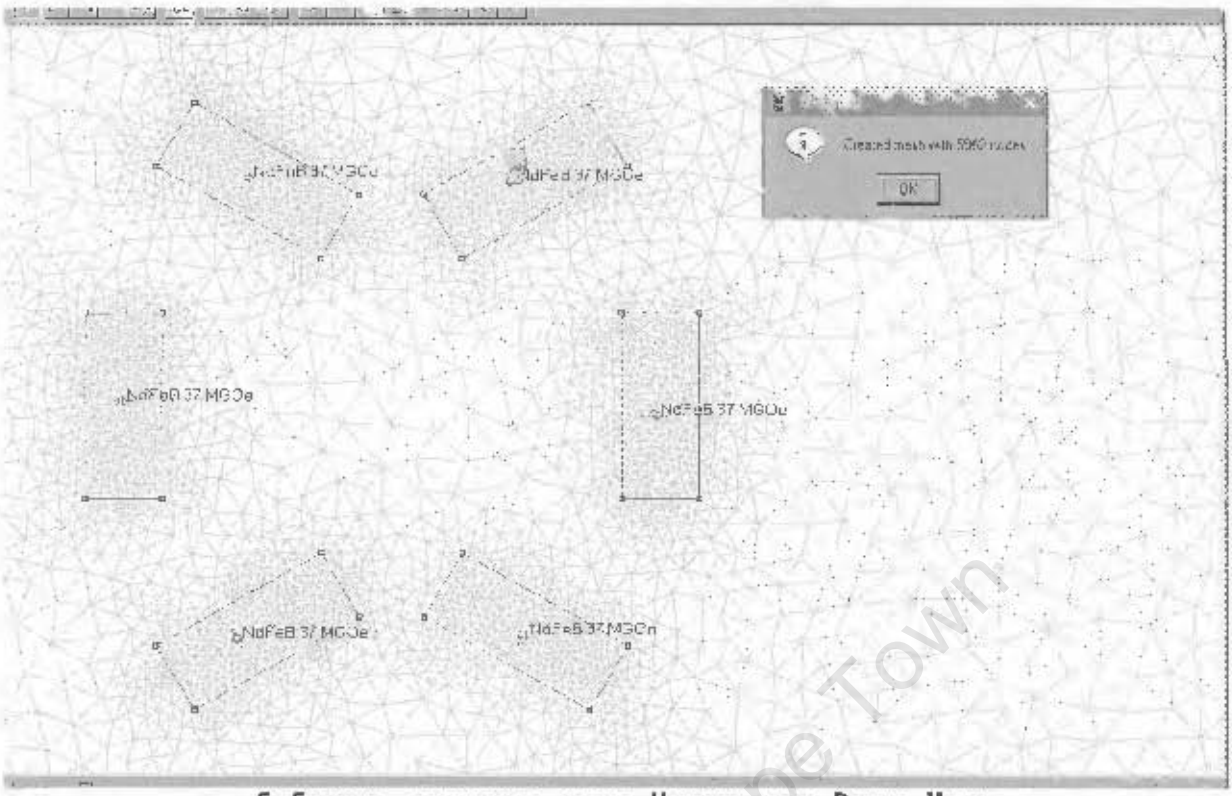

6 Segment, rectangular magnet Halbach array Dipole Model

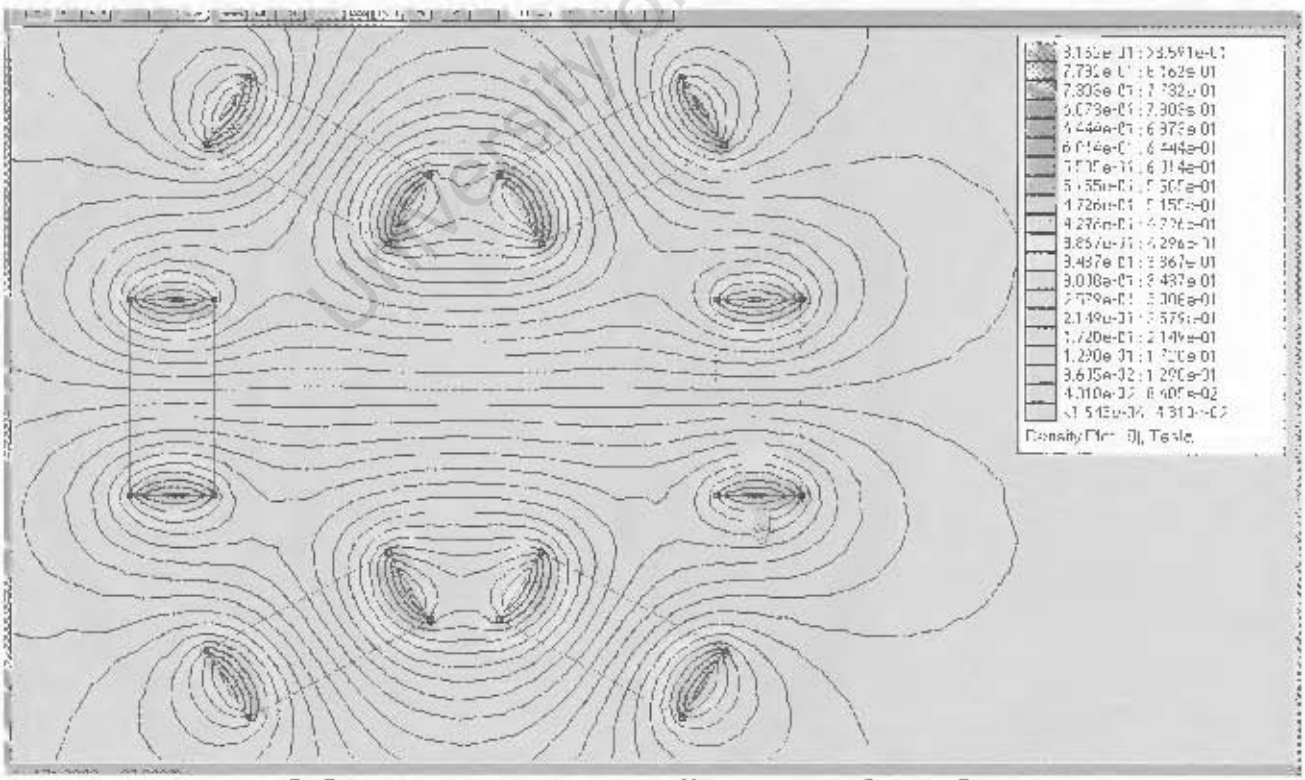

6 Segment, rectangular magnet Halbach array Dipole Result

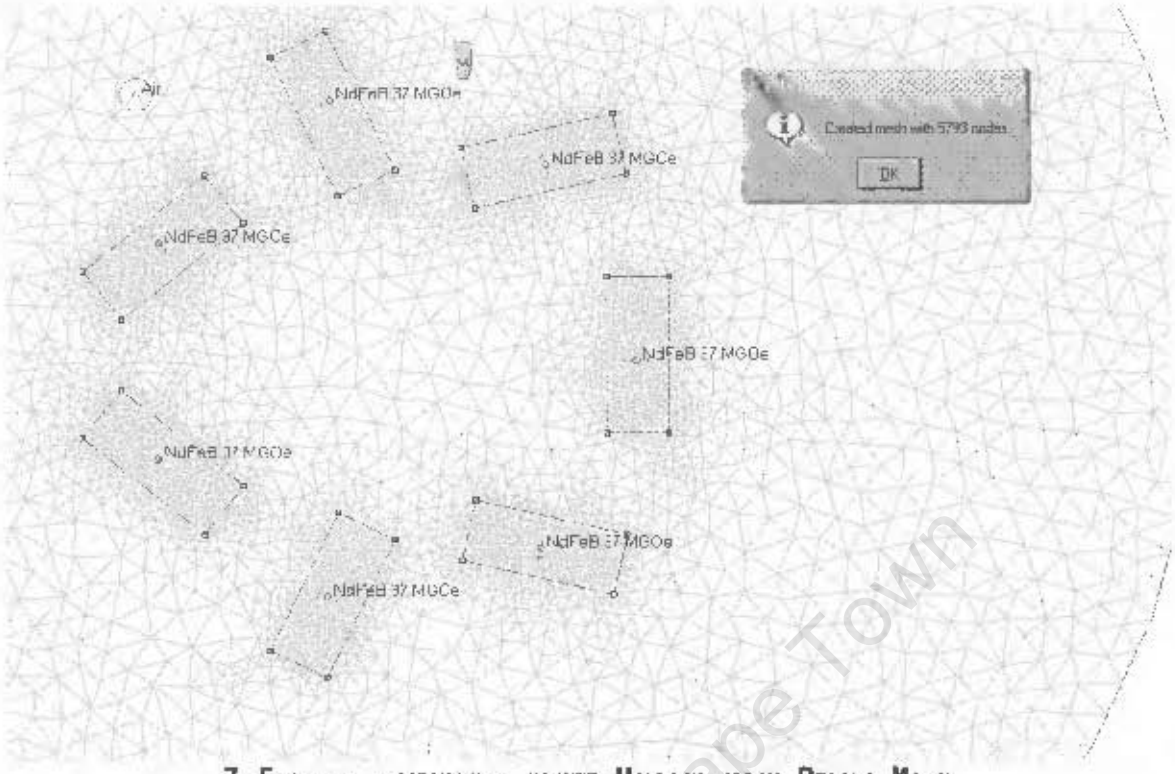

7 Segment, rectangular magnet Halbach array Dipole Model

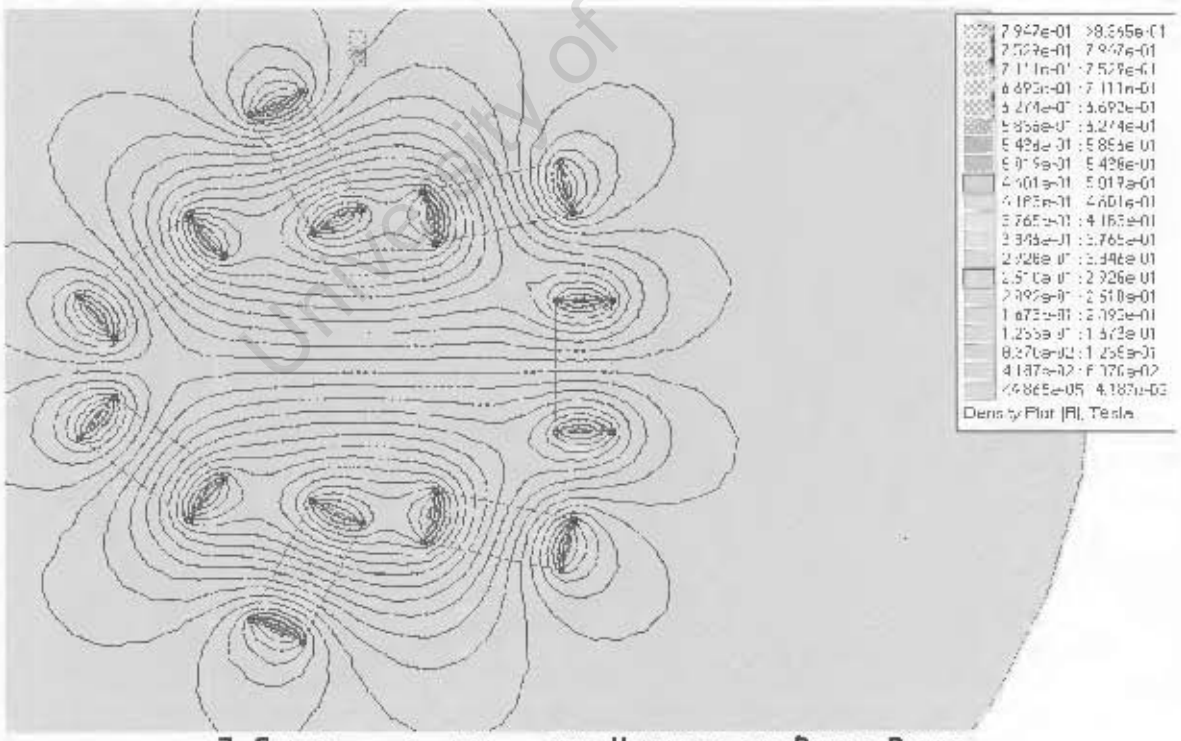

7 Segment, rectangular magnet Halbach array Dipole Result

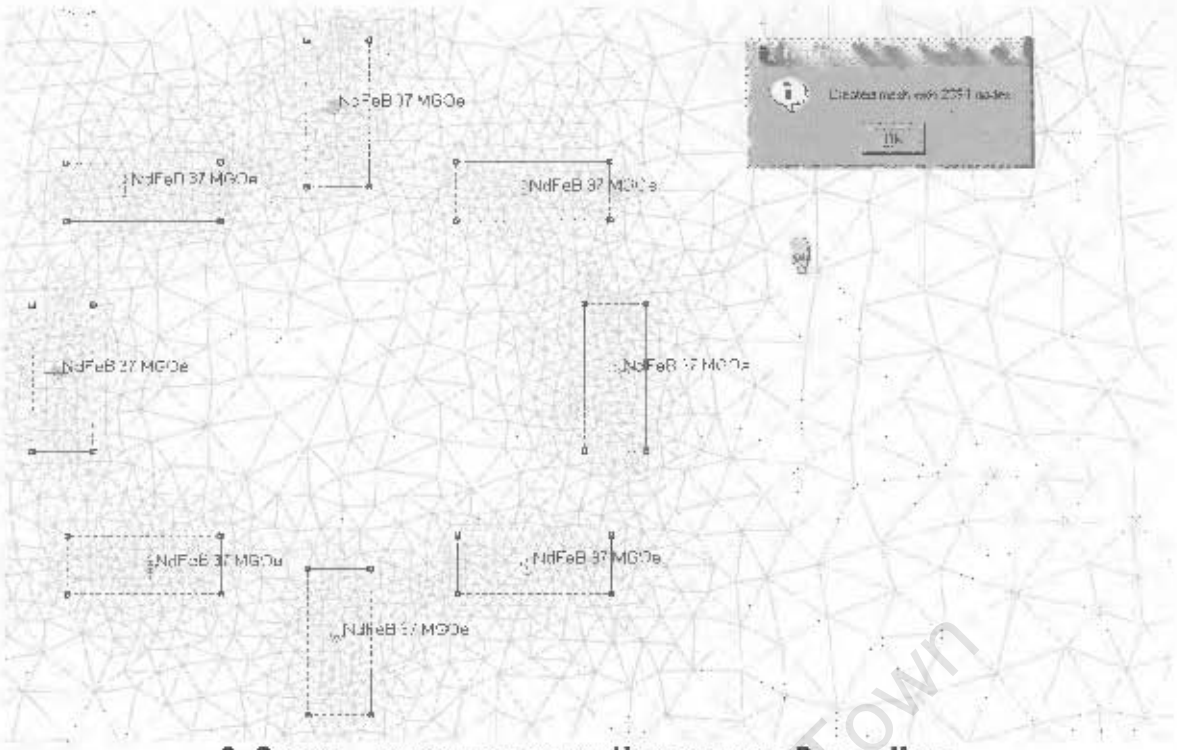

8 Segment, rectangular magnet Halbach array Dipole Model

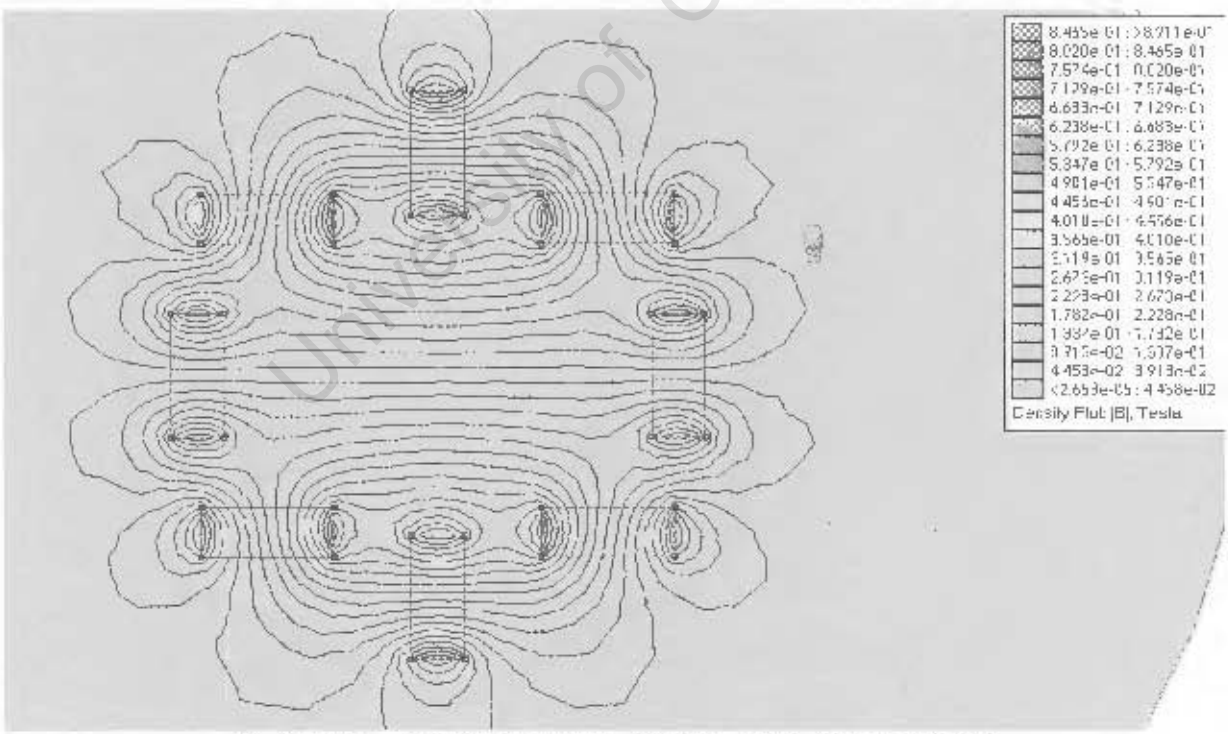

8 Segment, rectangular magnet Halbach array Dipole Result

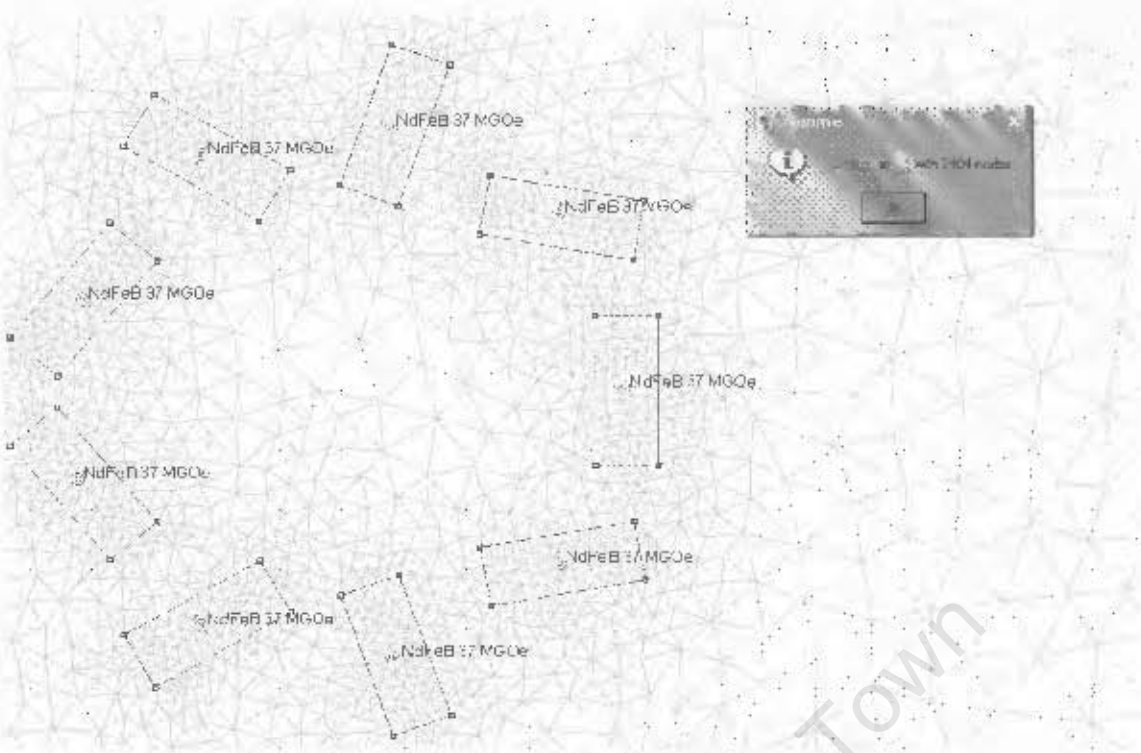

9 Segment, rectangular magnet Halbach array Dipole Model

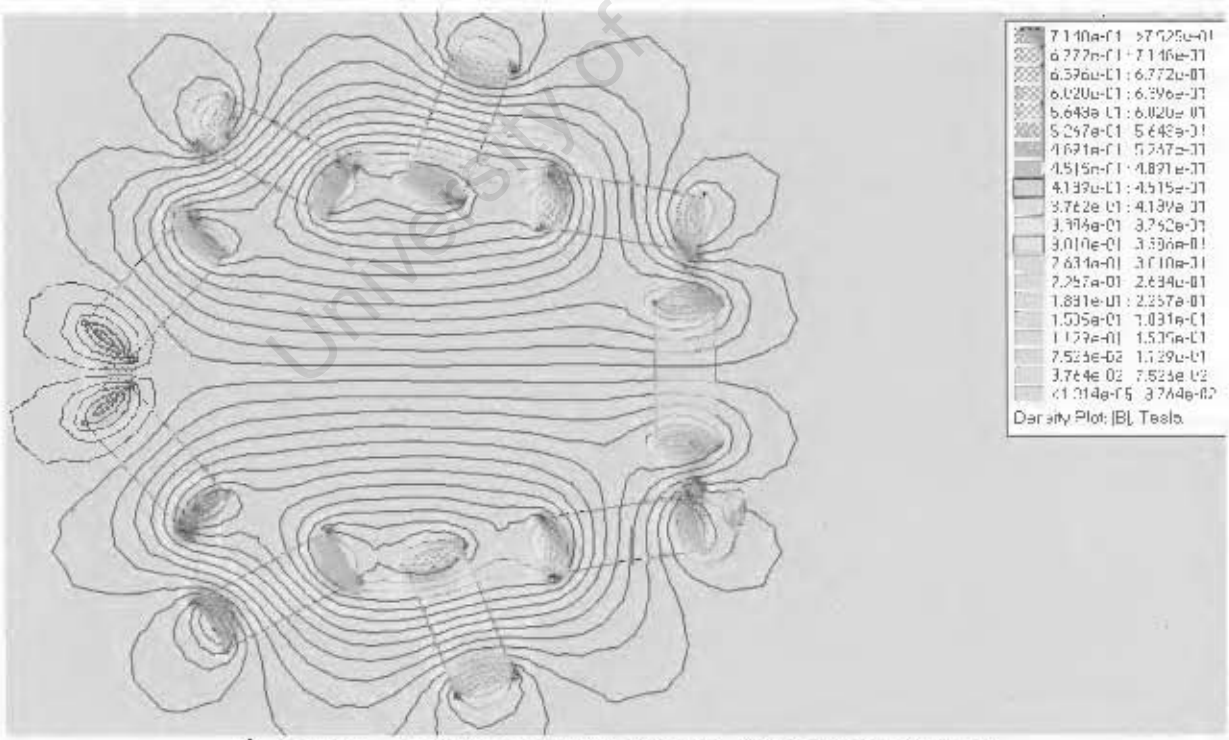

9 Segment, rectangular magnet Halbach array Dipole Result

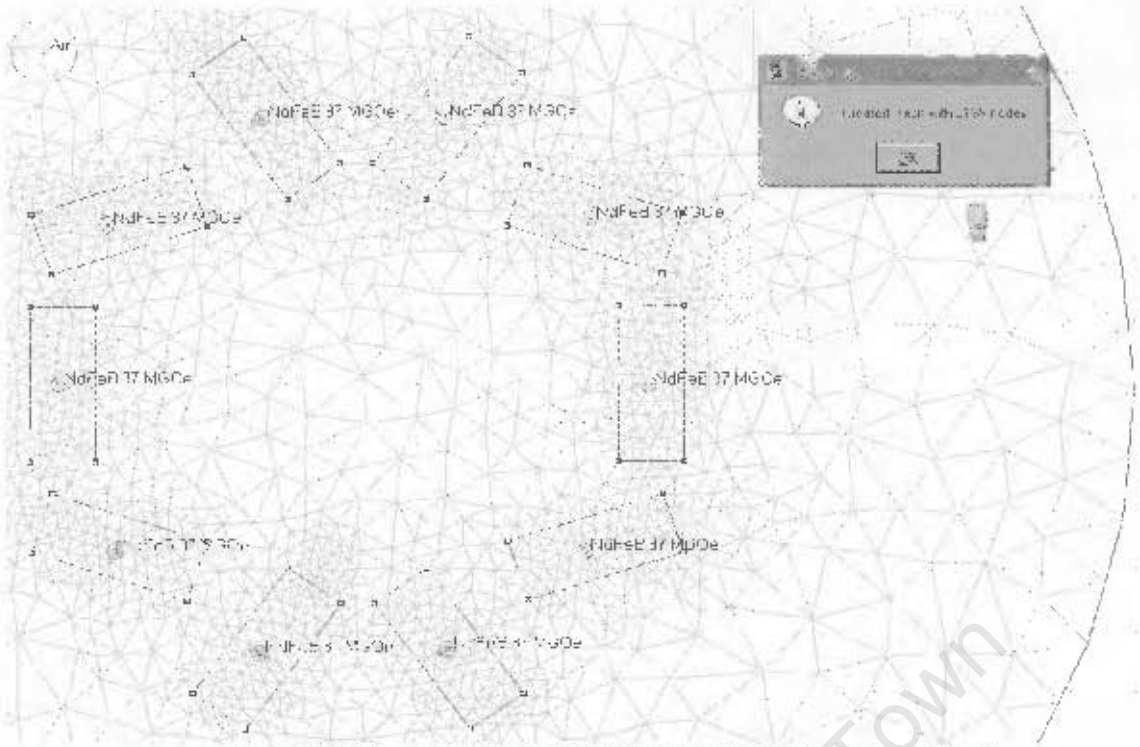

10 Segment, rectangular magnet Halbach array Dipole Model

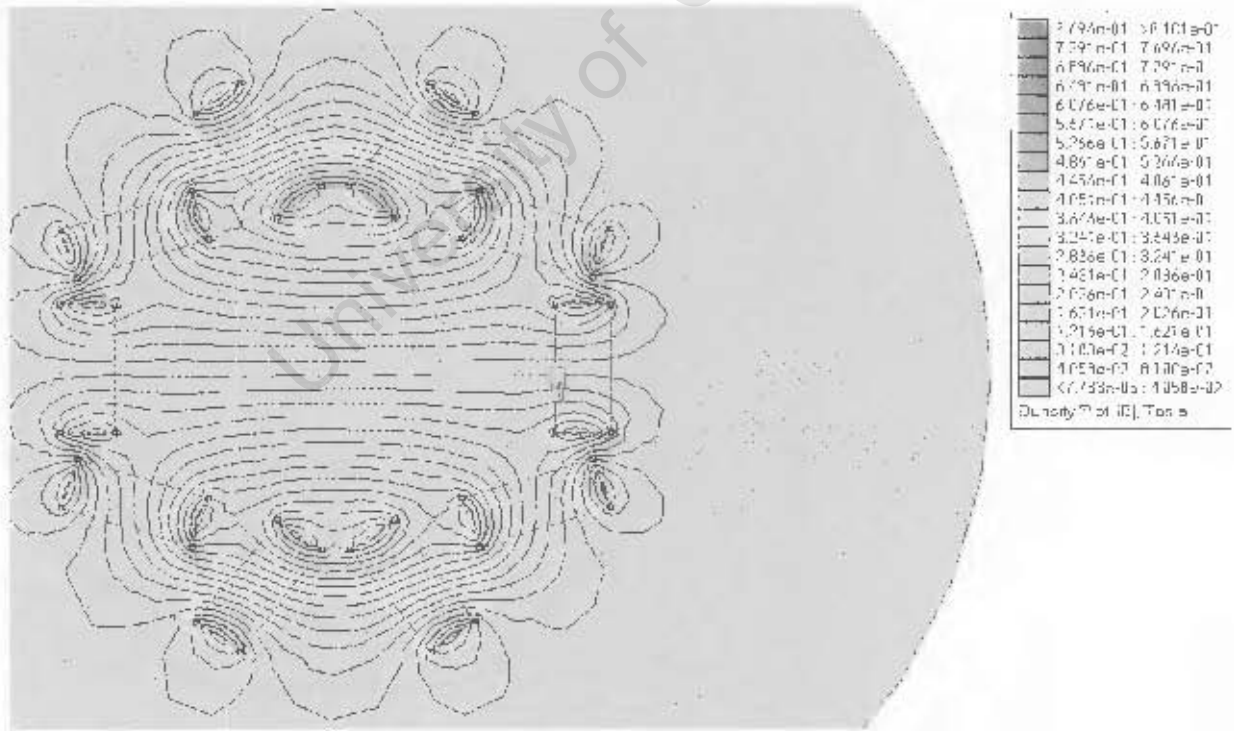

10 Segment, rectangular magnet Halbach array Dipole Result

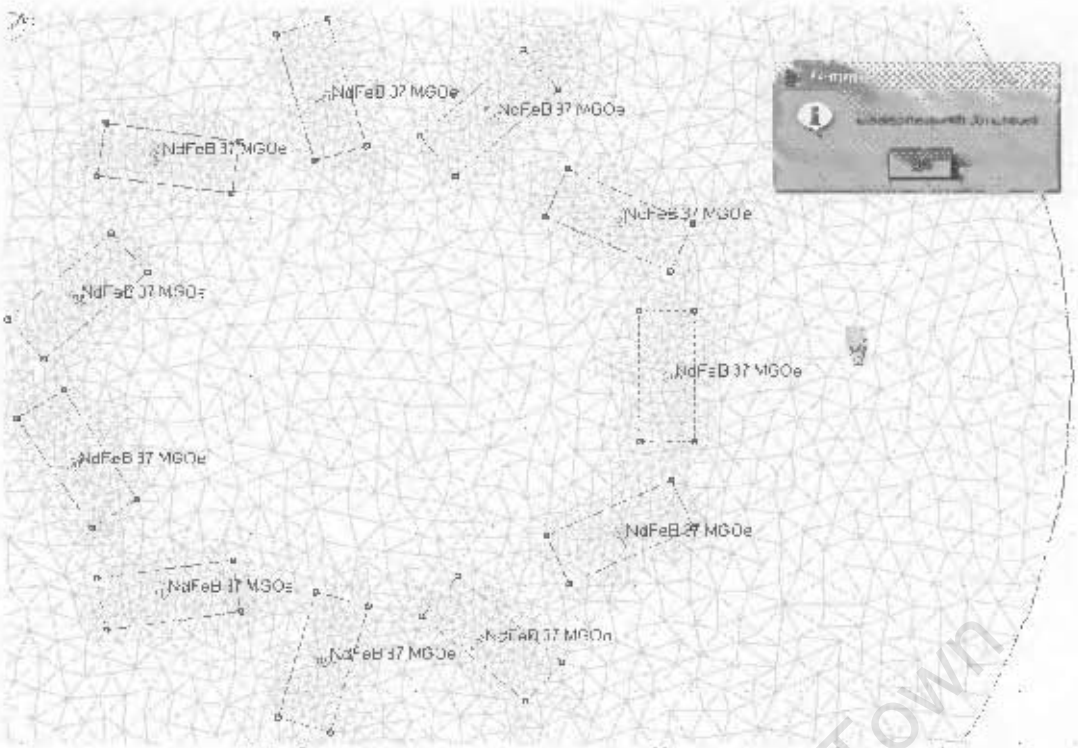

11 Segment, rectangular magnet Halbach array Dipole Model

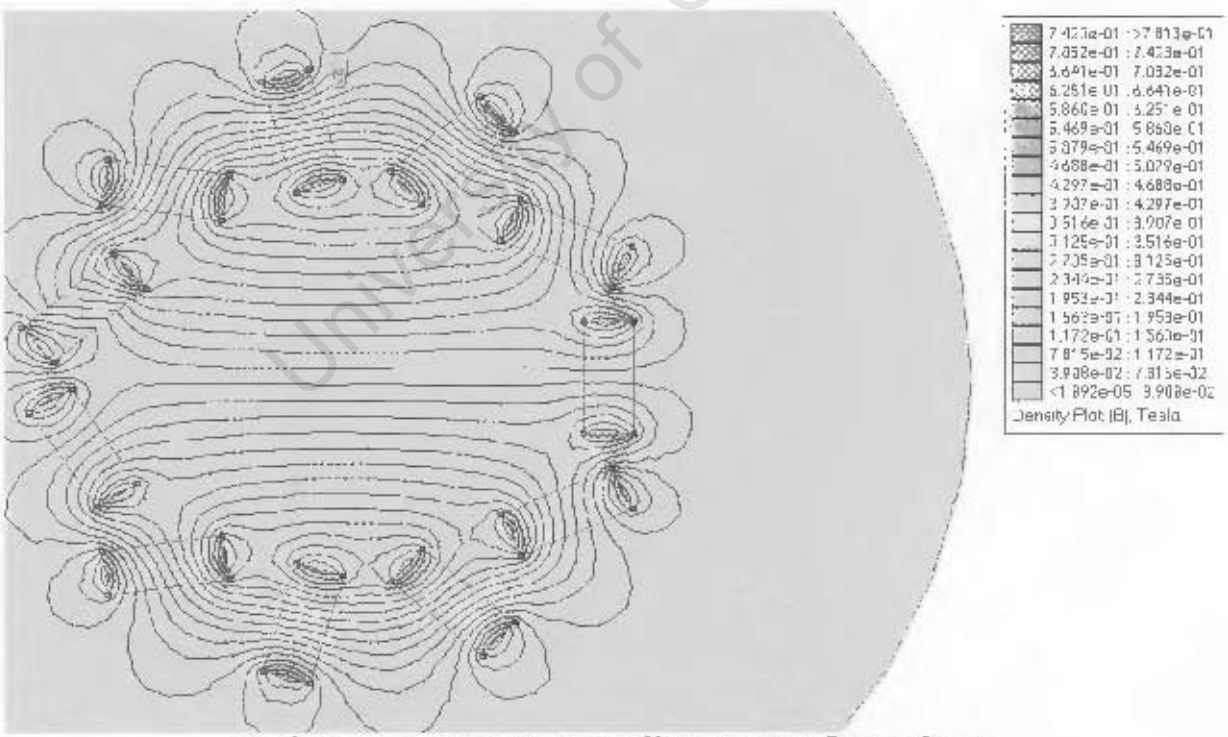

11 Segment, rectangular magnet Halbach array Dipole Result

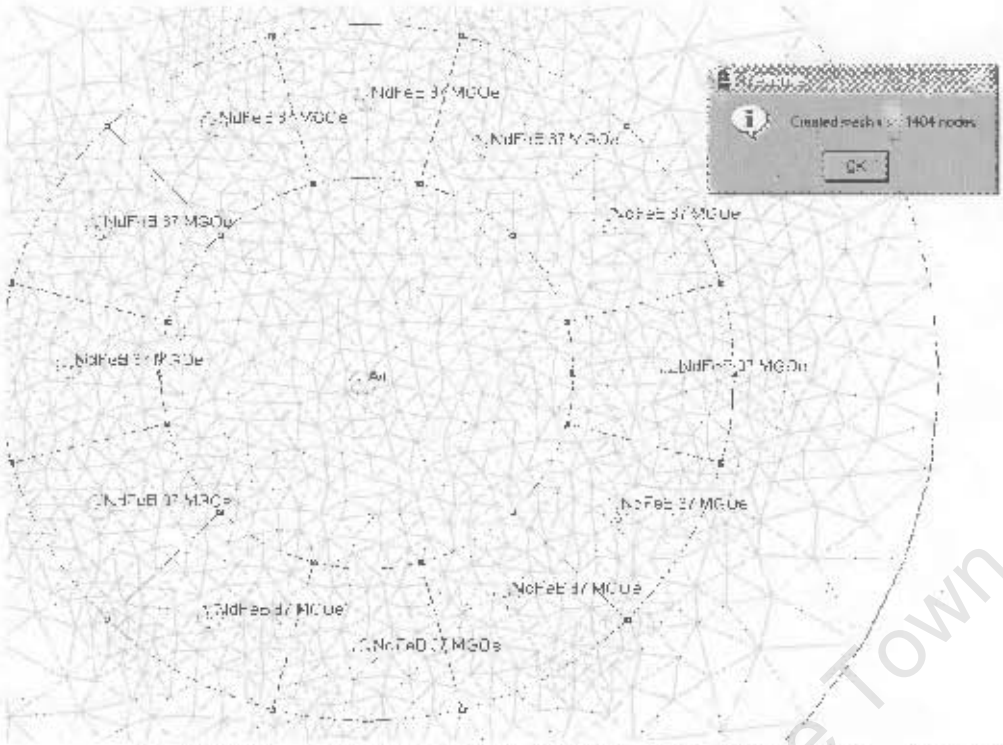

2 Segment, rectangular magnet Halbach array Dipole Model, 5 degree offset

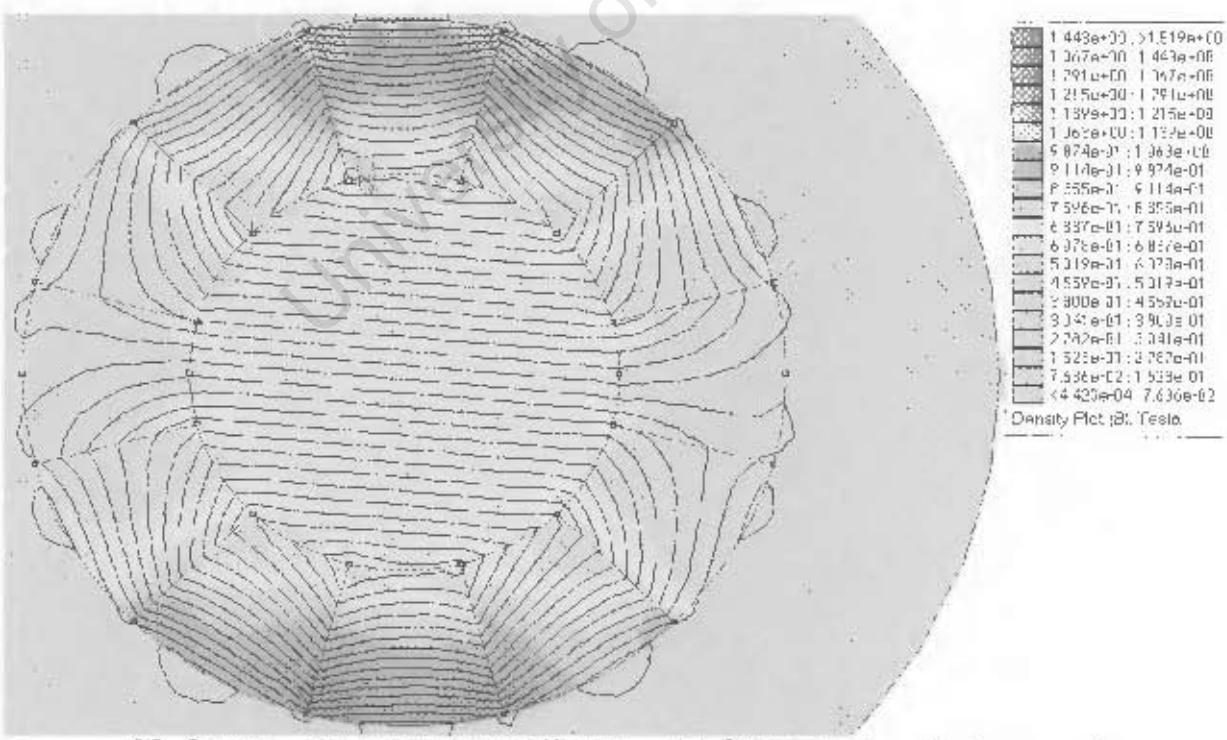

12 Segment, rectangular magnet Halbach array Dipole Result, 5 degree offset

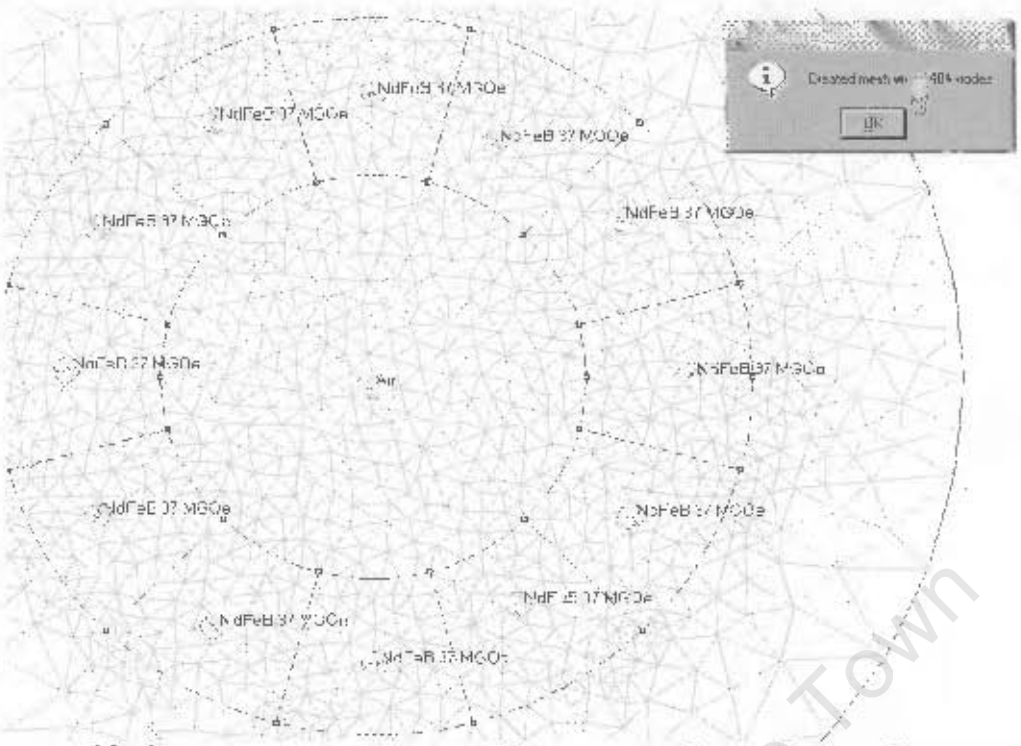

12 Segment, rectangular magnet Halbach array Dipole Model, 10 degree offset

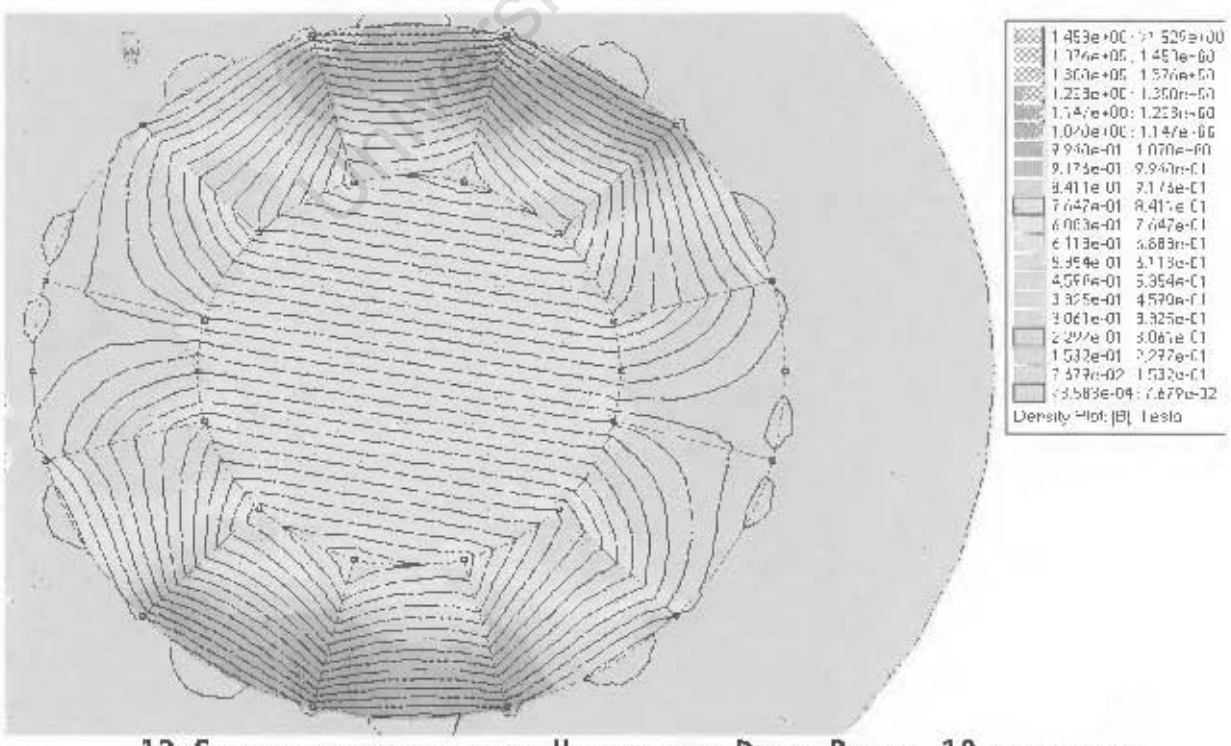

12 Segment, rectangular magnet Halbach array Dipole Result, 10 degree offset

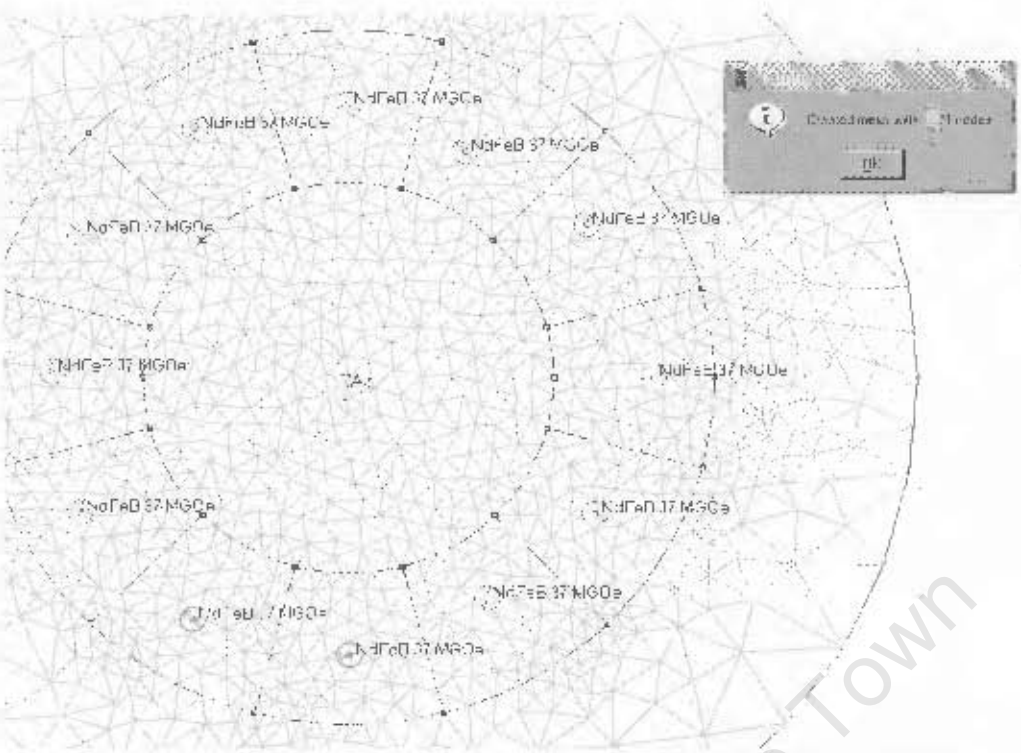

12 Segment, rectangular magnet Halbach array Dipole Model, 15 degree offset

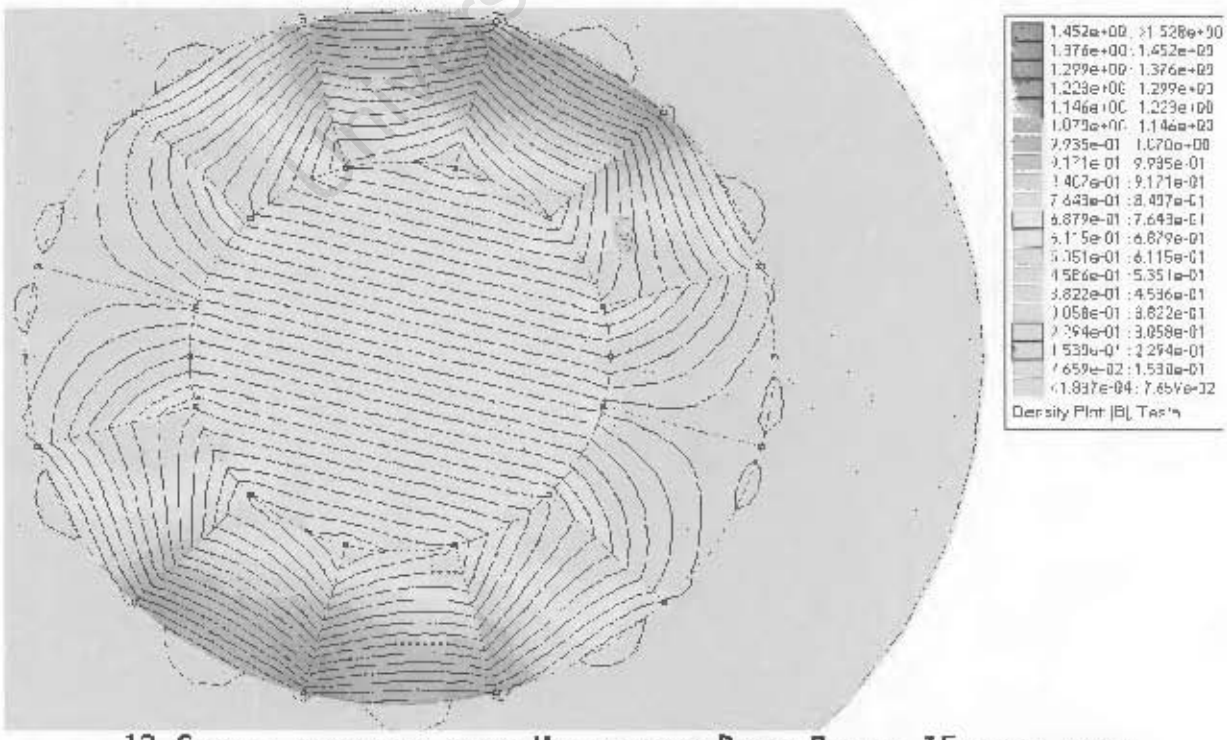

12 Segment, rectangular magnet Halbach array Dipole Result, 15 degree offset

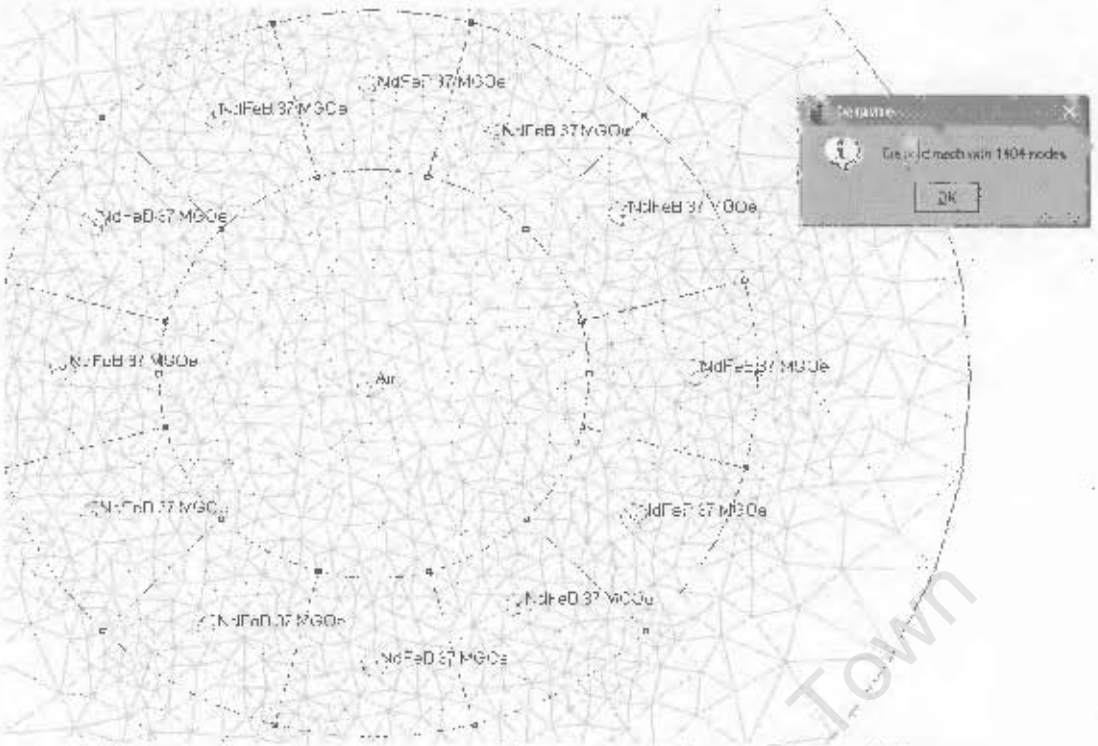

12 Segment, rectangular magnet Halbach array Dipole Model, 20 degree offset

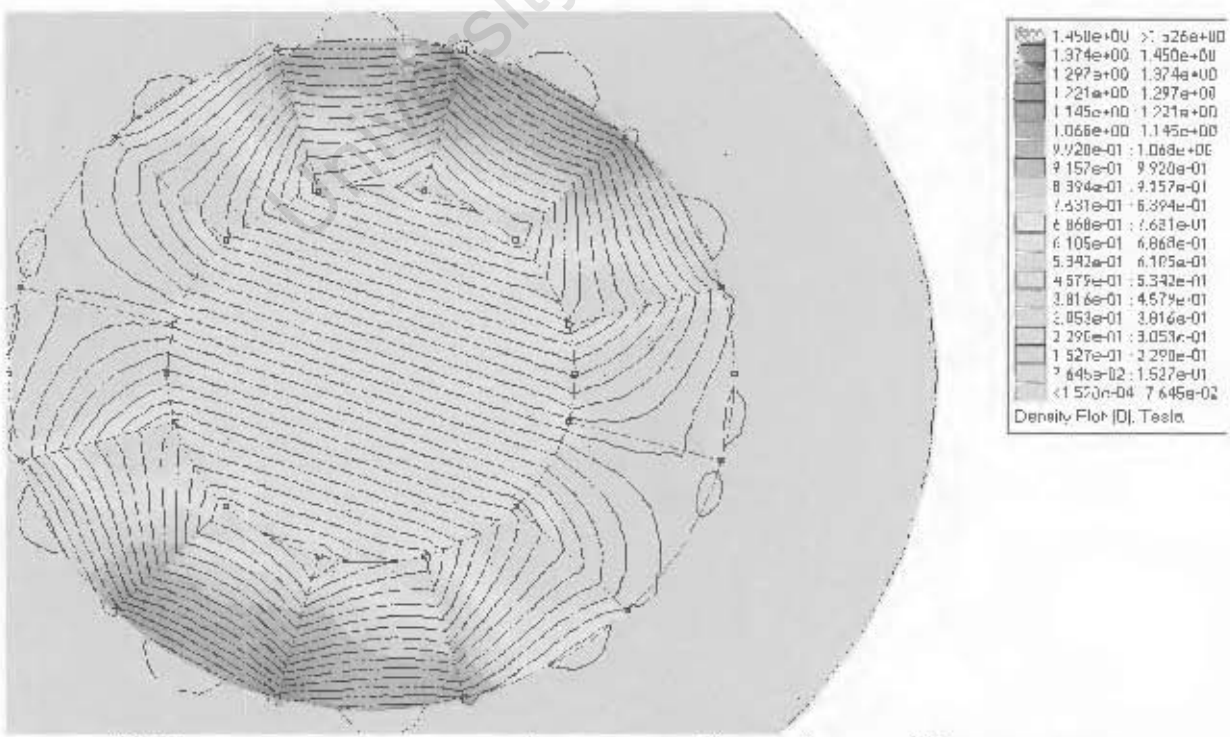

12 Segment, rectangular magnet Halbach array Dipole Result, 20 degree offset

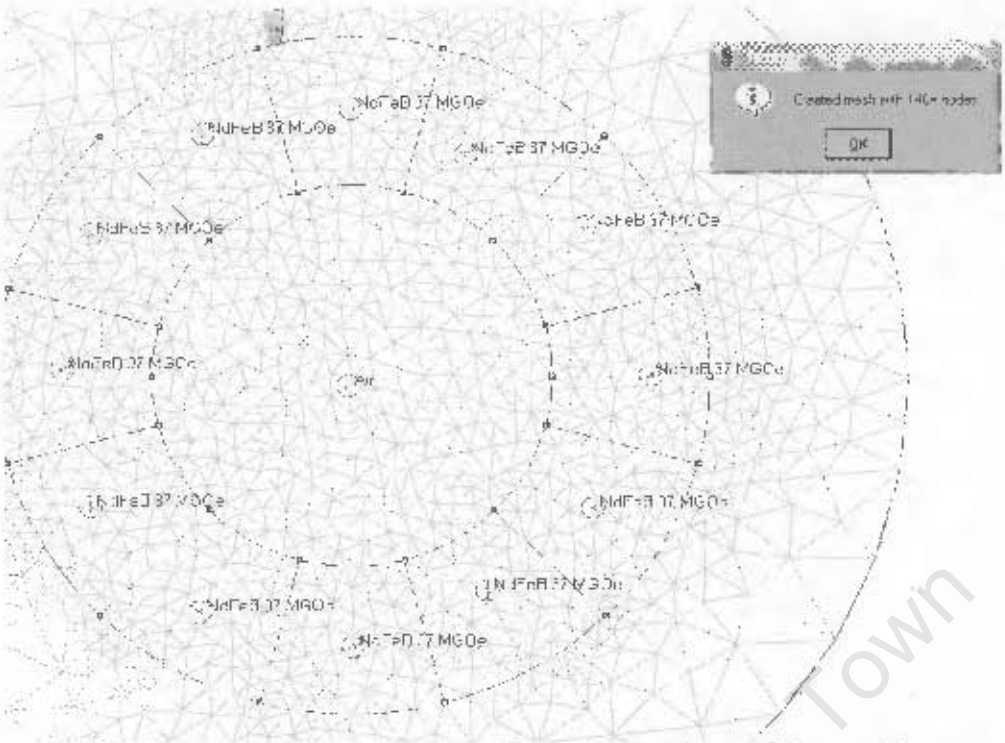

12 Segment, rectangular magnet Halbach array Dipole Model, 25 degree offset

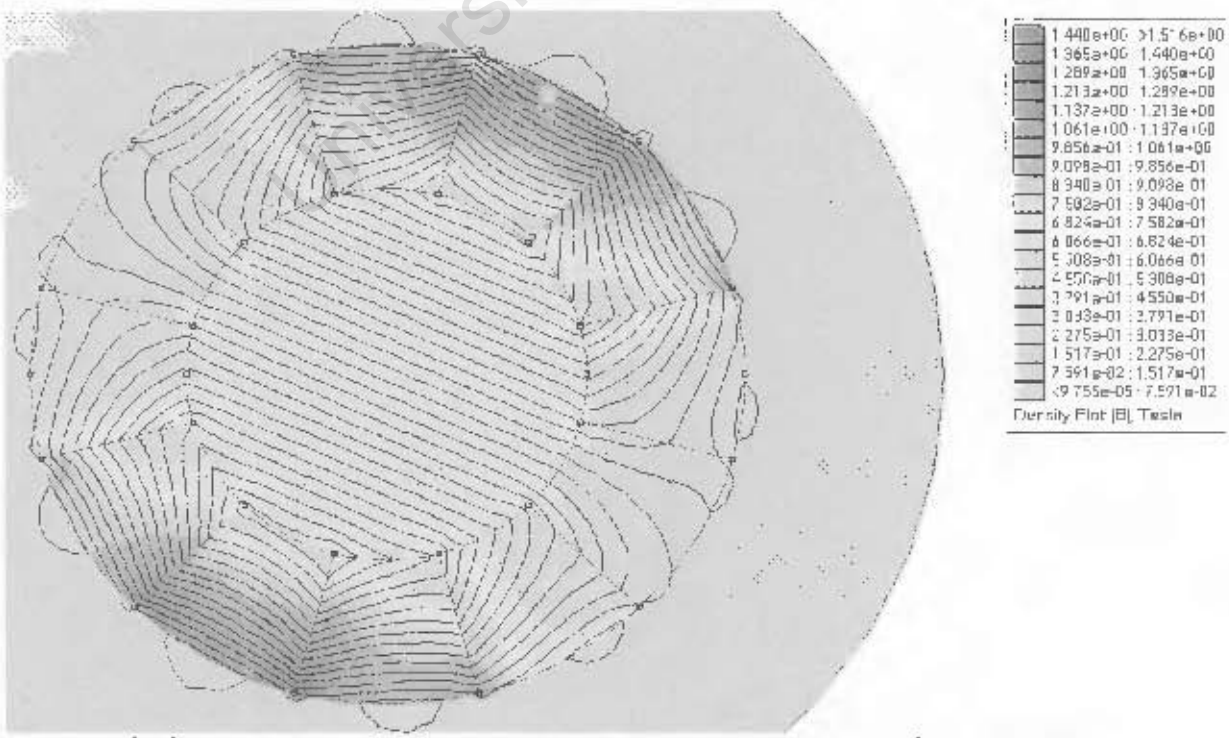

12 Segment, rectangular magnet Halbach array Dipole Result, 25 degree offset

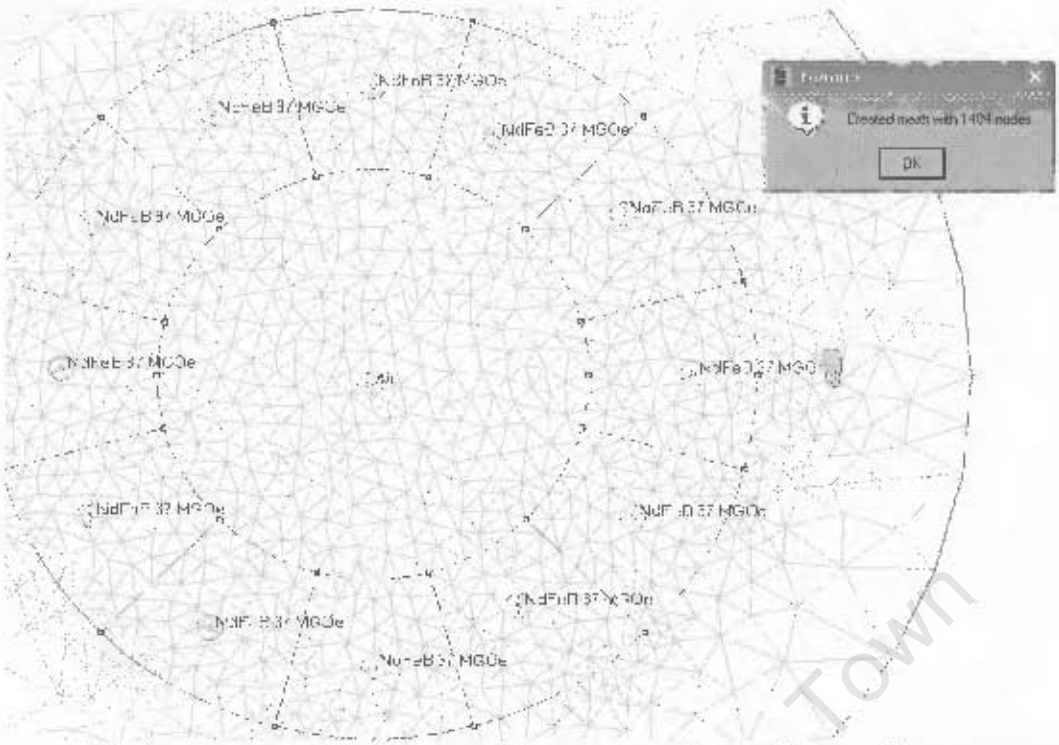

12 Segment, rectangular magnet Halbach array Dipole Model, 30 degree offset

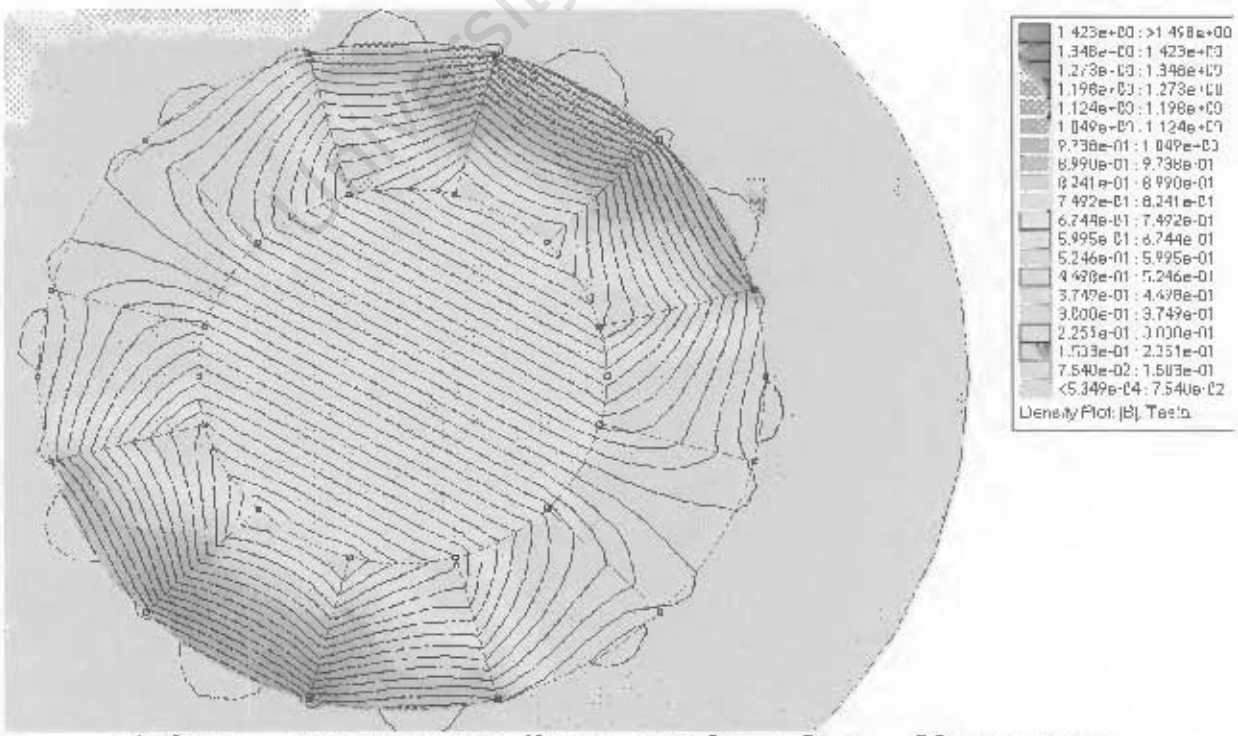

12 Segment, rectangular magnet Halbach array Dipole Result, 30 degree offset

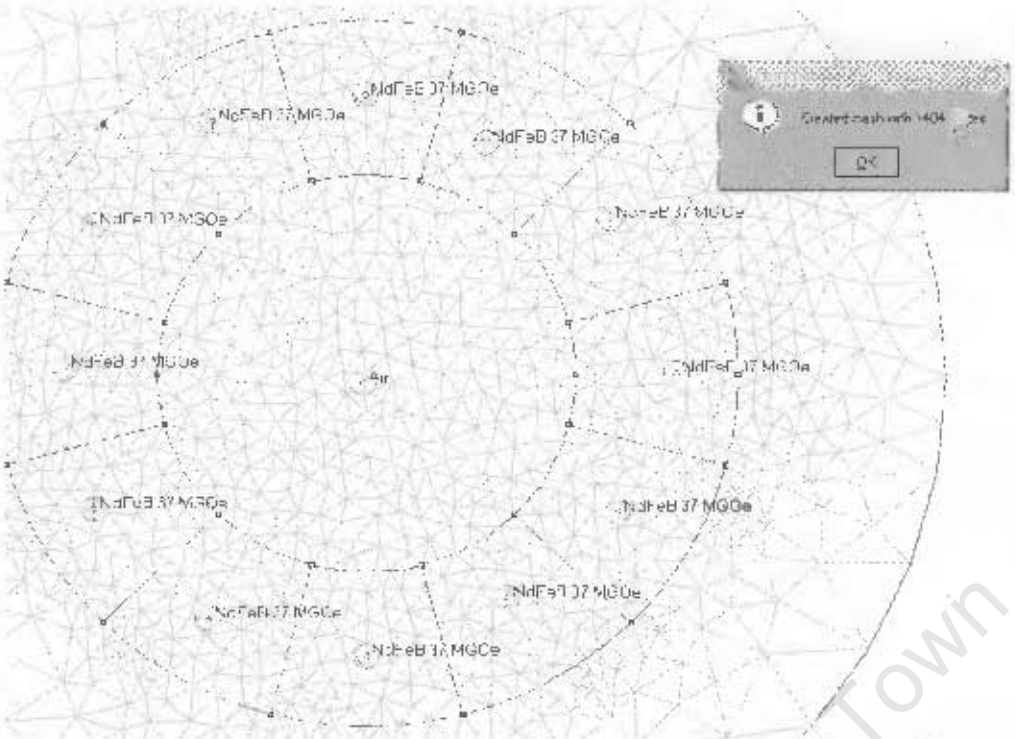

12 Segment, rectangular magnet Halbach array Dipole Model, 35 degree offset

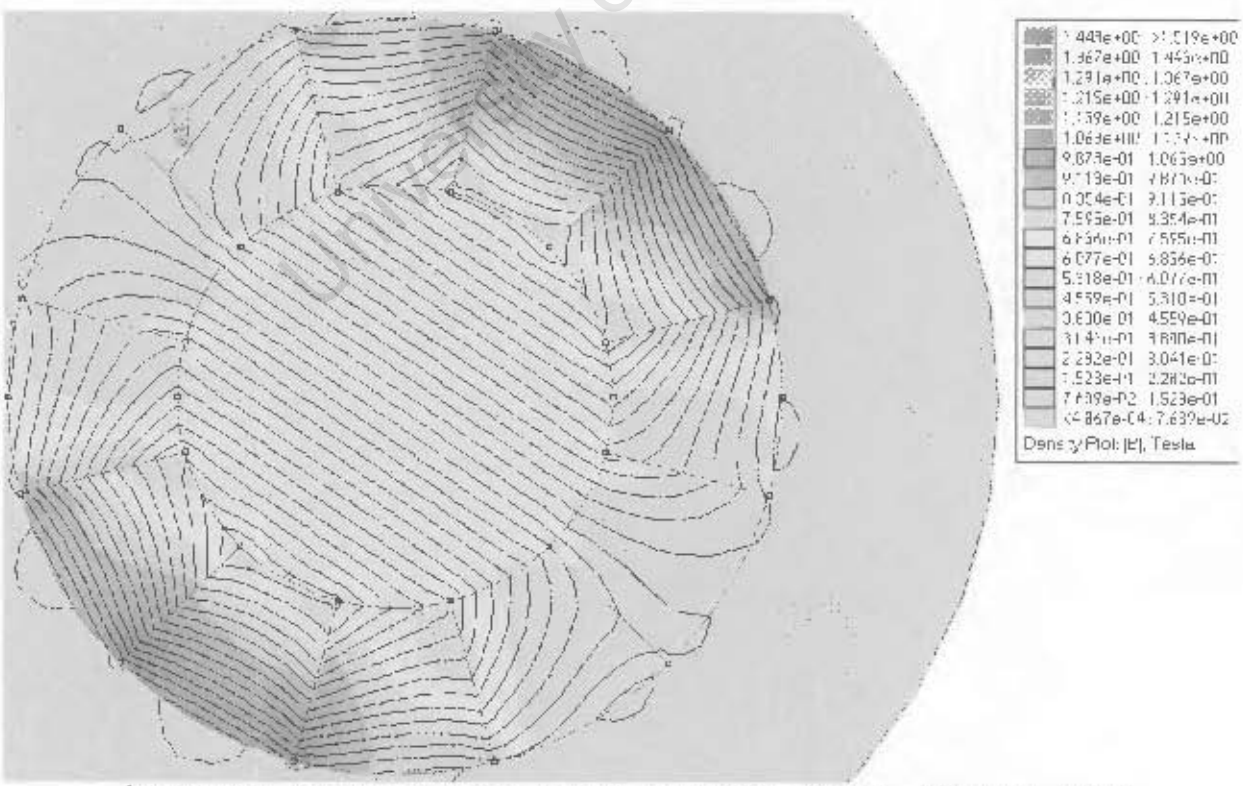

12 Segment, rectangular magnet Halbach array Dipole Result, 35 degree offset

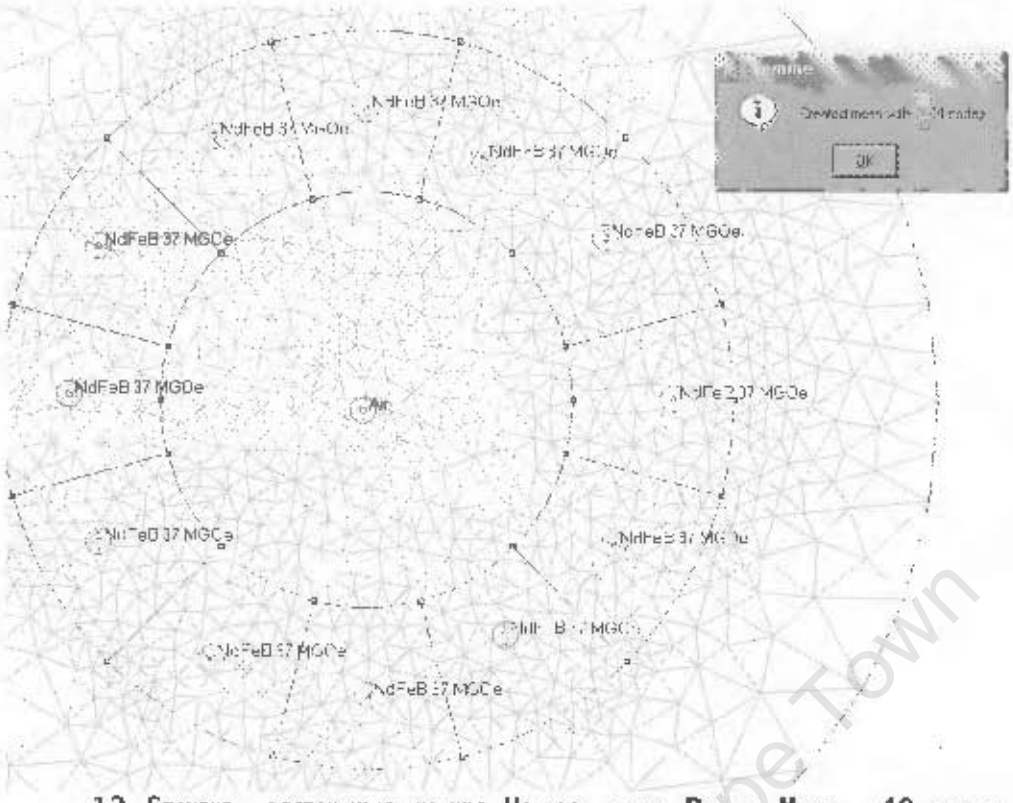

12 Segment, rectangular magnet Halbach array Dipole Model, 40 degree offset

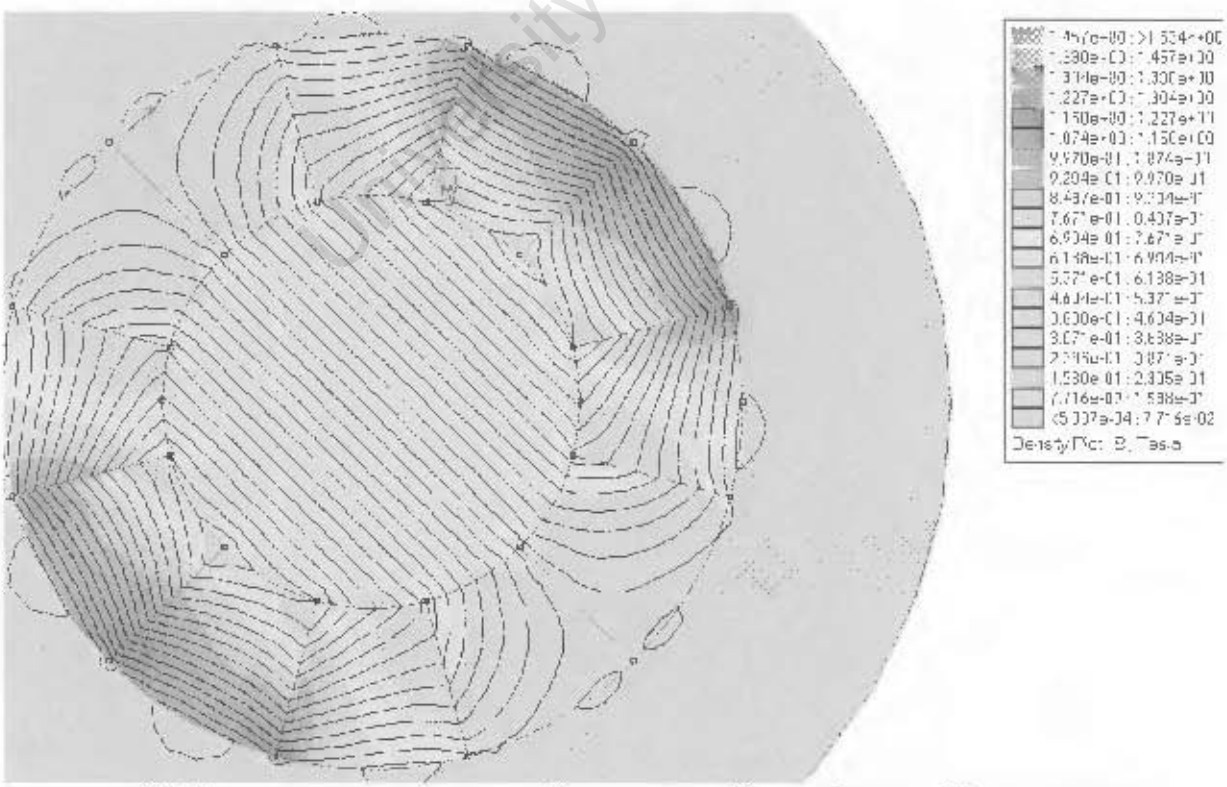

12 Segment, rectangular magnet Halbach array Dipole Result, 40 degree offset

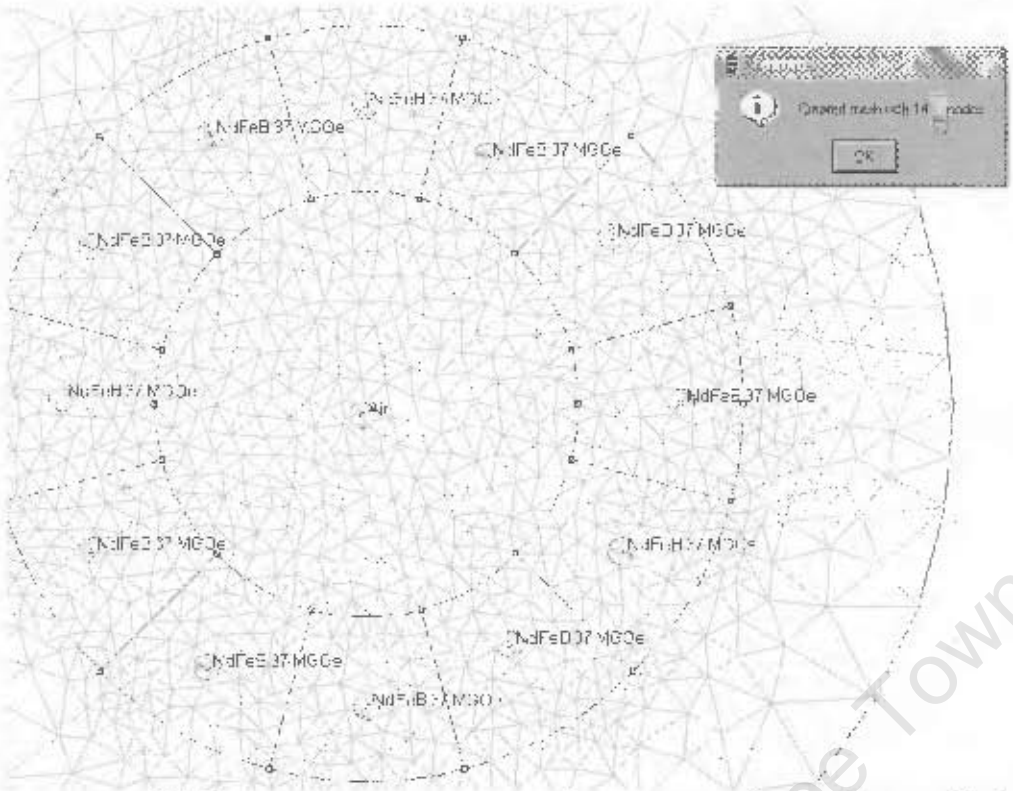

12 Segment, rectangular magnet Halbach array Dipole Model, 45 Degree offset

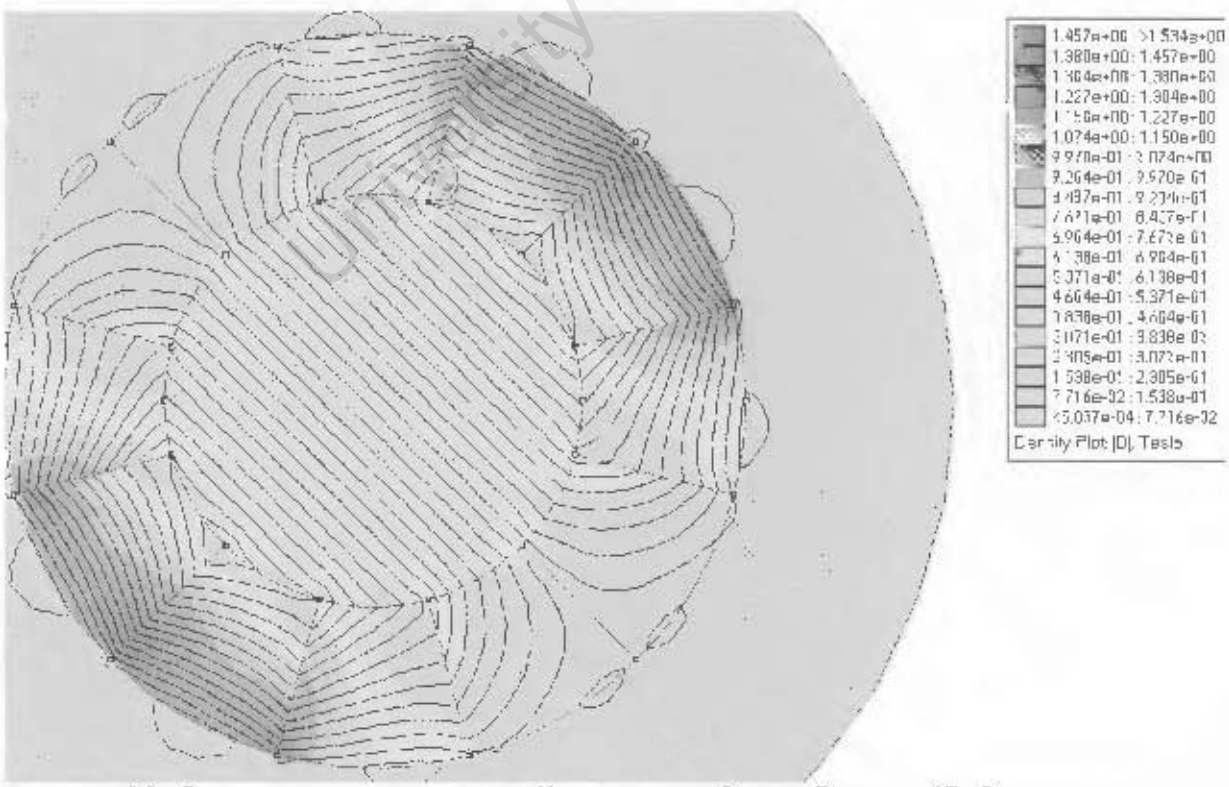

12 Segment, rectangular magnet Halbach array Dipole Result, 45 Degree offset

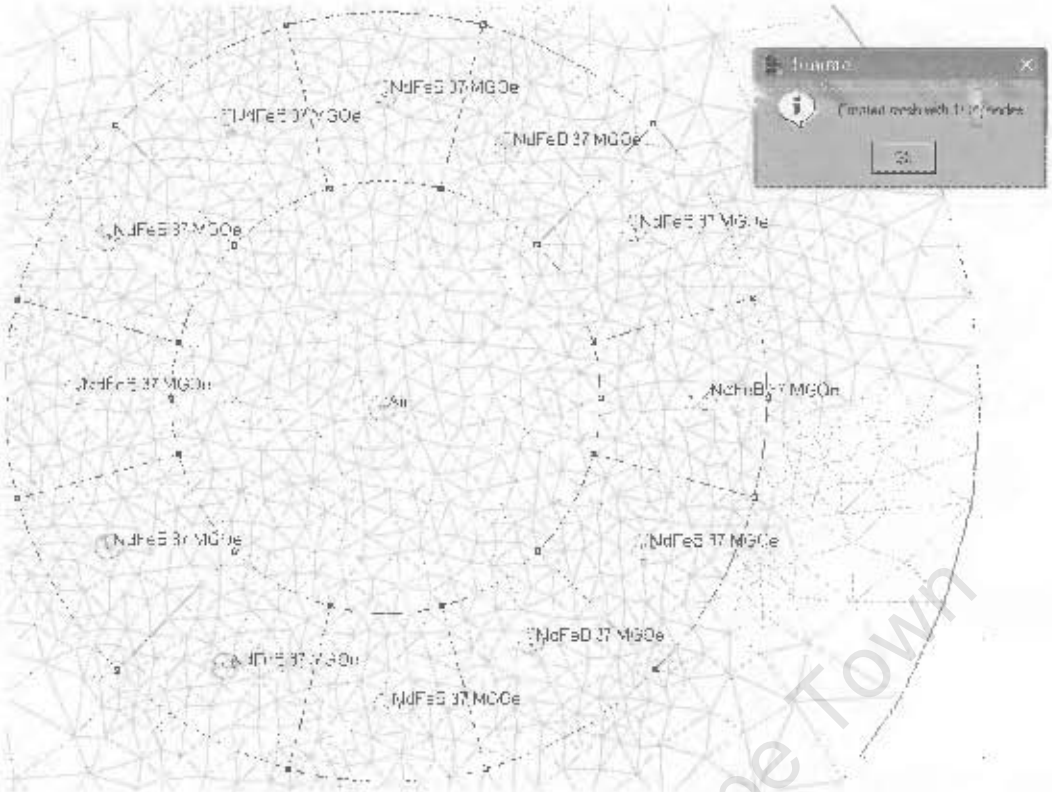

12 Segment, rectangular magnet Halbach array Dipole Model, 50 Degree offset

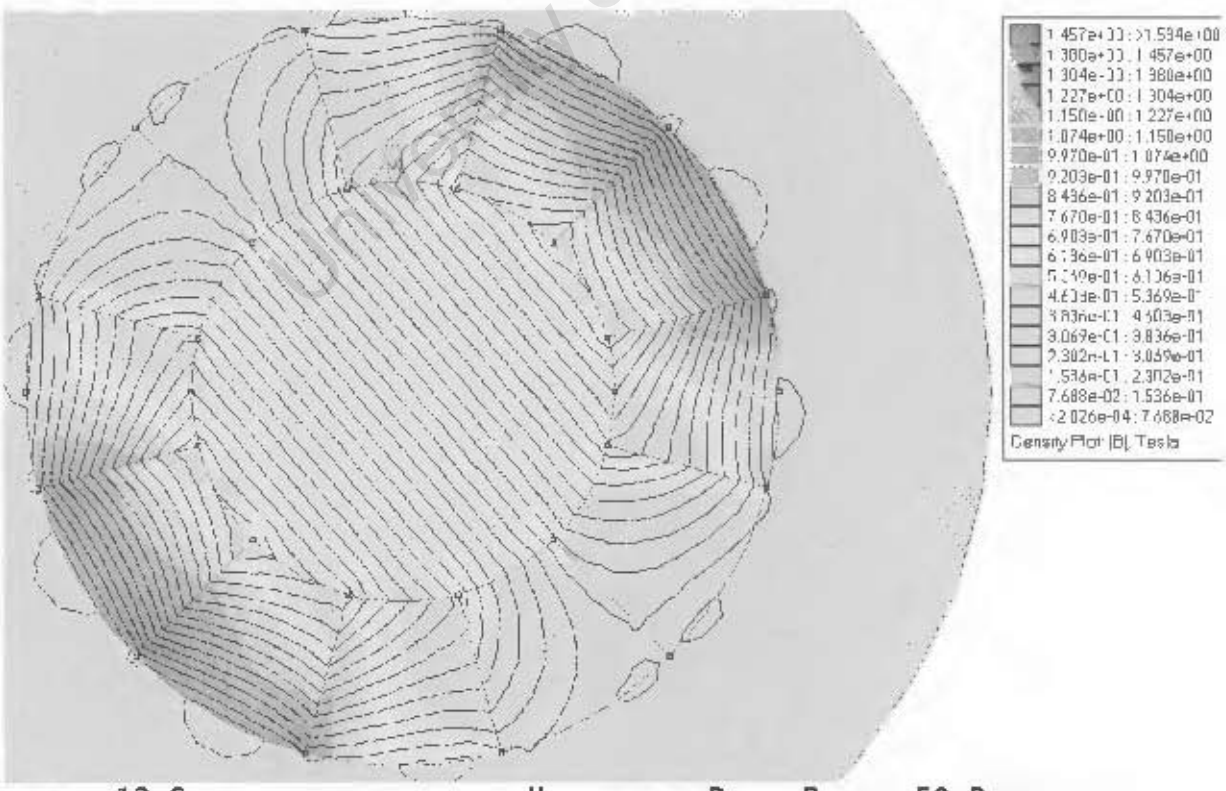

12 Segment, rectangular magnet Halbach array Dipole Result, 50 Degree offset

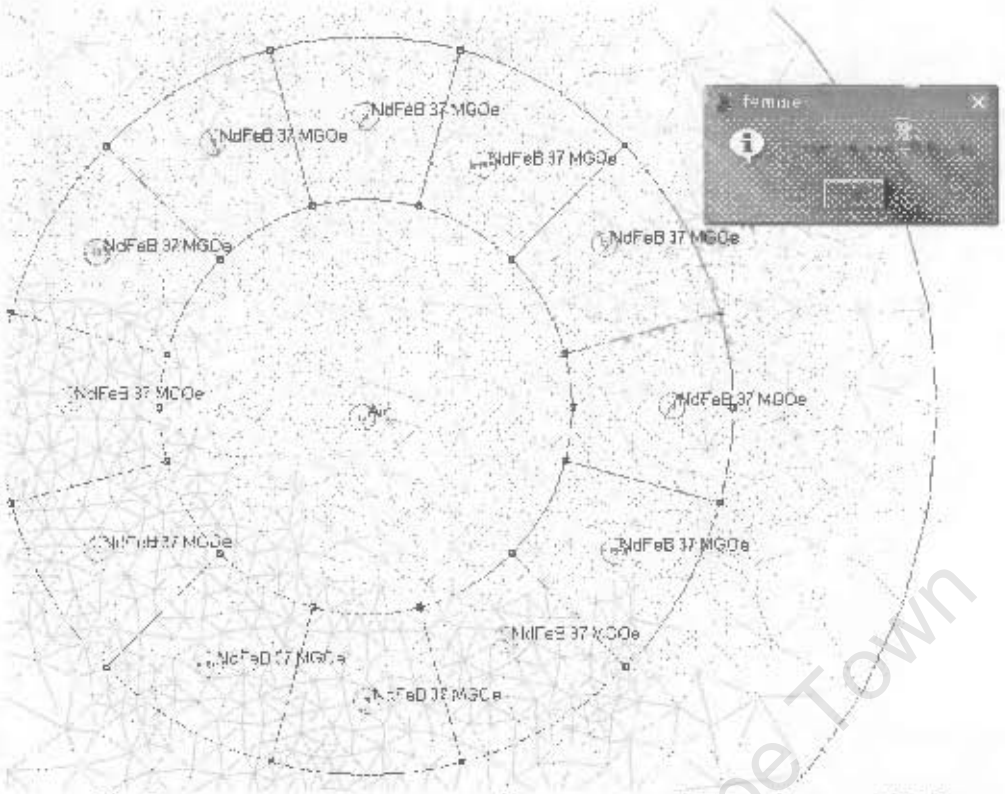

12 Segment, rectangular magnet Halbach array Dipole Model, 55 Degree offset

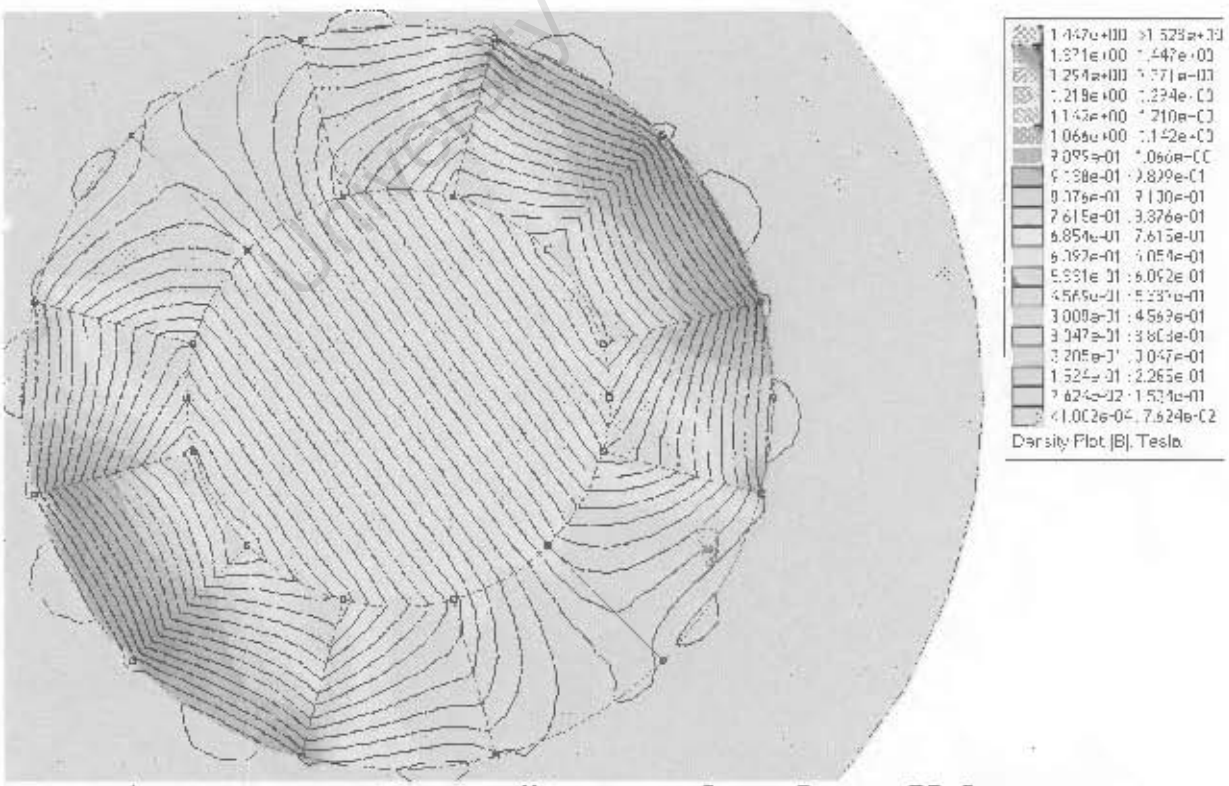

12 Segment, rectangular magnet Halbach array Dipole Result, 55 Degree offset

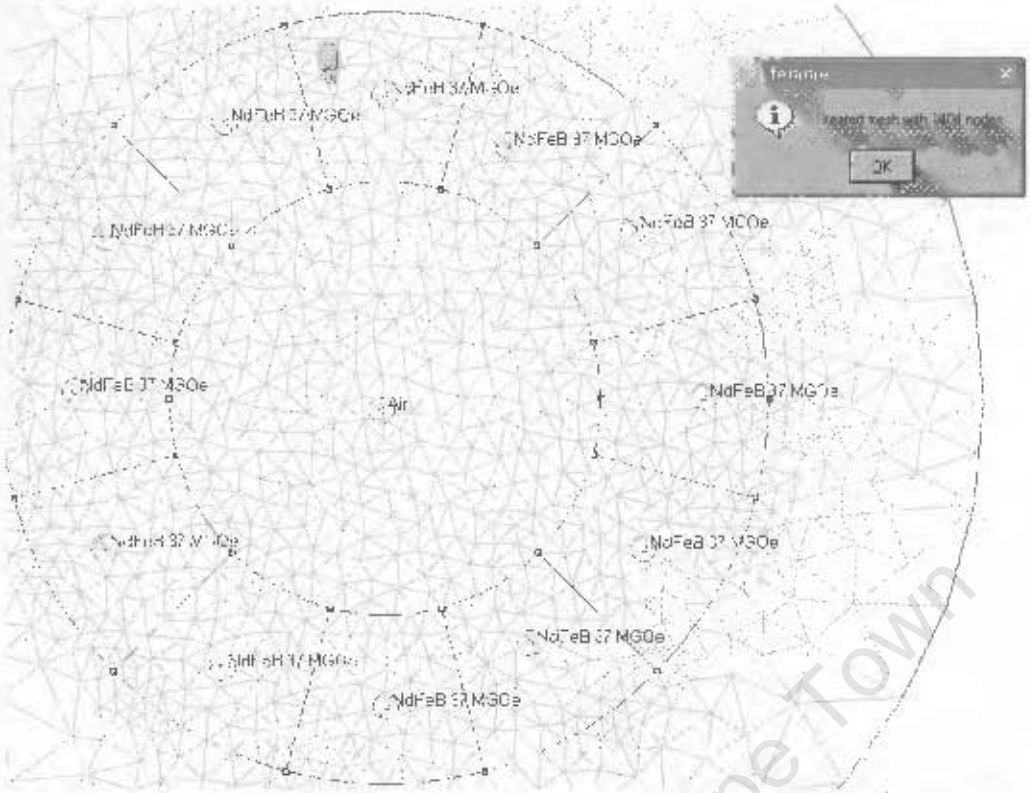

12 Segment, rectangular magnet Halbach array Dipole Model, 60 Degree offset

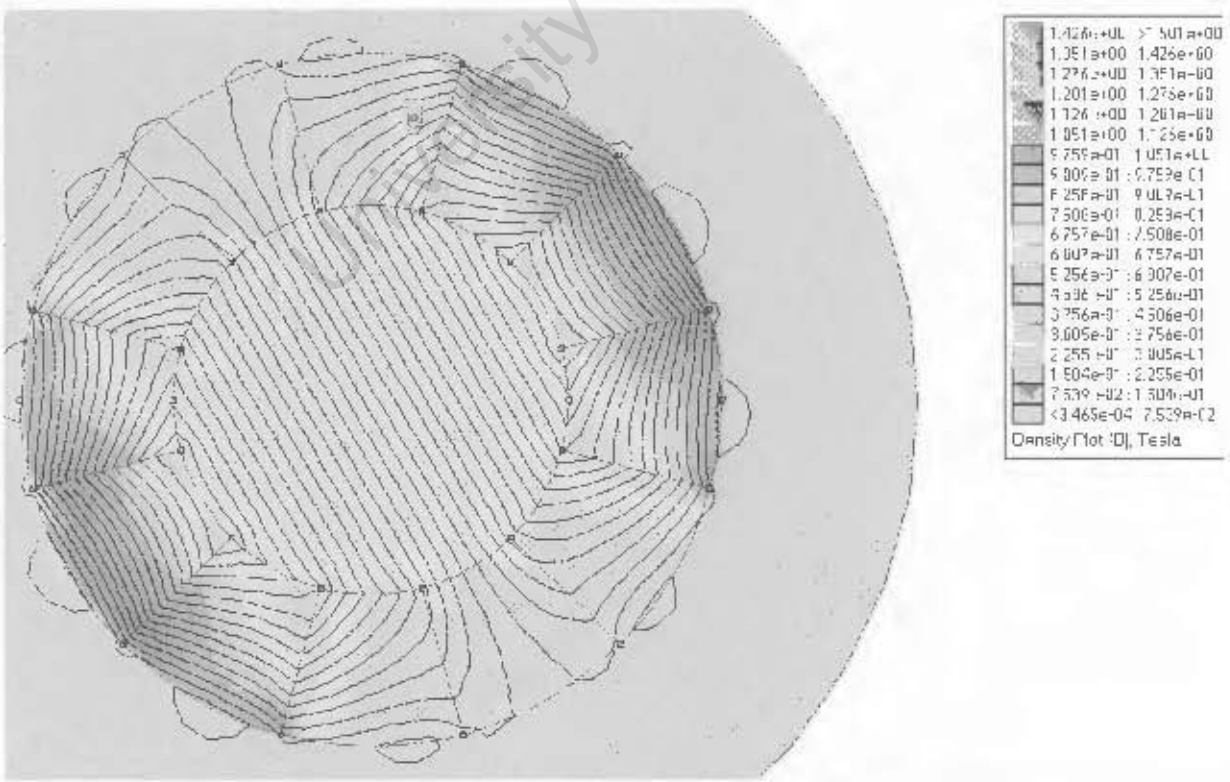

12 Segment, rectangular magnet Halbach array Dipole Result, 60 Degree offset

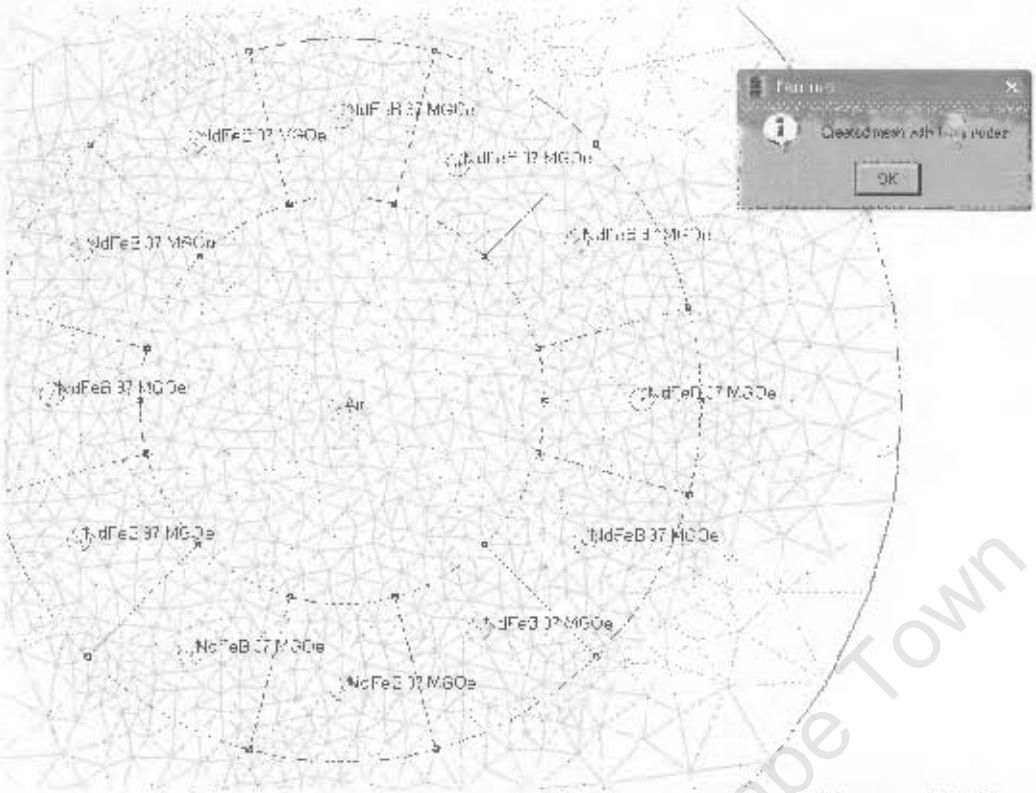

12 Segment, rectangular magnet Halbach array Dipole Model, 65 Degree offset

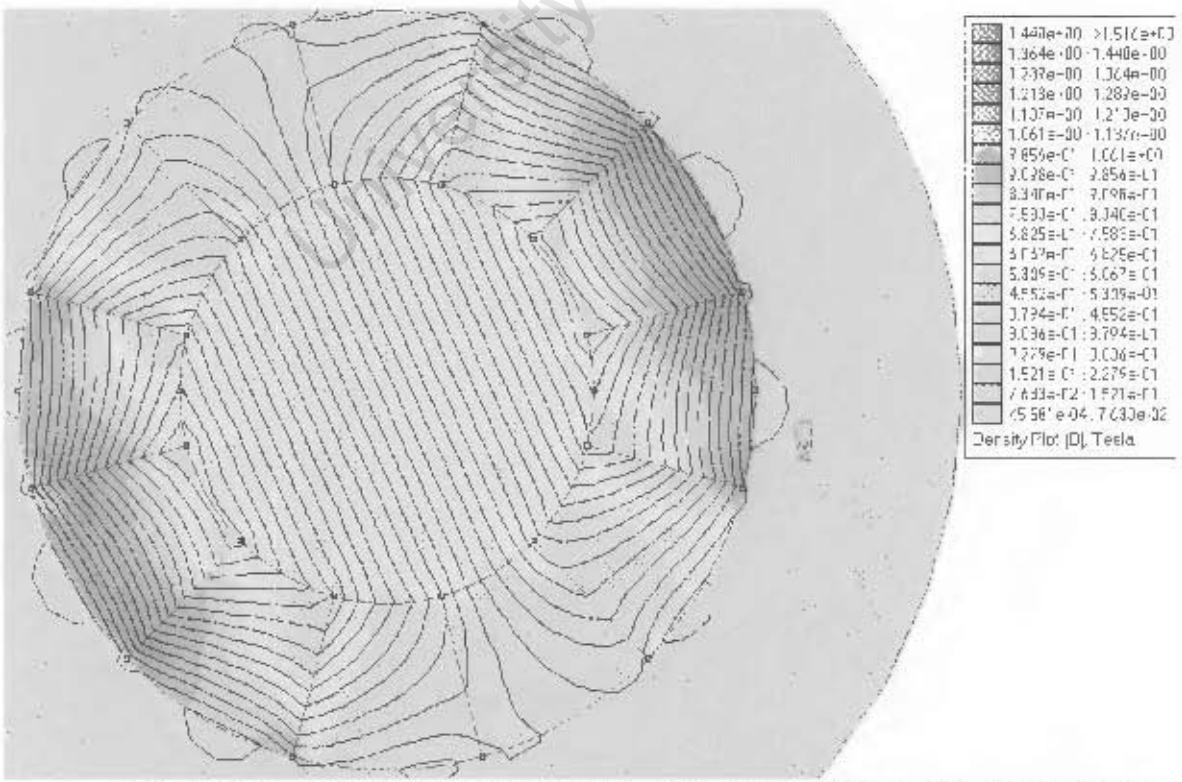

12 Segment, rectangular magnet Halbach array Dipole Result, 65 Degree offset

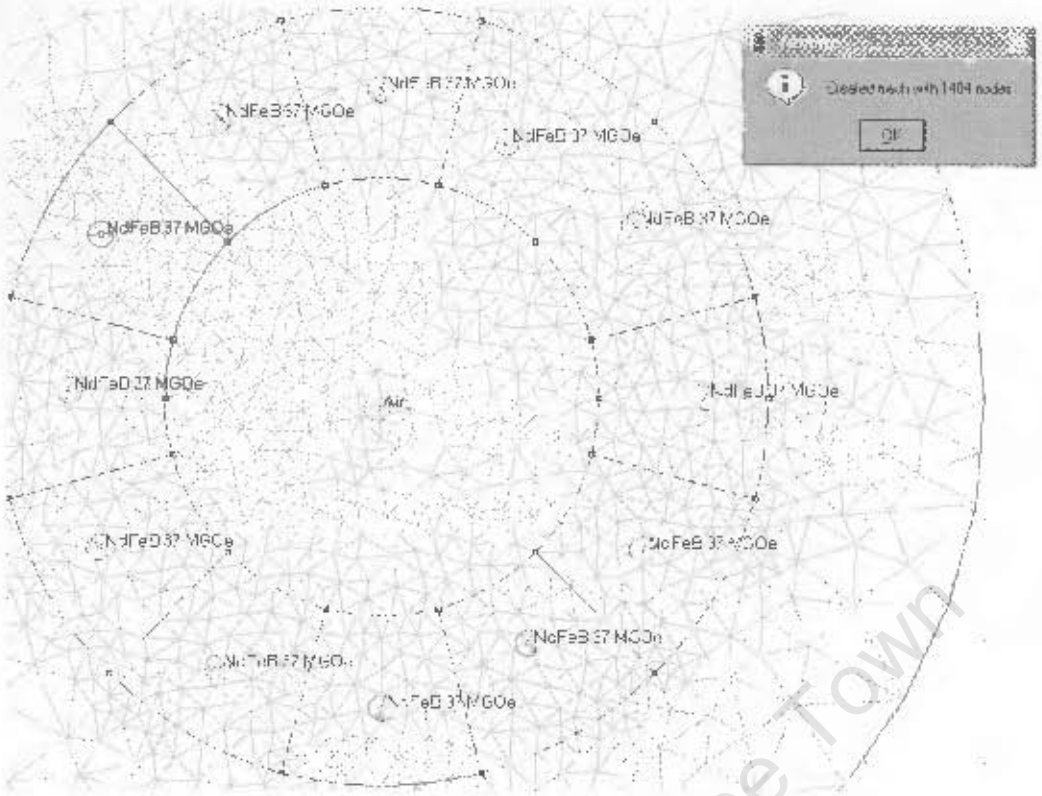

12 Segment, rectangular magnet Halbach array Dipole Model, 70 Degree offset

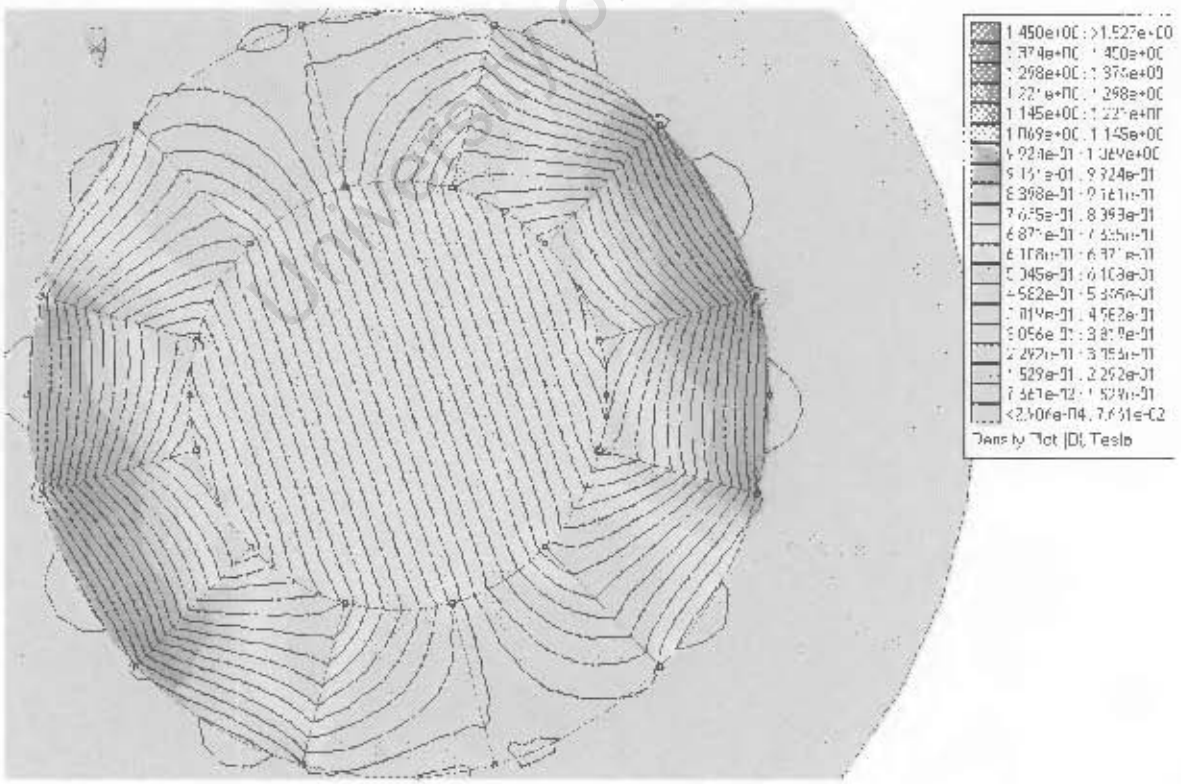

12 Segment, rectangular magnet Halbach array Dipole Result, 70 Degree offset

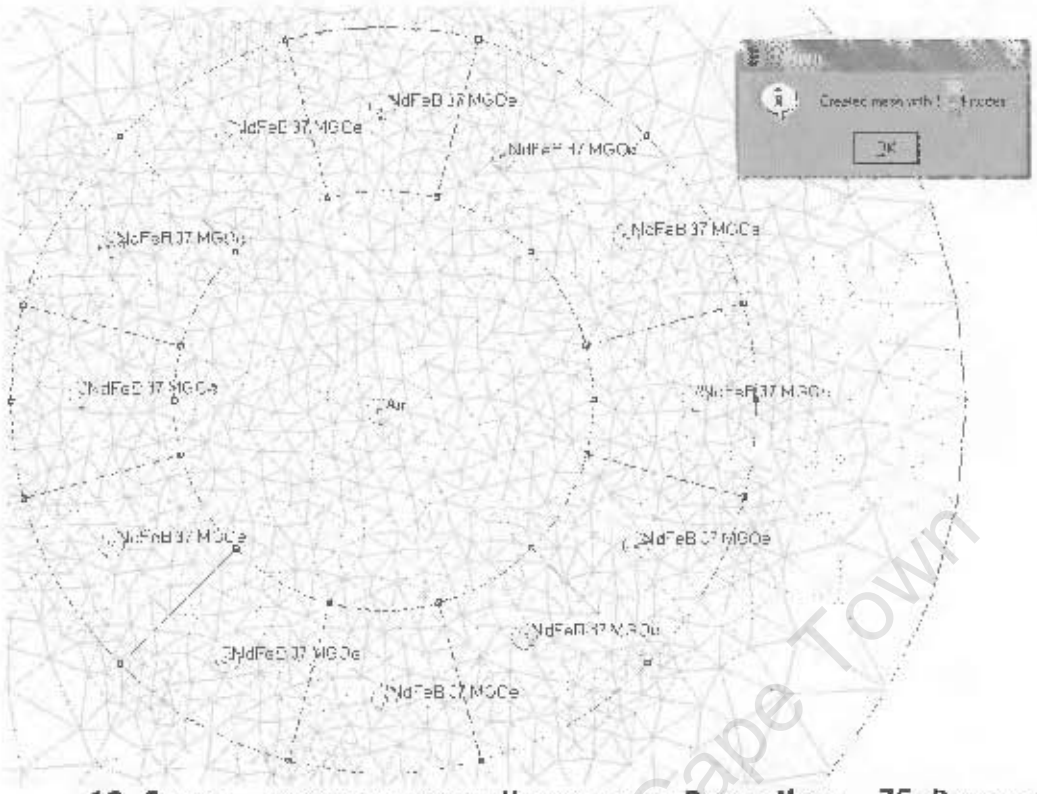

12 Segment, rectangular magnet Halbach array Dipole Model, 75 Degree offset

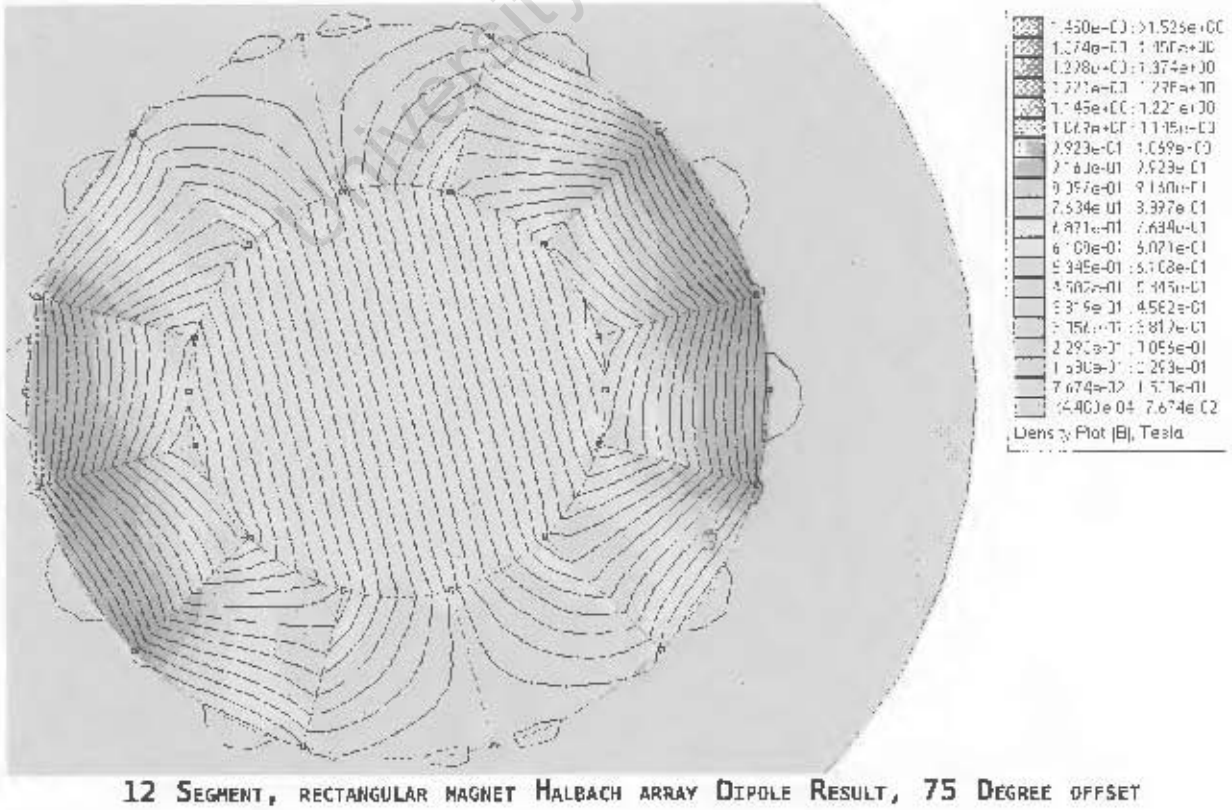

12 Segment, rectangular magnet Halbach array Dipole Result, 75 Degree offset

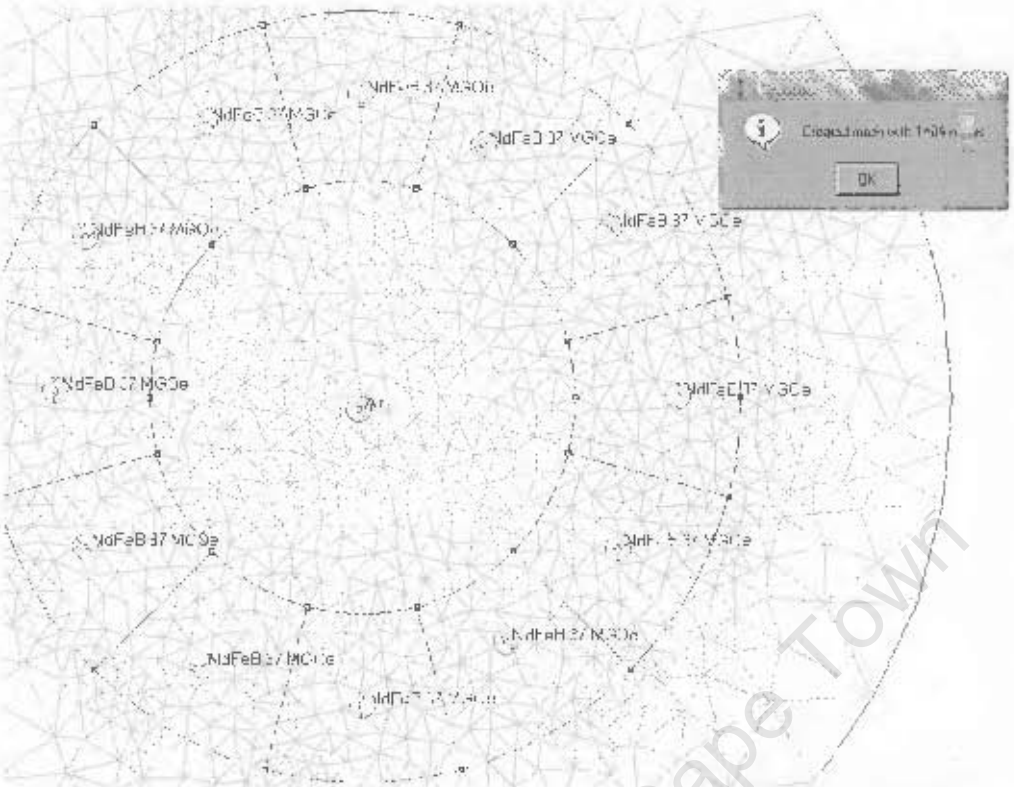

12 Segment, rectangular magnet Halbach array Dipole Model, 80 Degree offset

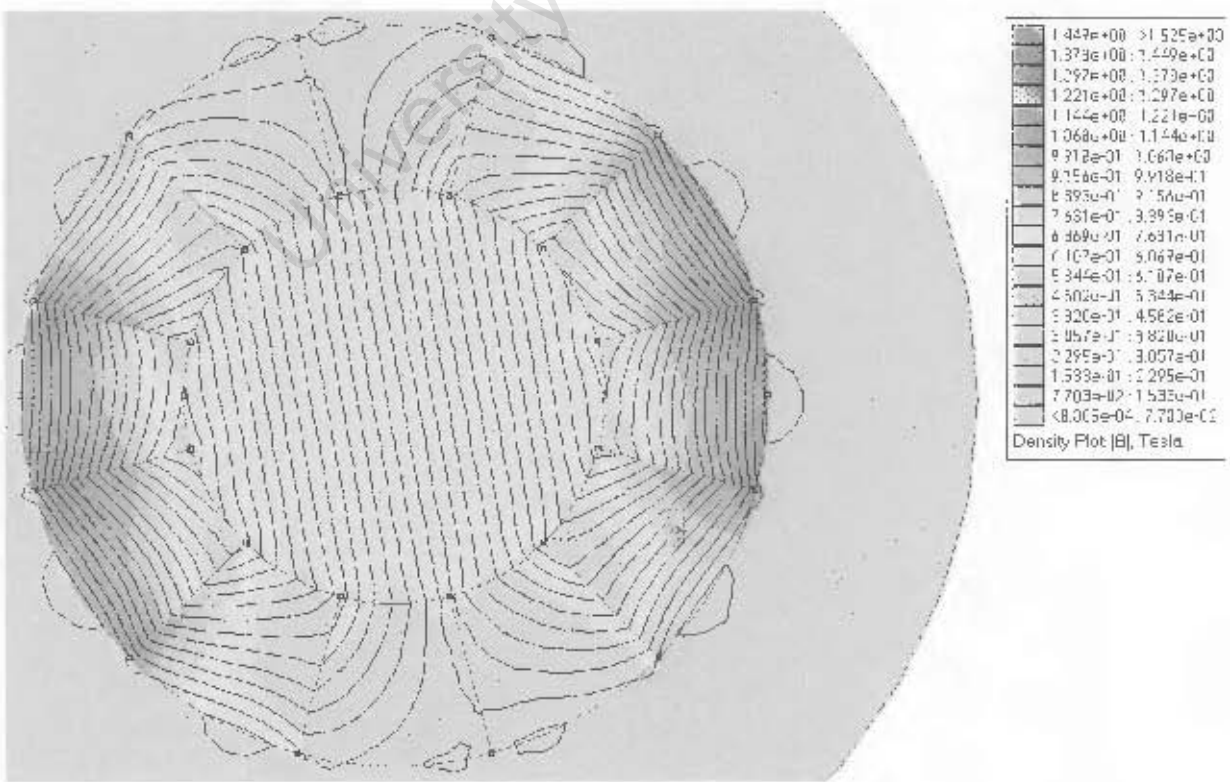

12 Segment, rectangular magnet Halbach array Dipole Result, 80 Degree offset

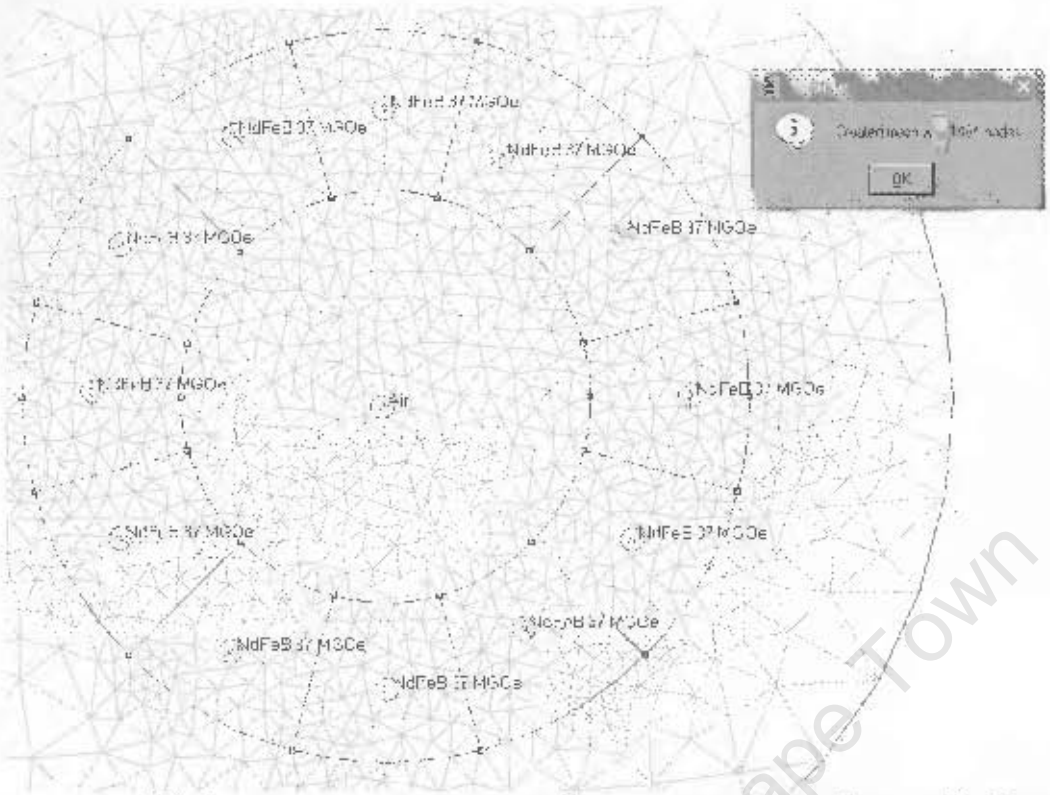

12 Segment, rectangular magnet Halbach array Dipole Model, 90 Degree offset

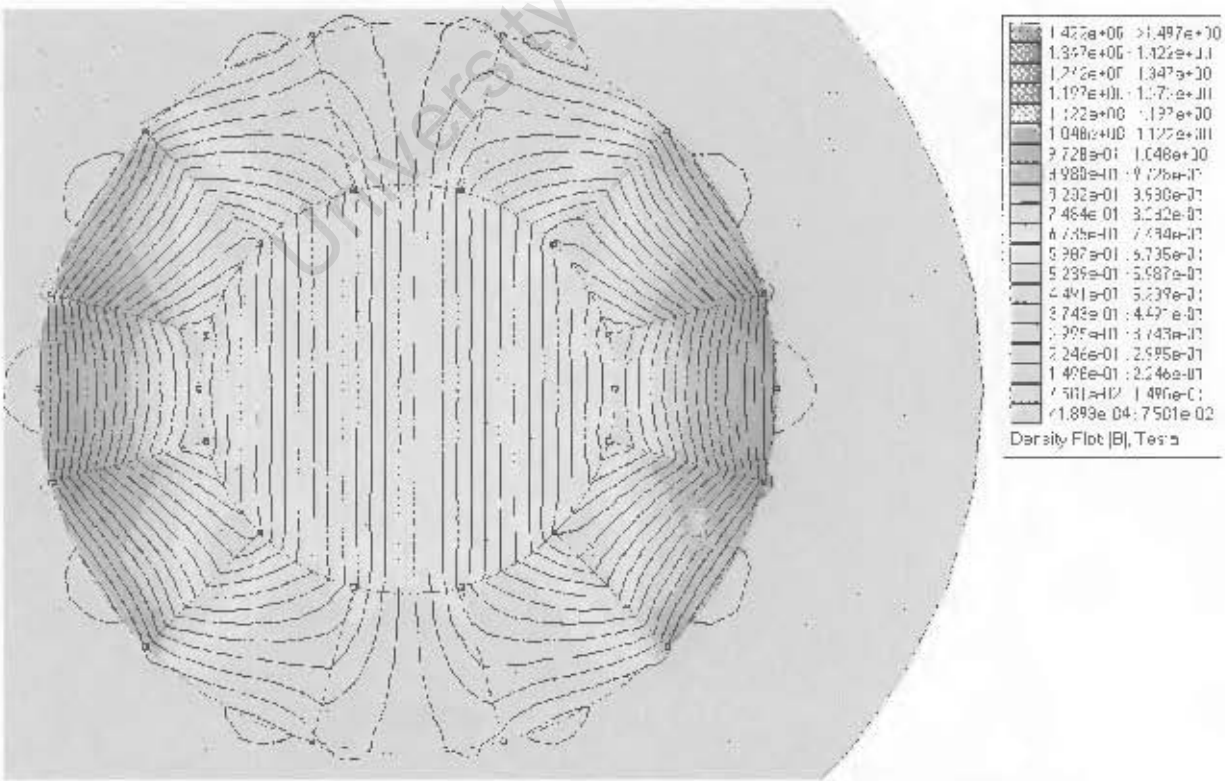

12 Segment, rectangular magnet Halbach array Dipole Result, 90 Degree offset

Note: An offset for 85 degrees was not tested as the tendency was

already apparent at this point in time

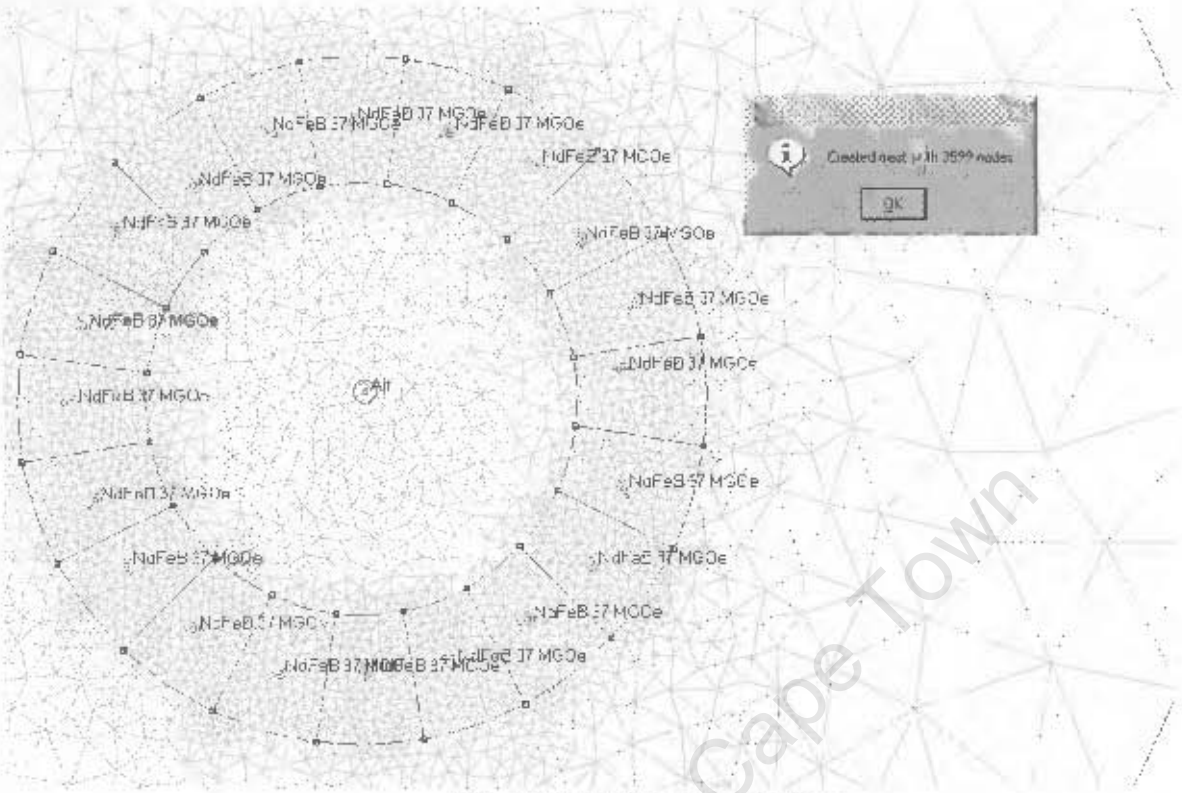

20 Segment Quadrupole Model

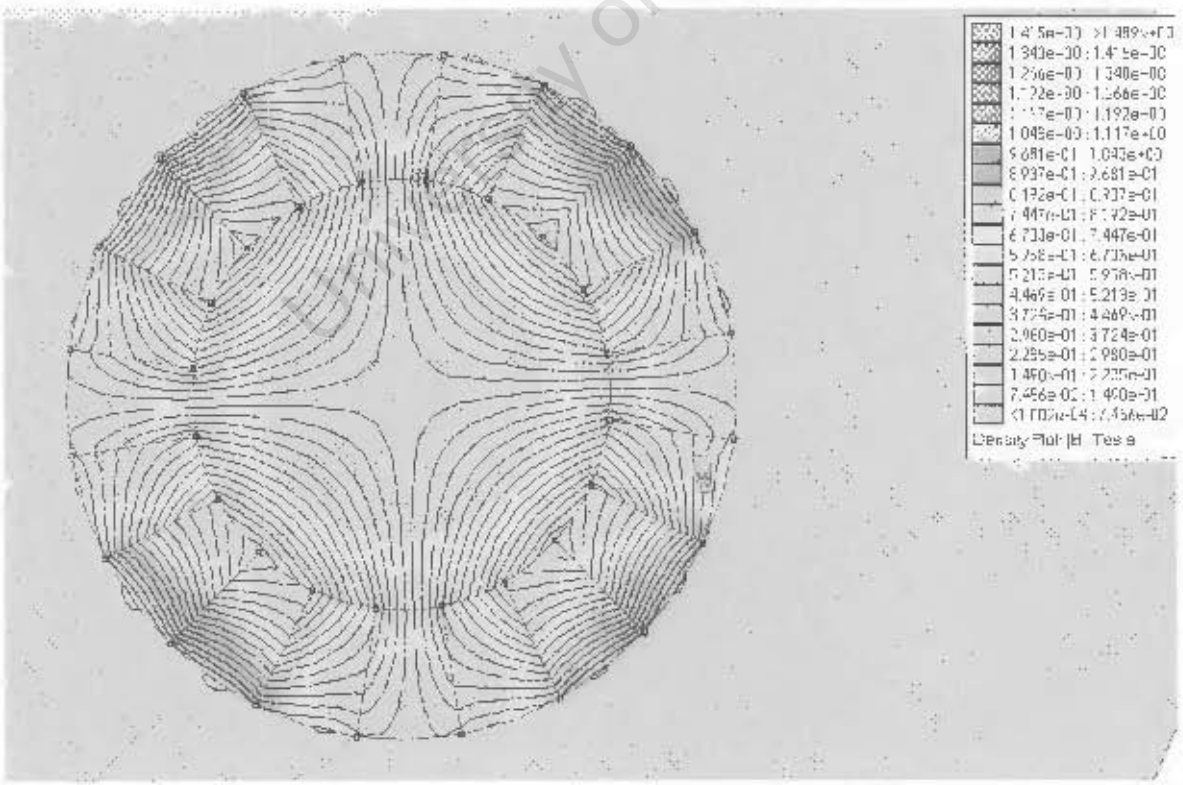

20 Segment Quadrupole Result

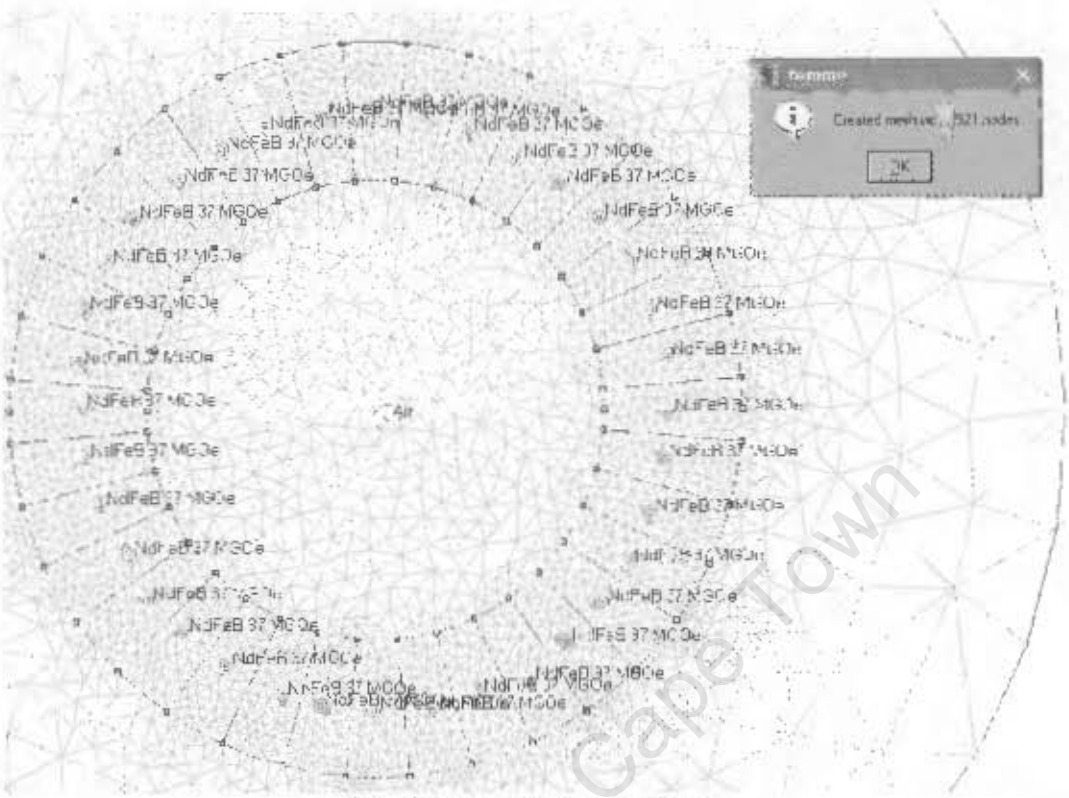

30 Segment Hexapole Model

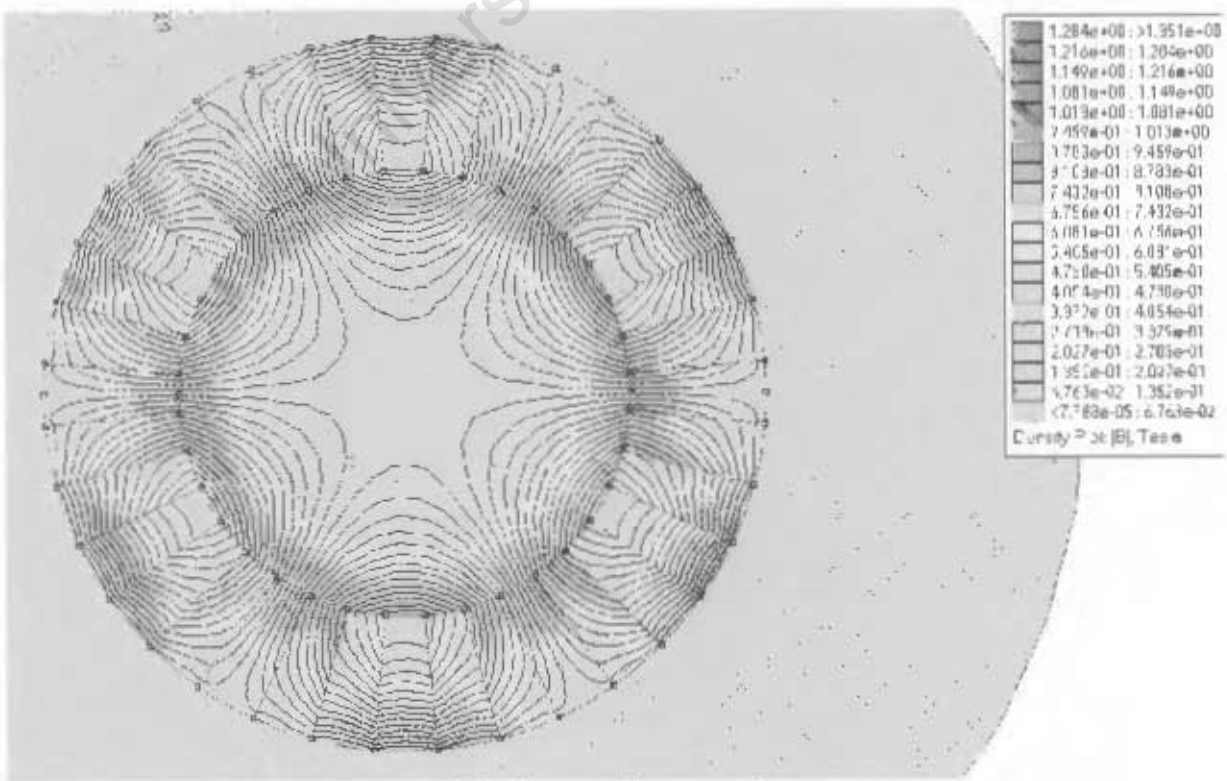

30 Segment Hexapole Result

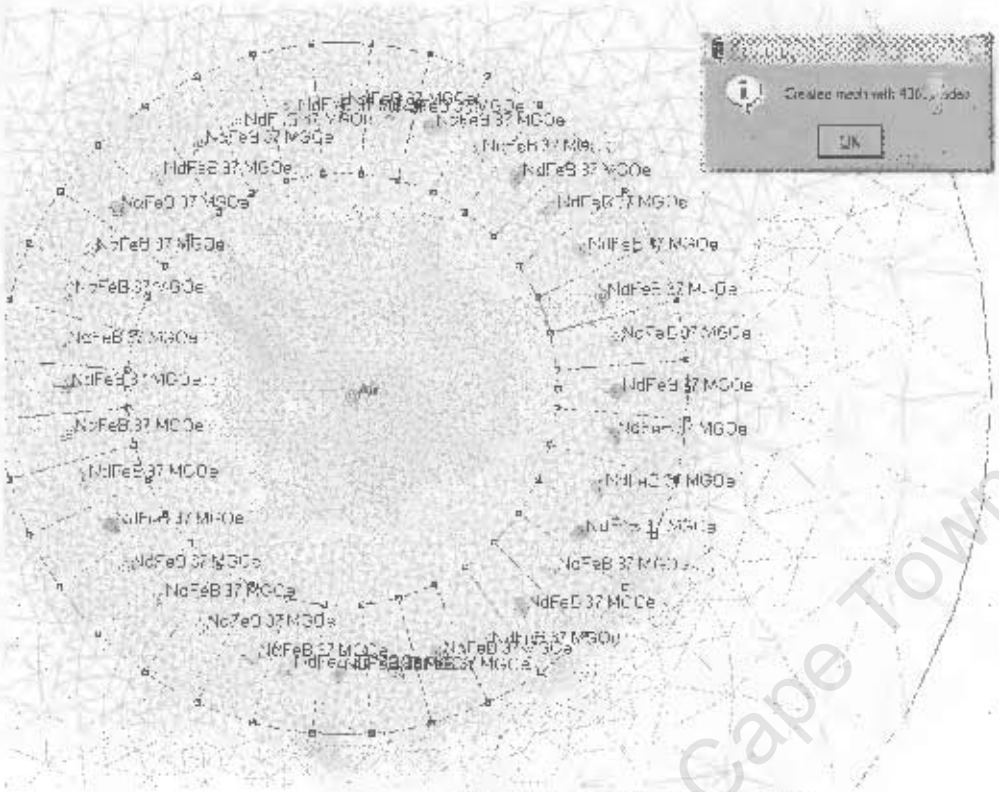

36 Segment Octapole Model

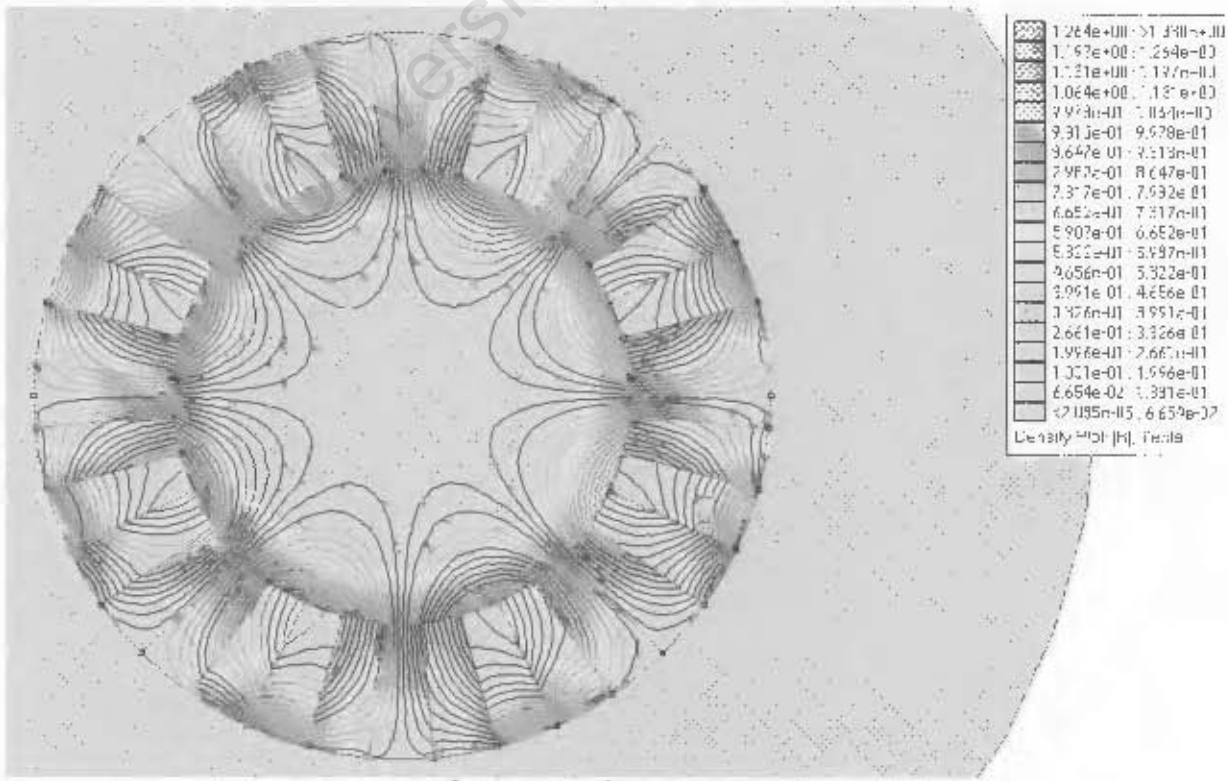

36 Segment Octapole Result

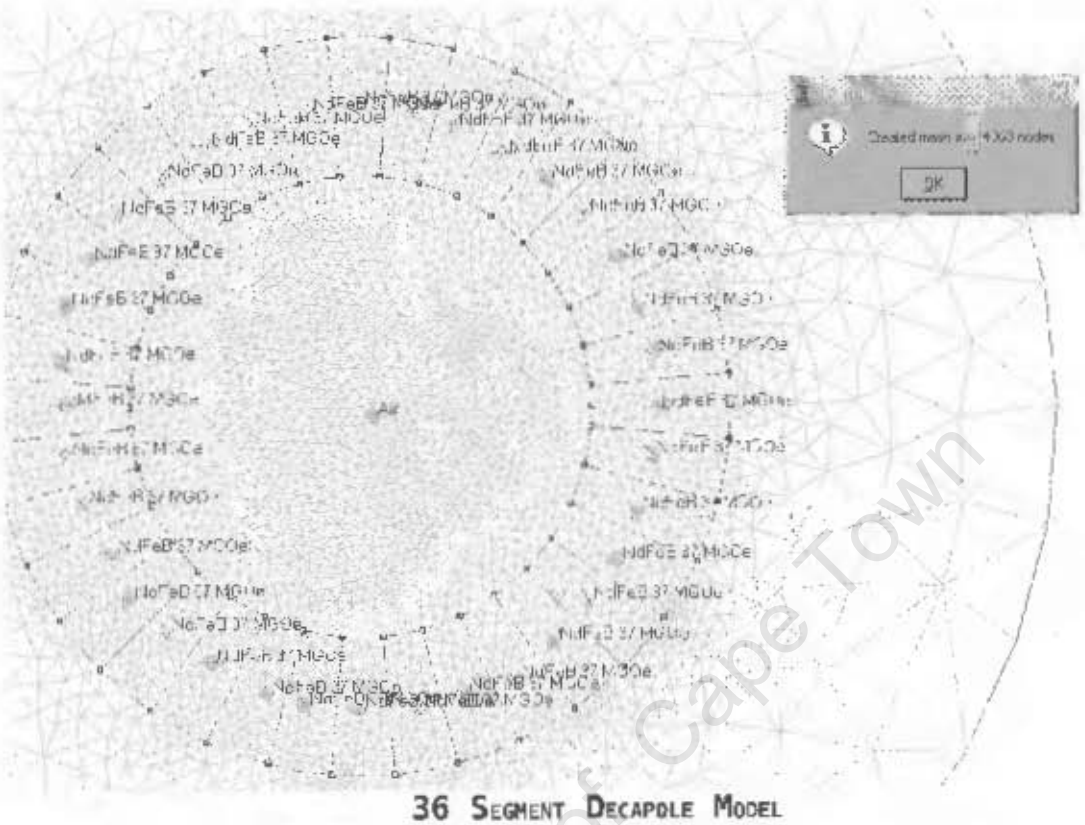

36 Segment Decapole Model

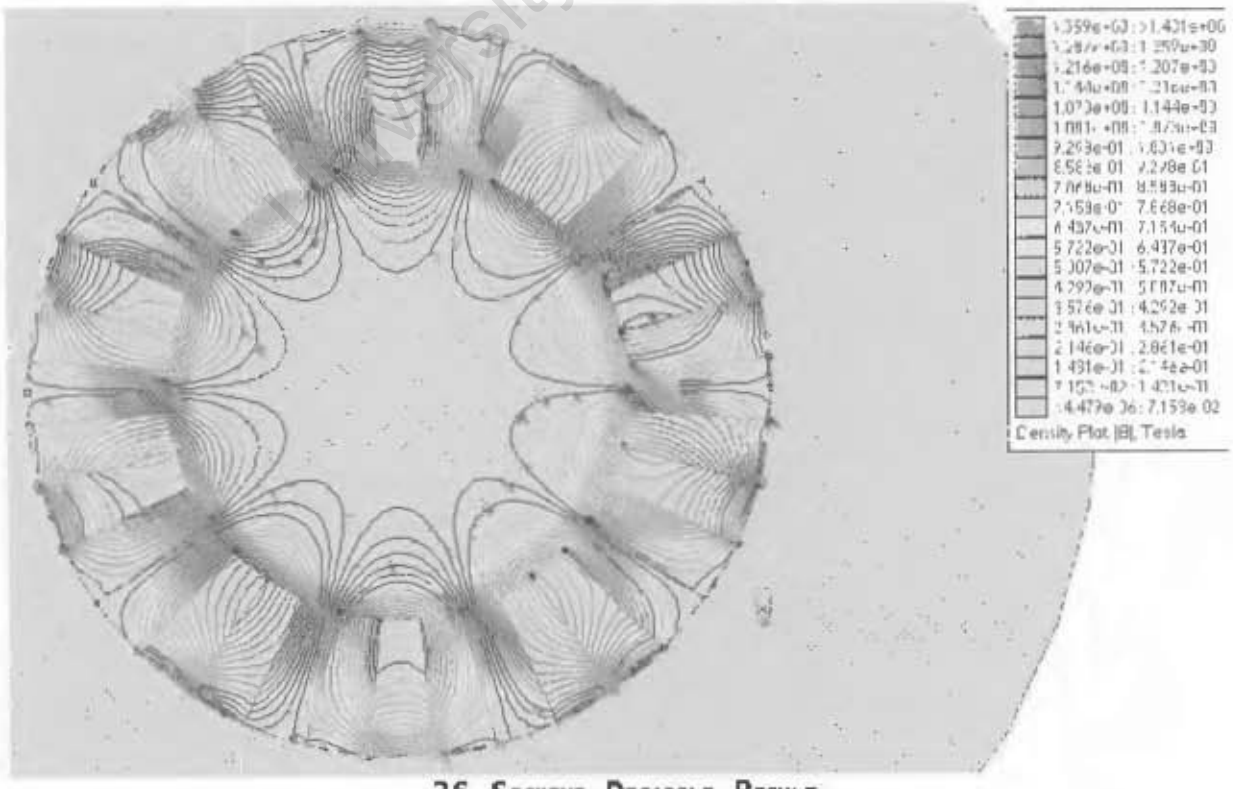

36 Segment Decapole Result

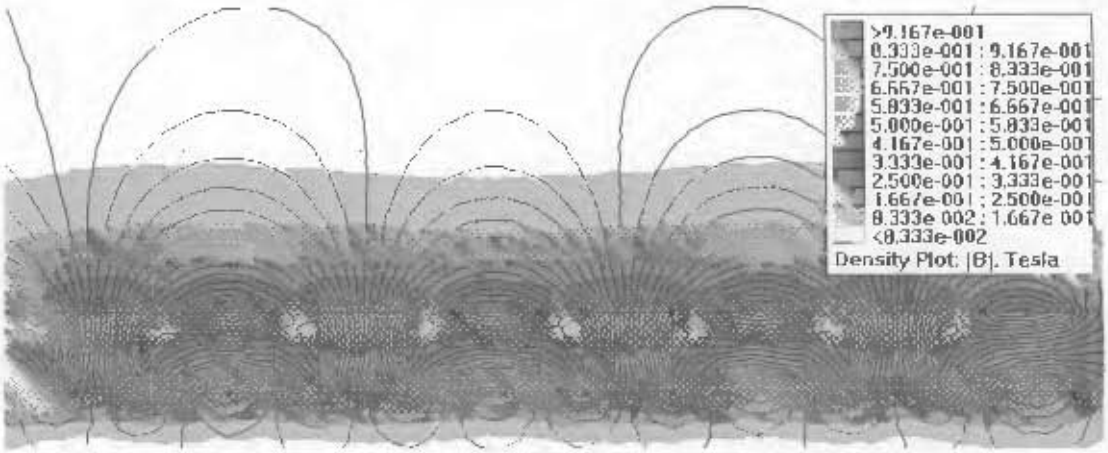

MIDWAY APPROXIMATION OF AXIAL FLUX HALBACH ARRAY WITH LINEAR ARRAY

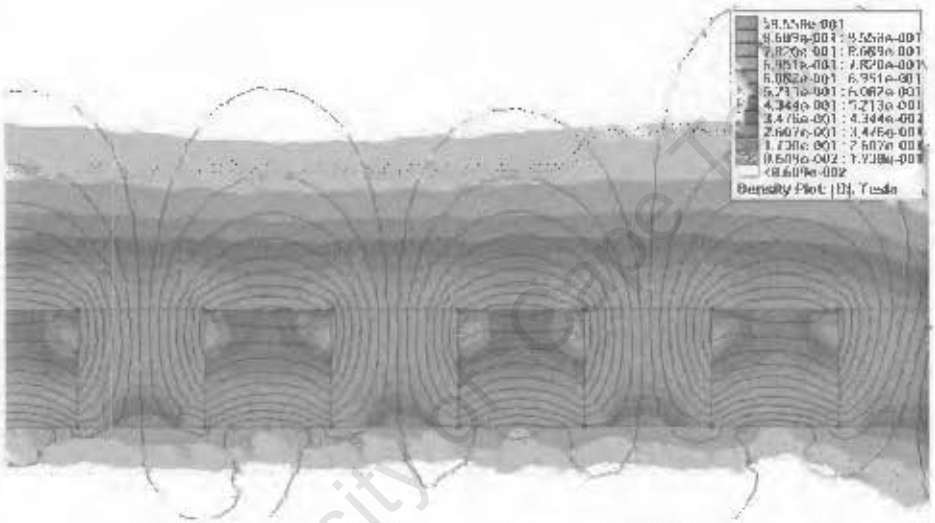

APPROXIMATION AT CENTRE OF AXIAL FLUX HALBACH ARRAY

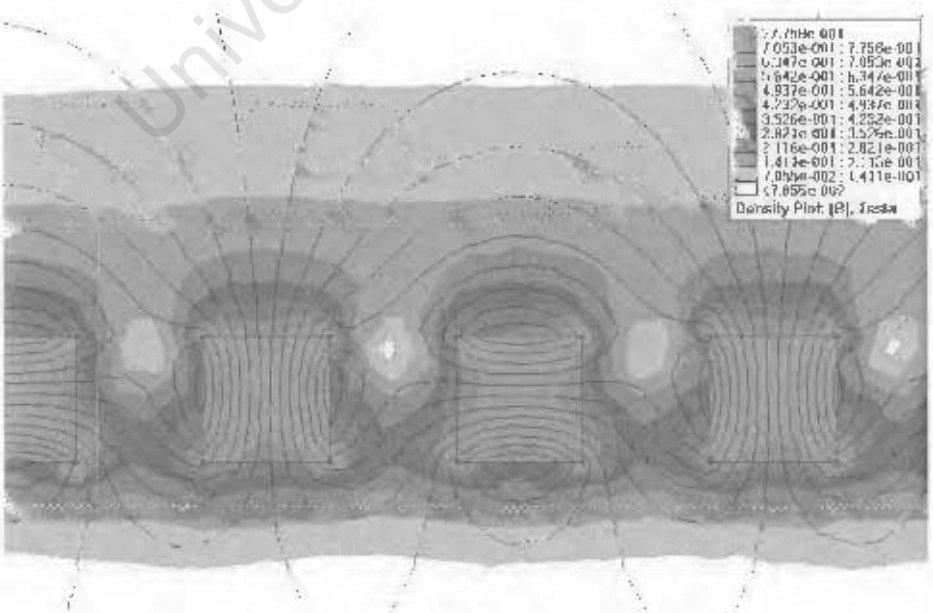

APPROXIMATION AT PERIMETER OF AXIAL FLUX HALBACH ARRAY

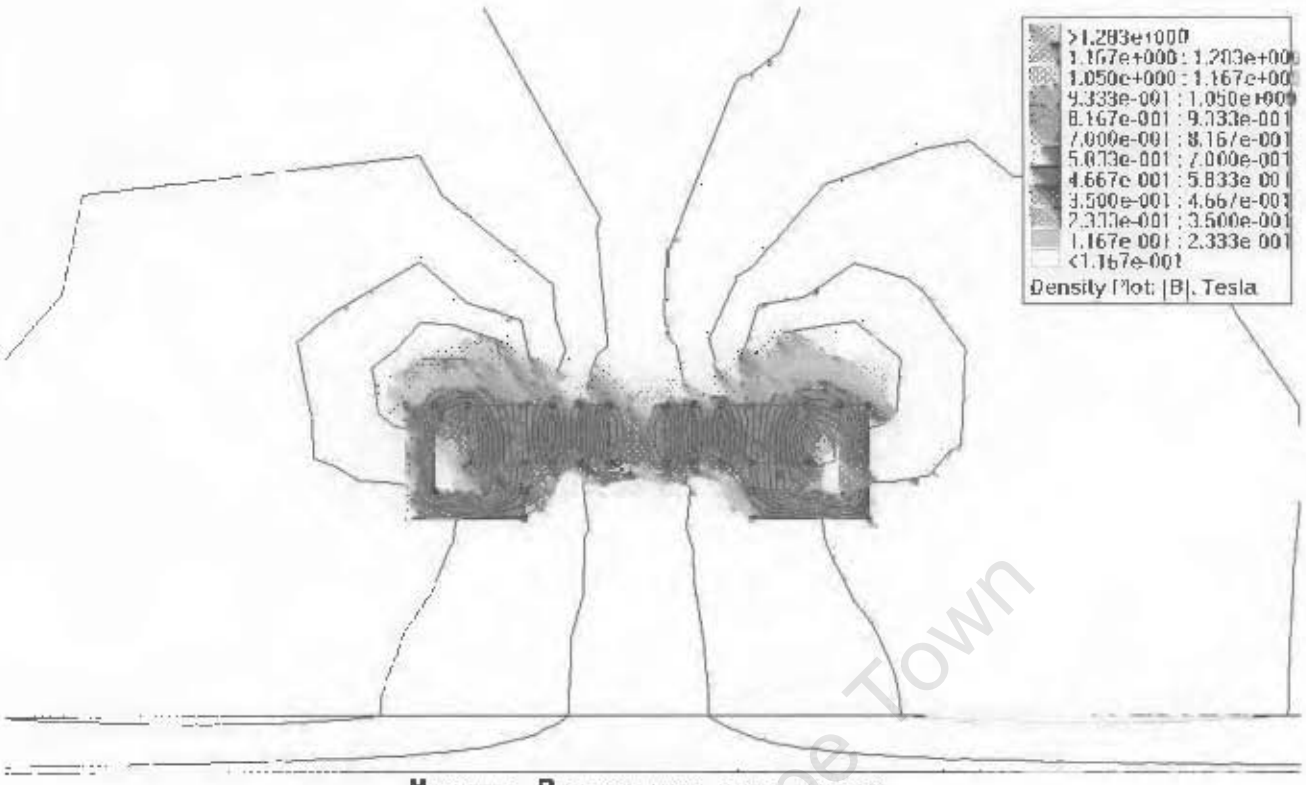

MAGNETIC BEARING WITH STEEL SHIELD

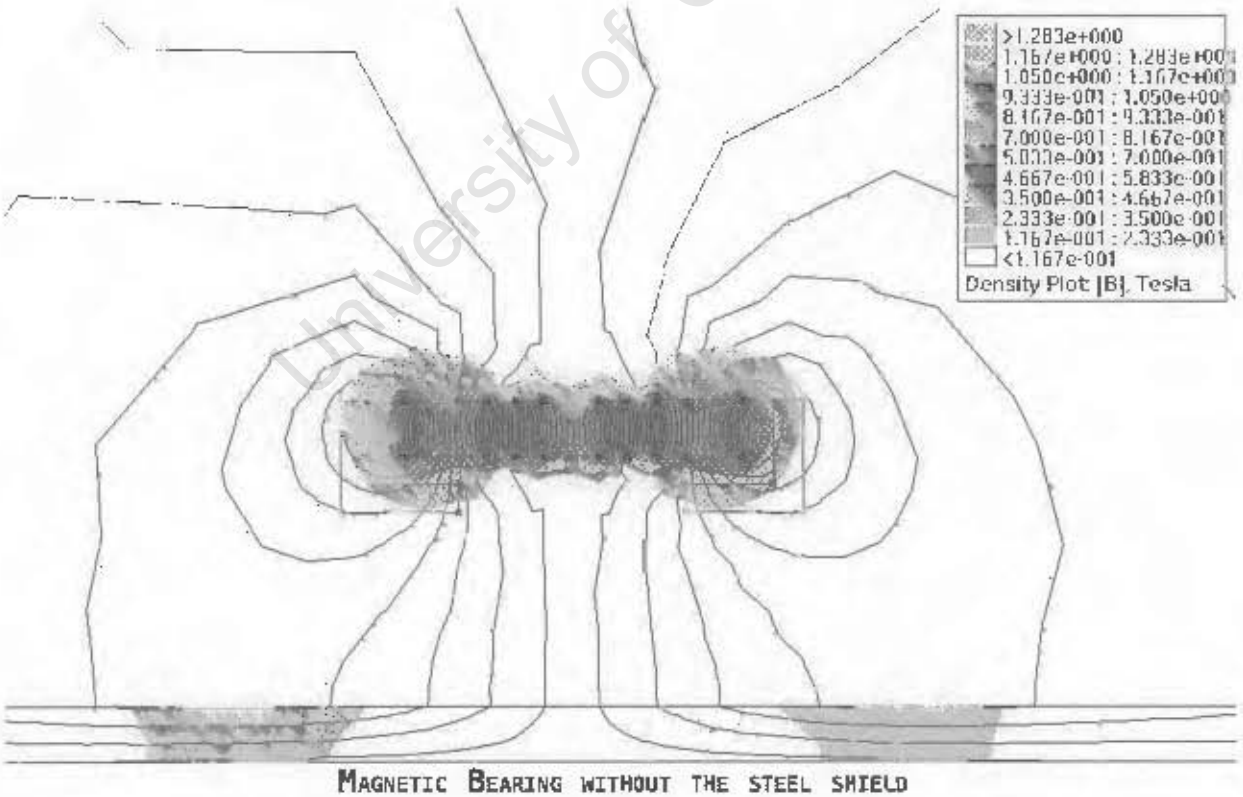

MAGNETIC BEARING WITHOUT THE STEEL SHIELD

(PROPERTIES OF CUP SET TO THAT OF AIR)

Appendix II – Maple spreadsheet listings

1. Program to Determine shapes for given speeds

A GENERAL EXACT OPTIMAL ANALYTICAL SHAPES

Let us analyse the differentiable configuration of the piecewise disk profiles ,it will be constructed from five basic shapes as we are going to give the proof :(this study is done when we see the involvement of the exponential shape ,i.e ,we assume to be in the medium-speed and also we are in the closed set or interval [0,1] and have different locations p[1]...p[6] that can vary according to the speed in the closed set):

> 1. Find The first shape w[1] that maximises e(k,w).

>

> The differentiable configuration of piecewise disk profile is a hole i.e e(k,w)=0 if and only if the shape w[1](r)=0.

>

>

$$\mathrm{e}(k,w)=\frac{k^2\left(\sum_{i=1}^{N}\int_{r_i}^{r_i+1} r^3 w_i(r)\,dr\right)}{\sum_{i=1}^{N}\int_{r_i}^{r_i+1} r\,w_i(r)\,dr}$$

In, this, case

$$p_1 := 0$$

$$p_6 := 1$$

$$N := 5$$

$$\mathrm{e}(k,w)=\frac{k^2\left(\int_0^{p_2} r^3 w_1(r)\,dr+\int_{p_2}^{p_3} r^3 w_2(r)\,dr+\int_{p_3}^{p_4} r^3 w_3(r)\,dr+\int_{p_4}^{p_5} r^3 w_4(r)\,dr+\int_{p_5}^{1} r^3 w_5(r)\,dr\right)}{\int_0^{p_2} r\,w_1(r)\,dr+\int_{p_2}^{p_3} r\,w_2(r)\,dr+\int_{p_3}^{p_4} r\,w_3(r)\,dr+\int_{p_4}^{p_5} r\,w_4(r)\,dr+\int_{p_5}^{1} r\,w_5(r)\,dr}$$

now, this, case, For, theFirst, shape, we, must, have

$$p_2 := p_3$$

$$p_3 := p_4$$

$$p_4 := p_5$$

$$p_5 := p_6$$

$$N := 5$$

$$e(k, w) = \frac{k^2 \int_{p_1}^{p_6} r^3 w_1(r)\, dr}{\int_{p_1}^{p_6} r\, w_1(r)\, dr}$$

now

As, We, know

To, maximise, $e(k, w)$*, At, this, stage,* $e(k, w)$*, must, be, Zero*

$$e(k, w) := 0$$

$$0 = \frac{k^2 \int_{p_1}^{p_6} r^3 w_1(r)\, dr}{\int_{p_1}^{p_6} r\, w_1(r)\, dr}$$

For, this, quotient, To, be, equal, To, zero, The, Denominator, must, be, different, To, Zero, And, we, Have

$$k^2 \int_{p_1}^{p_6} r^3 w_1(r)\, dr = 0$$

For, The, product, To, be, equal, To, zero, k^2*, must, be, different, To, zero*

And, we, obtain

$$\int_{p_1}^{p_6} r^3 w_1(r)\, dr = 0$$

the, same, way, of, thinking

The, Integral, Is, zero, when, $r^3 = 0$, *And,* $w_1(r) = 0$

Hence

The, First, basic, shape, In, the, interval, that, define, The, Hole, In, The, configuration, Of, piecewise, disk –

Is

$$w_1(r) := 0$$

> 2.Find The next shape w[2](r) that maximises e(k,w)

>

> The configuration of the Profile, at the location [p1,p3] in the medium speed k1<k2 ,of course ,is dominated or influenced by the involvement of a certain shape w[2](r),with the hole inside , But the whole is analysed already and w[2](r) starts from the point p[2] .So, we can assume the distance between p[1] and p[2],

>

In, this, case, From, the, low − speed, weassume

$$\delta(p_1, p_2) := .15$$

But, this, can, vary, according, To, The, speed

> Mathematically , Observing the involvement of the shape w[2](r) ,see fig 2 , we see two curves ,The logarithmic curve in one side symmetric to the exponential in another side in respect with the radius-axis.But if we look at the disk as a two-dimensional axisymmetrical problem ,we have a figure like a cuttaway while the disk is rotating. Now letus see how we can analyse the problem with Differential Equations;

>

>

>

>

$$e(k, w) = \frac{k^2 \left(\sum_{i=1}^{N} \int_{r_i}^{r_{i+1}} r^3 w_i(r)\, dr \right)}{\sum_{i=1}^{N} \int_{r_i}^{r_{i+1}} r\, w_i(r)\, dr}$$

In, the, interval, $[p_2, r]$

$$N := 5$$

$$p_1 := p_2$$

$$p_3 := r$$

$$p_3 := p_4$$

$$p_4 := p_5$$

$$p_5 := p_6$$

$$p_6 := r$$

$$e(k, w) = \frac{k^2 \int_{p_2}^{r} r^3 w_2(r)\, dr}{\int_{p_2}^{r} r\, w_2(r)\, dr}$$

$$e(k, w) := \frac{1}{2} \frac{k^2 (r^4 - {p_2}^4)}{r^2 - {p_2}^2}$$

$$e(k, w) := \frac{1}{2} (r^2 + {p_2}^2)\, k^2$$

In, the, section, $[r, q_3]$, *where, the, stress, Is, violated, For, The, first, time*

$$e(k, w) = \frac{k^2 \int_r^{q_3} r^3 w_2(r)\, dr}{\int_r^{q_3} r\, w_2(r)\, dr}$$

$$e(k, w) := \frac{1}{2} \frac{k^2 (q_3{}^4 - r^4)}{q_3{}^2 - r^2}$$

Hence

our, Profile, At, this, point q_3*, Is*

$$e(k, w) := \frac{1}{2} (q_3{}^2 + r^2)\, k^2$$

From, q_3*, the, exponential, profile, Is, pushed, To, the, left*

This, means

The, exponential – profile, $\mathbf{e}^{\left(\frac{1}{2}(q_3{}^2 + r^2)\, k^2\right)}$

gives, this, condition

$$w_3 = \mathbf{e}^{\left(\frac{1}{2}(q_3{}^2 + r^2)\, k^2\right)}$$

with

$$q_3 = \sqrt{-2 \frac{\ln(\delta)}{k^2}}$$

SO, with

p_3*, a, Negative, Number*

$$q_3 := \sqrt{-p_3{}^2}$$

Now, Knowing

$$w_3 = \mathbf{e}^{\left(\frac{1}{2}(q_3{}^2 + r^2)\, k^2\right)}$$

This, Implies

$$\frac{w_3}{e^{\left(\frac{1}{2}(q_3{}^2+r^2)\,k^2\right)}}=1$$

KnowingThat

$$q_3 := \sqrt{-p_3{}^2}$$

$$w_3\, e^{\left(-\frac{1}{2}(-p_3{}^2+r^2)\,k^2\right)}=1$$

The, Exponential, profile, serves, As, a, constant, stress, Profile, ie

$$s_R(r) := s_\tau(r) = 1$$

Therefore

$$w_3\, e^{\left(-\frac{1}{2}(-p_3{}^2+r^2)\,k^2\right)} = s_R(r, k, p_2, p_3)$$

For

$$p_2 \le r, r \le p_3$$

Hence

$w_2(r)$, *The, shape, drawn, From,* Q_3, *To,* p_3, *back, To, the, Center, Is*

$$q_3 := \sqrt{-p_3{}^2}$$

$$w_2(r) = w_3(r)\, e^{\left(\frac{1}{2}(p_3{}^2-r^2)\,k^2\right)}$$

For

$$p_2 \le r, r \le p_3$$

With

$w_3(r)$, *a, Constant − function, thatcould, be, found, In, the, low − speed*

>

>

> **3.The Optimal shape w[2](r) for High speed .**

>

> However,The minimum mass goal in the section(p[2]..p[3]) as implemented by locating p[3]for medium speed must now be changed .Instead of drawing an exponetial the bottom (q[3],w[3](r)) , an exponetial profile can be drawn, from the top center point (0,delta[U]) , down to the minimum thickness line .Here is the analytical form :

>

$$p_3 := 0$$

$$w_3(r) := \mathrm{w}(1)$$

$$\mathrm{w}(1) := w_5(r)$$

Hence

$$w_2(r) = \mathrm{w}(1)\, \mathrm{e}^{\left(-\frac{1}{2} r^2 k^2\right)}$$

>

>

> 4. The shape w[3](r) that maximises e(k,w).

>

> In geometric language, we can also say that through the point (p(3) ,p(4)) and at the maximum level (p(5) ,p(6)); there passes one and onlyone integral curve, on which these points are ordinary points and the tagents at these point are the straight line which are constants .

>

>

$$\mathrm{e}(k, w) = \frac{k^2 \int_{p_3}^{r} r^3 w_3(r)\, dr}{\int_{p_3}^{r} r\, w_3(r)\, dr}$$

now, this, case, For, theFirst, shape, we, must, have

$$p_1 := p_2$$

$$p_2 := p_3$$

$$p_4 := p_5$$

$$p_5 := p_6$$

$$p_6 := r$$

$$N := 5$$

$$e(k, w) = \frac{k^2 \int_{p_3}^{r} r^3 w_3(r)\, dr}{\int_{p_3}^{r} r\, w_3(r)\, dr}$$

$$w_{3\,..\,4} := \frac{1}{2} \frac{k^2 (r^4 - p_3{}^4)}{r^2 - p_3{}^2}$$

$$w_{3\,..\,4} := \frac{1}{2} (r^2 + p_3{}^2)\, k^2$$

Hence

$$w_{3\,..\,4} := constant = \delta_L$$

$$w_4(r) = \delta_L$$

> So , we fix this shape to a certain constant delta[L] to express the line with the respect to the geometrical restriction that determines the mass distribution at the both parts the rim and the hub.

>

> 5.Analyse the shape w[4](r) that maximises e(k,w).

>

>

> From, theGeometrical, Restriction

$$weAre, inThe, case, r, isIn, theInterval, p_4, p_5$$

$$\left| \frac{\partial}{\partial r} w(r) \right| \leq 2\,\sigma$$

$$Accordingto, RealAnalysis, we, sayFor, all, 0 < 2\,\sigma, ThereExist, Apoint, 0 < p_4, suchThat, \left| \frac{\partial}{\partial r} w(r) \right| \leq 2\,\sigma$$

$$Hence, thederivative, converge, tothePoint, 2\,\sigma$$

$$when, rTendTo, p_4$$

$$\lim_{r \to p_4} \frac{\partial}{\partial r} W(r) = 2\,\sigma$$

ByTheTheory, of, differential, of, nonlinearEquation, We, say, $\frac{\partial}{\partial r} W(r)$, *Approach,* $2\,\sigma$, *when, r, tendTo,* p_4

And, We, Write

$$\frac{\partial}{\partial r} w(r) = 2\,\sigma\,(r - p_4)$$

NOW, letUs, comebackto, our, study, Knowing

$$p_4 = p_3 + d$$

with, $w_{3\,..\,4} = w_3(r)$, *theShape, that, Correspond, toThe, point,* p_3, *which, is, equalTo,* δ_L

with, d, thedistanceThatTakes, theSlope, inOther, word, It, shows, how, Thepoint, inThe, slope, is, moving, FromOnePoint, Toanother, whichcorresponds, tothe, value, $2\,\sigma\,(r - p_4)$

andThe, shape, at, p_4, *Is,* w_4

Now, connecting, these, elements, according, what, weKnow, already, $p_4 = p_3 + d$

we, obtain

$$w_{p_4}(r) := \delta_L + 2\,\sigma\,(r - p_4)$$

with, r, inThe, interval, $p_4\,..\,p_5$

This, result, shows, how, the, maximumThickness, shrinks, Fromthe, top, till, a, certainpoint, p_4

>

>

> 6. The shape w[3](r) that maximises e(k,w).

>

> In geometric language, we can also say that through the point at the maximum level (p(5) ,p(6)); there passes one and onlyone integral curve, on which this point are ordinary points and the tagents at this point is the straight line which are constants .

>

>

>

$$e(k, w) = \frac{k^2 \int_{p_5}^{p_6} r^3 w_3(r)\, dr}{\int_{p_5}^{p_6} r\, w_3(r)\, dr}$$

$$w_{5..6} := \frac{1}{2} \frac{k^2 (p_6{}^4 - p_5{}^4)}{p_6{}^2 - p_5{}^2}$$

$$w_{5..6} := \frac{1}{2} (p_5{}^2 + p_6{}^2)\, k^2$$

$$w_{5..6} := \frac{1}{2} (p_5{}^2 + p_6{}^2)\, k^2 = constant$$

Hence

$$w_5(r) := \delta_U$$

>

>

> 5. A GENERAL OPTIMAL ANALYTICAL SHAPE The object of this part is to study the analytical method and obtain the general configuration of piecewise differentiable disk profiles, based on five shapes. The five basic shapes which must be analysed are defined as follow: 1.The shape which defines a hole . 2. The exponential constant(maximum)stress thickness shape. 3. The minimum thickness shape. 4. The maximum slope shape . 5. The maximum thickness shape.

>

```
seq(w[i](r),i=1..5)=piecewise(p[1]<=r,0,r<=p[2],0,p[2]<=r,delta[L]*ex
p((k^2/2)*(p[3]^2-r^2)),r<=p[3],delta[L]*exp((k^2/2)*(p[3]^2-
r^2)),p[3]<=r,delta[L],r<=p[4],delta[L],p[4]<=r,delta[L]+2*sigma[L]*(
r-p[4]),r<=p[5],delta[L]+2*sigma[L]*(r-
p[4]),p[5]<=r,delta[U],r<=p[6],delta[U]);;
```

$$(w_1(r), w_2(r), w_3(r), w_4(r), w_5(r)) = \begin{cases} 0 & p_1 \le r \\ 0 & r \le p_2 \\ \delta_L \, e^{\left(\frac{1}{2}k^2 (p_3{}^2 - r^2)\right)} & p_2 \le r \\ \delta_L \, e^{\left(\frac{1}{2}k^2 (p_3{}^2 - r^2)\right)} & r \le p_3 \\ \delta_L & p_3 \le r \\ \delta_L & r \le p_4 \\ \delta_L + 2\,\sigma_L (r - p_4) & p_4 \le r \\ \delta_L + 2\,\sigma_L (r - p_4) & r \le p_5 \\ \delta_U & p_5 \le r \\ \delta_U & r \le p_6 \end{cases}$$

> Let U1 = w(1) =0 and U5 = w(5) = d(L) the bounds of our integral e(k,w) in the range [0,1] And let U2=w(2),..,U4=w(4) be the bounds of e(k,w) in the range [p(2),p(5)] . ILLUSTRATIVE PROBLEM The optimisation problem is replaced by the discrete scheme. Practically we need to find w(i) which maximizes e(k,w) subject to some constraints.

>

FIND;{W[i]};WHICH,MAXIMISES;e(k,w):=k^2*sum('int(r^3*w(r),r=r[i]..r[i+1])','i'=1..N)/sum('int(r*w(r),r=r[i]..r[i+1])','i'=1..N);;subjectTO;subjectto;delta[L]<=W(r);W(r)<=delta[U];abs(W(r))<=2*delta;s[R](r)<=1;s[tau](r)<=1;

FIND

$$\{W_i\}$$

WHICH, MAXIMISES

$$e(k, w) := \frac{k^2 \left(\sum_{i=1}^{N} \int_{r_i}^{r_i + 1} r^3 \, w(r)\, dr \right)}{\sum_{i=1}^{N} \int_{r_i}^{r_i + 1} r \, w(r)\, dr}$$

$$\textit{subjectTO}$$

$$\textit{subjectto}$$

$$\delta_L \le W(r)$$

$$W(r) \le \delta_U$$

$$|W(r)| \le 2\,\delta$$

$$s_R(r) \le 1$$

$$s_\tau(r) \le 1$$

> Divide the interval at the points p(1),â€¦,p(6) with 0 <= p(2)â€¦â€¦<= p(5) <= 1.

>

> restart;n:=6;P[1]:=0;P[6]:=1;d[4..5]:=(delta[U]-delta[L])/(2*sigma);freeParameter;;P[4]:=p[4];;restart;P[5]:=piecewise(P[4]+d[4..5]<1,P[4]+d[4..5],p[4]+d[4..5]>=1,1);P[3]:=piecewise(0<=k[1],p[2],k[2]<=k[3],p[3]<=q[3],0<=r,q[3],r<=p[3],q[3]);{p[3]}<P[4];P[2]:=piecewise(p[1]+d[1..2]<p[3],p[1]+d[1..2],p[1]+d[1..2]>=p[3],p[3]);;

$$n := 6$$

$$P_1 := 0$$

$$P_6 := 1$$

$$d_{4\,..\,5} := \frac{1}{2}\frac{\delta_U - \delta_L}{\sigma}$$

$$\textit{freeParameter}$$

$$P_4 := p_4$$

$$P_5 := \begin{cases} P_4 + d_{4\,..\,5} & P_4 + d_{4\,..\,5} < 1 \\ 1 & 1 \le p_4 + d_{4\,..\,5} \end{cases}$$

$$P_3 := \begin{cases} p_2 & 0 \le k_1 \\ p_3 \le q_3 & k_2 \le k_3 \\ q_3 & 0 \le r \\ q_3 & r \le p_3 \end{cases}$$

$$(p_3) < P_4$$

$$p_2 := \begin{cases} p_1 + d_{1..2} & p_1 + d_{1..2} < p_3 \\ p_3 & p_3 \le p_1 + d_{1..2} \end{cases}$$

>

>

>

restart;W(R)=piecewise(p[1]<=p[2],0,p[2]<=p[3],exp(e(w,k)),p[3]<=p[4],diff(e(k,w),w)/e(k,w)=delta[L],p[4]<=p[5],diff(e(w,k),w),p[5]<=p[6],diff(e(k,w),w)/e(k,w)=delta[U]);;;;;;bound_cond:=abs(diff(w(r),r))<=2*delta;

$$\mathrm{W}(R) = \begin{cases} 0 & p_1 \le p_2 \\ e^{e(w,k)} & p_2 \le p_3 \\ \dfrac{\frac{\partial}{\partial w} e(k,w)}{e(k,w)} = \delta_L & p_3 \le p_4 \\ \frac{\partial}{\partial w} e(w,k) & p_4 \le p_5 \\ \dfrac{\frac{\partial}{\partial w} e(k,w)}{e(k,w)} = \delta_U & p_5 \le p_6 \end{cases}$$

$$bound\_cond := \left| \frac{\partial}{\partial r} \mathrm{w}(r) \right| \le 2\,\delta$$

> The integral will be transformed into a finite difference form by linearizing the DIsk e(k,w)1 â€¦.e(k,w)5 . At the location of p1 to p2 ,the shape is analysed as follow ; p1 < p2 and p2 = p3 = p4 = p5 = p6 ; as long as from the first fixed point p1 where no stress is applied and the sequence of k values is non zero, i.e the speed at this case start at low then goes to the high speed. Hence the integral e(k,w) at

$$e(k,w) = 0 = k^2 \frac{\int_0^{p2} r^3 w(r)\,dr}{\int_0^{p2} r\, w(r)\,dr}$$

this range is zero. For this integral to be equal to zero , the integral in the numerator must be zero with the condition the denominator different to zero and k different to zero . Then I'll

$$\int_0^{p2} r^3 w(r)\,dr = 0$$

have ; Hence ,w(r) = 0 with condition 0 <p(2).

>

>

restart;TheFirstShapeIs;;;e(k,w):=k*int(r^3*w(r),r=0..p[2])/int(r*w(r),r=0..p[2]);w[1](r):=e[0..p[2]](k,w)=int(r^3*w(r),r=0..p[2]);w[1](r):=int(r^3*w(r),r=0..p[2])=0;;

$$\mathit{TheFirstShapeIs}$$

$$e(k, w) := \frac{k \int_0^{p_2} r^3 \, w(r)\, dr}{\int_0^{p_2} r \, w(r)\, dr}$$

$$w_1(r) := e_{0\,..\,p_2}(k, w) = \int_0^{p_2} r^3 \, w(r)\, dr$$

$$w_1(r) := \int_0^{p_2} r^3 \, w(r)\, dr = 0$$

>

> Now, let us see what is happening to the next shape of this profile ;from the location p2; We have an exponential shape at the range p2 < p3 Where p1 = p2 and p3 = p4 = p5 = p6 ,and if we have a look to our linearized integral we have to compute only any the integral of any function at this range p2 to p3 , which will be our exponential function.Use The same technique for others.

>

>

> In geometric language, we can also say that through the point (p(3) ,p(4)) and at the maximum level (p(5) ,p(6)); there passes one and onlyone integral curve, on which these points are an ordinary points and the tagents at these point are the straight line which are constants .

>

restart;;w[3..4]:=factor(k^2*(simplify((int(r^3*w[p[1]<=p[2]],r=p[1]..p[1])+int(r^3*w[p[2]<=p[3]],r=p[2]..p[2])+int(r^3*w[p[3]<=p[4]],r=p[3]..r)+int(r^3*w[p[4]<=p[5]],r=p[5]..p[5])+int(r^3*w[p[5]<=p[6]],r=p[6]..p[6]))))/simplify(int(r*w[p[1]<=p[2]],r=p[1]..p[1])+int(r*w[p[2]<=p[3]],r=p[2]..p[2])+int(r*w[p[3]<=p[4]],r=p[3]..r)+int(r*w[p[4]<=p[5]],r=p[5]..p[5])+int(r*w[p[5]<=p[6]],r=p[6]..p[6]))));p[3]^2;Is,negative;p[3]:=sqrt(-p[3..4]^2);;w[3]:=w[3..4]=delta[L];

$$w_{3\,..\,4} := \frac{1}{2}(p_3{}^2 + r^2)\, k^2$$

$$p_3{}^2$$

Is, negative

$$p_3 := \sqrt{-p_{3..4}{}^2}$$

$$w_3 := \frac{1}{2}(-p_{3..4}{}^2 + r^2)\,k^2 = \delta_L$$

>

>

```
restart;;w[5..6]:=factor(k^2*(simplify((int(r^3*w[p[1]<=p[2]],r=p[1]..
p[1])+int(r^3*w[p[2]<=p[3]],r=p[2]..p[2])+int(r^3*w[p[3]<=p[4]],r=p
[3]..p[3])+int(r^3*w[p[4]<=p[5]],r=p[5]..p[5])+int(r^3*w[p[5]<=p[6]]
,r=r..p[5]))))/simplify(int(r*w[p[1]<=p[2]],r=p[1]..p[1])+int(r*w[p[2]<=
p[3]],r=p[2]..p[2])+int(r*w[p[3]<=p[4]],r=p[3]..p[3])+int(r*w[p[4]<=p
[5]],r=p[5]..p[5])+int(r*w[p[5]<=p[6]],r=r..p[5]))));p[5]:=sqrt(-
p[5..6]^2);;;w[5]:=eval(w[5..6],p[5]=sqrt(-p[5..6]))=delta[U];
```

$$w_{5..6} := \frac{1}{2}(p_5{}^2 + r^2)\,k^2$$

$$p_5 := \sqrt{-p_{5..6}{}^2}$$

$$w_5 := \frac{1}{2}(-p_{5..6}{}^2 + r^2)\,k^2 = \delta_U$$

>

>

> For high enough speed k ,the maximum level ; we locate a point q(3) where a strength constraint is first violated, the shape w(3) is now replaced in section [p(2),q(3)] by an exponential w(2) drawn from q(3) backwards to the center. at this point we multiply w(3) by the exponential function.

>

```
> restart;w[2](r):=w(3)=w[2];
```

$$w_2(r) := w(3) = w_2$$

>

> As a result the stresses drop in the whole disk below the maximum permitted level. In order to maintain the strengh conditions by applying the minimum mass at the section , point q(3) together with the exponential profile is pushed to the left untill a critical point q(3)=p(3) is reached for which the condition $s_2(p_3) = s_c(p_3) = 1$ Is met.

> Theorem Suppose that w(2)(r) is differentiable and non-zero on a shaped open set G. Then there is a differentiable function e(k,w) such

that , for r in G; $e^{e(k,w)} = w_2(r)$ **Notice: the disc D(p2 ,r) is in G**

>

>

>

```
restart;theNextpiecwiseintegral,FromTheLowSpeed,k,Is;restart;;e(k,w
)=k^2*int(r^3*w[2](r),r=p[2]..r)/int(r*w[2](r),r=p[2]..r);;thesecondSha
peIs;;;;;;;;;;;;;;;;;;;;Hence;;;;;;;;;;;;;restart;;;;;w[2](r):=exp(k^2*factor(((i
nt(r^3*w[p[1]<=p[2]],r=p[1]..p[1])+int(r^3*w[p[2]<=p[3]],r=r..p[3])+
int(r^3*w[p[3]<=p[4]],r=p[4]..p[4])+int(r^3*w[p[4]<=p[5]],r=p[5]..p[
5])+int(r^3*w[p[5]<=p[6]],r=p[6]..p[6])))/factor(int(r*w[p[1]<=p[2]],r
=p[1]..p[1])+int(r*w[p[2]<=p[3]],r=r..p[3])+int(r*w[p[3]<=p[4]],r=p[4
]..p[4])+int(r*w[p[4]<=p[5]],r=p[5]..p[5])+int(r*w[p[5]<=p[6]],r=p[6].
.p[6])))));p[33]:=sqrt(-p[3..4]^2);;w[2]:=eval(w[2](r),p[3]=p[33]);
```

$$theNextpiecwiseintegral,\ FromTheLowSpeed,\ k,\ Is$$

$$e(k, w) = \frac{k^2 \int_{p_2}^{r} r^3\, w_2(r)\, dr}{\int_{p_2}^{r} r\, w_2(r)\, dr}$$

$$thesecondShapeIs$$

$$Hence$$

$$w_2(r) := e^{\left(k^2\left(\frac{1}{2}r^2 + \frac{1}{2}p_3{}^2\right)\right)}$$

$$p_{33} := \sqrt{-p_{3\,..\,4}{}^2}$$

$$w_2 := e^{\left(k^2\left(\frac{1}{2}r^2 - \frac{1}{2}p_{3\,..\,4}{}^2\right)\right)}$$

> At this point the Exponential Profile serves a Constant stress profile i.e $S_R(r) = S_c(r) = 1$ **For 0 <= r <= p(3). So, this result gives the result of the proof of the Theorem for the High speed k ,**

$1 = 1/w_3(r)\,w_2(r) = \delta_L e^{-(e(k,w))} = 1$ **Creates the condition** $S_R(r) = S_c(r) = 1$ **Point at which a particular value is attained .**

> HENCE;w[3]:=delta[L];;W(2)(r):=w[3]*1/w[2]=w[3]*exp(-(k^2/2*(r^2-p[3..4]^2)));;

$$HENCE$$

$$w_3 := \delta_L$$

$$W(2)(r) := \frac{\delta_L}{w_2} = \delta_L \, e^{\left(-\frac{1}{2}k^2 (r^2 - p_{3\,..\,4}{}^2)\right)}$$

```
>
>
>
>
>
>
forall,2*sigma>0,Thereis,p[4]>0,such,That,abs(diff(W(r),r))<=2*delta;
Hence,limit(diff(W(r),r),r=p[4])=2*sigma;ByTheTheory,of,differential,o
f,nonlinearEquation,We,say,diff(W(r),r),Approach,2*sigma,when,r,tend
To,p[4];And,We,Write;;restart;diff(w(r),r)=2*sigma*(r-
p[4]);Now;TheSLOPE,As,definedBy,his,interval,p[4]..p[5],is;p[5]=p[4]+
d;;with;w[3..4]:=delta[L];weHave;;;;;;;;diff((w[p[4]<=p[5]])(r),r)=w[3..
4]+2*sigma*(r-p[4]);
```

$$forall,\ 0 < 2\,\sigma,\ Thereis,\ 0 < p_4,\ such,\ That,\ \left|\frac{\partial}{\partial r} W(r)\right| \le 2\,\delta$$

$$Hence,\quad \lim_{r \to p_4} \frac{\partial}{\partial r} W(r) = 2\,\sigma$$

$$ByTheTheory,\ of,\ differential,\ of,\ nonlinearEquation,\ We,\ say,\ \frac{\partial}{\partial r} W(r),\ Approach,\ 2\,\sigma,\ when,\ r,\ tendTo,\ p_4$$

$$And,\ We,\ Write$$

$$\frac{\partial}{\partial r} w(r) = 2\,\sigma\,(r - p_4)$$

$$Now$$

$$TheSLOPE,\ As,\ definedBy,\ his,\ interval,\ p_{4\,..\,5},\ is$$

$$p_5 = p_4 + d$$

$$with$$

$$w_{3\,..\,4} := \delta_L$$

$$weHave$$

$$\frac{\partial}{\partial r} w_{p_4 \le p_5}(r) = \delta_L + 2\,\sigma\,(r - p_4)$$

```
> MATHMATICAL,ANALYSIS,FOR,CRITICALPOINT;
```

MATHMATICAL, ANALYSIS, FOR, CRITICALPOINT

```
>
```

```
> TheFirst,derivativeIntegral;diff(s[R](r),r)=-(s[R]-s[tau])/r-
(diff(w(r),r)/w(r)*s[R]+k^2*r);
```

TheFirst, derivativeIntegral

$$\frac{\partial}{\partial r} s_R(r) = -\frac{s_R - s_\tau}{r} - \frac{\left(\frac{\partial}{\partial r} \mathrm{w}(r)\right) s_R}{\mathrm{w}(r)} - k^2 r$$

```
> restart;s[R]:=s[tau];s[tau]:=1;;;diff(s[R](r),r)=-(s[R]-s[tau])/r-
(diff(w(r),r)/w(r)*s[R]+k^2*r);;;eval(-(s[R]-s[tau])/r-
(diff(w(r),r)/w(r)*s[R]+k^2*r),r=p[3])=0;;;-
diff(w(p[3]),p[3])/w(p[3])=k^2*p[3];;;;;;;;int(-
diff(w(p[3]),p[3])/w(p[3]),p[3])=int(k^2*p[3],p[3]);
```

$$s_R := s_\tau$$

$$s_\tau := 1$$

$$0 = -\frac{\frac{\partial}{\partial r} \mathrm{w}(r)}{\mathrm{w}(r)} - k^2 r$$

$$-\frac{\left(\frac{\partial}{\partial r} \mathrm{w}(r)\right)\Big|_{r = p_3}}{\mathrm{w}(p_3)} - k^2 p_3 = 0$$

$$-\frac{\frac{\partial}{\partial p_3} \mathrm{w}(p_3)}{\mathrm{w}(p_3)} = k^2 p_3$$

$$-\ln(\mathrm{w}(p_3)) = \frac{1}{2} k^2 {p_3}^2$$

```
> restart;w(p[3]):=delta;-
ln(w(p[3]))=1/2*k^2*p[3]^2;Criticalpoint;;;p[3]:=sqrt(solve(-
ln(w(p[3]))=1/2*k^2*p[3]^2,p[3]^2));with;delta=delta[L]/delta[U];
```

$$\mathrm{w}(p_3) := \delta$$

$$-\ln(\delta) = \frac{1}{2} k^2 {p_3}^2$$

Criticalpoint

$$p_3 := \sqrt{-2\frac{\ln(\delta)}{k^2}}$$

with

$$\delta = \frac{\delta_L}{\delta_U}$$

>

>

>

>

> **Now,letUs,locate,theNextpoint;p[4]:=p[3]+delta[L];**

Now, letUs, locate, theNextpoint

$$p_4 := \sqrt{-2\frac{\ln(\delta)}{k^2}} + \delta_L$$

> **p[5]=p[4]+d;**

$$p_5 = \sqrt{-2\frac{\ln(\delta)}{k^2}} + \delta_L + d$$

>

>

>

restart;but,forHighspeed,criticalPoint,Is;theintersection,ofThe,curve,And,theLine,with,r=0;

but, forHighspeed, criticalPoint, Is

theintersection, ofThe, curve, And, theLine, with, $r = 0$

> **Hence;w[3]:=delta[L];w[2]:=delta[U]*exp(-k^2/2*p[3]^2);w[3]=w[2];p[3]^2=solve(w[2]=w[3],p[3]^2);p[3]:=sqrt(solve(w[2]=w[3],p[3]^2));**

Hence

$$w_3 := \delta_L$$

$$w_2 := \delta_U \, \mathbf{e}^{\left(-\frac{1}{2}k^2 {p_3}^2\right)}$$

$$\delta_L = \delta_U \, \mathbf{e}^{\left(-\frac{1}{2}k^2 {p_3}^2\right)}$$

$$p_3^2 = -2\frac{\ln\left(\frac{\delta_L}{\delta_U}\right)}{k^2}$$

$$p_3 := \sqrt{-2\frac{\ln\left(\frac{\delta_L}{\delta_U}\right)}{k^2}}$$

>

2. Program to determine Inertia and mass for given size

```
> A=(3+nu)/8*rho*omega^2*r2^2;
```

$$A = \frac{1}{8}(3+\nu)\,\rho\,\omega^2\,r2^2$$

```
> B=0;
```

$$B = 0$$

>

```
> sigma(r)=(3+nu)/8*rho*omega^2*r2^2-
(3+nu)/8*rho*omega^2*r^2,sigma(r);
```

$$\sigma(r) = \frac{1}{8}(3+\nu)\,\rho\,\omega^2\,r2^2 - \frac{1}{8}(3+\nu)\,\rho\,\omega^2\,r^2,\ \sigma(r)$$

>

```
> sigma(theta)=(3+nu)/8*rho*omega^2*r2^2-
(1+3*nu)/8*rho*omega^2*r^2;
```

$$\sigma(\theta) = \frac{1}{8}(3+\nu)\,\rho\,\omega^2\,r2^2 - \frac{1}{8}(1+3\nu)\,\rho\,\omega^2\,r^2$$

```
> restart; Ve:=int(delta*2*pi*r*exp(1/2*k^2*(p[3]^2-
r^2)),r=p[2]..p[3]);Vd:=pi*(p[4]^2-p[3]^2)*delta;
```

>

$$Ve := 2\frac{\delta\,\pi\left(-1+\mathbf{e}^{\left(\frac{1}{2}k^2\,(p_3^2-p_2^2)\right)}\right)}{k^2}$$

$$Vd := \pi\,(p_4^2-p_3^2)\,\delta$$

```
> restart; pi:=3.14; p[2]:=0.03; p[3]:=0.0884; p[4]:= 0.112;
delta:=0.02; rho:=1960;
k:=2.429;Ve:=int(delta*2*pi*r*exp(1/2*k^2*(p[3]^2-
r^2)),r=p[2]..p[3]);Vd:=pi*(p[4]^2-
p[3]^2)*delta;V:=Vd+2*Ve;m=rho*V;
```

$$\pi := 3.14$$

$$p_2 := .03$$

$$p_3 := .0884$$

$$p_4 := .112$$

$$\delta := .02$$

$$\rho := 1960$$

$$k := 2.429$$

$$Ve := .00043869342$$

$$Vd := .000297008832$$

$$V := .001174395672$$

$$m = 2.301815517$$

Appendix III – Schematic diagrams

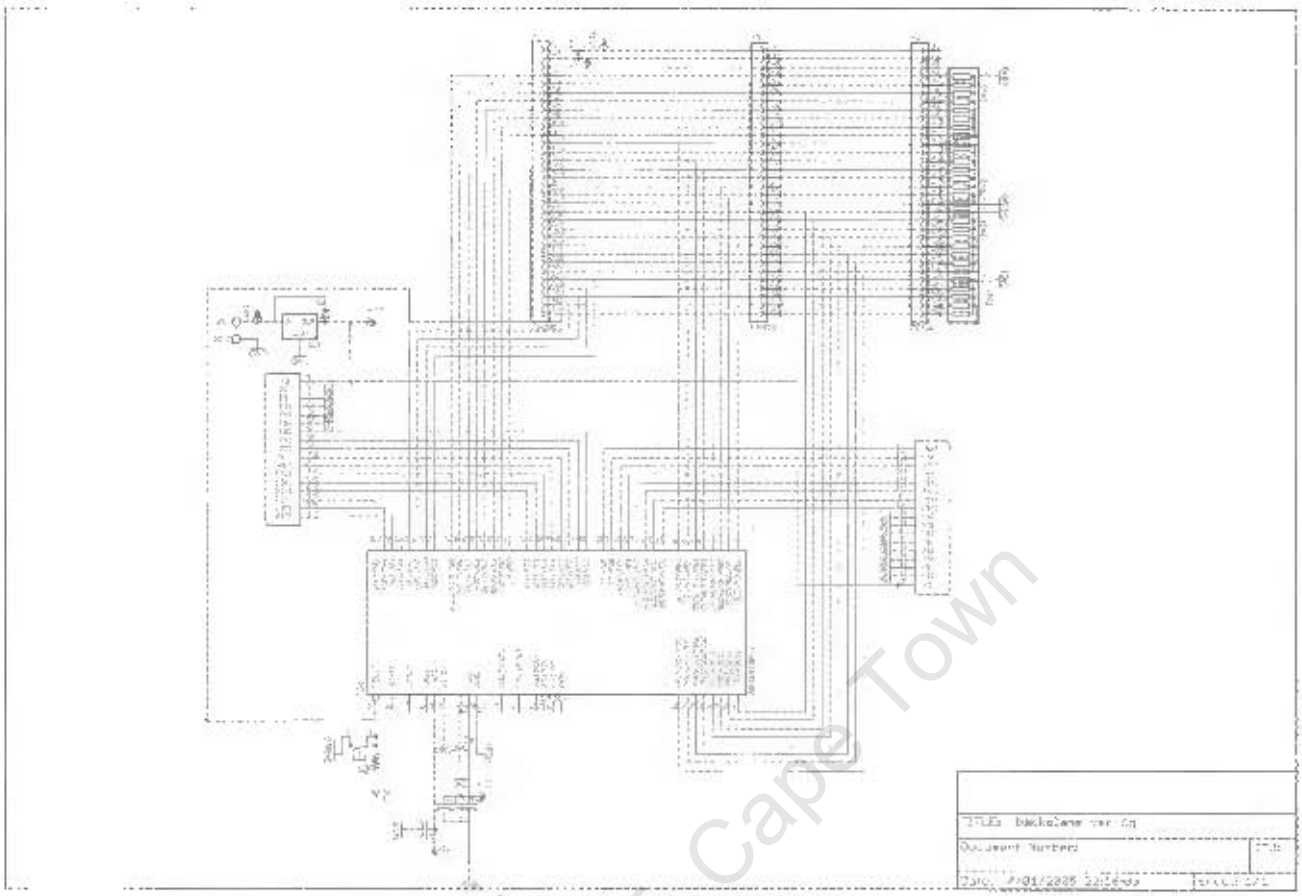

Schematic of backplane

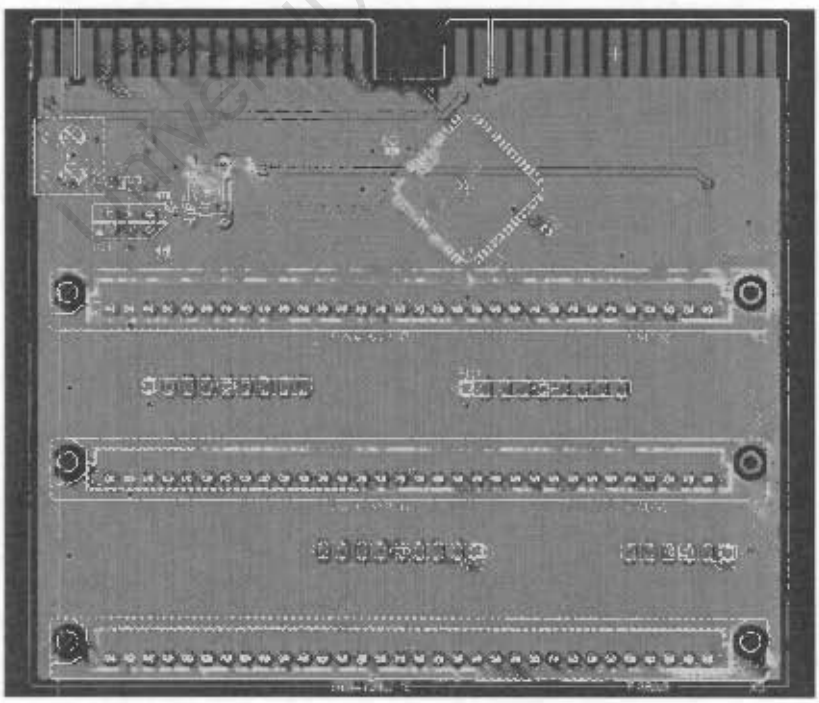

Backplane PCB

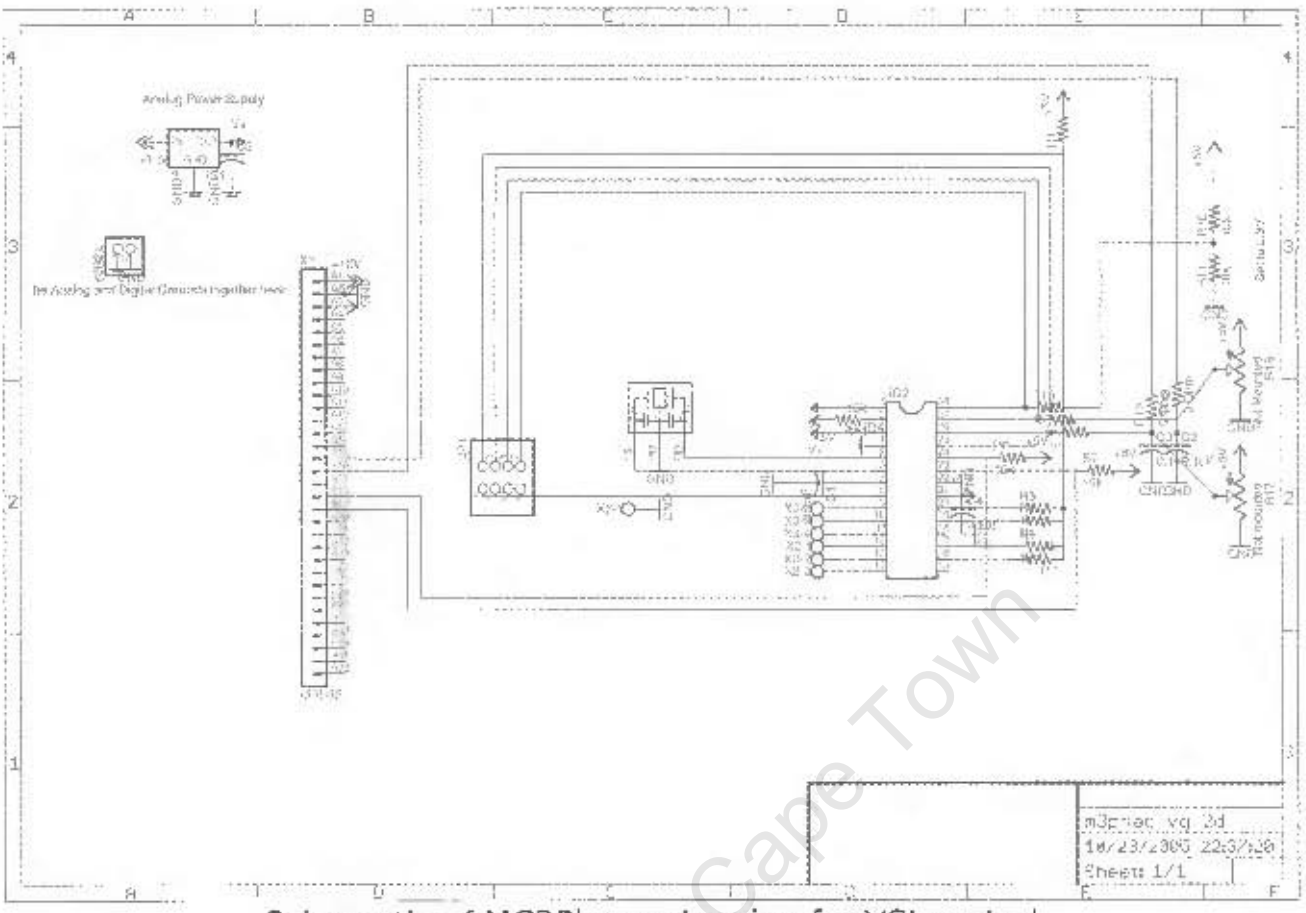

Schematic of MC3Phac extension for VSI control

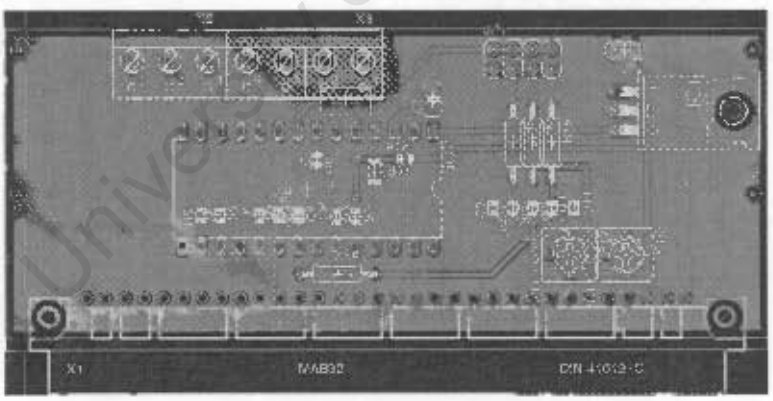

PCB of MC3Phac extension board

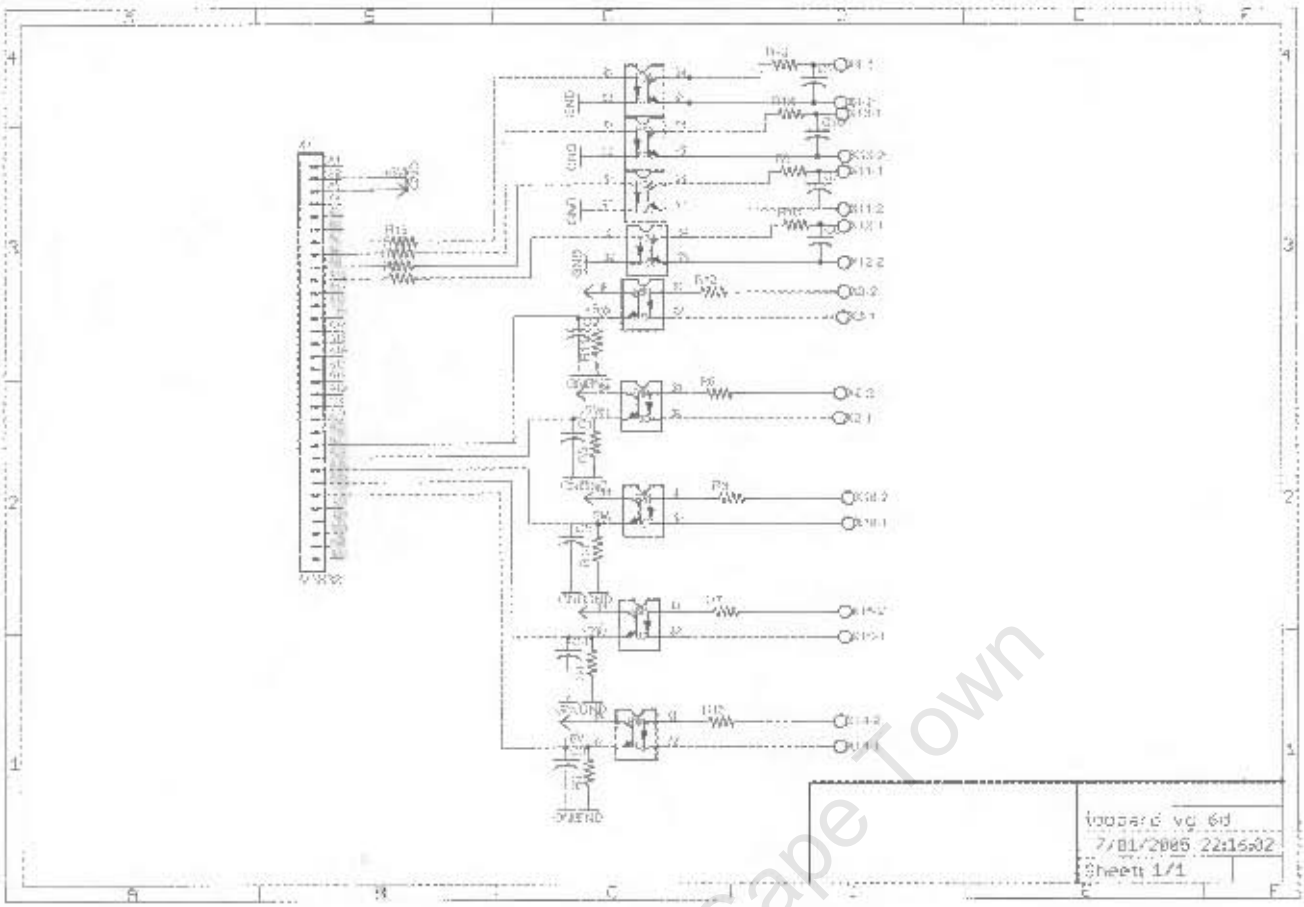

General IO extension board

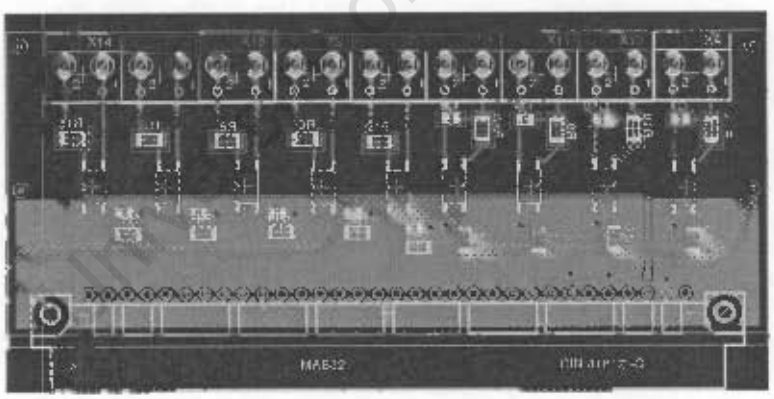

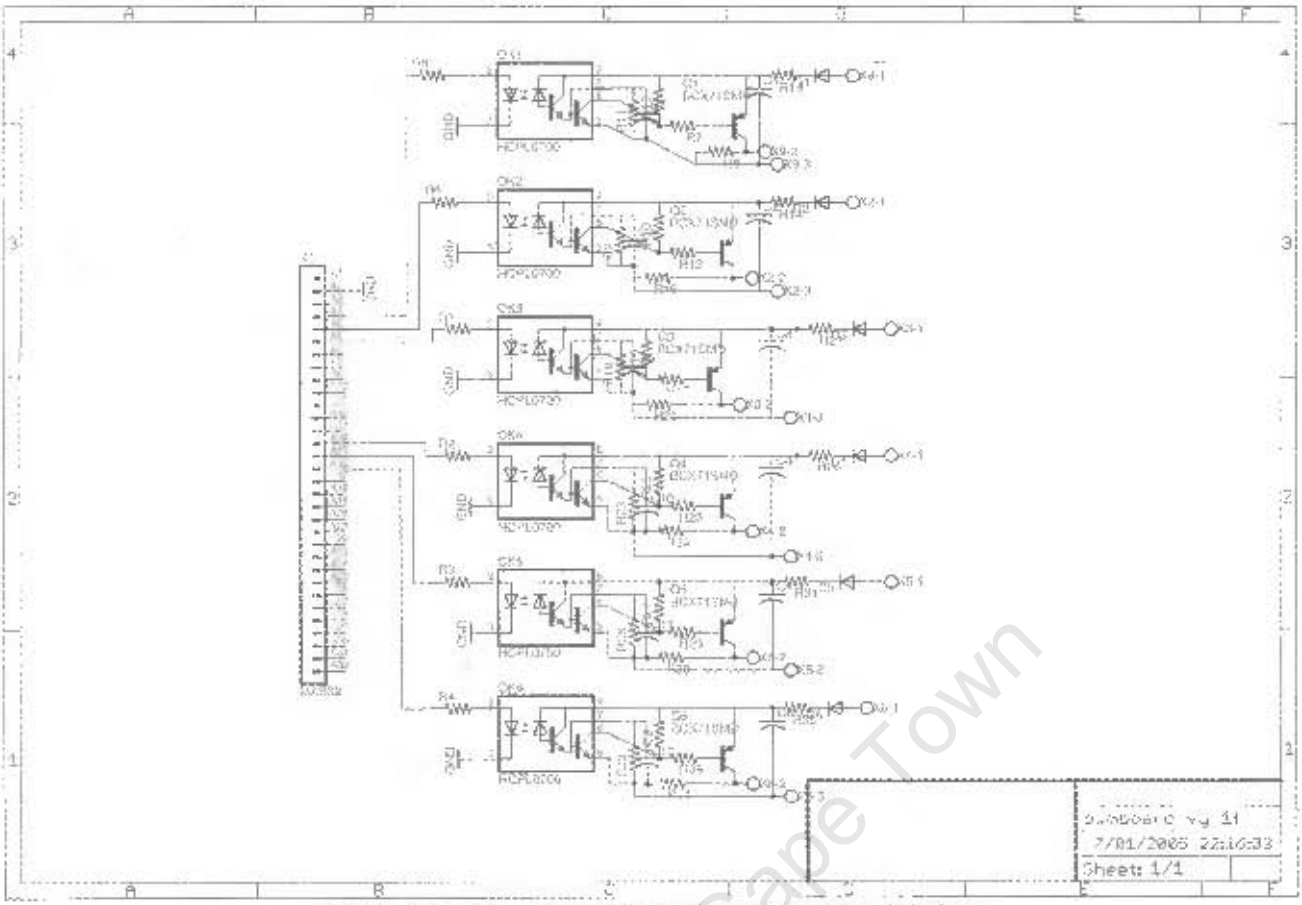

PWM board – used for direct BLDC driving

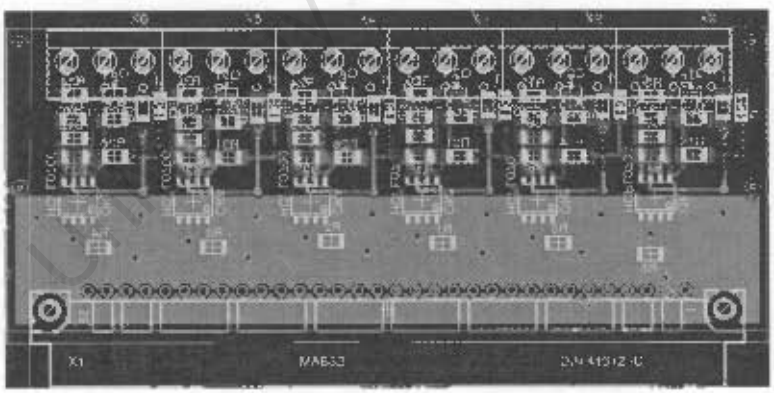

Appendix IV – ATMega 128 Brushless Controller Program Listing

Program 1: Single Phase drive with Hall sensors

```
/*****************************************
This program was produced by the
CodeWizardAVR V1.23.8d Standard
Automatic Program Generator
◆ Copyright 1998-2003 HP InfoTech s.r.l.
http://www.hpinfotech.ro
e-mail:office@hpinfotech.ro

Project : Single Phase drive with Hall sensors
Version :
Date    : 12/29/2006
Author  : Dave Johnson
Company : University of Capetown
Comments:


Chip type           : ATmega128
Program type        : Application
Clock frequency     : 8.000000 MHz
Memory model        : Small
External SRAM size  : 0
Data Stack size     : 1024
*****************************************/

#include <mega128.h>

#define FIRST_ADC_INPUT 0
#define LAST_ADC_INPUT 0
unsigned int adc_data[LAST_ADC_INPUT-FIRST_ADC_INPUT+1];
#define ADC_VREF_TYPE 0x40
// ADC interrupt service routine
// with auto input scanning
#pragma savereg-
interrupt [ADC_INT] void adc_isr(void)
{
#asm
   push r26
   push r27
   push r30
   push r31
```

```
   in   r30,sreg
   push r30
#endasm
register static unsigned char input_index=0;
// Read the AD conversion result
adc_data[input_index]=ADCW;
// Select next ADC input
if (++input_index > (LAST_ADC_INPUT-FIRST_ADC_INPUT))
  input_index=0;
ADMUX=(FIRST_ADC_INPUT|ADC_VREF_TYPE)+input_index;
// Start the AD conversion
ADCSRA|=0x40;
#asm
   pop  r30
   out  sreg,r30
   pop  r31
   pop  r30
   pop  r27
   pop  r26
#endasm
}
#pragma savereg+

// Declare your global variables here

void main(void)
{
// Declare your local variables here

char stateflag, trigflag;

// Input/Output Ports initialization
// Port A initialization
// Func0=In Func1=In Func2=Out Func3=In Func4=In Func5=In Func6=In Func7=In
// State0=T State1=T State2=0 State3=T State4=T State5=T State6=T State7=T
PORTA=0x00;
DDRA=0x04;

// Port B initialization
// Func0=In Func1=In Func2=In Func3=In Func4=In Func5=Out Func6=In Func7=In
// State0=T State1=T State2=T State3=T State4=T State5=0 State6=T State7=T
PORTB=0x00;
DDRB=0x20;
```

```
// Port C initialization
// Func0=In Func1=In Func2=In Func3=In Func4=In Func5=In Func6=In Func7=In
// State0=T State1=T State2=T State3=T State4=T State5=T State6=T State7=T
PORTC=0x00;
DDRC=0x00;

// Port D initialization
// Func0=In Func1=In Func2=In Func3=In Func4=In Func5=In Func6=In Func7=In
// State0=T State1=T State2=T State3=T State4=T State5=T State6=T State7=T
PORTD=0x00;
DDRD=0x00;

// Port E initialization
// Func0=Out Func1=Out Func2=Out Func3=Out Func4=Out Func5=Out Func6=Out Func7=Out
// State0=0 State1=0 State2=0 State3=0 State4=0 State5=0 State6=0 State7=0
PORTE=0x00;
DDRE=0xFF;

// Port F initialization
// Func0=In Func1=In Func2=In Func3=In Func4=In Func5=In Func6=In Func7=In
// State0=T State1=T State2=T State3=T State4=T State5=T State6=T State7=T
PORTF=0x00;
DDRF=0x00;

// Port G initialization
// Func0=In Func1=In Func2=In Func3=In Func4=In
// State0=T State1=T State2=T State3=T State4=T
PORTG=0x00;
DDRG=0x00;

// Timer/Counter 0 initialization
// Clock source: System Clock
// Clock value: Timer 0 Stopped
// Mode: Normal top=FFh
// OC0 output: Disconnected
ASSR=0x00;
TCCR0=0x00;
TCNT0=0x00;
OCR0=0x00;

// Timer/Counter 1 initialization
// Clock source: System Clock
// Clock value: Timer 1 Stopped
// Mode: Normal top=FFFFh
```

```
// OC1A output: Discon.
// OC1B output: Discon.
// OC1C output: Discon.
// Noise Canceler: Off
// Input Capture on Falling Edge
TCCR1A=0x00;
TCCR1B=0x00;
TCNT1H=0x00;
TCNT1L=0x00;
OCR1AH=0x00;
OCR1AL=0x00;
OCR1BH=0x00;
OCR1BL=0x00;
OCR1CH=0x00;
OCR1CL=0x00;

// Timer/Counter 2 initialization
// Clock source: System Clock
// Clock value: Timer 2 Stopped
// Mode: Normal top=FFh
// OC2 output: Disconnected
TCCR2=0x00;
TCNT2=0x00;
OCR2=0x00;

// Timer/Counter 3 initialization
// Clock source: System Clock
// Clock value: Timer 3 Stopped
// Mode: Normal top=FFFFh
// OC3A output: Discon.
// OC3B output: Discon.
// OC3C output: Discon.
TCCR3A=0x00;
TCCR3B=0x00;
TCNT3H=0x00;
TCNT3L=0x00;
OCR3AH=0x00;
OCR3AL=0x00;
OCR3BH=0x00;
OCR3BL=0x00;
OCR3CH=0x00;
OCR3CL=0x00;

// External Interrupt(s) initialization
```

```
// INT0: Off
// INT1: Off
// INT2: Off
// INT3: Off
// INT4: Off
// INT5: Off
// INT6: Off
// INT7: Off
EICRA=0x00;
EICRB=0x00;
EIMSK=0x00;

// Timer(s)/Counter(s) Interrupt(s) initialization
TIMSK=0x00;
ETIMSK=0x00;

// Analog Comparator initialization
// Analog Comparator: Off
// Analog Comparator Input Capture by Timer/Counter 1: Off
// Analog Comparator Output: Off
ACSR=0x80;
SFIOR=0x00;

// ADC initialization
// ADC Clock frequency: 125.000 kHz
// ADC Voltage Reference: AVCC pin
// ADC High Speed Mode: Off
ADMUX=FIRST_ADC_INPUT|ADC_VREF_TYPE;
ADCSRA=0xCE;
SFIOR&=0xEF;

// Global enable interrupts
#asm("sei")

stateflag = 1 ;
trigflag = 0;

while (1)
    {
// Determine whether hall sensor has crossed threshold and toggle inverter switch state
            if (trigflag==0){
                        if (adc_data[0] < 573 )  trigflag=1 ;
                        if (adc_data[0] > 572 ) stateflag=0 ;
                        goto forward ;
```

```
                    };
            if (trigflag==1){
                    if (adc_data[0] < 573 )  trigflag=0 ;
                    if (adc_data[0] > 572 ) stateflag=1 ;
                    };
forward: // Jump here to alternate between states every second bump
// Set inverter switch state - first turn do turnoffs to prevent cross conduction
            if (stateflag == 1)        {
                    PORTE.2=0;          // Leg 1 low side switch
                    PORTB.5=1;          // Leg 1 high side switch
                    PORTE.7=0;          // Leg 2 high side switch
                    PORTA.2=1;          // Leg 2 low side switch
            }
            else {
                    PORTB.5=0;          // Leg 1 high side switch
                    PORTE.2=1;          // Leg 1 low side switch
                    PORTA.2=0;          // Leg 2 low side switch
                    PORTE.7=1;          // Leg 2 high side switch
                    };

    };
}
```

Program 2: Three Phase drive with optical sensors

```
/*****************************************
This program was produced by the
CodeWizardAVR V1.23.8d Standard
Automatic Program Generator
 Copyright 1998-2003 HP InfoTech s.r.l.
http://www.hpinfotech.ro
e-mail:office@hpinfotech.ro

Project : Three Phase drive with optical sensors
Version :
Date    : 2006/04/01
Author  : Dave Johnson
Company : University of Cape Town
Comments:

Converted to AVR-GCC
Date    : 2006/07/11
Author  : Dave Johnson
Company : University of Cape Town


Chip type           : ATmega128
Program type        : Application
Clock frequency     : 16.000000 MHz
Memory model        : Small
External SRAM size  : 0
Data Stack size     : 1024
*****************************************/

#include <stdio.h>
#include <stdint.h>
#include <stdlib.h>
#include <avr/io.h>
#include <avr/eeprom.h>
#include <avr/interrupt.h>
#include <avr/pgmspace.h>
#include <avr/sfr_defs.h>
#include <util/delay.h>


// * * * * * * * * * * * * * * *
```

```
// Declare your global variables
//
// * * * * * * * * * * * * * * *

// * * * * * * * * * * * *
// Define Boolean values
//
// * * * * * * * * * * * *
#define FALSE        0
#define TRUE         1

// * * * * * * * * * * * * * * * * * * * * * * *
// define ADC parameter  and variable string
// * * * * * * * * * * * * * * * * * * * * * * *
#define FIRST_ADC_INPUT 0
#define LAST_ADC_INPUT 2
volatile uint16_t adc_data[LAST_ADC_INPUT-FIRST_ADC_INPUT+1];
#define ADC_VREF_TYPE 0x40
volatile uint8_t input_index;


// * * * * * * *
// Define flags
// * * * * * * *

//uint8_t timflag


// * * * * * * * * * * * *
// Define Other variables
//
// * * * * * * * * * * * *

// int8_t   ;  // 8 bit integers
// uint16_t ;// Unsigned 16 interger
// int32_t    ;              // 32 bit interger

// * * * * * * * * * * * * * * * * * * * * * * * * * * * * * *
// Define the control parameter Variables/Flash and EEprom
//      defautls for Velocity and Current PI loops
// * * * * * * * * * * * * * * * * * * * * * * * * * * * * * *
// float ee_K_Pv __attribute__((section(".eeprom"))) = 5.000;
//uint16_t ee_V_Off __attribute__((section(".eeprom"))) = 503;
```

```
//****************
// Declare function prototypes
//
//****************

 void delay_ms(uint16_t ms);
 void delay_us(uint16_t us);

//********************
//                        INTERRUPT SERVICE ROUTINES

//********************

// External Interrupt 0 service routine
//  Trip routine for Bus over Current
//********************
/*ISR(INT0_vect)
{

}*/


//********************
// External Interrupt 1 service routine
// Trip routine for I2t over time limit
//********************
/*ISR(INT1_vect)
{
            return;
} */

//************************
//    External Interrupt 2 service routine
//            used on azimuth for synchronizing clocks
//************************
/*ISR(INT2_vect)
{
            return;
}*/

//********************
// External Interrupt 6 service routine
//  Trip routine for Bus under Voltage
//********************
```

```
/*ISR(INT6_vect)
{
        return;
}*/

// * * * * * * * * * * * * * * * * * * *
// External Interrupt 7 service routine
//  Trip routine for Bus over Voltage
// * * * * * * * * * * * * * * * * * * *
/*ISR(INT7_vect)
{
        return;
} */

// * * * * * * * * * * * * * * * * * * * * * *
// Timer 1 overflow interrupt service routine
//  Interrupt routine for inverter sync
//  Sends synchonization pulse to elevation
//   drive once every 16 000 000 clocks
// * * * * * * * * * * * * * * * * * * * * * *
/*ISR(TIMER1_OVF_vect)// void timer1_ovf_isr(void)
{
        return;
}*/

// * * * * * * * * * * * * * * * * * * * * * *
// Timer 2 overflow interrupt service routine
//          Interrupt routine for I2t timing
// * * * * * * * * * * * * * * * * * * * * * *
/*ISR(TIMER2_OVF_vect) //void timer2_ovf_isr(void)
{
        return;
}*/

// * * * * * * * * * * * * * * * * * * * * *
//                  ADC interrupt service routine
//  Interrupt routine for auto ADC convertion
/* * * * * * * * * * * * * * * * * * * * * *
ADC0 - Velocity
ADC1 - Velocity Setpoint
ADC2 - Current
* * * * * * * * * * * * * * * * * * * * * */
ISR(ADC_vect)
{
```

```
        adc_data[input_index]=ADCW;
        if (++input_index > (LAST_ADC_INPUT-FIRST_ADC_INPUT))input_index=0;
        ADMUX=(FIRST_ADC_INPUT|ADC_VREF_TYPE)+input_index;
        ADCSRA|=0x40;
        return;
}

// * * * * * * * * * * * * * * * * * * *
//                                              FUNCTIONS
//
// * * * * * * * * * * * * * * * * * * *

// * * * * * * * * * * * * * * * * * * *
// Long delay routine - 1 ms increments
//          Increased range for _delay_ms
// * * * * * * * * * * * * * * * * * * *

void delay_ms(uint16_t ms)
{
        uint16_t time = 0 ;
        while(time < ms){
                _delay_ms(1);
                time++;
                }
        return;
}

// * * * * * * * * * * * * * * * * * * *
// Long delay routine - 1 us increments
//          Increased range for _delay_us
// * * * * * * * * * * * * * * * * * * *

void delay_us(uint16_t us)
{
        uint16_t time = 0 ;
        while(time < us){
                _delay_us(1);
                time++;
                }
        return;
}

// * * * * * * * * * * * * * * * * * * * * * *
//                                                      Main loop
```

```
//
// * * * * * * * * * * * * * * * * * * * * * * * *

int main(void){
// Declare your variables
int A=0, B=0, C=0;
char cnt ;

// IO Ports initialization

// Port A initialization
//
// Notes: Port A set up by lcd routine

PORTA = 0x00; // Set all pins to low
//PORTA = 0xff; // Set all pins high/Pullup
//DDRA  = 0xff; // Set all pins as outputs
//DDRA  = 0x00; // Set all pins as inputs

// Pin state 0=low / 1=high
//PORTA = 0b11000011;
//Set in/output pins 0=in | 1=out
DDRA  = 0b00000101 ;

// Port B initialization
//
// Notes:

PORTB = 0x00; // Set all pins to low
//PORTB = 0xff; // Set all pins high/Pullup
//DDRB  = 0xff; // Set all pins as outputs
//DDRB  = 0x00; // Set all pins as inputs

// Pin state 0=low / 1=high
//PORTB = 0b11000011;
//Set in/output pins 0=in | 1=out
DDRB = 0b00111000;

// Port C initialization
//
//Notes :

DDRC  = 0x00; // Set all pins as inputs
//DDRC  = 0xff; // Set all pins as outputs
```

```
PORTC = 0x00; // Set all pins to low
//PORTC = 0xff; // Set all pins high/Pullup

//Pin State: 0=low | 1 = high
//PORTC = 0b00000000;
//Set in/output pins 0=in | 1=out
//DDRC  = 0b00111100;

// Port D initialization
//
// Notes:

PORTD = 0x00; // Set all pins to low
//PORTD = 0xff; // Set all pins high/Pullup
//DDRD  = 0xff; // Set all pins as outputs
DDRD  = 0x00; // Set ll pins as inputs

//Pin State: 0=low | 1 = high
//PORTD = 0b00000000;
//Set in/output pins 0=in | 1=out
//DDRD  = 0b00000000;

// Port E initialization
//
// Notes:

//PORTE = 0xff; // Set all pins high
PORTE = 0x00;          // Set all pins low
//DDRE  = 0xff; // Set all pins as outputs
//DDRE  = 0x00; // Set ll pins as inputs

// Pin state 0=low / 1=high
//PORTE = 0b00000000;
// Data Direction 0=in/1=out
DDRE = 0b00001110 ;

// Port F initialization
//
// Notes:

PORTF = 0x00; // Set all pins to low
//PORTF = 0xff; // Set all pins high/Pullup

//DDRF  = 0xff; // Set all pins as outputs
```

```
//DDRF  = 0x00; // Set ll pins as inputs

// Pin state 0=low / 1=high
//PORTF = 0b00000000
// Data Direction 0=in/1=out
DDRF = 0b01100000 ;

// Port G initialization
//
// Notes:

PORTG = 0x00; // Set all pins to low
//PORTG = 0xff; // Set all pins high/Pullup

//DDRG  = 0xff; // Set all pins as outputs
DDRG  = 0x00; // Set ll pins as inputs

// Pin state 0=low / 1=high
//PORTG = 0b0000000 ;
// Data Direction 0=in/1=out
//DDRG  = 0b0000000 ;

// Timer/Counter 0 initialization
// Clock source: System Clock
// Clock value: Timer 0 Stopped
// Mode: Normal top=FFh
// OC0 output: Disconnected
ASSR=0x00;
TCCR0=0x00;
TCNT0=0x00;
OCR0=0x00;

// Timer/Counter 1 initialization
// Clock source: System Clock
// Clock value: 16000.000 kHz
// Mode: Ph. correct PWM top=ICR1
// OC1A output: Non-Inv.
// OC1B output: Inverted
// OC1C output: Discon.
// Noise Canceler: Off
// Input Capture on Falling Edge
TCCR1A=0x00;
TCCR1B=0x00;
TCNT1H=0x00;
```

```
TCNT1L=0x00;
OCR1AH=0x00;
OCR1AL=0x00;
OCR1BH=0x00;
OCR1BL=0x00;
OCR1CH=0x00;
OCR1CL=0x00;

// Timer/Counter 2 initialization
// Clock source: System Clock
// Clock value: 15.625 kHz
// Mode: Normal top=FFh
// OC2 output: Disconnected
TCCR2=0x00;
TCNT2=0x00;
OCR2=0x00;

// Timer/Counter 3 initialization
// Clock source: System Clock
// Clock value: 16000.000 kHz
// Mode: Ph. correct PWM top=ICR3
// OC3A output: Non-Inv.
// OC3B output: Inverted
// OC3C output: Discon.
TCCR3A=0x00;
TCCR3B=0x00;
TCNT3H=0x00;
TCNT3L=0x00;
OCR3A=0;
OCR3B=0;
OCR3C=0;
OCR3AL=0x00;
OCR3BL=0x00;
OCR3CL=0x00;


// External Interrupt(s) initialization
// INT0: On
// INT0 Mode: Rising Edge
// INT1: On
// INT1 Mode: Rising Edge
// INT2: On
// INT2 Mode: Rising Edge
// INT3: Off
```

```
// INT4: Off
// INT5: Off
// INT6: On
// INT6 Mode: Rising Edge
// INT7: On
// INT7 Mode: Rising Edge
EICRA=0x00;
EICRB=0x00;
EIMSK=0x00;
EIFR=0x00;

// Timer(s)/Counter(s) Interrupt(s) initialization
TIMSK=0x40;
ETIMSK=0x00;

// Analog Comparator initialization
// Analog Comparator: Off
// Analog Comparator Input Capture by Timer/Counter 1: Off
// Analog Comparator Output: Off
ACSR=0x80;
SFIOR=0x00;

// ADC initialization
// ADC Clock frequency: 125.000 kHz
// ADC Voltage Reference: AVCC pin

ADMUX=FIRST_ADC_INPUT|ADC_VREF_TYPE;
ADCSRA=0xCE;
SFIOR&=0xEF;

// Read the default values from EEProm
//eeprom_busy_wait();
//eeprom_read_block(&K_Pv ,&ee_K_Pv, sizeof(K_Pv));

// Global enable interrupts
sei();

//                                        Multitasking loop begins
// All interrupts overide the functions in this loop
while (1)
{
        if (adc_data[0] < 654) A = 0;
        if (adc_data[0] > 675) A = 1;
        if (adc_data[1] < 654) B = 0;
```

```
if (adc_data[1] > 675) B = 1;
if (adc_data[2] < 654) C = 0;
if (adc_data[2] > 675) C = 1;

if (cnt<1){                    // Toggle a pin once per revolution for motor speed measurement
            cnt++;
            PORTA |= _BV(PA2);
            }
else {
            cnt=0;
            PORTA &= ~_BV(PA2);
            };


if ((A==1)&&(B ==0)&&(C==1)) {          // Set the inverter o/p for rotor position
            PORTB &= ~_BV(PB5);
            PORTB |= _BV(PB3);
            PORTE |= _BV(PE3);
            PORTE &= ~_BV(PE1);
            PORTF &= ~_BV(PF6);
            PORTA &= ~_BV(PA0);
            }
if ((A==1)&&(B ==0)&&(C==0)) {
            PORTB &= ~_BV(PB5);
            PORTB |= _BV(PB3);
            PORTE &= ~_BV(PE3);
            PORTE &= ~_BV(PE1);
            PORTF |= _BV(PF6);
            PORTA &= ~_BV(PA0);
            }
if ((A==1)&&(B ==1)&&(C==0)) {
            PORTB &= ~_BV(PB5);
            PORTB &= ~_BV(PB3);
            PORTE &= ~_BV(PE3);
            PORTE |= _BV(PE1);
            PORTF |= _BV(PF6);
            PORTA &= ~_BV(PA0);
            }
if ((A==0)&&(B ==1)&&(C==0)) {
            PORTB |= _BV(PB5);
            PORTB &= ~_BV(PB3);
            PORTE &= ~_BV(PE3);
            PORTE |= _BV(PE1);
            PORTF &= ~_BV(PF6);
```

```
                PORTA &= ~_BV(PA0);
                }
        if ((A==0)&&(B ==1)&&(C==1)) {
                PORTB |= _BV(PB5);
                PORTB &= ~_BV(PB3);
                PORTE &= ~_BV(PE3);
                PORTE &= ~_BV(PE1);
                PORTF &= ~_BV(PF6);
                PORTA |= _BV(PA0);
                }
        if ((A==0)&&(B ==0)&&(C==1)) {
                PORTB &= ~_BV(PB5);
                PORTB &= ~_BV(PB3);
                PORTE |= _BV(PE3);
                PORTE &= ~_BV(PE1);
                PORTF &= ~_BV(PF6);
                PORTA |= _BV(PA0);
                }

};
}
```

Appendix V – Experimental data

1. Hall sensor oscilloscope captures

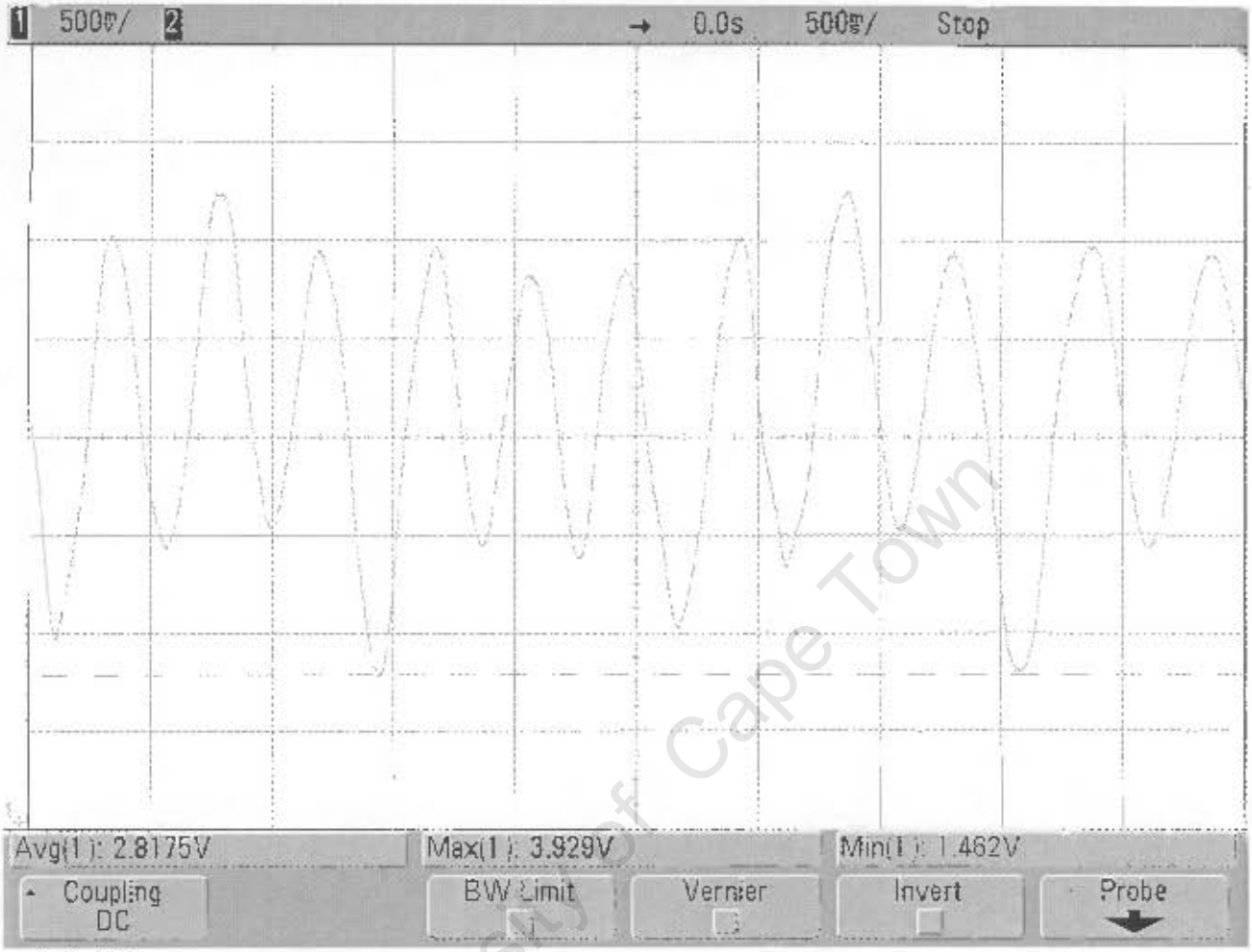

print_00

Hall sense data with UGN3503
Avg: 2.8V
Max: 3.93
Min: 1.46

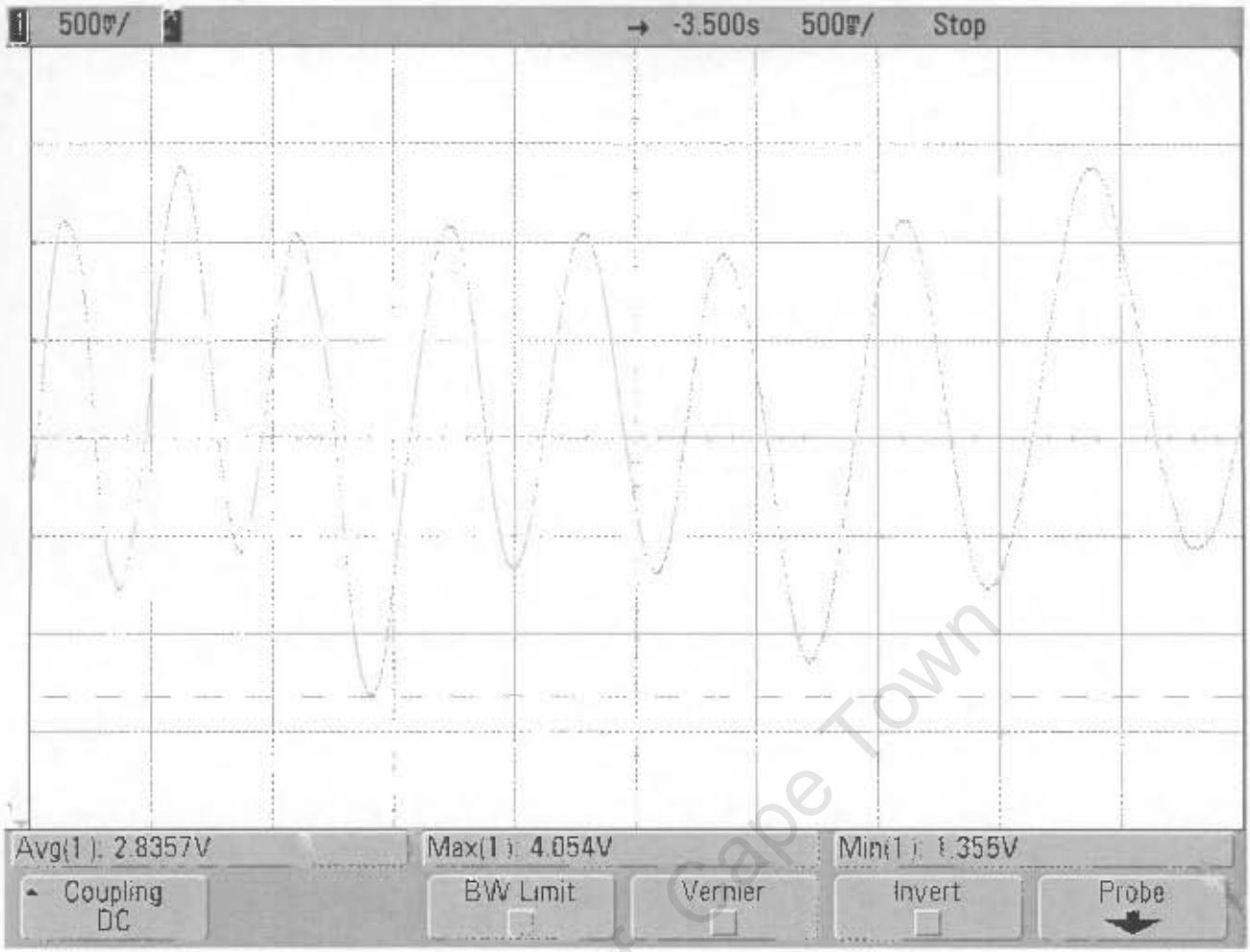

print_01

Hall probe moved slightly
Avg : 2.84
Max : 4.05
Min : 1.36

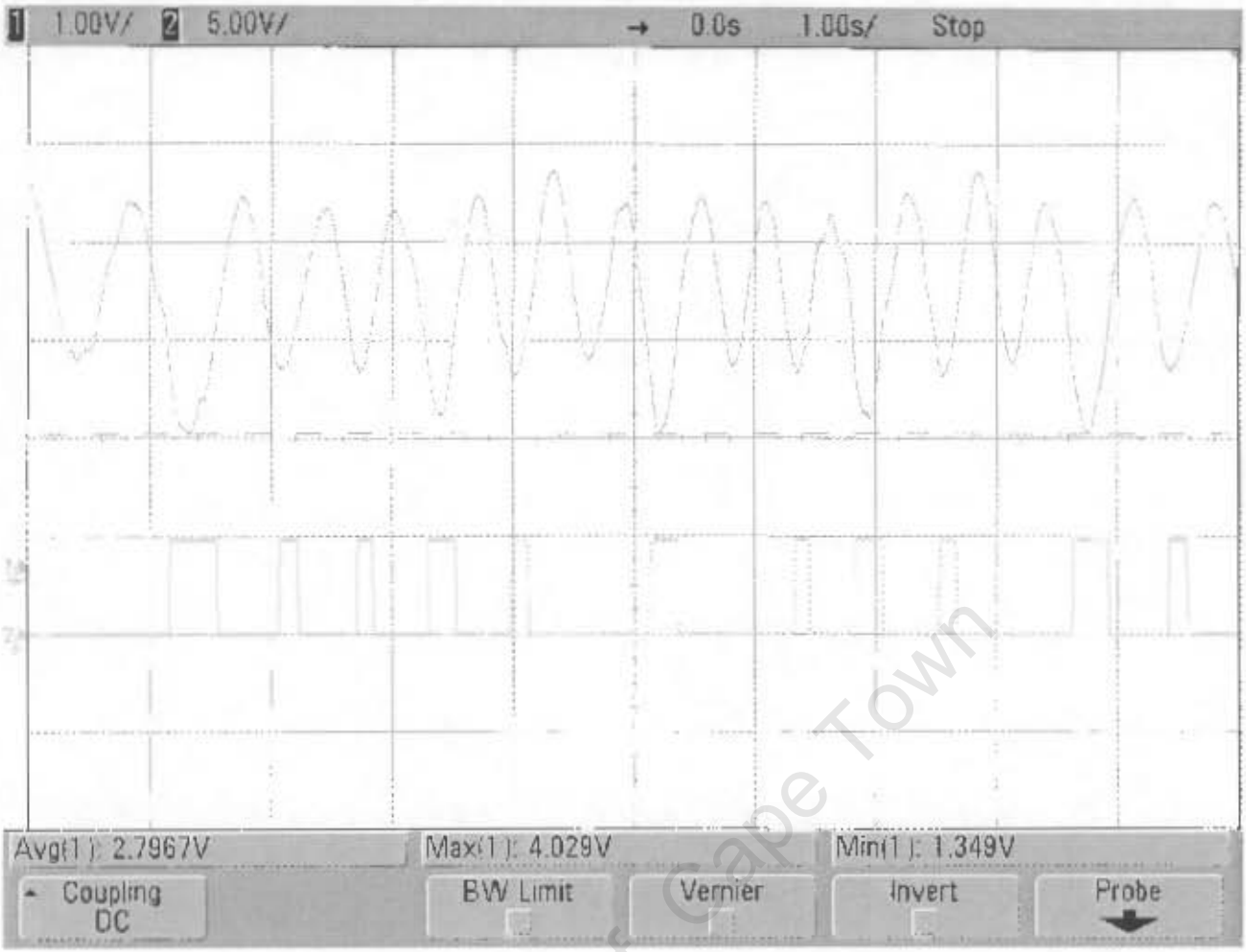

print_02

Hall + firing signal
Levels on ADC
Low level: 416 / 1023
High level: 512 / 1023

New levels needed:
High level: 3.75/5V*1023 = 767
Low level :1.55/5V*1023 = 317

Low level not triggering every time : Try
High level: 760
Low level: 323

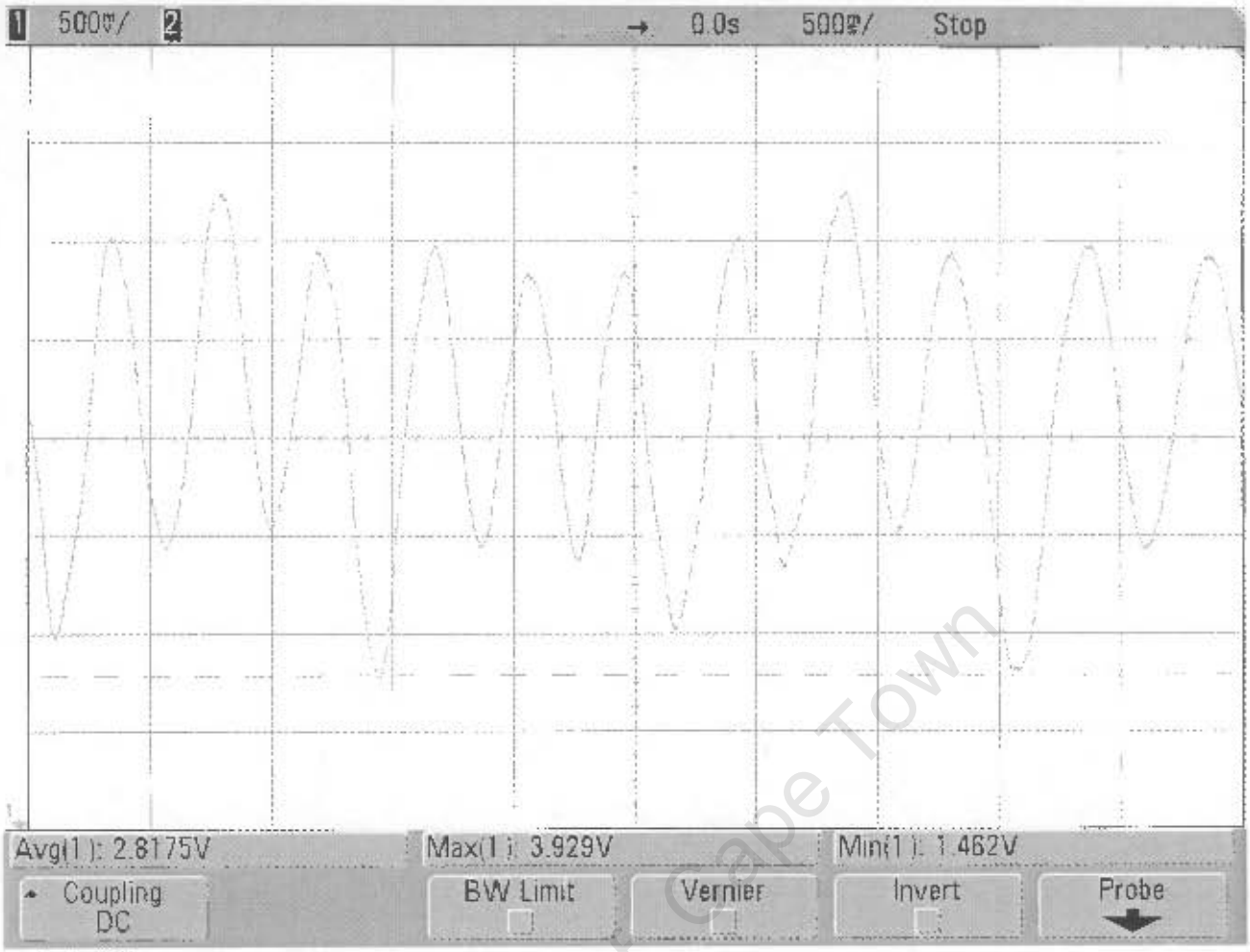

print_00

Hall sense data with UGN3503
Avg: 2.8V
Max: 3.93
Min: 1.46

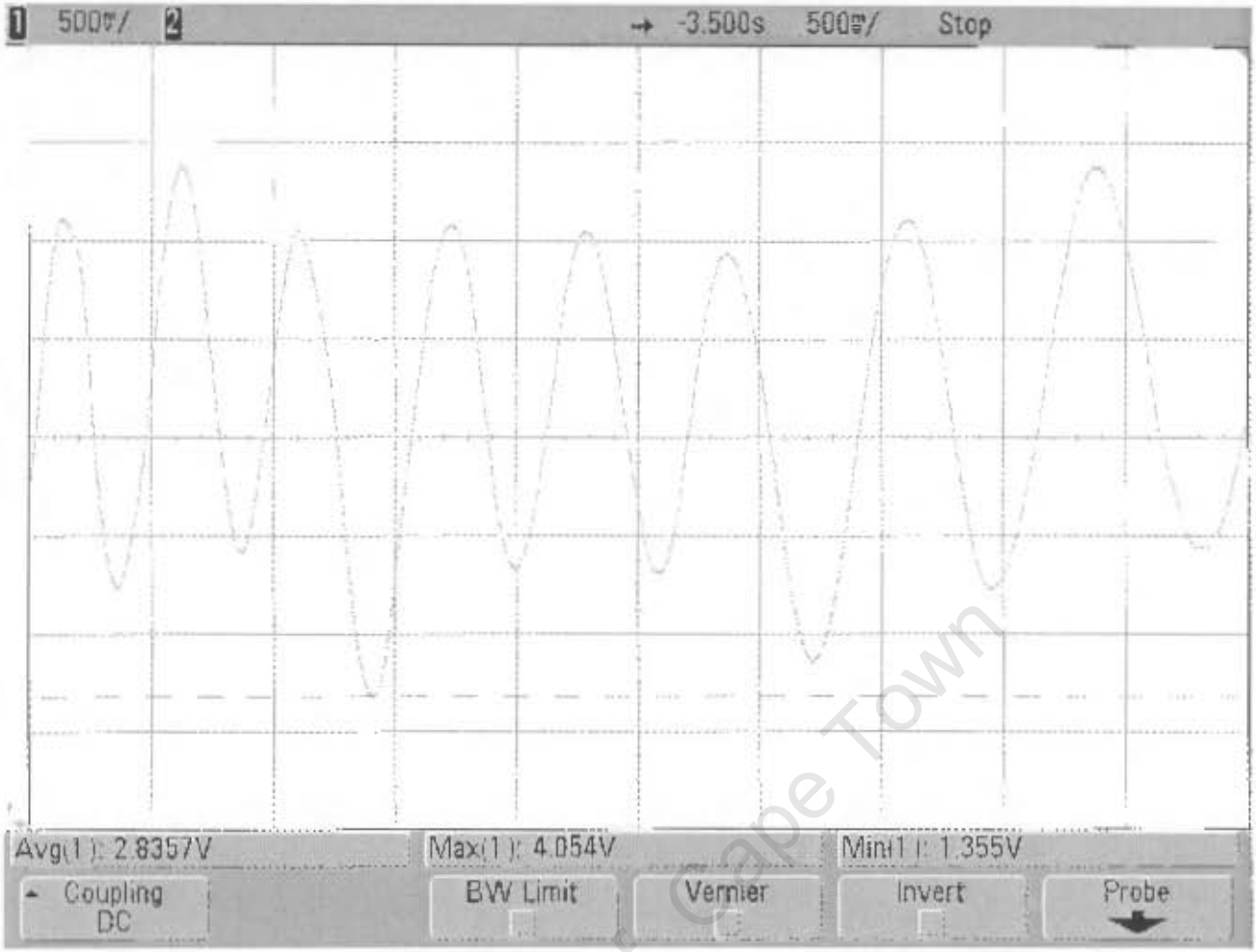

print_01

Hall probe moved slightly
Avg : 2.84
Max : 4.05
Min : 1.36

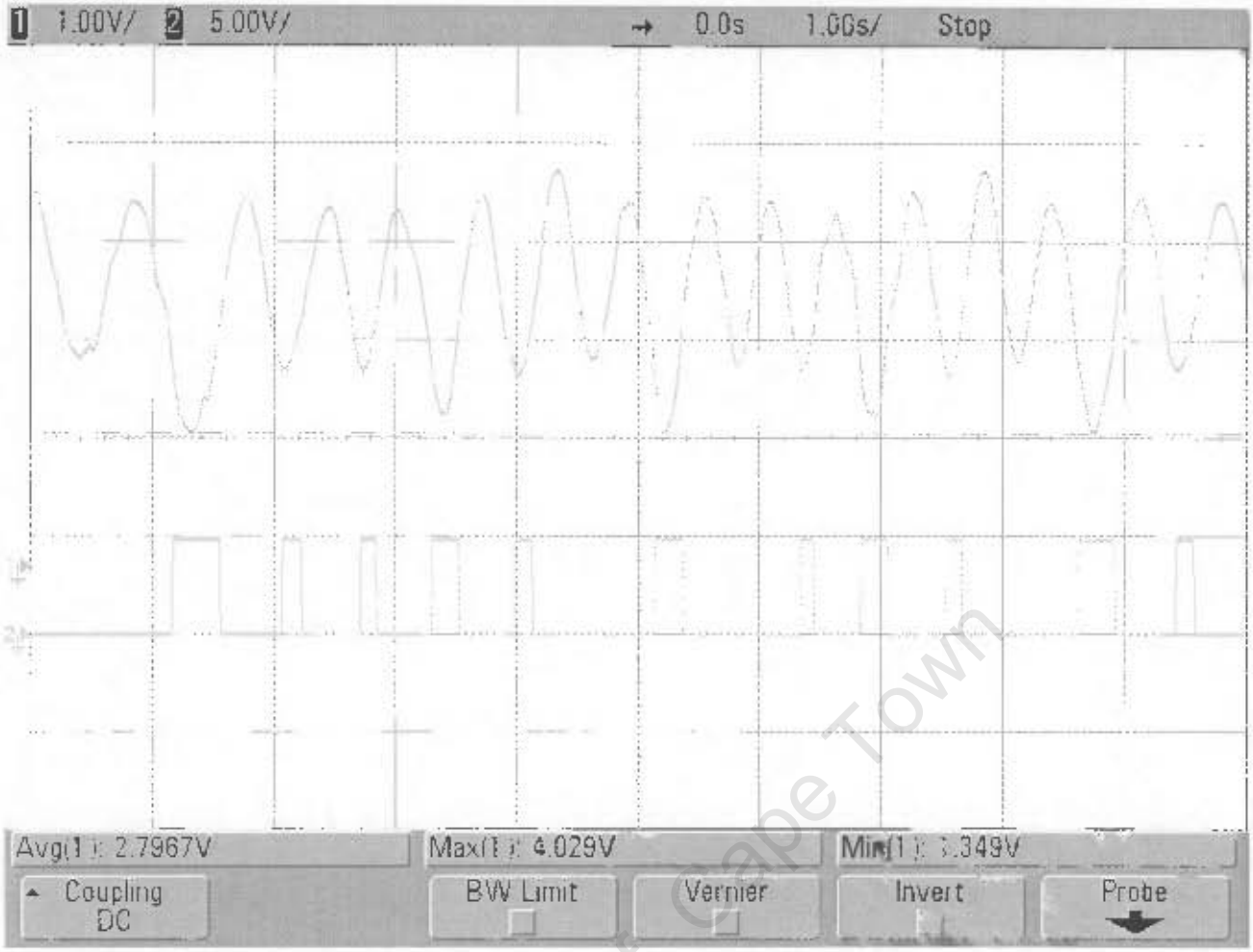

print_02

Hall + firing signal
Levels on ADC
Low level: 416 / 1023
High level: 512 / 1023

New levels needed:
High level: 3.75/5V*1023 = 767
Low level :1.55/5V*1023 = 317

Low level not triggering every time : Try
High level: 760
Low level: 323

2. Performance data acquisition with Oscilloscope captures

Rundown Curves using Oscilloscope

Rundown time		19.24	
T	t	Hz	RPM
-26.8	0	1.31580	78.95
-26.04	0.76	1.25000	75
-25.24	1.56	1.19050	71.43
-23.96	2.84	1.13640	68.18
-23.52	3.28	1.08700	65.22
-23.08	3.72	1.04170	62.5
-22.12	4.68	1.00000	60
-21.64	5.16	0.96514	57.91
-20.6	6.2	0.92593	55.56
-19.52	7.28	0.86207	51.72
-18.92	7.88	0.83333	50
-17.72	9.08	0.78125	46.88
-17.08	9.72	0.73529	44.12
-16.44	10.36	0.67568	40.54
-15.72	11.08	0.64103	38.46
-14.96	11.84	0.59524	35.71
-14.16	12.64	0.55556	33.33
-13.28	13.52	0.49020	29.41
-12.36	14.44	0.42373	25.42
-11.28	15.52	0.33784	20.27

Correlation coeef
0.99660
Linear regression line
-3.57

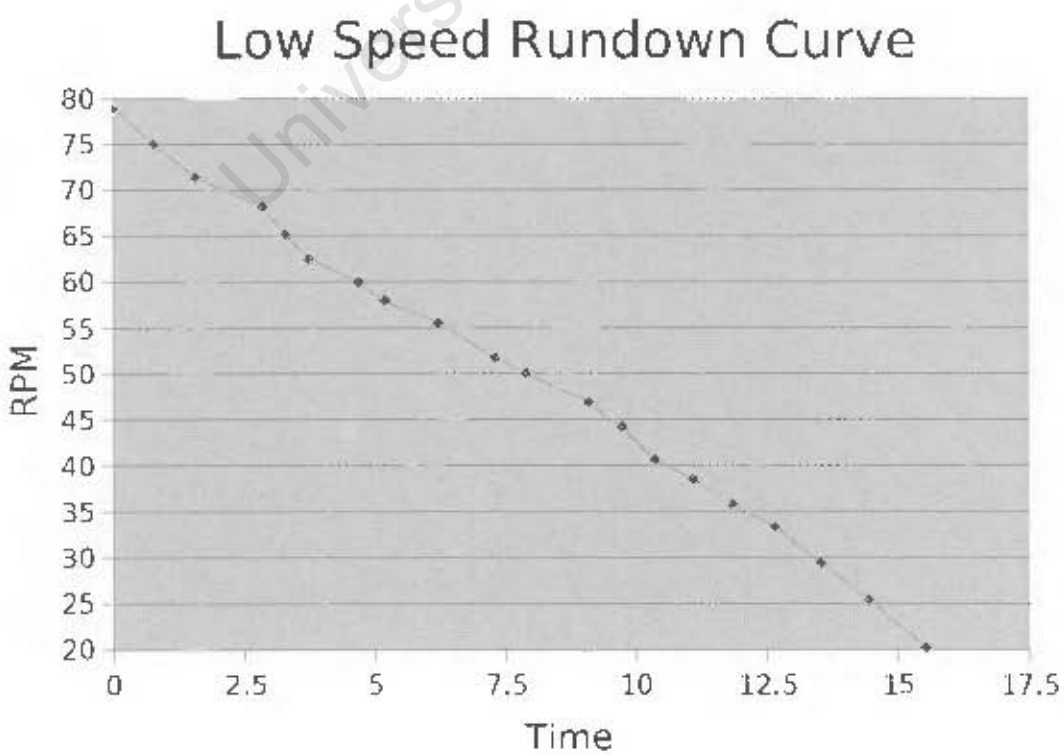

Rundown time		19.24	
T	t	Hz	RPM
-26.8	0	1.31580	78.95
-26.04	0.76	1.25000	75
-25.24	1.56	1.19050	71.43
-23.96	2.84	1.13640	68.18
-23.52	3.28	1.08700	65.22
-23.08	3.72	1.04170	62.5
-22.12	4.68	1.00000	60
-21.64	5.16	0.96514	57.91
-20.6	6.2	0.92593	55.56
-19.52	7.28	0.86207	51.72
-18.92	7.88	0.83333	50
-17.72	9.08	0.78125	46.88
-17.08	9.72	0.73529	44.12
-16.44	10.36	0.67568	40.54
-15.72	11.08	0.64103	38.46
-14.96	11.84	0.59524	35.71
-14.16	12.64	0.55556	33.33
-13.28	13.52	0.49020	29.41
-12.36	14.44	0.42373	25.42
-11.28	15.52	0.33784	20.27

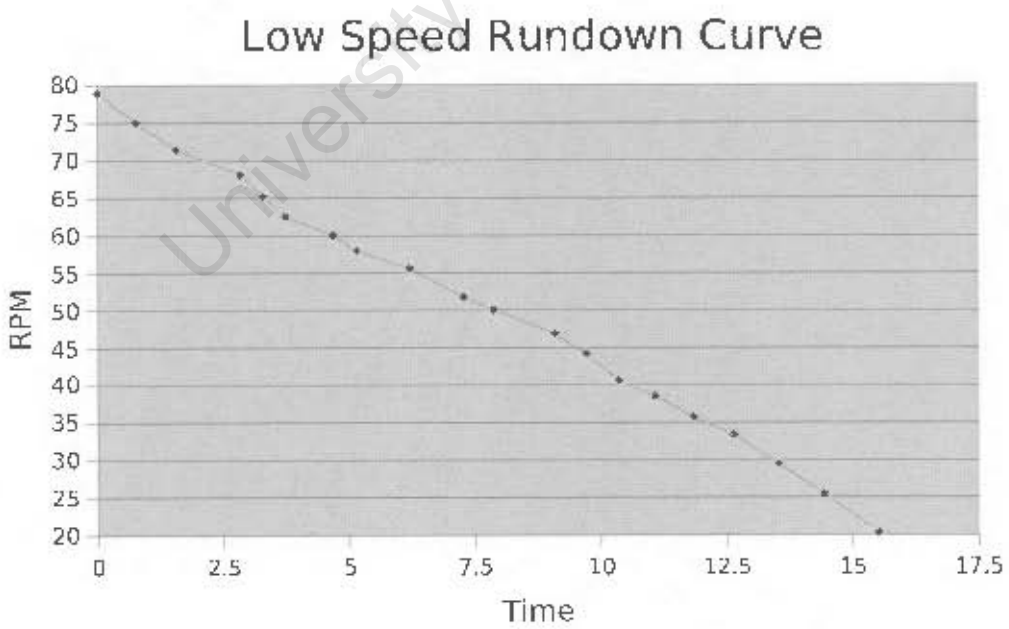

Run Curve at constant Power of 33W

Runup 0

f	I	Time	
	2.7	15	0
	3.23	15	32.75
	4.2	15.5	38.14
	4.7	14.5	54.74
	5.1	14	70.23

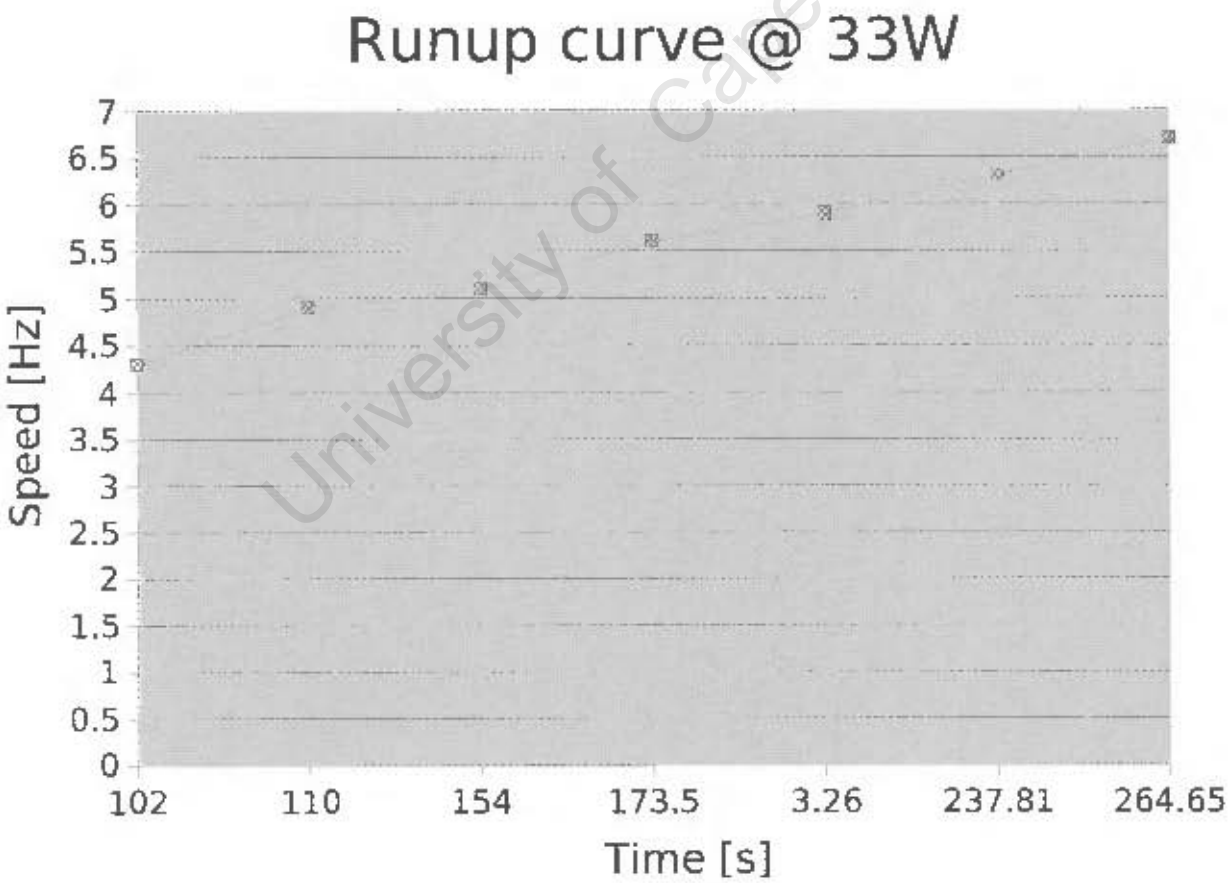

Rundown curves

Time	w*2	T	RPM	
	0	6	170	180
	4.69	5.7	175	171
	13.38	5.1	195	153
	24.41	4.5	220	135
	35.45	3.8	260	114
	48.75	3.13	320	93.9
	61.59	2.41	415	72.3
	74.21	1.69	590	50.7

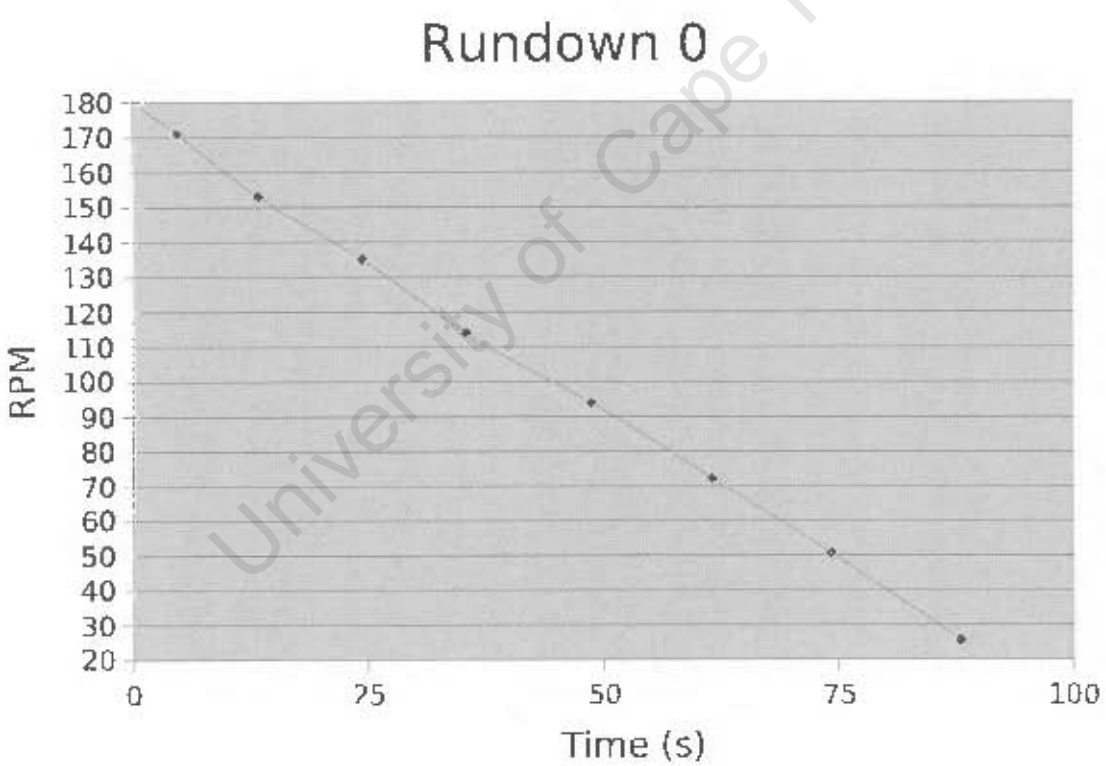

Rundow 1

Time	Time(s)	w*2	T	RPM
-107.4	0	5.32	188	319.14
-104.6	2.8	5.26	190	315.79
-101.5	5.9	5.21	192	312.5
-98.39	9.01	5.1	196	306.12
-93.95	13.45	5	200	300
-91.44	15.96	4.85	206	291.24
-88.78	18.62	4.81	208	288.46
-83.97	23.43	4.72	212	283.02
-80.73	26.67	4.55	220	272.73
-77.82	29.58	4.39	228	263.16
-75.37	32.03	4.17	240	250.02
-71.77	35.63	3.88	258	232.56
-69.26	38.14	3.73	268	223.86
-66.21	41.19	3.47	288	208.32
-63.37	44.03	3.19	314	191.1
-59.96	47.44	2.94	340	176.46
-57.71	49.69	2.82	354	169.49
-54.62	52.78	2.67	374	160.44
-52.12	55.28	2.51	398	150.76
-48.41	58.99	2.29	436	137.62
-45.95	61.45	2.16	464	129.31
-42.83	64.57	1.99	502	119.52
-38.62	68.78	1.77	566	106.02
-34.13	73.27	1.54	648	92.58
-30.39	77.01	1.36	734	81.74
-28.12	79.28	1.25	800	75
-25.64	81.76	1.14	880	68.18
-21.89	85.51	0.95	63.36	56.82
-14.38	93.02	0.59	102	35.29
-10.71	96.69	0.42	142.8	25.21
-7.44	99.96	0.18	333.6	10.79

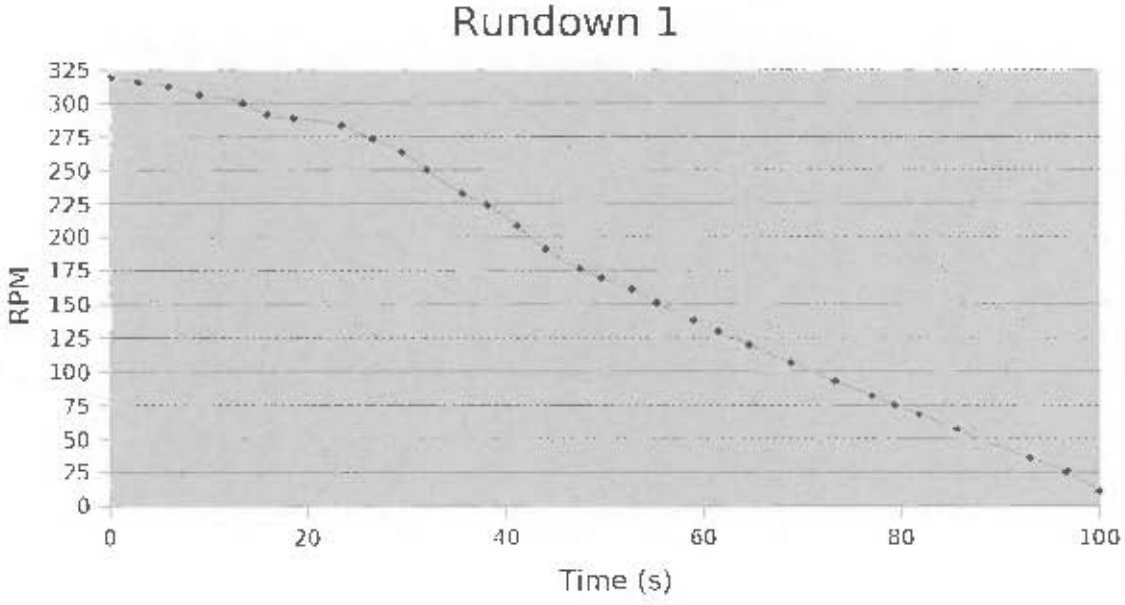

time	speed x2	speed	RPM
10.85	11.1	5.55	333
20.84	8.3	4.15	249
29.53	6.9	3.45	207
39.45	5.6	2.8	168
48.87	4.5	2.25	135
57.9	3.39	1.7	101.7
67	2.15	1.08	64.5
78.5	0.52	0.26	15.45

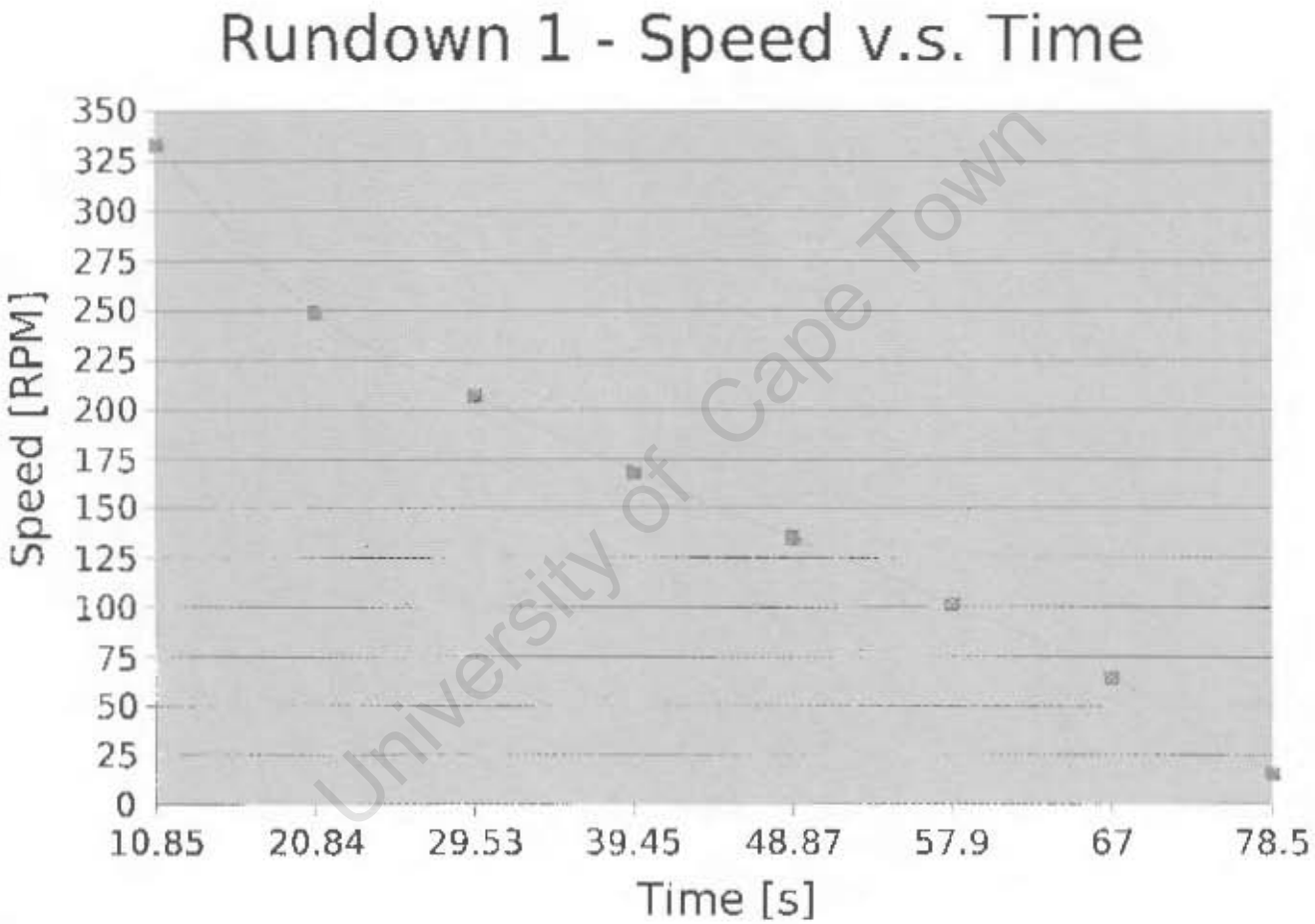

time	speed x2	speed	RPM
0	13	6.5	390
7.84	10	5	300
15.53	9.5	4.75	285
27.2	8.3	4.15	249
7.1	7.7	3.85	231
49.9	6.3	3.15	189
58.3	5.3	2.65	159
67.08	4.4	2.2	132
75.13	3.64	1.82	109.2

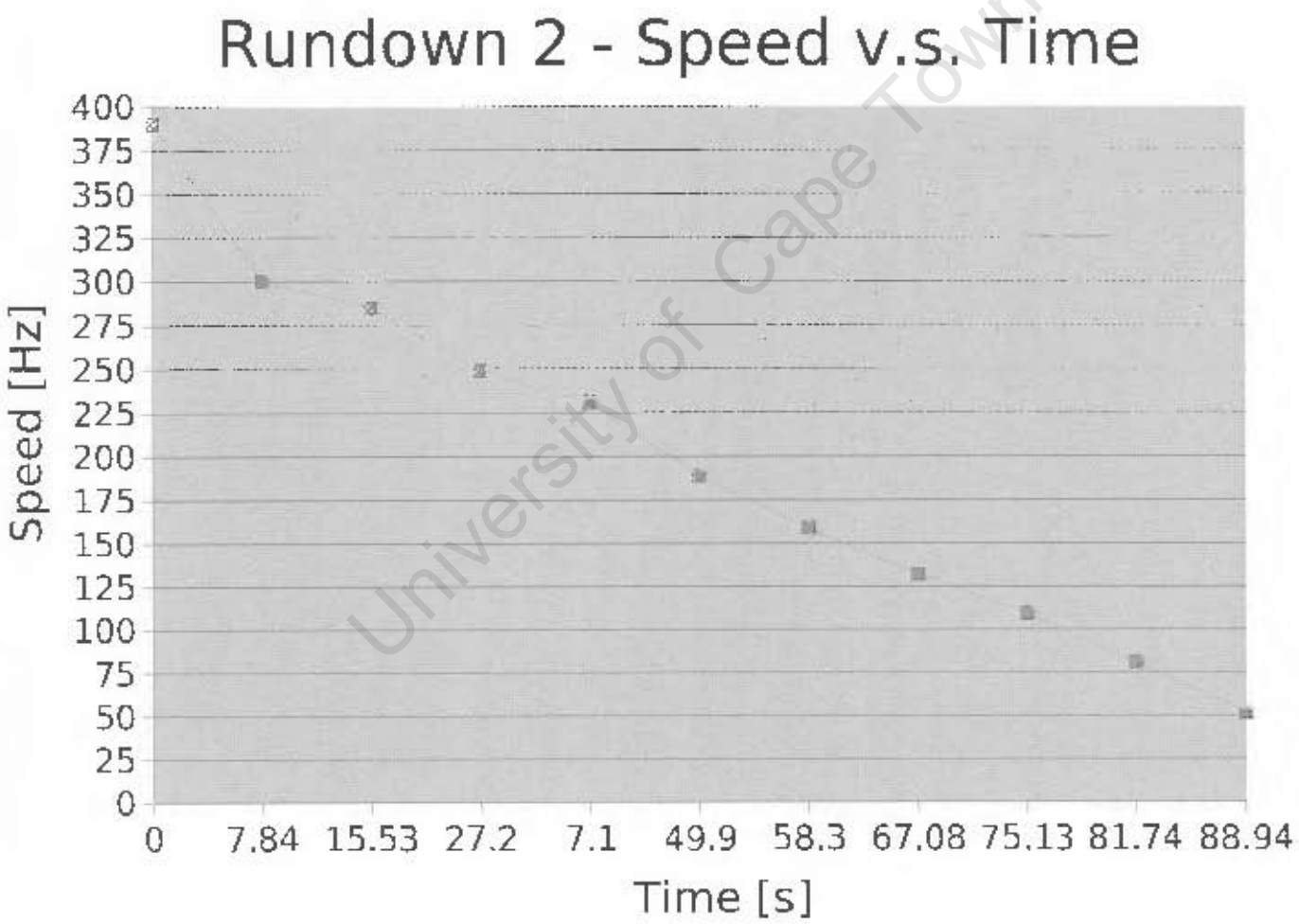

time	speed	RPM	$T_{decellerate}$	$P_{decellerate}$
0	7.5	450	#DIV/0!	
6.01	5.55	333	5.8	37.86
13.1	5	300	-3.61	-19.05
23.73	4.55	273	-11.9	-56.8
28.45	4.15	249	-22.81	-99.24
34.64	3.85	231	-27.75	-111.01
42.43	3.45	207	-34.13	-124.57
47.11	3.35	201	-41.98	-142.74
52.12	3.05	183	-46.74	-149.58
56.6	2.7	162	-51.82	-148.98
61.6	2.45	147	-56.35	-145.1
66.52	2.15	129	-61.4	-141.21
71.38	1.85	111	-66.36	-132.71
76.54	1.5	89.7	-71.26	-119.18
81.59	1.07	63.9	-76.46	-97.87
86.75	0.64	38.1	-81.54	-69.31

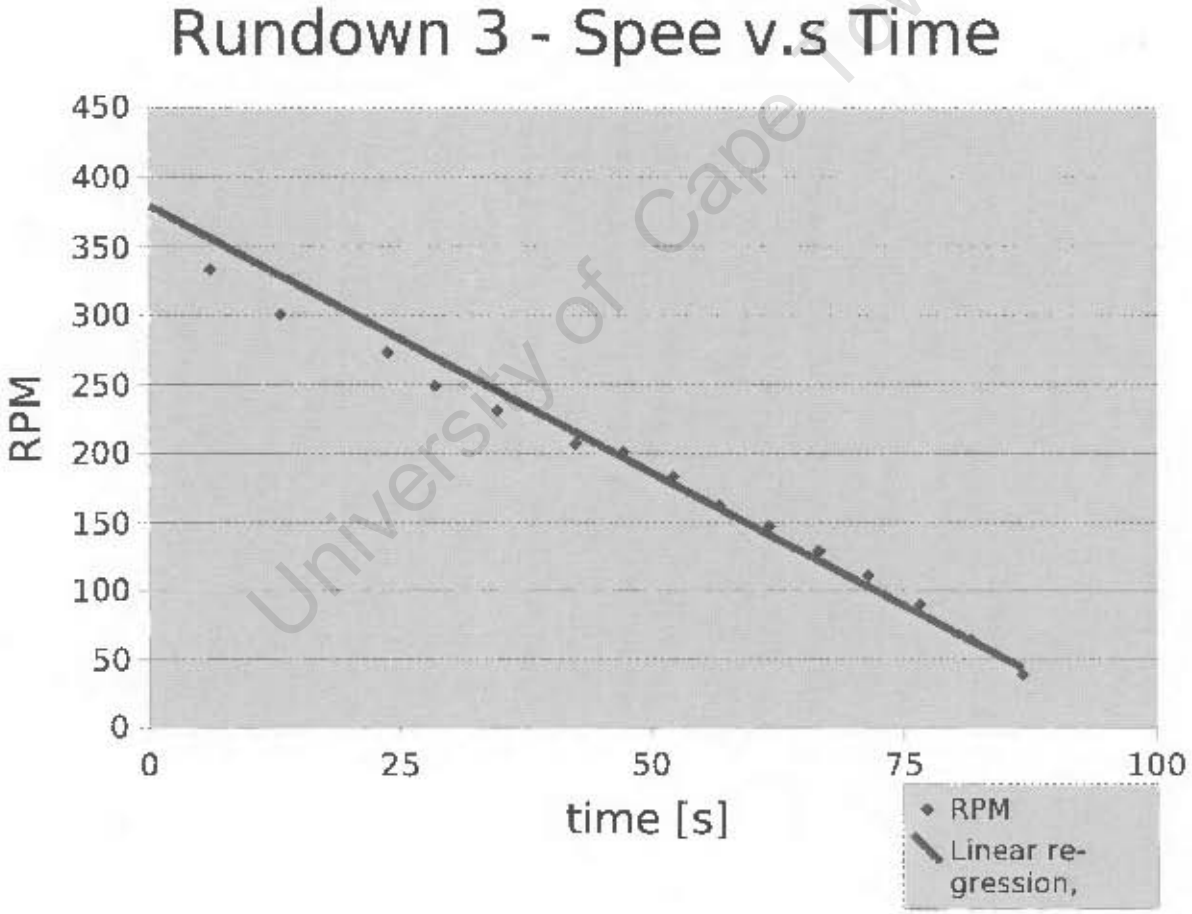

powered rundown – constant current of 10A

with 10A applied time	speed x2	speed
0	9.1	4.55
6.01	8.3	4.15
10.29	7.7	3.85
15.07	6.9	3.45
19.15	6.1	3.05
23.29	5.3	2.65
27.59	4.4	2.2
31.67	3.7	1.85
36.35	2.63	1.32
41.17	1.69	0.85
48.93	0.57	0.29

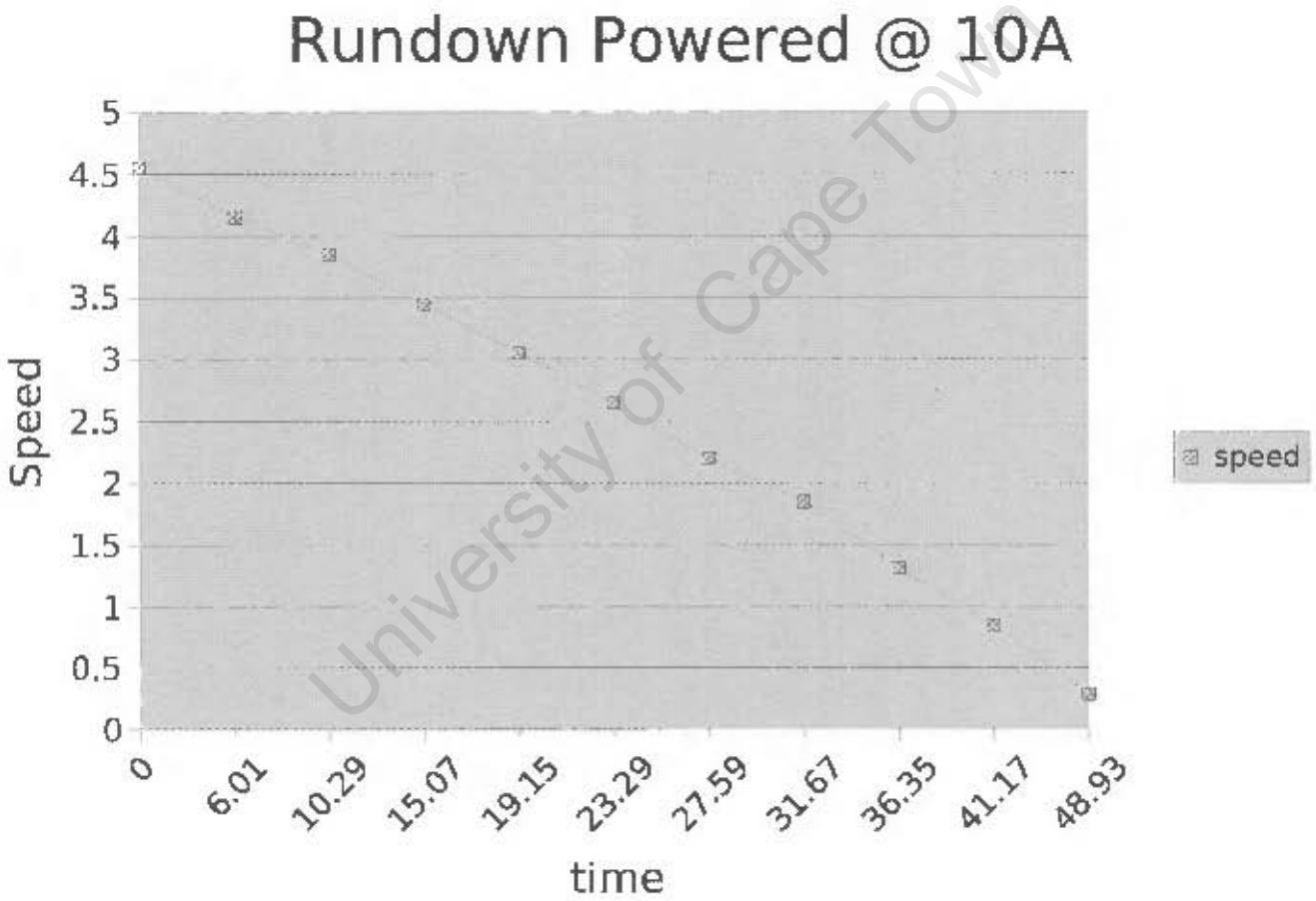

Powered rundown 5A – bearing lifted

time	speed x 2	speed
0	17	8.5
6.27	15	7.5
15.68	13	6.5
22.1	11.8	5.9
27.37	11.1	5.55
31.7	9.5	4.75
37.33	8	4
42.63	6.1	3.05
47.48	4.3	2.15
51.96	2.67	1.34
57.08	1.04	0.52

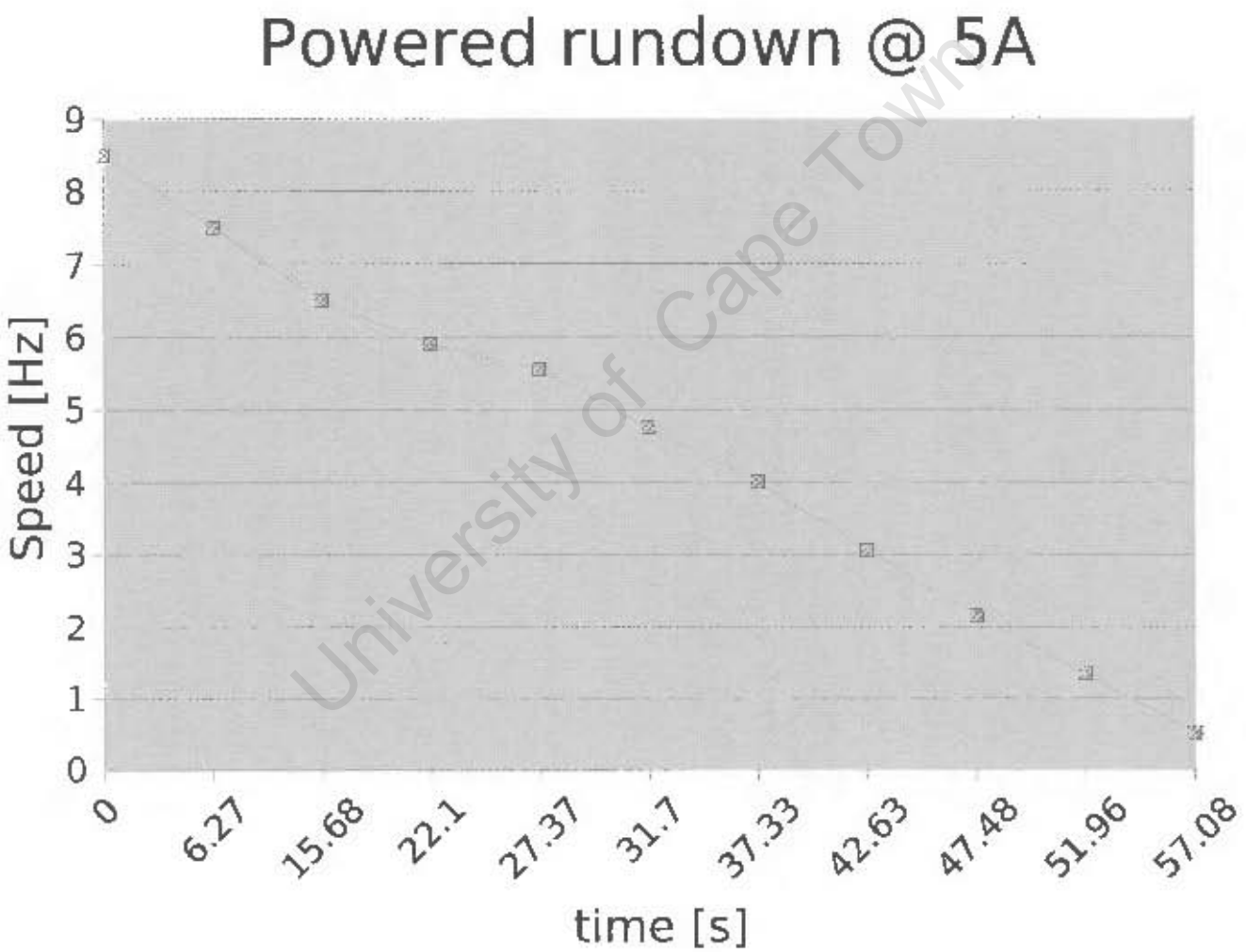

Powered @ 5A

Time	Speed x 2	Speed
6.4	8.7	4.35
10.5	6.5	3.25
14.23	5.1	2.55
18.15	4.1	2.05
22.37	3.13	1.57
27.04	2.15	1.08
32.51	1.03	0.51

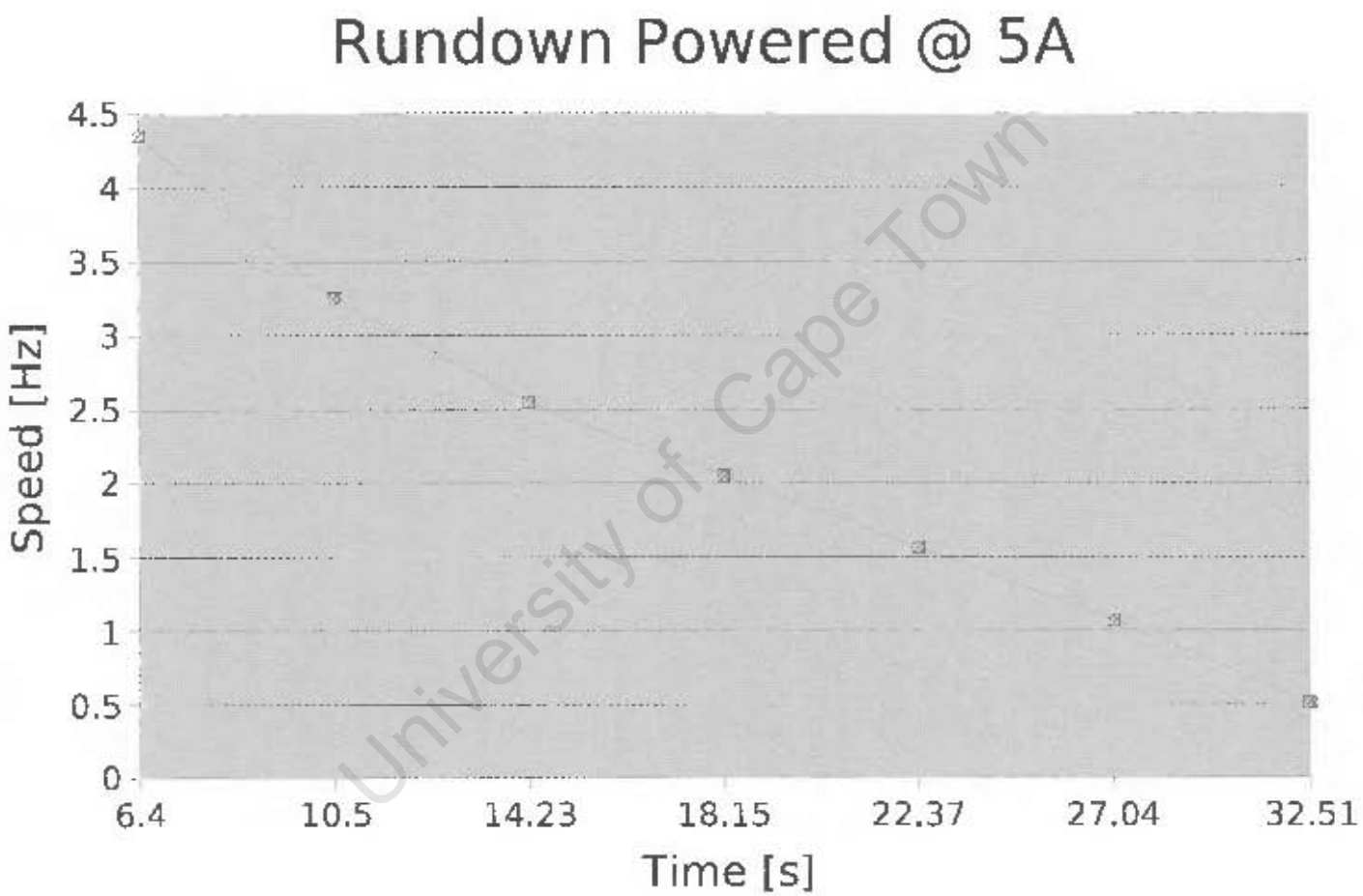

Rundown Powered @ 6A

Time	Speed x 2	Speed	RPM
0	14	7	420
5.64	9.5	4.75	285
10.13	7.7	3.85	231
14.11	6.3	3.15	189
17.95	5	2.5	150
21.71	4	2	120
25.95	2.9	1.45	87
30.15	1.89	0.95	56.7
34.99	0.81	0.4	24.24

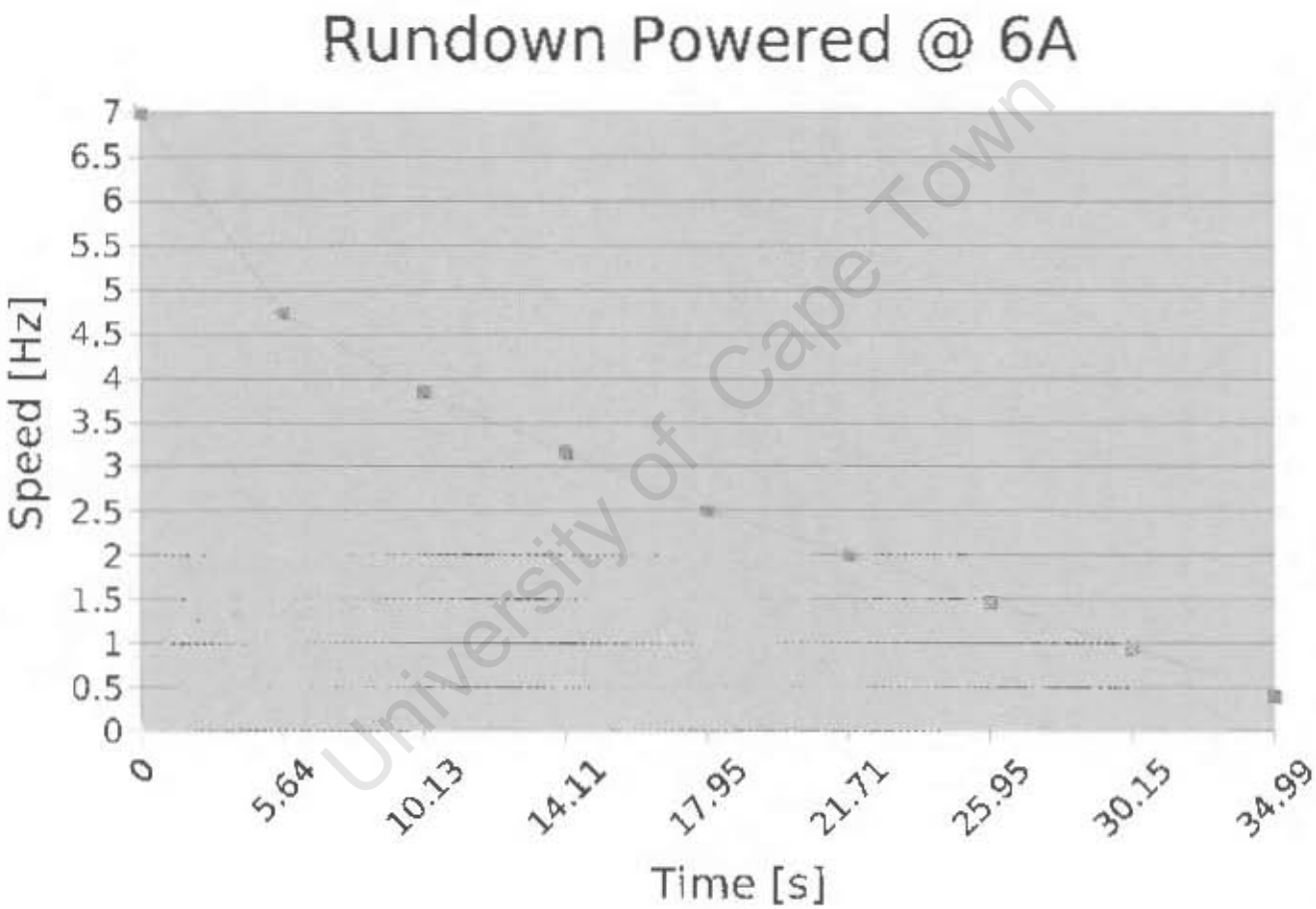

Voltage generated v.s. speed relationship

mV	freq
8	11.1
7.7	10
6.8	8.7
6.1	7.7
5.2	6.3
4.2	5.1
3.5	3.46
2	2.5
1.2	1.8
0.3	0.55

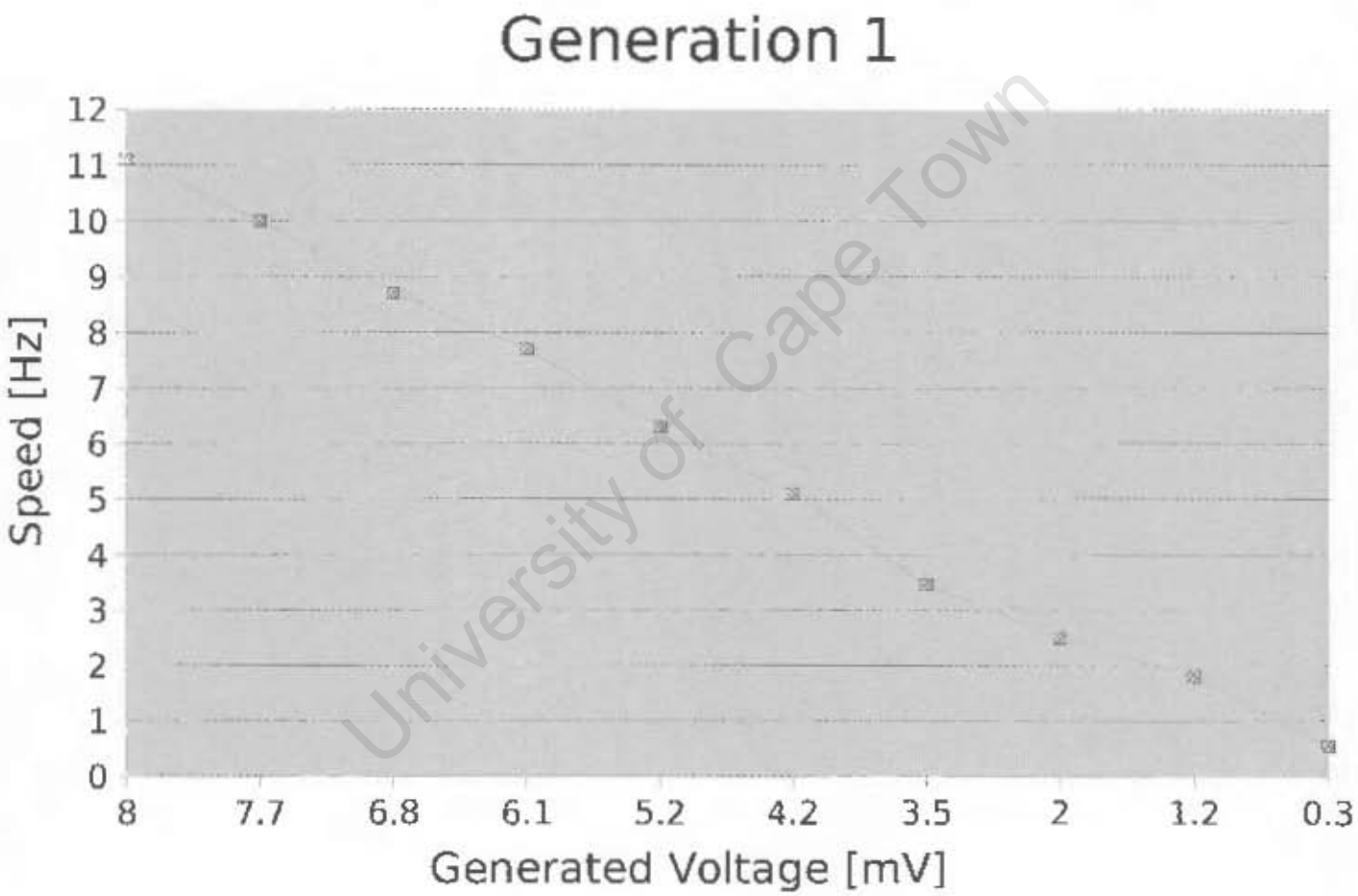

mV	speed x 2
9.2	13
8.8	11.1
7	8.9
6.1	7.4
4.2	5.1
3.2	3.1
1.5	1.3
0	0.75

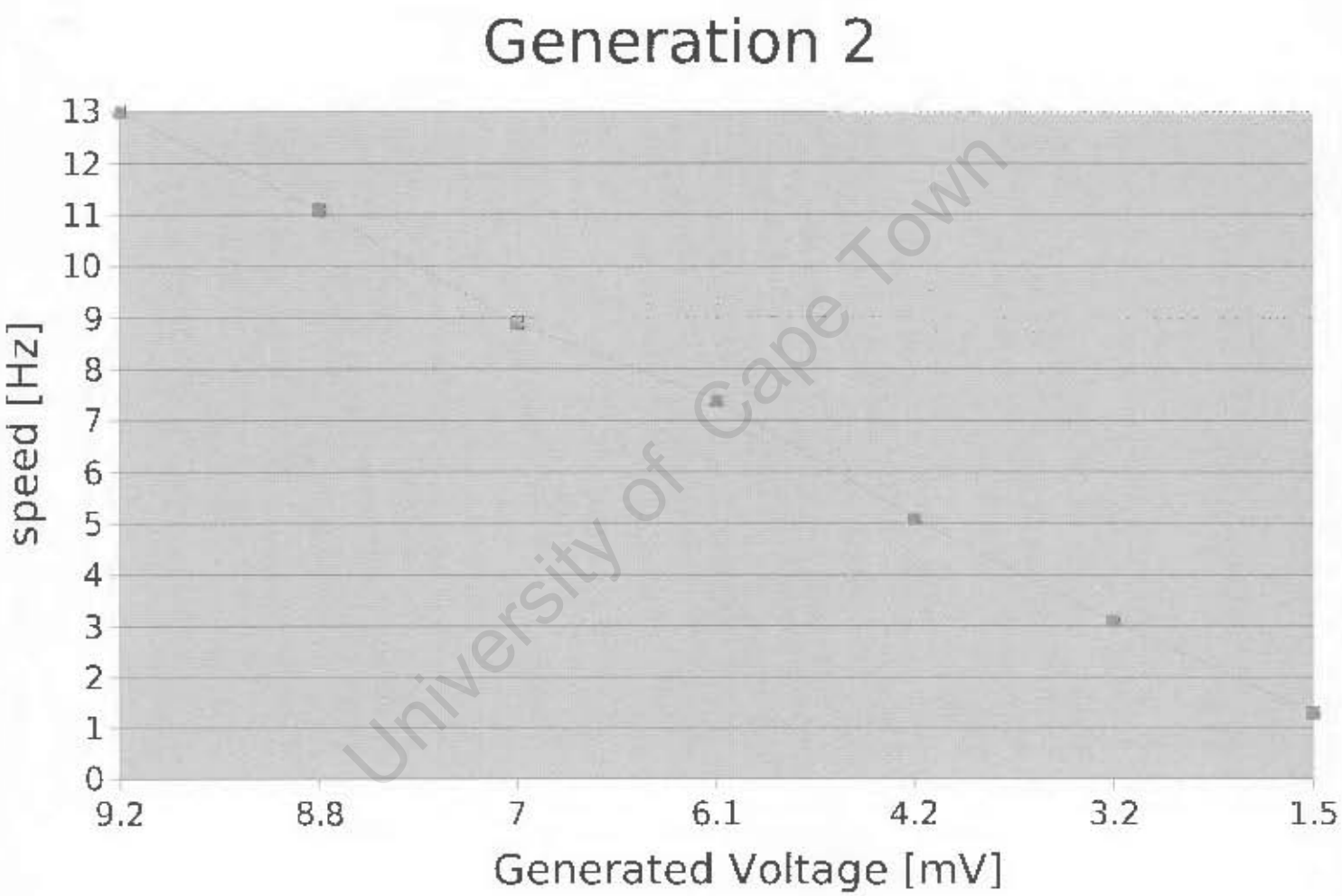

3. Performance Data by acquisition from with AVR Microprocessor with 11bit oversampling and decimation

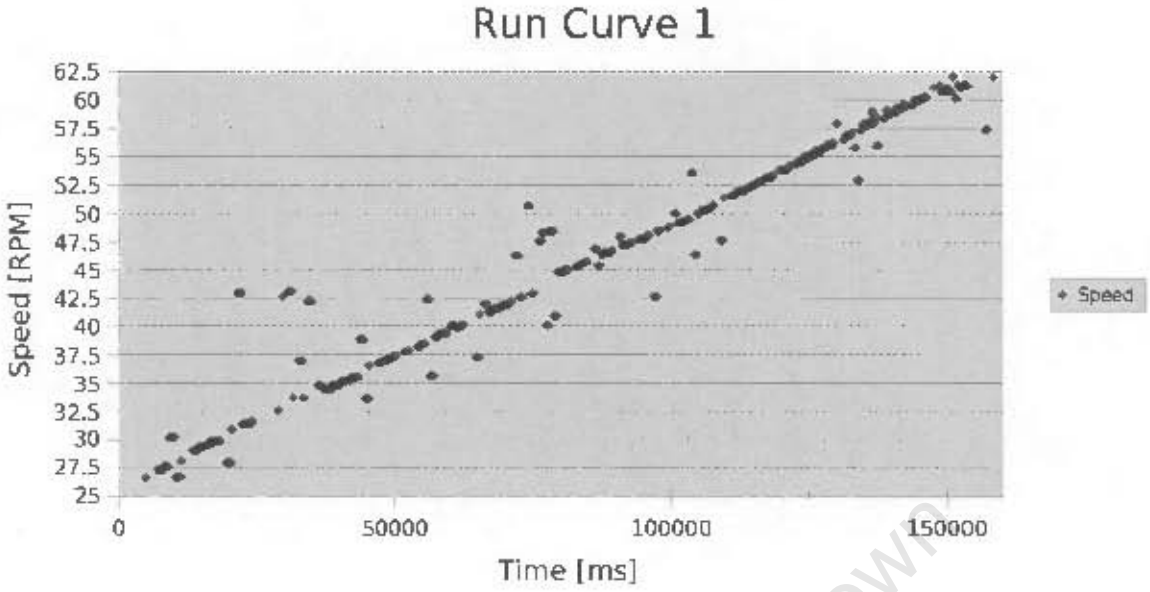

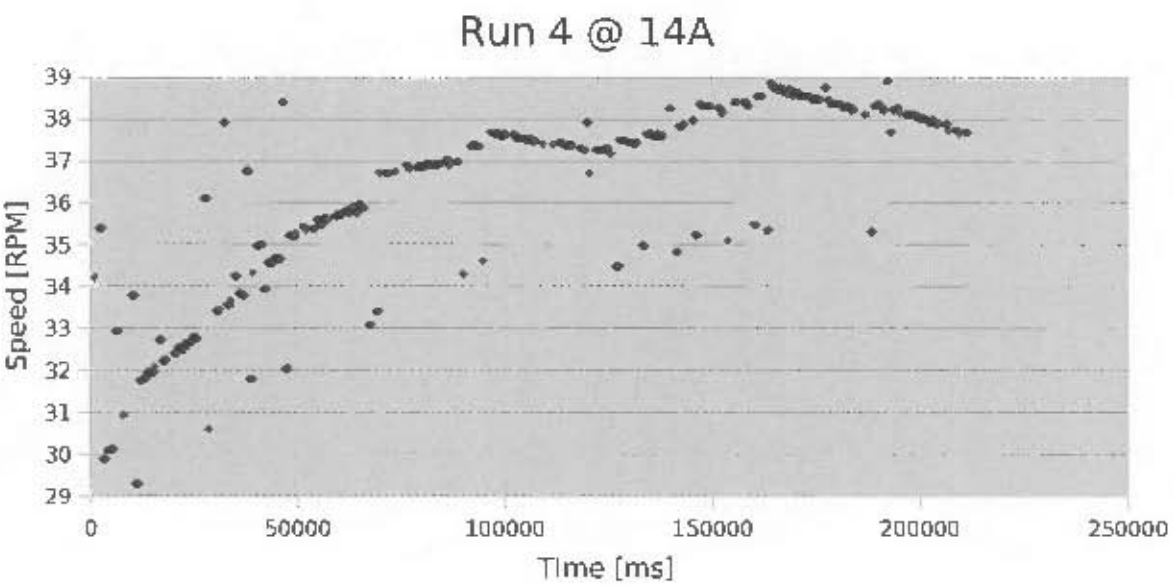

4. Performance Data by acquisition from with AVR Microprocessor with 12bit oversampling and decimation

4.1 Run results

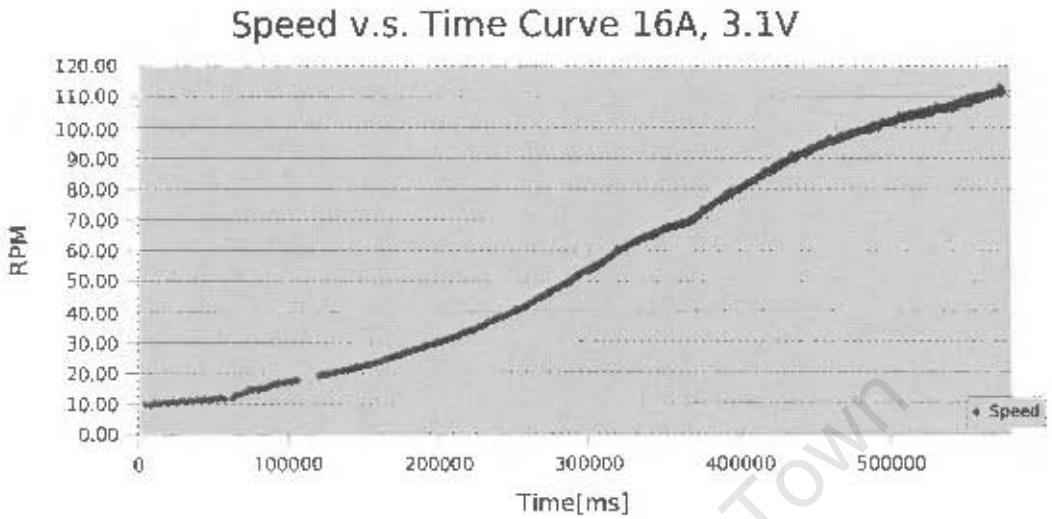

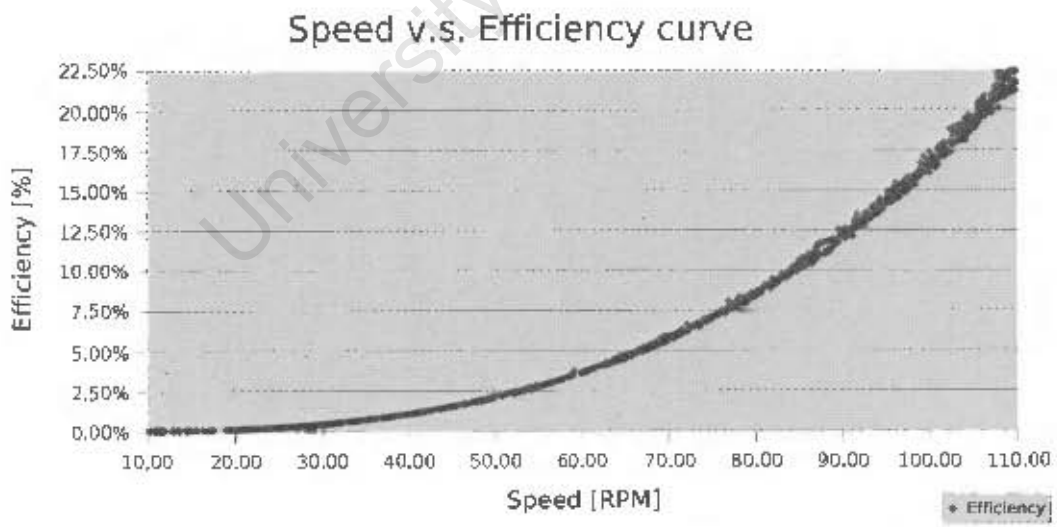

4.Rundown Results

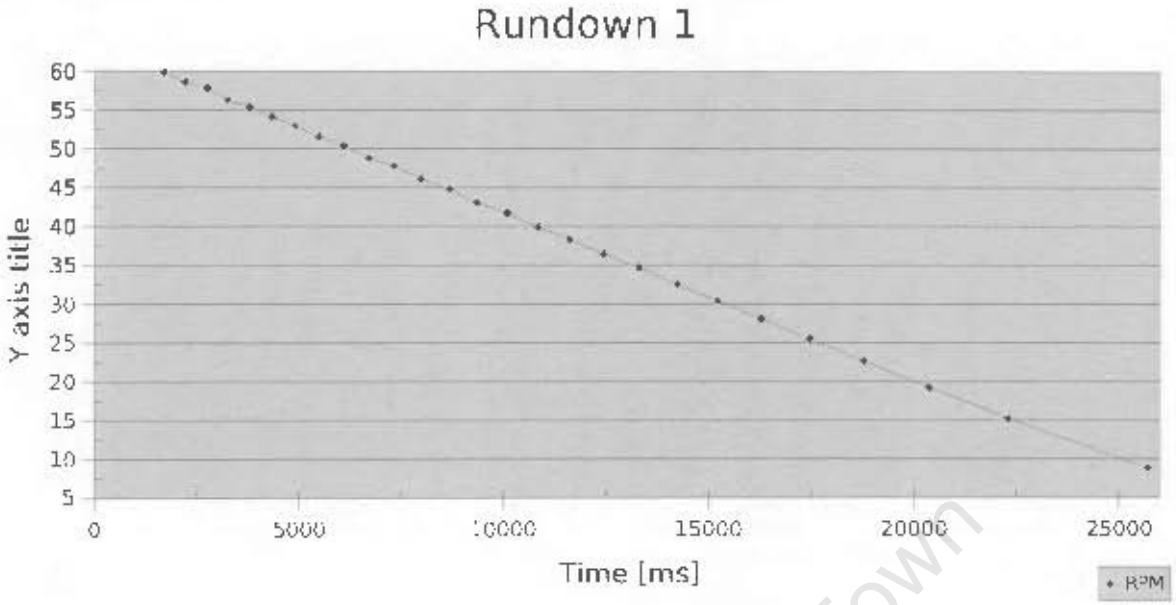

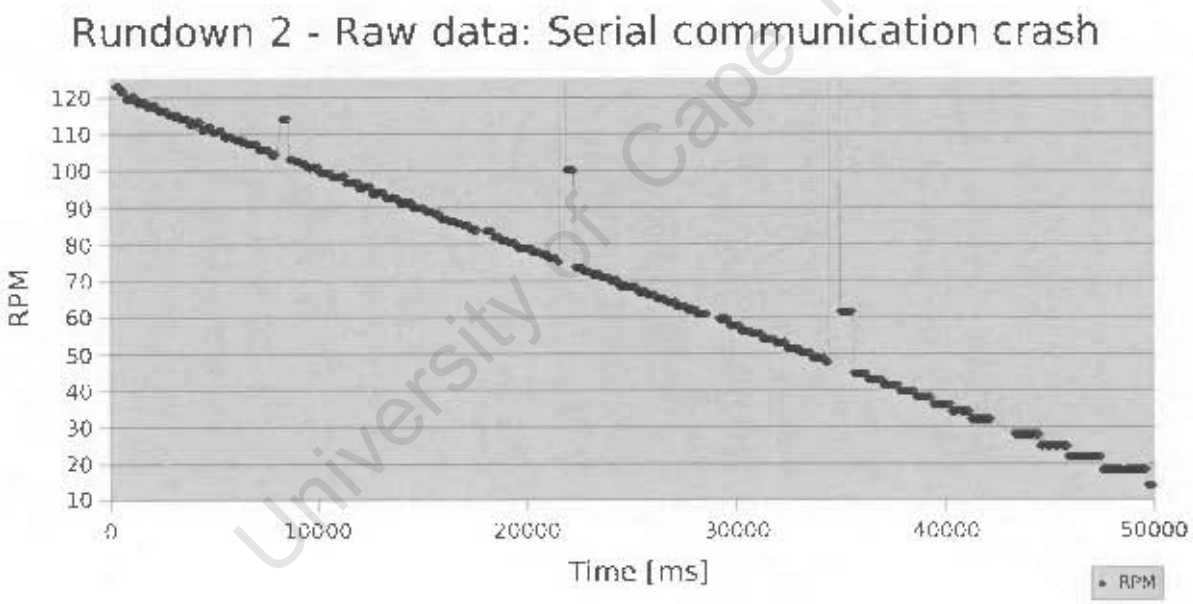

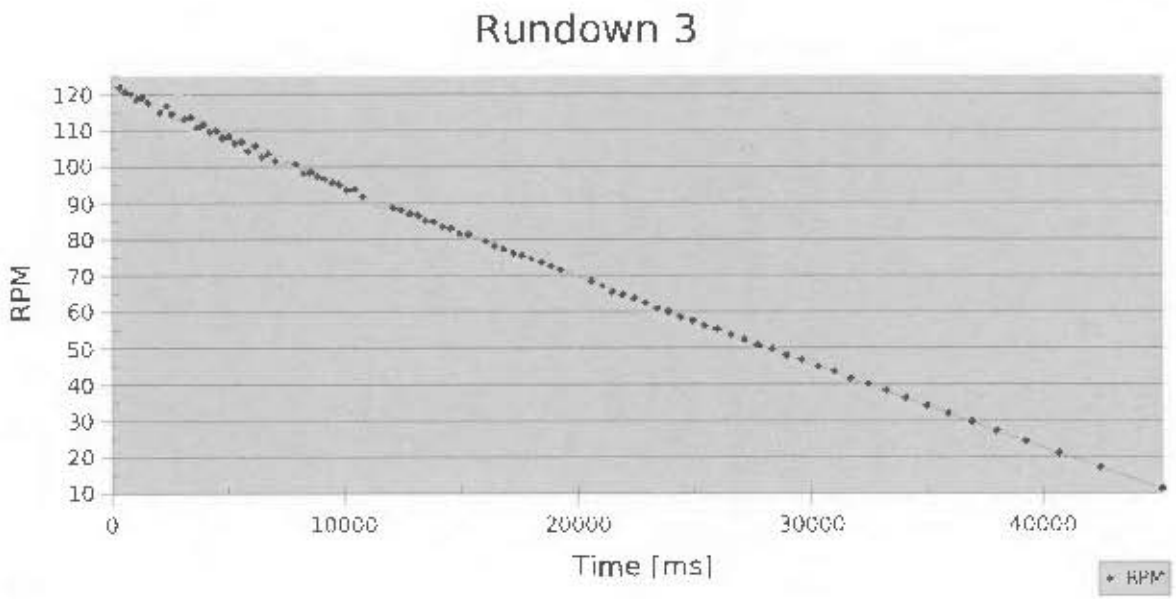

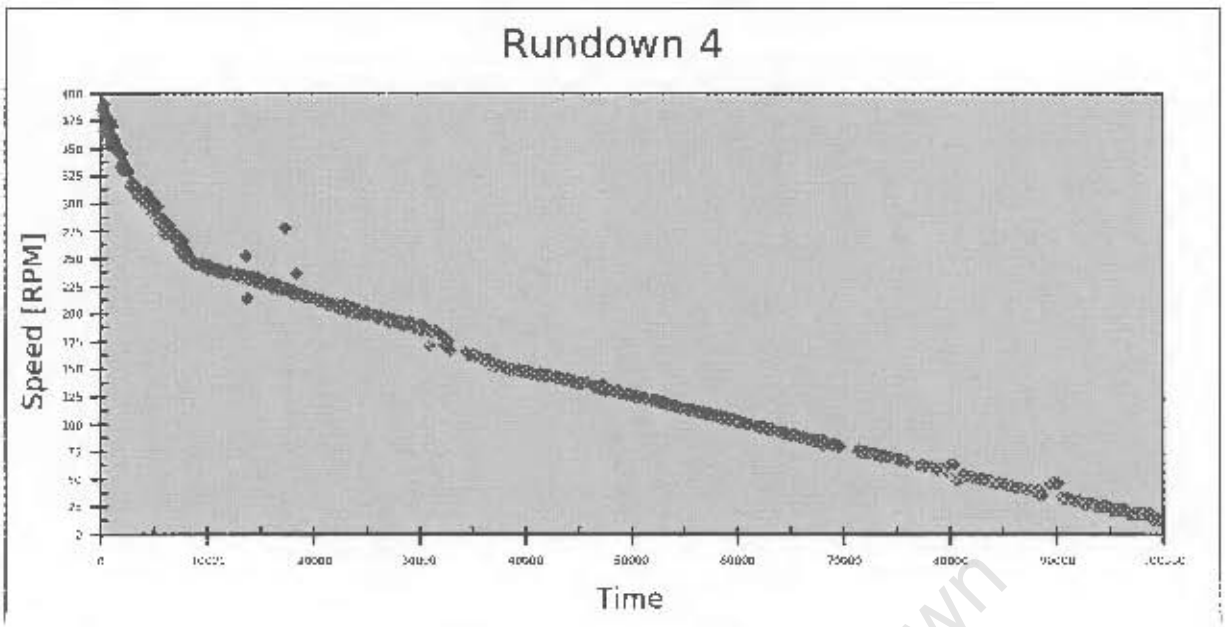

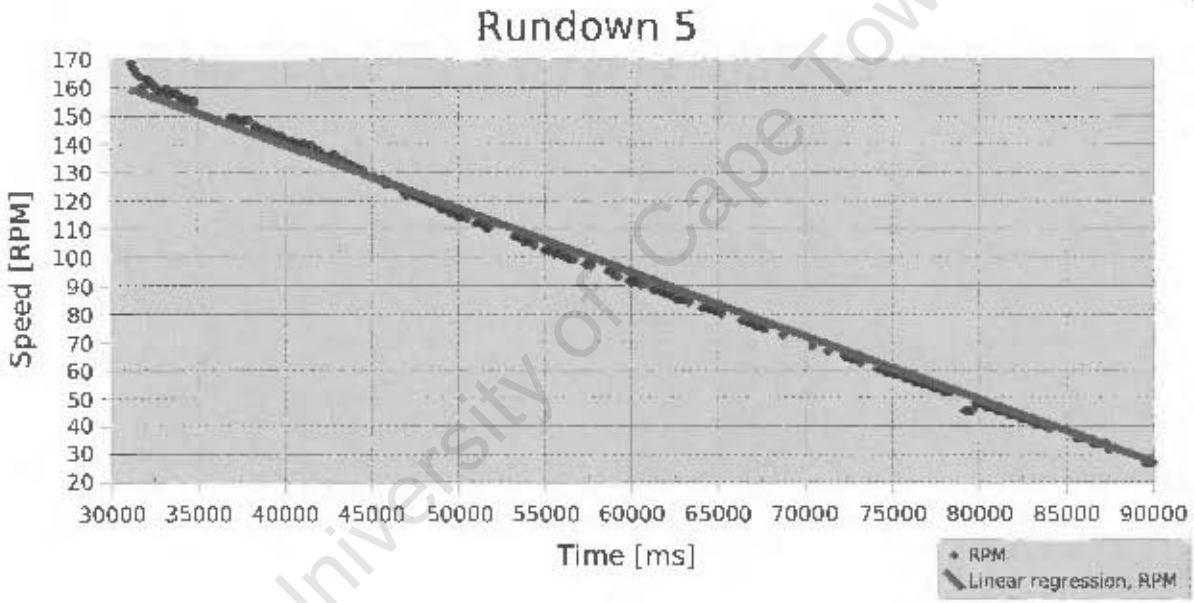

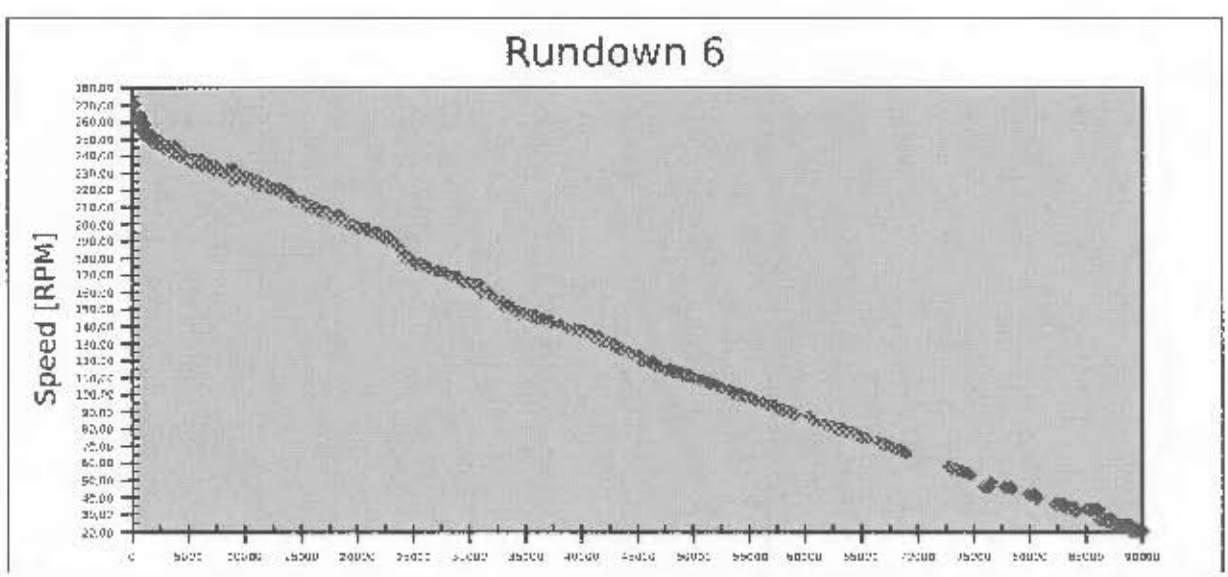

Analog to Digital converter calibration

nmeter Ran	I	ADC_I	ltmeter ran	V	ADC_V
1	0.2	46.1	2	0.0000	0
1	0.39	102.4	2	0.0750	1
1	0.61	179.5	2	0.1154	3.95
1	0.8	243	2	0.1394	6.5
1	1	301	2	0.1779	9.9
3	2	674	2	0.3780	32
3	2	674	2	0.3780	32
10	3	1155	2	0.6280	59.4
10	4	1491	2	0.7840	78.5
10	5	1835	2	0.9680	99
10	6	2105	2	1.0970	113
10	7	2447	2	1.2730	133.4
10	8	2780	2	1.4500	153.4
30	15	3625	2	1.9580	214
30	20	4970	10	3.6300	405

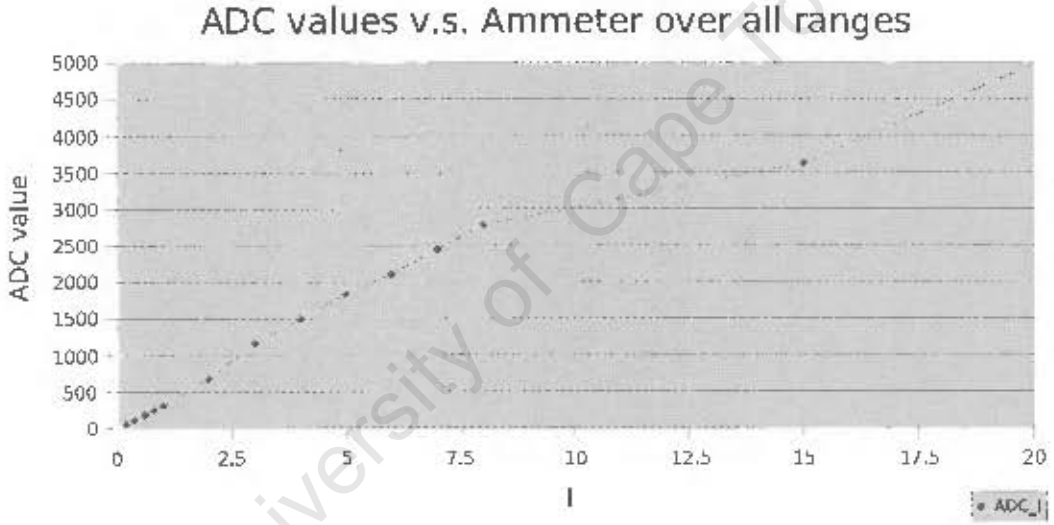

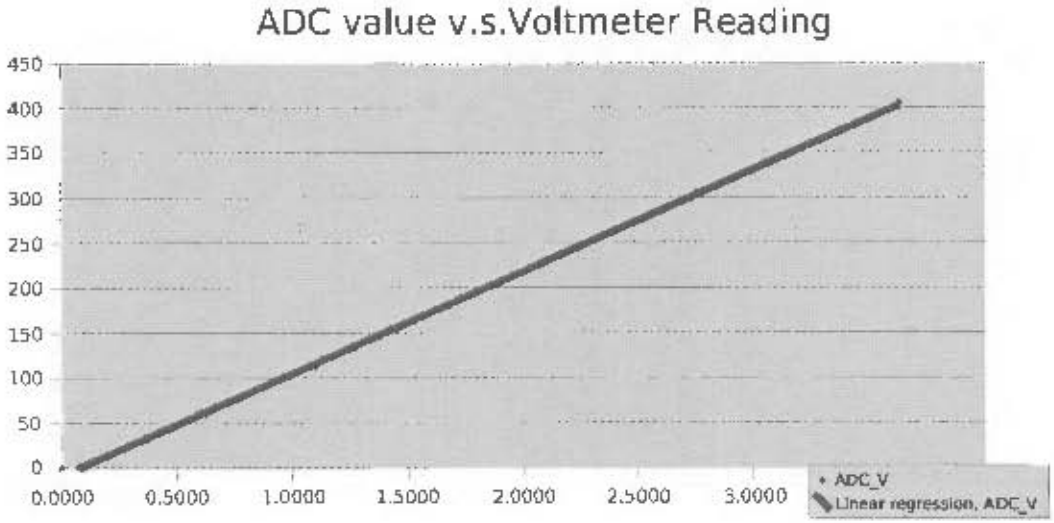

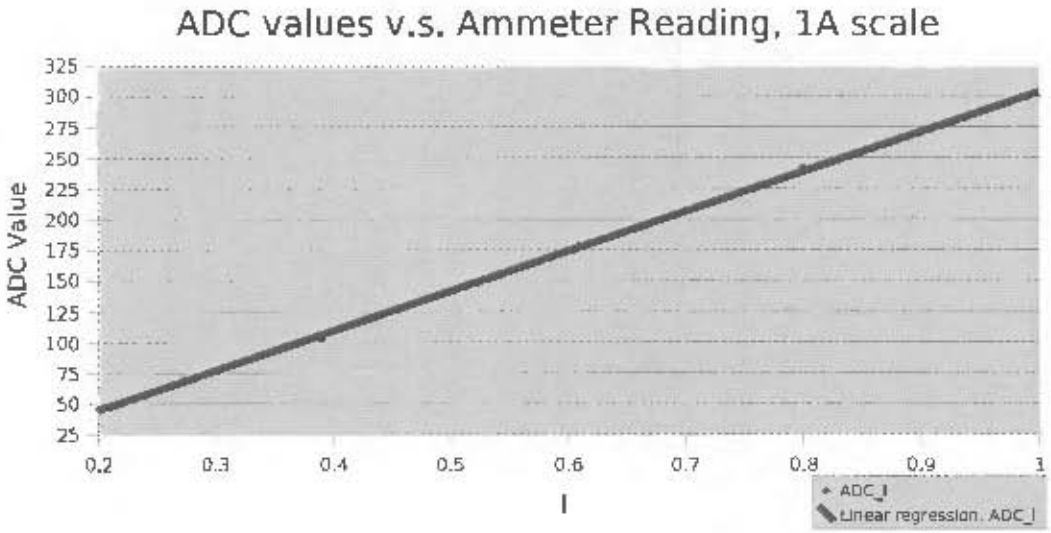

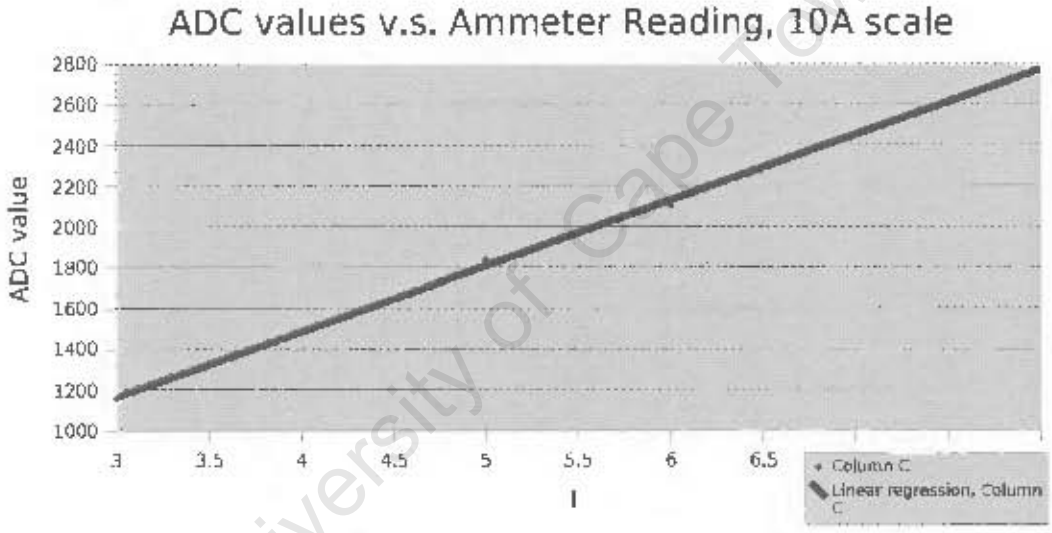

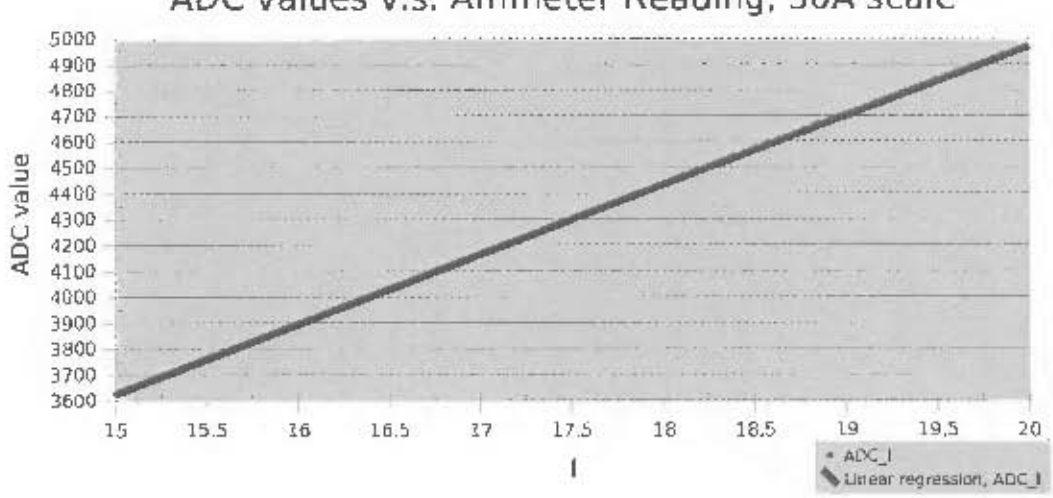

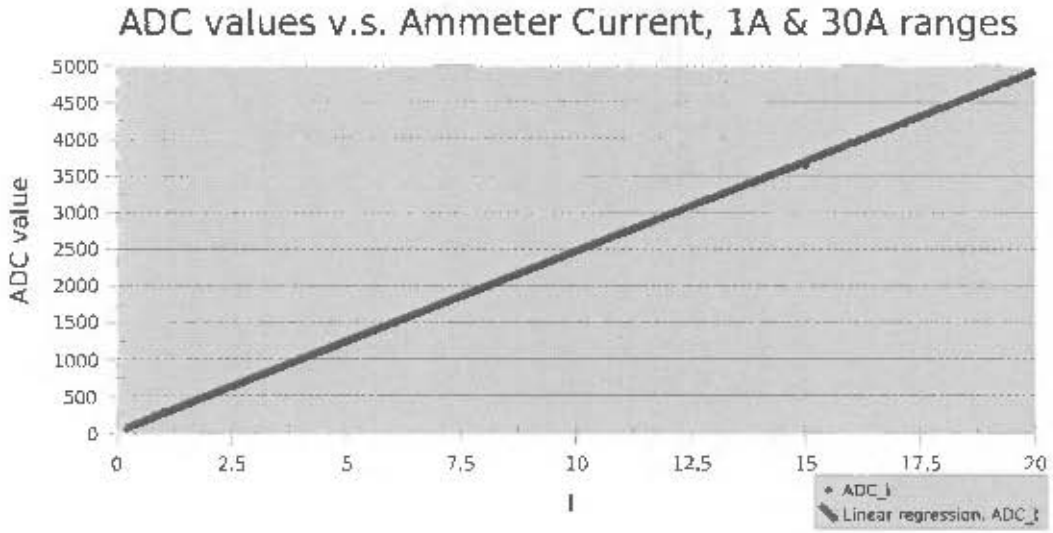

Appendix VI – ATMEL application note AVR121 : Enhancing ADC resolution by oversampling

AVR121: Enhancing ADC resolution by oversampling

8-bit AVR Microcontrollers

Application Note

Features

- Increasing the resolution by oversampling
- Averaging and decimation
- Noise reduction by averaging samples

1 Introduction

Atmel's AVR controller offers an Analog to Digital Converter with 10-bit resolution. In most cases 10-bit resolution is sufficient, but in some cases higher accuracy is desired. Special signal processing techniques can be used to increase the resolution of the measurement. By using a method called 'Oversampling and Decimation' higher resolution might be achieved, without using an external ADC. This Application Note explains the method, and which conditions need to be fulfilled to make this method work properly.

Figure 1-1. Enhancing the resolution.

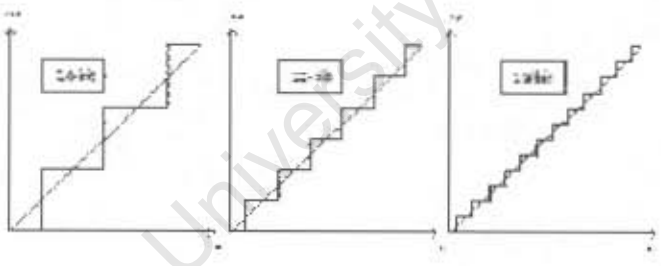

AVR121: Enhancing ADC resolution by oversampling

8-bit AVR Microcontrollers

Application Note

Features

- Increasing the resolution by oversampling
- Averaging and decimation
- Noise reduction by averaging samples

1 Introduction

Atmel's AVR controller offers an Analog to Digital Converter with 10-bit resolution. In most cases 10-bit resolution is sufficient, but in some cases higher accuracy is desired. Special signal processing techniques can be used to improve the resolution of the measurement. By using a method called 'Oversampling and Decimation' higher resolution might be achieved, without using an external ADC. This Application Note explains the method, and which conditions need to be fulfilled to make this method work properly.

Figure 1-1. Enhancing the resolution.

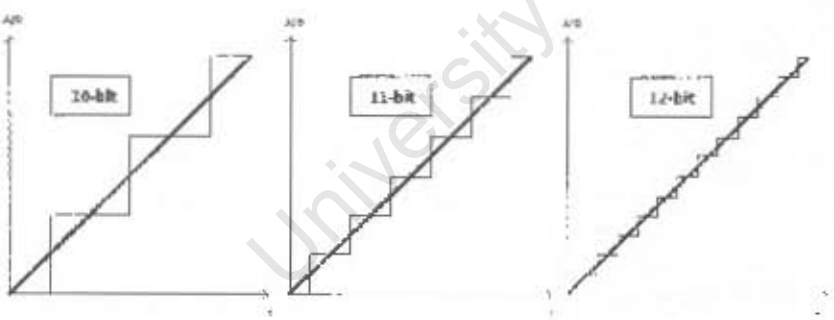

Rev. 8003A-AVR-09/05

2 Theory of operation

Before reading the rest of this Application Note, the reader is encouraged to read Application Note AVR120 - 'Calibration of the ADC', and the ADC section in the AVR datasheet. The following examples and numbers are calculated for Single Ended Input in a Free Running Mode. ADC Noise Reduction Mode is not used. This method is also valid in the other modes, though the numbers in the following examples will be different.

The ADCs reference voltage and the ADCs resolution define the ADC step size. The ADC's reference voltage, V_{REF}, may be selected to AVCC, an internal 2.56V / 1.1V reference, or a reference voltage at the AREF pin. A lower V_{REF} provides a higher voltage precision but minimizes the dynamic range of the input signal. If the 2.56V V_{REF} is selected, this will give the user ~2.5mV accuracy on the conversion result, and the highest input voltage that is measured is 2.56V. Alternatively one could consider using the ADC input channels with gain stage. This will give the user the possibility of measuring an analog signal with better voltage precision, at the expense of the ADCs dynamic range. If it is not acceptable to trade dynamic range for better voltage resolution, one could choose to trade oversampling of the signal for improved resolution. This method is however limited by the characteristic of the ADC. Using oversampling and decimation will only lower the ADCs quantization error, it does not compensate for the ADCs integral non-linearity.

2.1 Sampling frequency

The Nyquist theorem states that a signal must be sampled at least twice as fast as the bandwidth of the signal to accurately reconstruct the waveform; otherwise, the high frequency content will *alias* at a frequency inside the spectrum of interest (passband). The minimum required sampling frequency, in accordance to the Nyquist Theorem, is the Nyquist Frequency.

Equation 2-1. The Nyquist Frequency

$$f_{nyquist} > 2 \cdot f_{signal}$$

Where f_{signal} is the highest frequency of interest in the input signal. Sampling frequencies above $f_{nyquist}$ are called 'oversampling'. This sampling frequency, however, is just a theoretical absolute minimum sampling frequency. In practice the user usually wishes the highest possible sampling frequency, to give the best possible representation of the measured signal, in time domain. One could say that in most cases the input signal is already oversampled.

The sampling frequency is a result of prescaling the CPU clock; a lower prescaling factor gives a higher ADC clock frequency. At a certain point, a higher ADC clock will decrease the accuracy of the conversion as the Effective Number Of Bits, ENOB, will decrease. All ADCs has bandwidth limitations, AVRs ADC is no exception. According to the datasheet, to get a 10 bits resolution on the conversion result, the ADC clock frequency should be 50kHz – 200kHz. When the ADC clock is 200kHz, the sampling frequency is ~15kSPS, which confines the upper frequency in the sampled signal to ~7.5kHz. According to the datasheet, the ADC clock can be driven on frequencies up to 1Mhz, though this will lower the ENOB.

3 Theory

3.1 Oversampling and decimation

The theory behind 'Oversampling and decimation' is rather complex, but using the method is fairly easy. The technique requires a higher amount of samples. These extra samples can be achieved by oversampling the signal. For each additional bit of resolution, n, the signal must be oversampled four times. Which frequency to sample the input signal with, is given by Equation 3-1. To get the best possible representation of a analog input signal, it is necessary to oversample the signal this much, because a larger amount of samples will give a better representation of the input signal, when averaged. This is to be considered as the main ingredient of this Application Note, and will be further explained by the following theory and examples.

Equation 3-1. Oversampling frequency

$$f_{(oversampling)} = 4^n \cdot f_{(nyquist}$$

3.2 Noise

To make this method work properly, the signal-component of interest should not vary during a conversion. However another criteria for a successful enhancement of the resolution is that the input signal has to vary when sampled. This may look like a contradiction, but in this case variation means just a few LSB. The variation should be seen as the noise-component of the signal. When oversampling a signal, there should be noise present to satisfy this demand of small variations in the signal. The quantization error of the ADC is at least 0.5LSB. Therefore, the noise amplitude has to exceed 0.5 LSB to toggle the LSB. Noise amplitude of 1-2 LSB is even better because this will ensure that several samples do not end up getting the same value.

Criteria's for noise, when using the decimation technique:

- The signal-component of interest should not vary significantly during a conversion.
- There should be some noise present in the signal.
- The amplitude of the noise should be at least 1 LSB.

Normally there will be some noise present during a conversion. The noise can be thermal noise, noise from the CPU core, switching of I/O-ports, variations in the power supply and others. This noise will in most cases be enough to make this method work. In specific cases though, it might be necessary to add some artificial noise to the input signal. This method is refereed to as Dithering. Figure 3-1 (a) shows the problem of measuring a signal with a voltage value that is between two quantization steps. Averaging four samples would not help, since the same low value would be the result. It may only help to attenuate signal fluctuation. Figure 3-1 (b) shows that by adding some artificial noise to the input signal, the LSB of the conversion result will toggle. Adding four of these samples halves the quantization steps, producing results that gives better representations of the input value, as shown in Figure 3-1 (c). The ADCs 'virtual resolution' has increased from 10 to 11-bit. This method is refereed to as Decimation and will be explained further in section 3-3.

Figure 3-1. Increasing the resolution from 10-bit to 11-bit.

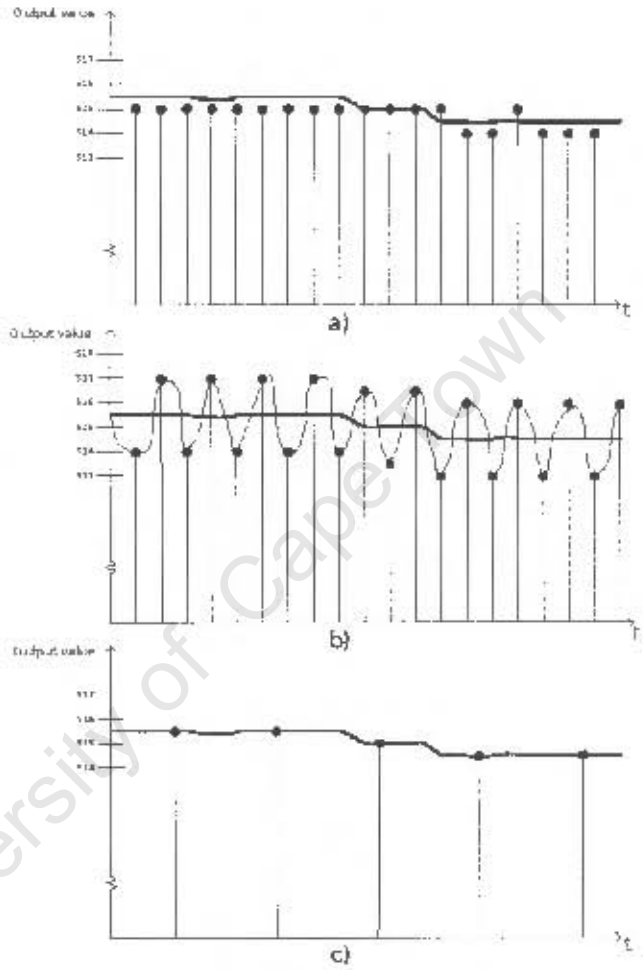

Another reason to use this method is to increase the Signal to Noise Ratio. Enhancing the Effective Number Of Bits, ENOB, will spread the noise over a greater binary number. The noises influence on each binary digit will decrease. Doubling the sampling frequency will lower the in-band noise by 3dB, and increase the resolution of the measurement by 0.5 bits.

3.3 Averaging

The conventional meaning of averaging is adding *m* samples, and dividing the result by *m*. Refereed to as *normal* averaging. Averaging data from an ADC measurement is equivalent to a low-pass filter and has the advantage of attenuating signal fluctuation or noise, and flatten out peaks in the input signal. The Moving Average method is very often used to do this. It means taking *m* readings, place them in a cyclic queue and average the most recent *m*. This will give a slight time delay, because each sample is a representation of the last *m* samples. This can be done with or without overlapping windows. Figure 3.2 shows seven (Av1-Av7), independently Moving Average result without overlapping.

Figure 3-2. Moving Average principle

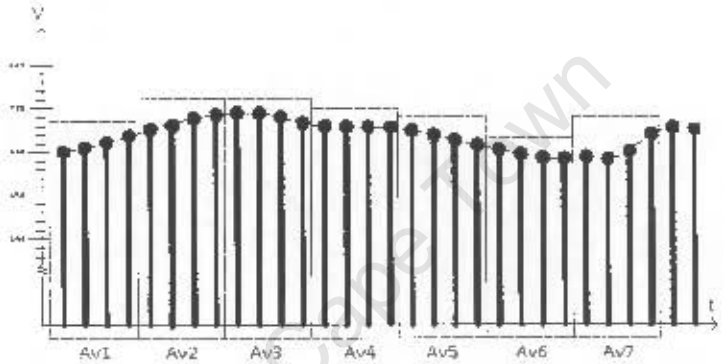

It is important to remember that normal averaging does not increase the resolution of the conversion. Decimation, or interpolation, is the averaging method, which combined with oversampling, which increases the resolution. Digital signal processing that oversamples and lowpass-filters a signal is often referred to as interpolation. In this sense, interpolation is used to produce new samples as a result of 'averaging' a larger amount of samples. The higher the number of samples averaged is, the more selective the low-pass filter will be, and the better the interpolation. The extra samples, *m*, achieved by oversampling the signal are added, just as in normal averaging, but the result are not divided by *m* as in normal averaging. Instead the result is right shifted by *n*, where *n* is the desired extra bit of resolution, to scale the answer correctly. Right shifting a binary number once is equal to dividing the binary number by a factor of 2. As seen from Equation 3-1, increasing the resolution from 10-bits to 12-bits requires the summation of 16 10-bit values. A sum of 16 10-bit values generates a 14-bit result where the last two bits are not expected to hold valuable information. To get 'back' to 12-bit it is necessary to scale the result. The scale factor, *sf*, given by Equation 3-2, is the factor, which the sum of 4^n samples should be divided by, to scale the result properly. *n* is the desired number of extra bit.

Equation 3-2.

$$sf = 2^n$$

3.4 When will 'Oversampling and Decimation' work?

Normally a signal contains some noise, this noise very often has the characteristic of Gaussian noise, more commonly known as White noise or Thermal noise, recognized by the wide frequency spectrum and that the total energy is equally divided over the entire frequency range. In these cases the method of 'Oversampling and decimation' will work, if the amplitude of the noise is sufficient to toggle the LSB of the ADC conversion.

In other cases it might be necessary to add artificial noise signal to the input signal, this method is referred to as Dithering. The waveform of this noise should be Gaussian noise, but a periodical waveform will also work. What frequency this noise signal should have depends on the sampling frequency. A rule of thumb is: "When adding *m* samples, the noise signals period should not exceed the period of *m* samples". The amplitude of the noise should be at least 1 LSB. When adding artificial noise to a signal, it is important to remember that noise has mean value of zero; insufficient oversampling therefore may cause an offset, as shown in Figure 3-3.

Figure 3-3. Offset caused by insufficient sampling.

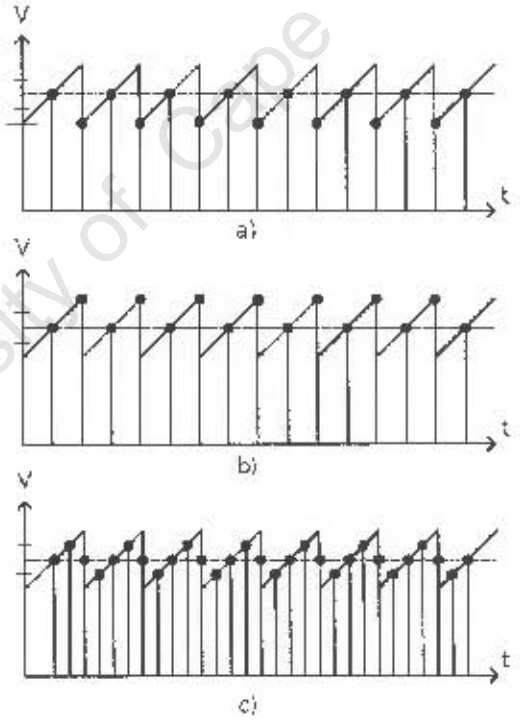

The stippled line illustrates the averaged value of the sawtooth signal. Figure 3-3 (a) will cause a negative offset. Figure 3-3 (b) will cause a positive offset. In Figure 3-3

(c) the sampling is sufficient, and offset is avoided. To create an artificial noise signal, one of the AVRs counters can be used. Since the counter and the ADC use the same clock source, this gives the possibility of synchronizing the noise and the sampling frequencies to avoid offset.

3.5 Example 1

A Brew Master in Dublin wants to measure the temperature of a process in his brewery. A slow varying signal represents the temperature measurement, and the nominal voltage in its environmental temperature is 2.5 V. Figure 3-4 shows the characteristic of the temperature-measuring device.

Figure 3-4. Voltage / Temperature function

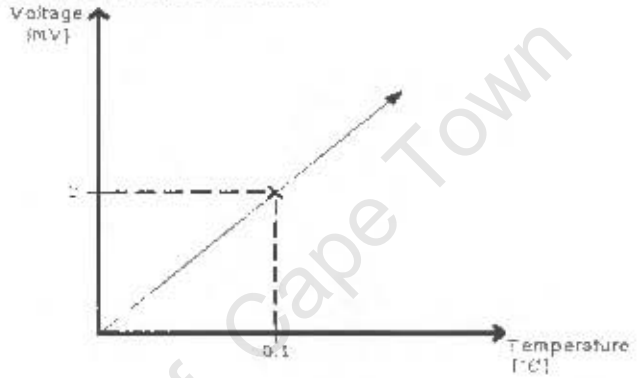

The Brew Master doesn't want to minimize the dynamic range of the input signal and chooses a 5V reference voltage for the ADC. In this case a 10-bit ADC cannot provide a conversion result accurate enough, since the result's LSB represents a ~5mV 'step'. This is unacceptable since this will give a result that may be up to 0.25°C off. The Brew Master desires the result to have 0.1°C accuracy, which demands a voltage resolution below 2mV. If the measurement was represented by a 12 bits ADC, the voltage 'step' representing LSB would decrease to ~1.22mV. What the Brew Master needs to do is to transform the 10-bit ADC to a virtual 12-bit ADC. The input signal is varying very slowly; a very high sampling frequency is therefore not required. According to the datasheet, the ADC clock frequency should be between 50kHz and 200kHz to ensure 10-bit effective resolution. The Brew Master therefore chooses a 50kHz ADC clock frequency. Then the sampling frequency becomes ~3800 SPS. At one point the DC value that represent the temperature measurement is 2.4729V. Table 3-1 shows the different resolution options measuring this value when Vin =2.4729V and VREF =5V.

Table 3-1. Resolution options

Resolution	Voltage resolution	Oversampled	Right shifted	Ideal decimated result	Ideal voltage representation	Maximum Bandwidth
10 bit	~5 mV	NA	NA	NA	2.4683V	~7600Hz [1]
11 bit	~2.5 mV	4X	1X	1012	2.4707V	~1900Hz [1]
12 bit	~1.22mV	16X	2X	2025	2.4719V	~475Hz [1]
13 bit	~610 uV	64X	3X	4051	2.4725V	~118Hz [1]
14 bit	~300 uV	256X	4X	8103	2.4728V	~29Hz [1]
15 bit	~150 uV	1024X	5X	16206	2.4728V	~7Hz [1]
16 bit	~75 uV	4096X	6X	32413	2.4729V	~3Hz [1]

Notes: 1. ADC Clock = 200kHz

The result of a single conversion is 505, which at first glance may seem correct. But this binary number also corresponds to for instance 2.4663V. This makes the user uncertain and causes errors in the temperature measurement. In certain cases this might be critical. As concluded before; a signal normally includes enough noise to make the decimation method feasible.

To increase the resolution by one bit, four samples from the same 'neighborhood' are added. These samples have values that differ from each other by a few LSB, because of the noise. These four samples are added: 508 + 507 + 505 + 505 = 2025. According to the decimation principle the answer now need to be scaled back to 11-bit. It needs to be right shifted n times, where n is the desired extra number of bits. The result is 1012. After increasing the resolution, it suddenly is possible to achieve samples between the original quantization steps. Still, the signal is oversampled enough to increase the resolution further, to 12 bit. Adding 16 10-bit samples and right-shifting the result 2 times will do this. The result is 2025. This number is more reliable, since the error margin is reduced to ~1.22mV using a 12 bit result. This example shows that the user who started off with a slow varying signal, sampled 3800 times per second, with a voltage accuracy of ~5mV, now has 240 samples per second with a 12-bit resolution, and a voltage accuracy of ~1.22mV.

The user might still want to even out signal fluctuations by averaging 16 12-bit samples, the conventional way. This is done by adding 16 samples and dividing the result by 16. At the end the user has 15 SPS consisting of 16 averaged 12-bit adjacent samples, (15 • 16 • 16 = 3840).

- Normal averaging will minimize the consequences of random noise.
- 'Oversampling and decimation' will utilize the noise to enhance the resolution.

3.6 Example 2

To show the efficiency of this method, the following example will show that it is not necessary to use an external ADC to get higher accuracy. A signal generator is used to produce a linear ramp signal from 0V to 5V. In a 'low noise' environment, with a signal generator and an AVR controller plugged into an STK500 board, there may not be enough noise to toggle the last few bits of the 10-bit signal. It is therefore necessary to add artificial 'noise' to the input signal, to make the LSB toggle. Four methods were used successfully:

- Adding noise, generated by a signal generator, directly to the input signal.
- Generating noise with the AVR, using PWM, and adding it to the input signal.
- Adding noise, generated by the AVR, to AREF when using AVCC as VREF.
- Adding noise, generated by the AVR, to AREF when using AREF as VREF.

The easiest way to dither a signal is to add white noise directly to the signal, but in most cases the user does not have, or does not want to have, this kind of noise signal in the measuring environments. A more available method is to set up one of the counters in the AVR to produce a PWM signal and then low pass filter this 'noise' to appear as a DC with a ripple peak-to-peak value of a few LSB. An example of such a filter's details and component values are shown in Figure 3-5.

Figure 3-5. LP-filter

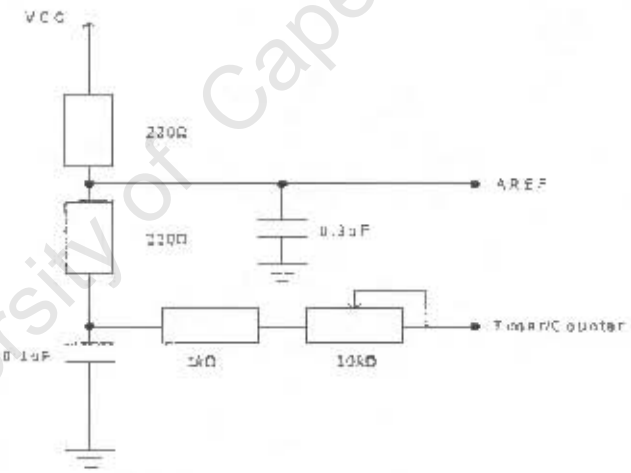

If VCC = 5V, the filtered signal at the AREF pin appears as 2.5V when the counter's duty-cycle is 0%, and as 5V when the counter's duty-cycle is 100%. In this example the duty cycle of the PWM-signal is 50%, and the base frequency is ~3900Hz. The 10kΩ potentiometer is used to adjust this ripple. The PWM- signal is used either as the reference voltage to the ADC at AREF, or as a noise generator connected to the AREF pin. With AVCC set as ADC reference voltage. The idea is that small variations in the reference voltage will give the same effect as small variations in the input signal, without disturbing the input signal.

Measuring a linear ramp signal as shown in Figure 3-6, gives the four graphs as shown in Figure 3-7, Figure 3-8, Figure 3-9 and Figure 3-10. Figure 3-7 shows a 10-bit discrete representation of the input ramp signal, measured without artificial noise

added. The quantization steps are very marked. To increase the resolution, the quantization steps need to be reduced.

Figure 3-8 shows a 12-bit discrete representation of the input signal when AREF is the ADC reference voltage, and AREF is added a few LSB noise. According to Equation 3-1, each 12-bit result consists of 16 10-bit samples. The offset was adjusted for the ADC, and in accordance with Application Note AVR120, the gain-error also needed adjustment. Figure 3-9 shows a 14-bit discrete representation of the input signal and Figure 3-10 shows the 16-bit discrete representation of the input signal. When measuring a signal containing noise, or when the reference voltage is varying like in this example, it is important to remember that the top and bottom values are decreased by the same value as the amplitude of the noise signal, giving a slight reduction in the dynamic range of the measured signal. In this certain case, as a safety margin, the offset was adjusted for 100mV.

Figure 3-6. Ramp Signal, 0-5V, 100% synchronous.

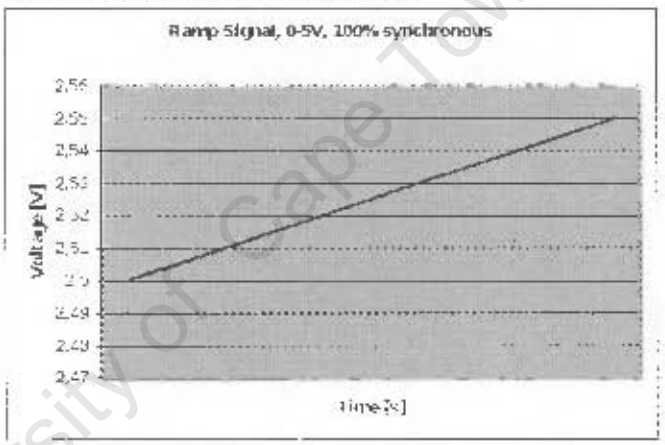

Figure 3-7. Ramp Signal reproduced with 10-bit resolution

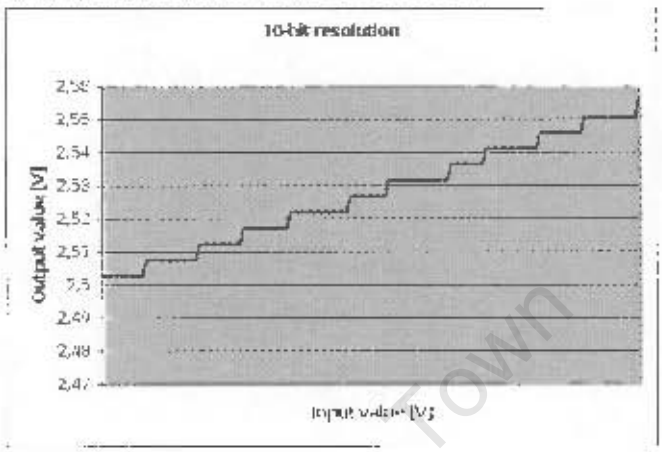

Figure 3-8. Ramp Signal reproduced with 12-bit resolution

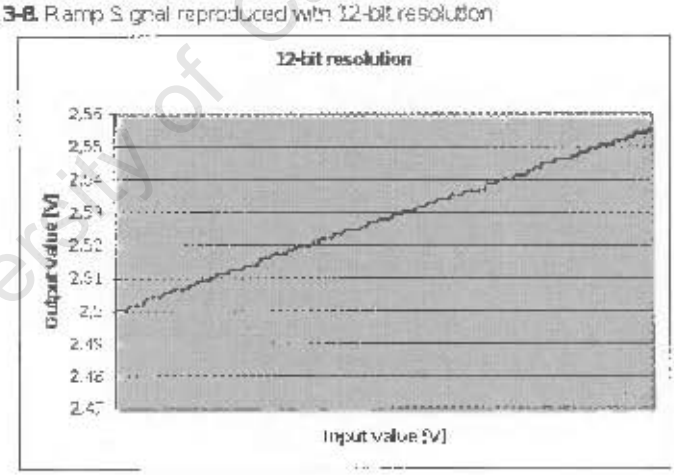

Figure 3-9. Ramp Signal reproduced with 14-bit resolution

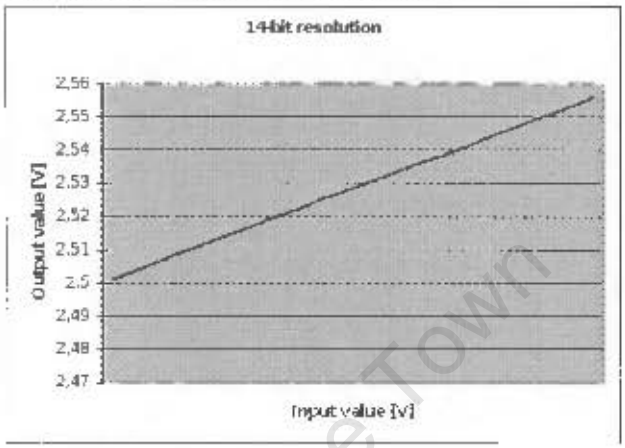

Figure 3-10. Ramp Signal reproduced with 16-bit resolution

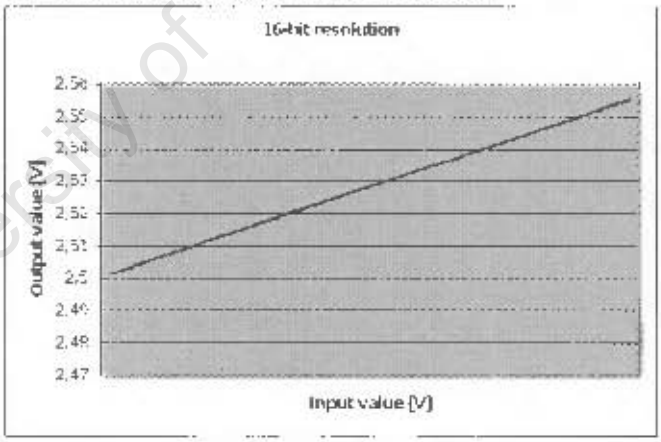

One can easily see that by using the oversampling and decimation method, it is possible to increase resolution significantly.

Summary

When the ADC samples a signal, it quantizes the signal in discrete steps. This introduces some error, often referred to as quantization error. Normal averaging will only even out signal fluctuations, while Decimation will increase the resolution. In a 4-times-oversampled signal, four adjacent data points are averaged to produce a new data point. Which frequency to oversample the signal with, can be calculated by equation 3-1. Adding these extra samples and right-shifting the result by a factor n, yields a result with resolution increased by n bits. Averaging four ADC results to get a new ADC result is the same as if the ADC sampled at ¼ of the rate, but also has the effect of averaging the quantization noise, which improves SNR. This will increase the ENOB and reduce the quantization error. With the availability of faster ADCs and with low memory cost, the advantages of oversampling are cost effective and desirable.

- Some noise has to be present in the signal, at least 1 LSB.
- If the noise amplitude is not sufficient, add noise to the signal.
- Accumulate 4^n 10-bit samples, where n is the desired extra number of bits in the resolution.
- Scale the accumulated result, by right shifting it n times.
- Compensate for errors, according to Application Note AVR120.

Atmel Corporation

2325 Orchard Parkway
San Jose, CA 95131, USA
Tel: 1(408) 441-0311
Fax: 1(408) 487-2600

Regional Headquarters

Europe
Atmel Sarl
Route des Arsenaux 41
Case Postale 80
CH-1705 Fribourg
Switzerland
Tel: (41) 26-426-5555
Fax: (41) 26-426-5500

Asia
Room 1219
Chinachem Golden Plaza
77 Mody Road Tsimshatsui
East Kowloon
Hong Kong
Tel: (852) 2721-9778
Fax: (852) 2722-1369

Japan
9F, Tonetsu Shinkawa Bldg.
1-24-8 Shinkawa
Chuo-ku, Tokyo 104-0033
Japan
Tel: (81) 3-3523-3551
Fax: (81) 3-3523-7581

Atmel Operations

Memory
2325 Orchard Parkway
San Jose, CA 95131, USA
Tel: 1(408) 441-0311
Fax: 1(408) 436-4314

Microcontrollers
2325 Orchard Parkway
San Jose, CA 95131, USA
Tel: 1(408) 441-0311
Fax: 1(408) 436-4314

La Chantrerie
BP 70602
44306 Nantes Cedex 3, France
Tel: (33) 2-40-18-18-18
Fax: (33) 2-40-18-19-60

ASIC/ASSP/Smart Cards
Zone Industrielle
13106 Rousset Cedex, France
Tel: (33) 4-42-53-60-00
Fax: (33) 4-42-53-60-01

1150 East Cheyenne Mtn. Blvd.
Colorado Springs, CO 80906, USA
Tel: 1(719) 576-3300
Fax: 1(719) 540-1759

Scottish Enterprise Technology Park
Maxwell Building
East Kilbride G75 0QR, Scotland
Tel: (44) 1355-803-000
Fax: (44) 1355-242-743

RF/Automotive
Theresienstrasse 2
Postfach 3535
74025 Heilbronn, Germany
Tel: (49) 71-31-67-0
Fax: (49) 71-31-67-2340

1150 East Cheyenne Mtn. Blvd.
Colorado Springs, CO 80906, USA
Tel: 1(719) 576-3300
Fax: 1(719) 540-1759

Biometrics/Imaging/Hi-Rel MPU/ High Speed Converters/RF Datacom
Avenue de Rochepleine
BP 123
38521 Saint-Egreve Cedex, France
Tel: (33) 4-76-58-30-00
Fax: (33) 4-76-58-34-80

Literature Requests
www.atmel.com/literature

8003A-AVR-03/05

Appendix VII – Detail design drawing

Assembly Exploded

Isometric View - Flywheel

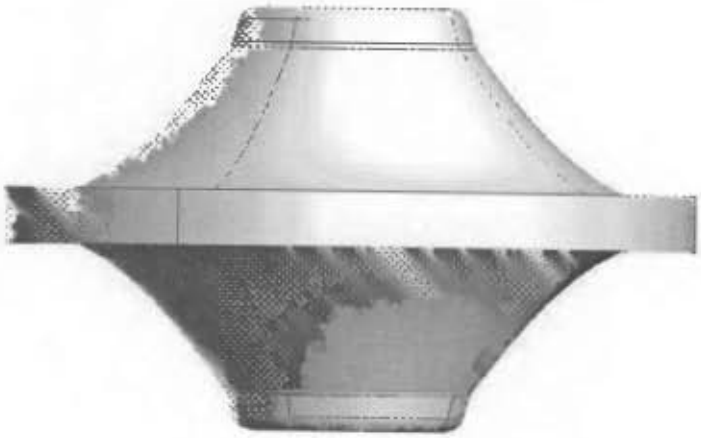

Flywheel - Side view

Flywheel - Plan view

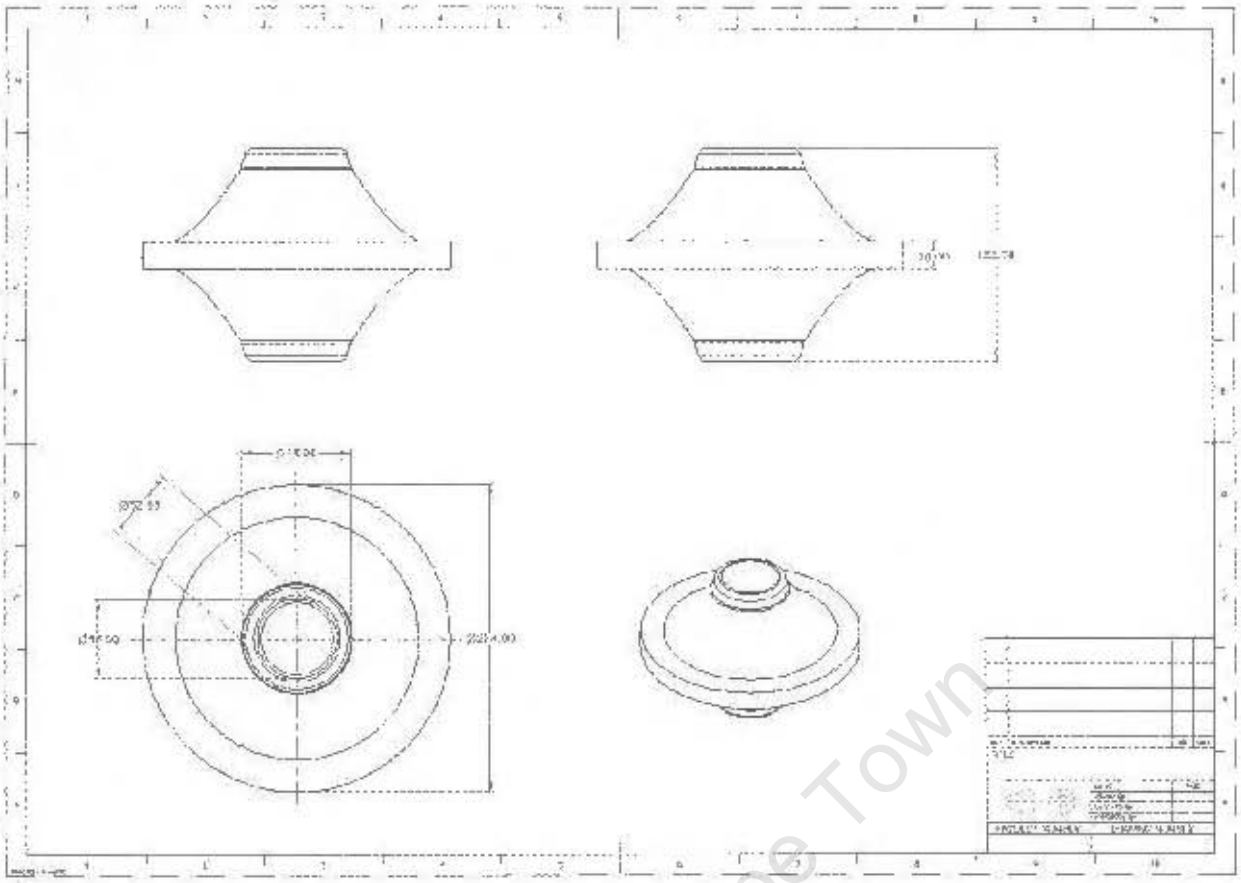

Flywheel detailed drawing

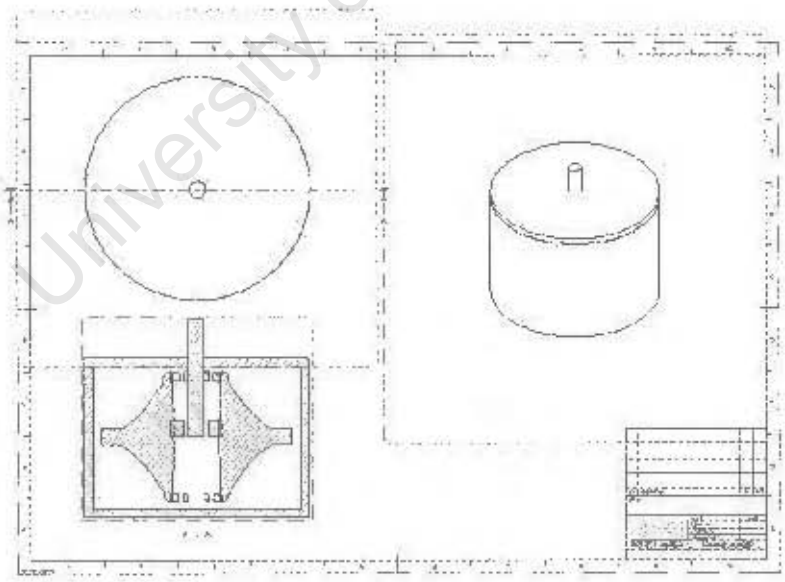

Flywheel Assembly drawing

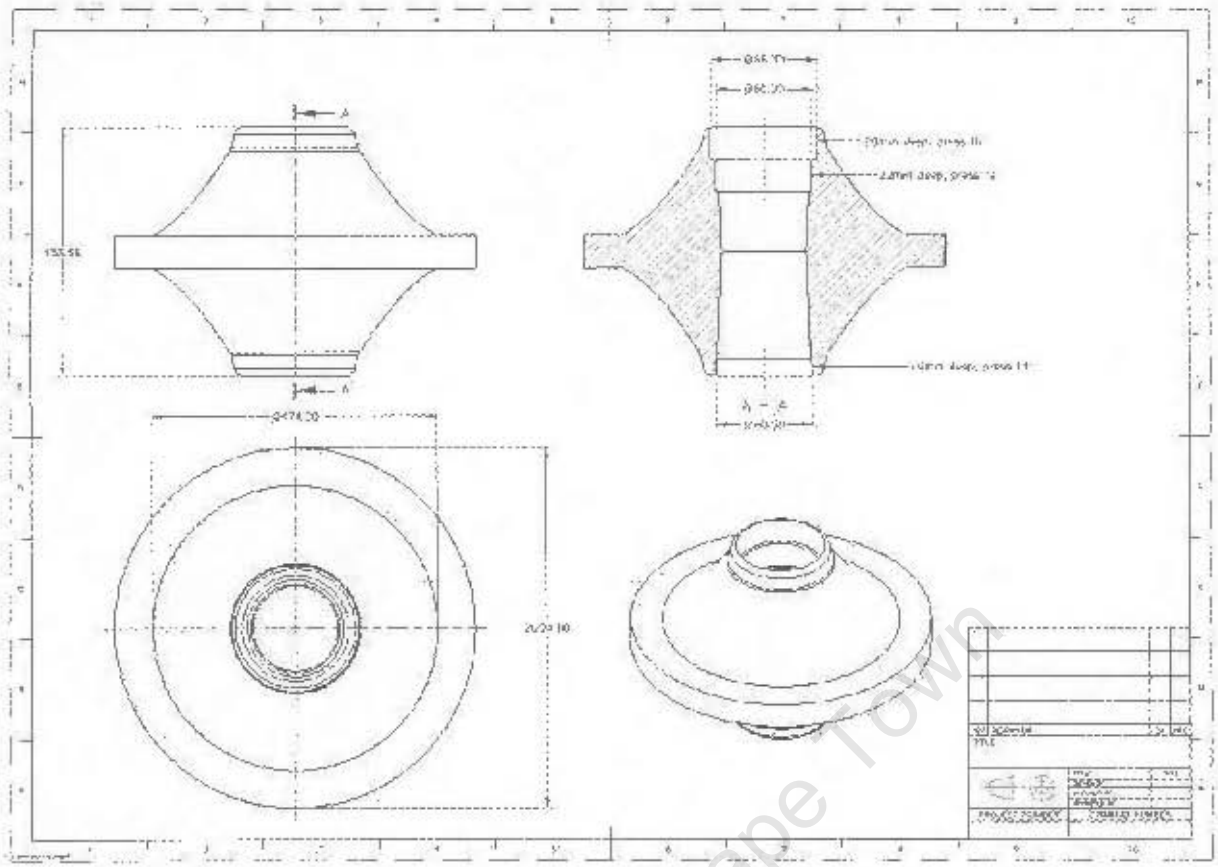

Flywheel modified drawing to accommodate machine and bearing components

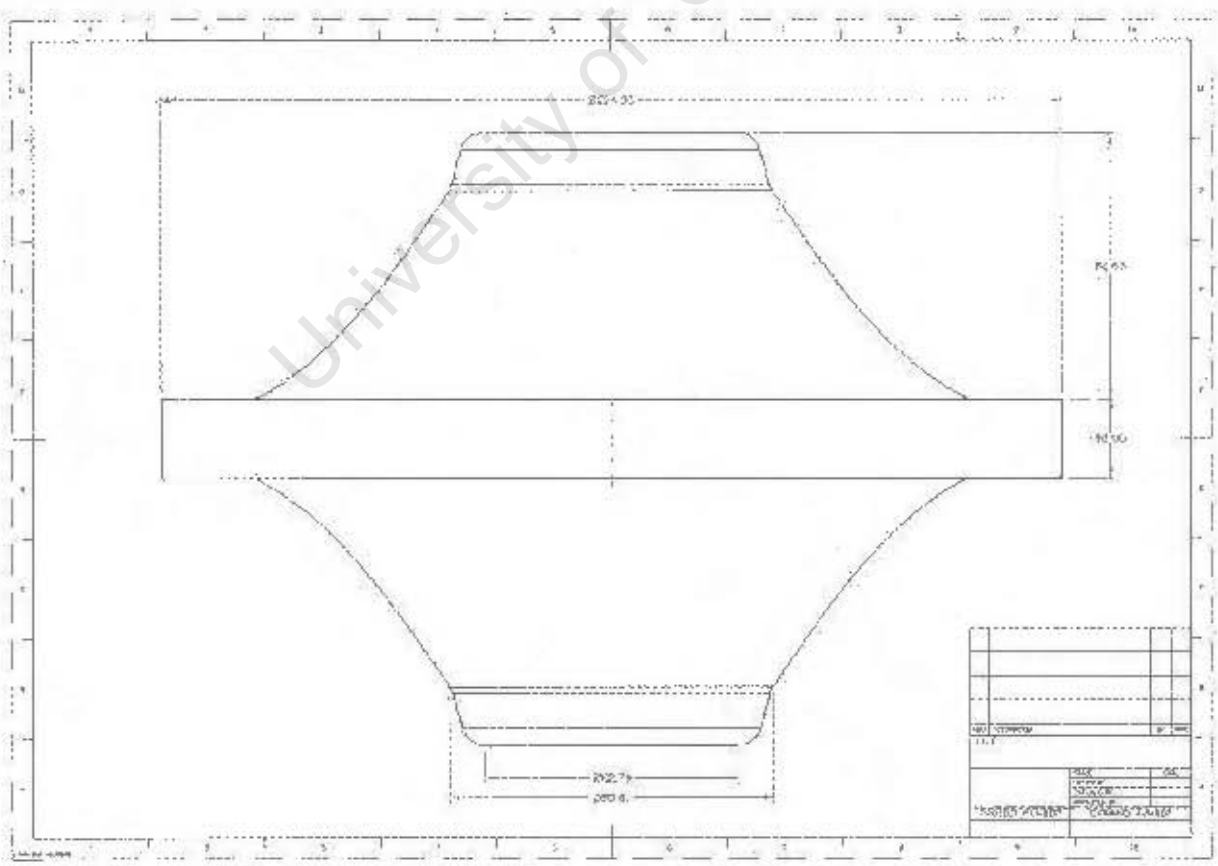

Flywheel profile for mould manufacture